Title

Structural and Biochemical Studies of the Amyloid-Forming Proteins Human Islet Amyloid Polypeptide and Amyloid-Beta

Author

Krotee, Pascal Alfreda Lombardo

Publication Date

2017

UNIVERSITY OF CALIFORNIA

Los Angeles

Structural and Biochemical Studies of the Amyloid-Forming Proteins Human Islet Amyloid Polypeptide and Amyloid-Beta

A dissertation submitted in partial satisfaction of the
requirements for the degree Doctor of Philosophy
in Molecular Biology

by

Pascal Alfreda Lombardo Krotee

2017

ABSTRACT OF THE DISSERTATION

Structural and Biochemical Studies of the Amyloid-Forming Proteins Human Islet Amyloid Polypeptide and Amyloid-Beta

by

Pascal Alfreda Lombardo Krotee
Doctor of Philosophy in Molecular Biology
University of California, Los Angeles, 2017
Professor David S. Eisenberg, Chair

Amyloid fibrils are associated with several diseases, including Type-II diabetes (T2D) and Alzheimer's disease (AD). The fibrils observed in each disease are composed of a particular protein; in T2D and AD, fibrils are primarily composed of human islet amyloid polypeptide (hIAPP), and amyloid-ß (Aß) and tau, respectively. Although these fibrils are associated with disease, the link of fibril structure to cytotoxicity remains elusive. Here, we use structural and biochemical studies of these proteins to uncover new insights into structural elements that may be important for cytotoxicity.

For hIAPP, we observe that fibrils are cytotoxic to cultured pancreatic ß-cells, leading us to determine the structure and cytotoxicity of protein segments that compose its amyloid spine. Using the cryo-electron microscopy (cryoEM) method micro-electron diffraction (MicroED), we discover that one segment, 19-29 S20G, forms pairs of ß-sheets mated by a dry interface that share structural features with and are similarly cytotoxic to

full-length hIAPP fibrils. In contrast, a second segment, 15-25 WT, forms non-toxic labile β-sheets. These segments possess different structures and cytotoxic effects; however, both can seed full-length hIAPP, and cause hIAPP to take on the cytotoxic and structural features of that segment. These results suggest that protein segment structures represent polymorphs of their parent protein and that segment 19-29 S20G may serve as a model for the toxic spine of hIAPP. We apply some of what we learned from these studies and combine it with previous structural studies to generate two putative models of full-length hIAPP fibrils.

Using MicroED and inhibitors developed using structure-based design, we discover that the spines of hIAPP (19-29 S20G) and Aβ (24-34) are similar in sequence and structure. The compatibility of the atomic structures prompts a molecular model as to how cross-seeding occurs between Aβ and hIAPP both *in vitro* and *in vivo.* Consistent with this observation, the inhibitors, designed against the hIAPP spine, reduce cytotoxicity of both full-length hIAPP and Aβ. However, the mechanisms of action of the inhibitors are different for the two proteins: they reduce hIAPP cytotoxicity by reducing fibril formation, while they reduce Aβ cytotoxicity by reducing some other prefibrillar assembly.

Next, using mass spectrometry and molecular dynamics (MD) simulations, we explore the potential for select segments of Aβ to form cylindrins, a β-barrel-shaped model for a toxic amyloid oligomer. Oligomers are small, soluble precursors to fibrils and are hypothesized to be the toxic type of Aβ aggregate. We observe that several segments, predicted to form cylindrins using Rosetta, form assemblies with similar cross-sections to the original cylindrin. Furthermore, one segment, Aβ 24-34, forms a trimer of dimers that is recognized by the oligomer-specific antibody, A11, an architecture reminiscent of the original cylindrin.

Last, we describe the development of novel peptide-based inhibitors of tau fibril formation developed using a MD-based method. This method reveals that the most effective

peptide-based inhibitors reduce fibril formation by competitive inhibition. The peptide-based inhibitors developed using this method may serve as potential pharmaceutical therapeutics for AD and the class of diseases known as tauopathies.

Taken together, these studies provide insights into potentially disease-relevant structures formed by proteins implicated in T2D and AD as well as novel strategies for mitigating such structures. Going forward, these studies may inform our development of more relevant therapeutics for these diseases.

The dissertation of Pascal Alfreda Lombardo Krotee is approved.

Lin Jiang

James U. Bowie

Carla Marie Koehler

Feng Guo

David S. Eisenberg, Committee Chair

University of California, Los Angeles

2017

To the scientists, teachers, family, and friends that inspired me to go on this journey.

Thank you.

TABLE OF CONTENTS

LIST OF FIGURES

LIST OF TABLES

ACKNOWLEDGEMENTS

The chapters in this doctoral thesis embody work completed alongside many collaborators that contributed valuable experiments, comments, discussions, and perspectives. I list them and their contributions in the following paragraphs.

Chapter 1 is composed of the reprinted article, Pascal Krotee, Jose A. Rodriguez, Michael R. Sawaya, Duilio Cascio, Francis E. Reyes, Dan Shi, Johan Hattne, Brent L. Nannenga, Marie E. Oskarsson, Stephan Philipp, Sarah L. Griner, Lin Jiang, Charles G. Glabe, Gunilla T. Westermark, Tamir Gonen, David S. Eisenberg. Atomic structures of fibrillar segments of hIAPP suggest tightly mated ß-sheets are important for cytotoxicity. *Elife.* 2017 Jan 3;6. pii: e19273. doi: 10.7554/eLife.19273. Sarah contributed supporting materials for dot blot assays performed for a series of cytotoxicity studies that appeared in earlier drafts of the article. Lin provided valuable guidance related to the cytotoxicity studies on seeded hIAPP in Figure 1.6. Stephan and Charles contributed the dot blot assays supporting the second round of cytotoxicity studies featured in the published article. Gunilla and Marie contributed the FRET-based biosensor assays to evaluate the cytotoxicity of the spine segments. The atomic structures in this article would not have been determined without Tamir and his research group, Francis, Dan, Johan, and Brent, who supported the MicroED data collection at Janelia Research Campus. Jose collected the MicroED data. Duilio processed diffraction data and worked with Michael and me to determine the atomic structures. Michael processed diffraction data, worked with Duilio and me to determine the atomic structure, calculated the fibril diffraction patterns in Figure 1.3, wrote part of the manuscript, and provided valuable discussion. David provided relentless support for and valuable discussion of the experiments and manuscript. I performed the cytotoxicity studies, processed diffraction data, worked with Duilio and

Michael to determine the atomic structure, performed all of the biochemical assays, and wrote the manuscript.

Chapter 2 is a draft manuscript for publication, Pascal Krotee, Michael R. Sawaya, Kevin Murray, Lin Jiang, David S. Eisenberg. Putative models of full-length hIAPP fibrils. Lin contributed the classic β-hairpin model using previously determined steric zipper structures from hIAPP, 19-29 S20G and 28-33 WT, and select ssNMR measurements of hIAPP fibrils from Luca and co-workers. Michael contributed the double S-shaped model using the ssNMR structure of amyloid-β determined by Griffin and co-workers paired with energy minimizations using FoldIt. Kevin provided some preliminary analysis of the double S-shaped model, also using FoldIt. I analyzed the models and wrote the chapter. David acted as the project director. We thank Robert Tycko for providing updated secondary structure predictions from TALOS for the development of our β-hairpin model.

Chapter 3 is a draft of a manuscript for publication, Pascal Krotee, Sarah Griner, Michael R. Sawaya, Jose A. Rodriguez, Stephan Phillipp, Francis E. Reyes, Dan Shi, Johan Hattne, Brent L. Nannenga, Kevin Murray, Ji Lee, Paul Seidler, Charles Glabe, Tamir Gonen, Lin Jiang, David Eisenberg. Common Fibrillar Spines of Amyloid-β and hIAPP Revealed by MicroED and Inhibitors Developed Using Structure-Based Design. Ji and Paul contributed fibril formation assays using the designed inhibitors and transthyretin and tau, respectively. Kevin contributed the hetero-assembly model in Figure 3.7. Stephan and Charles contributed dot blot assays of amyloid-β treated with the designed inhibitors. Tamir and his research group, Francis, Dan, Johan, and Brent, supported the MicroED data collection at Janelia Research Campus. Jose collected the MicroED data. Duilio processed diffraction data and worked with Michael and Sarah to determine the atomic structure. Michael processed diffraction data, worked with Duilio and Sarah to determine the atomic structure, performed the structural overlay of the two fibrillar spines, and calculated the fiber diffraction of the amyloid-β spine. Lin designed the peptide-based inhibitors using Rosetta. Sarah determined the atomic structure with Duilio and Michael, performed the *in vitro* kinetic studies of amyloid-β and the inhibitors, and wrote part of the manuscript. I performed all cytotoxicity assays, assisted with the design of the peptide-based inhibitors, performed *in vitro* kinetic studies of hIAPP and the inhibitors, and wrote the manuscript. David provided relentless support for and valuable discussion of the work.

Chapter 4 is composed of unpublished work and the reprinted article, Thanh D. Do, Nicholas E. LaPointe, Rebecca Nelson, Pascal Krotee, Eric Y. Hayden, Brittany Ulrich, Sarah Quan, Stuart C. Feinstein, David B. Teplow, David Eisenberg, Joan Emma Shea, Michael T. Bowers. Amyloid β-Protein C-Terminal Fragments: Formation of Cylindrins and β-Barrels. *J Am Chem Soc.* 2016 Jan 20;138(2):549-57. doi: 10.1021/jacs.5b09536. Eric performed the *in vitro* kinetic assays. Brittany and Sarah supported the kinetic assays. Nicholas performed the transmission electron microscopy analysis. Rebecca contributed the Rosetta energy calculations of the cylindrin-predicted protein segments. I performed the size exclusion chromatography (SEC) studies, dot blot studies, and re-wrote parts of the chapter. For this version in my dissertation, I added recombinant expression and protein purification data for the tandem-repeat peptides, electron microscopy of these peptides, the section on Aβ(21-30), and a cytotoxicity assay of Aβ. Thanh performed the mass spectrometry and molecular dynamics (MD) studies. Sarah, David T., David E., and Joan supervised the work. Thanh and Michael designed research and wrote the manuscript. All authors contributed comments to the manuscript.

Chapter 5 is a draft of a manuscript for publication, Jiyong Park, Pascal Krotee, Stuart Sievers, David Eisenberg. Multistage optimization of non-natural amino-acid inhibitors of tau fibril formation. Jiyong and Stuart spearheaded the design of the peptide-based inhibitors. Along with Stuart, I tested the *in vitro* efficacy of the inhibitors in delaying tau fibril formation. Stuart performed the NMR binding assays. Jiyong and I generated the figures and wrote the manuscript. In 2016, Paul Seidler began testing the efficacy of the inhibitors at blocking spread of tau aggregation in a cell model. His work is not shown in this chapter, but he continues that work today. David acted as the project director.

In addition to the co-authors of my doctoral dissertation, I have worked with an abundance of inspiring and talented scientists during my graduate career, and I am extremely thankful for each and every one of them. First, I thank my advisor, David Eisenberg, for opening the door to structural biology of amyloid proteins. Before we met, I was sure I wanted to study cancer metabolism, but he abruptly changed my mind with one lecture during my first year of graduate school. I was immediately taken by David's fervor for amyloid protein structure and its implications for disease. Over the following years, he was relentlessly supportive of me as I learned about crystallography and amyloid proteins, and struggled to determine an atomic structure. Finally, four years into my PhD, I obtained two atomic structures using MicroED. This work was supported by Tamir Gonen, Jose Rodriguez, and of course the dynamic structure determination duo, Duilio Cascio and Michael Sawaya. I am very thankful for Duilio and Mikey's wisdom, guidance, and friendship. Thank you.

Elsewhere around the Eisenberg laboratory, I had the pleasure of working with Dan Anderson, Stuart Sievers, Magda Ivanova, Mari Gingery, Luki Goldschmidt, Heather McFarlane, Jiyong Park, Linda Millau, Meytal Landau, Lukasz Salwinski, Harold Aschmann, Rebecca Nelson, Boris Brumshtein, Arturo Medrano-Soto, Jung-Reem Woo, Weixia Yu, Zack Plat, Shannon Esswein, Angela Soriaga, Anni Zhao, Howard Chang, Alice Soragni, Dan Li, Cong Liu, Andrew Min, Lorena Saelices, Lin Jiang, Alex Lisker, Tom Holton, Smriti Sangwan, Elizabeth Guenther, Sarah Griner, Michael Hughes, Sangho Lee, Icaro Marques, Qin Cao, Lisa Johnson, Anh Nguyen, Derek Pitman, Nhan Phan, Meng Zhang, Paul Seidler, Nicole Wheatley, Jeannette Bowler, Kevin Murray, David Boyer, Binsen Li, Shruti Sahay, and Cindy Chau. I thank all of you for supporting me during the different phases of my graduate career. Every little bit was meaningful, from sharing stories over lunch and coffee to sharing reagents in the lab. I am thankful for those that offered support through their humor and friendship, especially Shannon, Elizabeth, Boris, Lukasz, Luki, Mari, and Heather. I want to especially thank Dan Anderson for his wisdom, scientific rigor, and sharp wit.

Additionally, numerous facilities and their staff provided me with valuable support during my graduate career. I thank the Advanced Photon Source (APS) staff for beamline support: M. Capel, K. Rajashankar, N. Sukumar, J. Schuermann, I. Kourinov and F. Murphy at NECAT beam lines 24-ID. At UCLA, I thank Mike Collazo at the UCLA-DOE Crystallization Core, Mark Arbing at the Protein Expression Technology Center (PETC), and Ivo Atanazov at the EICN in CNSI. I thank Arnold Berk and Carol Eng for allowing me to use their biosafety cabinets and mammalian cell incubators for my cell culture studies. I thank Julian Whitelegge for performing multiple native mass spectrometry studies related to my research projects. I thank Callie Glynn for help in addressing the important yet daunting question of hIAPP cytotoxicity during her rotation in our laboratory. On the administrative side, I thank the Molecular Biology Institute Interdepartmental Program and the Whitcome Pre-Doctoral Fellowship program for support. Last, I thank my doctoral committee: Jim Bowie, Feng Guo, Lin Jiang, and Carla Koehler.

Numerous scientists inspired my scientific curiosity that led me to pursue a doctoral degree. I thank Barbara Wagner and Barbara Barry for sparking my interest in science in middle and high school, respectively. I thank Lee and Jane Bardwell, and their lab members, Jeff Rogers, Tom Whisenant, Lamar Blackwell, Kandarp Shah, Jillian Ory, and

Elizabeth Gordon, for mentoring me in the research laboratory during my undergraduate years at UC Irvine.

Last, I thank my creative, hardworking, inspiring, and loving family for their support. I thank Fritz Bahn for the support he provides my family and myself. I am forever grateful for my sweet, goofy, and enduring girlfriend, Kaycie. She has listened to me complain about every failed experiment and she has helped me celebrate the successful ones. I could not have finished this journey without you to support me every step of the way. I thank Kaycie for sharing her wonderful and generous family with me: Kathy, Randy, and Kristopher; they have unofficially adopted me as their second daughter. My sister, Gina, is my best friend and she is the light that guides me out of dark times; she helps me find the good in every situation. Through her own example, my mother showed me how to balance the pursuit of a good education and career with keeping love and family at my focal center. She has helped me maintain graduate school in the perspective of the grand scheme of things, thus minimizing the sometimes-difficult effects of its minutiae. I could not have accomplished everything I have without her to guide me. Thank you, mama.

VITA

2013-2015	Lecturer and Teaching Assistant University of California—Los Angeles
2010-2011	Junior Specialist University of California—Irvine
2006-2010	Undergraduate Research Assistant University of California—Irvine
2009	B.S., Developmental & Cell Biology | Minor in Business Management University of California—Irvine
2014-2015	Philip J. Whitcome Pre-Doctoral Fellowship University of California—Los Angeles
2015	Outstanding Poster Award UCLA Molecular Biology Institute Annual Retreat
2015	Margaret Etter Lecture Award American Crystallographic Associate Annual Meeting
2012	Honorable Mention | Graduate Research Fellowship Program National Science Foundation

Select Publications and Presentations

"The CryoEM Method MicroED Structure Determination of a Cytotoxic Fibrillary Segment from hIAPP." Invited Talk for CryoEM Sub-Group Meeting, Biophysical Society Annual Meeting, New Orleans, February 2017

Krotee P, Rodriguez JA, Sawaya MR, Cascio D, Reyes FE, Shi D, Hattne J, Nannenga BL, Oskarrson ME, Philipp S, Griner S, Jiang L, Glabe C, Westermark GT, Gonen T, Eisenberg DS. Atomic Structures of Fibrillar Segments of Human Islet Amyloid Polypeptide Suggest Tightly Mated β-Sheets Are Important for Cytotoxicity. eLife. 2017 Jan 3. doi: 10.7554/eLife.19273

Hong CS, Graham NA, Gu W, Espindola Camacho C, Mah V, Maresh EL, Alavi M, Bagryanova L, **Krotee P**, Gardner BK, Behbahan IS, Horvath S, Chia D, Mellinghoff IK, Hurvitz SA, Dubinett SM, Critchlow SE, Kurdistani SK, Goodglick L, Braas D, Graeber TG, Christofk HR. MCT1 Modulates Cancer Cell Pyruvate Export and Growth of Tumors that Co-express MCT1 and MCT4. Cell Rep. 2016 Feb 23;14(7):1590-601. doi: 10.1016/j.celrep.2016.01.057.

Do TD, LaPointe NE, Nelson R, **Krotee P**, Hayden EY, Ulrich B, Quan S, Feinstein SC, Teplow DB, Eisenberg D, Shea JE, Bowers MT. Amyloid β-Protein C-Terminal Fragments:

Formation of Cylindrins and β-Barrels. J Am Chem Soc. 2016 Jan 20;138(2):549-57. doi: 10.1021/jacs.5b09536.

"Structural Basis for Cytotoxic Effects of IAPP Amyloid Fibrils Revealed By Micro-Electron Diffraction," Biological Chemistry Seminar Series, UCLA, November 2015

"Micro Electron Diffraction Structure Determination of Type II Diabetes-Related Protein Segments," American Crystallographic Association Annual Meeting, Philadelphia, July 2015

Poster: **Krotee P**, Rodriguez J, Sawaya MR, Cascio D, Reyes F, Shi D, Hattne J, Nannenga B, Oskarrson M, Westermark G, Jiang L, Gonen T, Eisenberg DS. "Structural Basis for Cytotoxic Effects of Type-II Diabetes Related Amyloid Fibrils," FASEB Conference on Molecular Mechanisms and Physiological Consequences of Protein Aggregation, West Palm Beach, FL, June 2015

Poster: **Krotee P**, Rodriguez J, Sawaya MR, Cascio D, Reyes F, Shi D, Hattne J, Nannenga B, Gonen T, Eisenberg DS. "Micro Electron Diffraction Structure Determination of Type II Diabetes-Related Protein Segments," Molecular Biology Retreat, UCLA, April 2015

Gordon EA, Whisenant TC, Zeller M, Kaake RM, Gordon WM, **Krotee P**, Patel V, Huang L, Baldi P, Bardwell L. Combining docking site and phosphosite predictions to find new substrates: identification of smoothelin-like-2 (SMTNL2) as a c-Jun N-terminal kinase (JNK) substrate. Cell Signal. 2013 Dec;25(12):2518-29. doi: 10.1016/j.cellsig.2013.08.004.

Poster: **Krotee P**, Griner S, Goldschmidt L, Nelson R, Eisenberg D. "Analysis of Amyloid-β Oligomeric Structures and Their Cytotoxic Mechanisms," FASEB Conference on Molecular Mechanisms and Physiological Consequences of Protein Aggregation, Big Sky, MT, June 2013

Rusconi B, Maranhao AC, Fuhrer JP, **Krotee P**, Choi SH, Grun F, Thireou T, Dimitratos SD, Woods DF, Marinotti O, Walter MF, Eliopoulos E. Mapping the Anopheles gambiae odorant binding protein 1 (AgamOBP1) using modeling techniques, site directed mutagenesis, circular dichroism and ligand binding assays. Biochim Biophys Acta. 2012 Aug;1824(8):947-53. doi: 10.1016/j.bbapap.2012.04.011.

Poster: **Krotee P**, Whisenant T, Gordon E, Bardwell L. "Investigating the Role of Protein Domains in D-Site Mediated Interactions." P50 Scientific Advisory Board Poster Session, Center for Complex Biological Systems, Univ. of Calif.—Irvine, June 2009

"Interaction of Mixed Lineage Leukemia 4 Protein with the JNK MAP Kinase." Excellence in Research Program in Biological Sciences, School of Biological Sciences, Univ. of Calif.—Irvine, May 2008

CHAPTER 1

Atomic structures of fibrillar segments of hIAPP suggest tightly mated β-sheets are important for cytotoxicity

INTRODUCTION

Amyloid fibrils are associated with more than 25 diseases, including Alzheimer's disease, Parkinson's disease, and Type-II Diabetes (T2D) (1). The fibrils observed in each disease are composed of a particular protein; in T2D, amyloid fibrils are composed of human islet amyloid polypeptide (hIAPP) (2,3). hIAPP is a 37 residue polypeptide hormone that is co-secreted with insulin to modulate glucose levels (4,5).

Researchers have accumulated substantial evidence for a correlation between hIAPP aggregation and pancreatic β-cell death in the course of the disease, T2D. Approximately 90% of pancreatic tissue samples taken post-mortem from T2D patients contain islet amyloid primarily composed of hIAPP (6). The extent of islet amyloid positively correlates with pancreatic β-cell loss and insulin dependence (7–9). Additional support for a link comes from comparison of human and mouse IAPP: mouse IAPP differs from human IAPP by only 6 residues, 3 of which are β-strand breaking prolines. Consequently, mouse IAPP does not aggregate (10,11). Moreover, mice can be induced to develop islet amyloid and T2D when they are engineered to express human IAPP and fed a high fat diet (12,13). Perhaps the strongest support for a link is the mutation in hIAPP, hIAPP-S20G; segments that contain this mutation aggregate more quickly, contribute to increased pancreatic β-cell apoptosis, and are associated with early onset T2D in families who carry this lesion (14–19).

Although a link between hIAPP aggregation and pancreatic β-cell death is well established, precisely which type of hIAPP aggregate contributes to pancreatic β-cell death and insulin dependence remains undetermined. Using mostly *in vitro* studies, researchers have presented evidence for toxicity of multiple types of hIAPP aggregates. Early studies suggest that amyloid fibrils are the primary cytotoxic species because preparations that contain fibrillar hIAPP were more cytotoxic than soluble preparations of the protein (20–23). Using cells and transgenic rodents as disease models, other studies found hIAPP fibrils to be associated with apoptosis, β-cell loss, and T2D severity (24–29). In contrast, some studies show that the process of hIAPP fibril formation, not the amyloid fibrils themselves, is the source of toxicity (30,31). However, most current research studies suggest soluble pre-fibrillar oligomers are the primary type of toxic aggregate. Support for oligomers as the primary cytotoxic species comes from the observation of oligomers associated with caspase activity and ER stress, which precede the formation of extracellular amyloid fibrils (32–39). Several recent studies show that hIAPP fibrils are relatively inert and do not exert obvious toxicity. Despite these extensive *in vitro* studies, it is not clear that the toxic aggregates they describe also elicit toxicity *in vivo*.

In closer agreement with earlier studies, we find that hIAPP preparations that contain fibrils are cytotoxic to a rat pancreatic β-cell line, thus motivating us to determine the structure of the spine of hIAPP fibrils. If fibrils are a bona fide type of toxic aggregate *in vivo,* then determining the atomic structure of the spine of hIAPP fibrils is a logical approach for advancing our understanding of disease-relevant targets(40–42). Furthermore, we can utilize atomic structures as scaffolds for structure-based design of novel therapeutics that may protect against pancreatic β-cell death. Although full-length amyloid proteins have so far been resistant to crystallization, select protein segments that form the spines of amyloid fibrils do form crystals(43–45). Indeed, the atomic structures of nearly 90 amyloid spines have been revealed in this manner. Other studies have taken an alternative approach: they successfully employed solid-state NMR to gain detailed structural insights into hIAPP fibril structure (46,47); some of these structures have spurred successful inhibitor designs (48). Here, we use the cryoEM method MicroED to determine the atomic structure of two 11-residue segments, termed spine segments, that span the amyloid spine of hIAPP.

RESULTS

hIAPP preparations that contain fibrils are cytotoxic to cultured rat pancreatic β-cells

To compare the cytotoxic effects of oligomeric and fibrillar hIAPP, we generated hIAPP preparations that contained either amyloid oligomers or fibrils. We did this by aging the same concentration of hIAPP for 0 and 24 h time periods. Aging hIAPP for 24 h yielded amyloid fibrils and no detectable oligomers as assessed by Thioflavin-T (ThT) binding, negative-stain transmission electron microscopy (TEM), and a dot blot assay using the fibrillar oligomer-sensitive antibody LOC (Figure 1.1A). Aging hIAPP for 0 h, which is a freshly dissolved hIAPP sample, yielded oligomers as assessed by a dot blot assay using LOC, and no amyloid fibrils (Figure 1.1—Figure Supplement 1A). Of note, we probed both hIAPP preparations with 25 different conformational antibodies that are known to bind soluble oligomers, but only LOC showed binding to any of our preparations. Although LOC was raised against hIAPP fibrils (49), studies show that it also recognizes fibrillar oligomers (50), which share structural epitopes with amyloid fibrils and are structurally distinct from A11-positive pre-fibrillar oligomers.

We observe that hIAPP preparations that contain fibrils are significantly more cytotoxic to rat pancreatic β-cells than hIAPP preparations that contain oligomers but no detectable fibrils (Figure 1.1B, 1.1C). We assayed the cytotoxicity of the hIAPP preparations to Rin5F cells, a rat pancreatic β-cell line (51) using two metrics: 3-(4,5-

dimethylthiazol-2-yl)-2,5-diphenyltetrazolium bromide (MTT) dye reduction, an indicator of good metabolic health (52,53), and activation of caspase-3/7, an indicator of apoptosis (54). Furthermore, the insoluble fraction of the hIAPP 24 h sample, which contains fibrils (Figure 1.1—Figure Supplement 1B), is cytotoxic, while the soluble fraction is not (Figure 1.1D), further suggesting that fibrils are the toxic aggregate in our studies.

Although we do not detect oligomers in the 24 h sample, we cannot rule out the possibility that it may contain some undetectable population of slowly forming, yet highly toxic oligomers that associate with fibrils. Despite this possibility, we chose to focus on studying fibrillar structures of hIAPP.

Selection of amyloid spine segments for structural studies

Given that hIAPP fibrils are cytotoxic, we sought to identify the residues that compose their amyloid spine. We identified residues 15-29 as the amyloid spine based on several lines of evidence and previous work by others (11,55–57) . First, the sequence of mouse IAPP (mIAPP), which is non-amyloidogenic, differs from human IAPP only within this region (Figure 1.1E). Second, the only known familial disease mutation in hIAPP, hIAPP-S20G, also occurs within this region (Figure 1.1E) (14,15). Third, previous work by our laboratory has shown that Phe15 may be part of the amyloid spine because it is required for stabilizing an on-pathway alpha-helical dimer and mutating this residue can delay fibril formation (58).

For these reasons, we chose to focus on two overlapping 11-residue segments within this region of the sequence: residues 19-29 and residues 15-25. We chose to study the WT and early onset S20G mutation segments (Figure 1.1F). All four spine segments form amyloid fibrils or crystals (Figure 1.1—Figure Supplement 2) that seed full-length hIAPP fibril formation (Figure 1.1G, Figure 1.1—Figure Supplement 3), suggesting that the spine segments embody structural characteristics of full-length hIAPP fibrils.

Segment 19-29 S20G forms pairs of β-sheets tightly mated by a dry interface

To determine the structure of segment 19-29 S20G, we used Micro-Electron Diffraction (MicroED). MicroED employs a standard cryo electron microscope (cryoEM) in diffraction mode for data collection from 3D crystals only a few hundred nanometers thick (Figure 1.2A; Figure 1.3A) (59–63). Such thin crystals are capable of producing measurable Bragg peaks because electrons interact with matter more strongly than X-rays. Indeed, we found that the nano-sized 3D crystals used for MicroED produced higher resolution diffraction than relatively larger crystals suited for structure determination at a microfocus X-ray beamline (Figure 1.2A). Evidently, micron-thick needle crystals are sufficient for X-ray structure determination with six or seven residue peptides, but not for 11-residue peptides. These experiences closely mirrored those in the determination of the atomic structure of the toxic core of α-synuclein (45), an 11-residue segment that forms the spine of amyloid fibrils associated with Parkinson's disease.

The MicroED atomic structure of segment 19-29 S20G reveals pairs of parallel in-register β-sheets mated face-to-face by interdigitation of side-chains and exclusion of water molecules (Figure 1.3B, 1.3C). This arrangement is termed a class I steric-zipper. Such features are observed for amyloid spines of other proteins and have been associated with pathology (43,44,64–66). This zipper contains a tightly packed hydrophobic core consisting of Phe23, Ala25, and Ile27. Phe23 is the central and largest contributor the hydrophobic core, consistent with multiple other experiments (57,67–69). The dry interface buries 265 Å^2 of surface area per strand, which equates to 24 Å^2 per residue. This interface is one of the largest and most complementary of any structurally determined steric-zipper interface (Table 1.2); it has a shape complementary of 0.85. The dry interface is nearly as large as the toxic core of α-synuclein (45), but with higher shape complementarity.

The ß-sheets of the 19-29 S20G atomic structure possess a curvature that is not common in shorter hIAPP protein segments (40–42). To assess ß-sheet curvature, we compared the root mean square deviations (RMSD's) of sheets from planarity across all hIAPP protein segment atomic structures determined to date (Table 1.2). The 19-29 S20G structure ranks in the upper half of the list (Figure 1.3—Figure Supplement 1), containing both sheet curvature and a sharp kink. Most of the shorter peptides are nearly flat, but some have sharp kinks. The significance of deviation from planarity is not yet clear.

The similarity between the fiber diffraction pattern calculated from this steric-zipper and the fiber diffraction pattern collected from full-length hIAPP fibrils tends to validate the 19-29 S20G steric-zipper interface as a model for the amyloid spine of full-length hIAPP (Figure 1.3D). The diffraction patterns share several key features, including reflections at 4.7 Å and 2.4 Å along the meridian, a reflection at 3.7 Å along the off-meridian (left panel), and reflections at 10.0 Å and 5.0 Å along the equator (right panel).

Structural studies performed here and elsewhere by others suggest that 19-29 WT can form a similar dry interface to the one observed in the 19-29 S20G atomic structure. Radial profiles calculated from X-ray fiber diffraction of 19-29 WT and 19-29 S20G fibrils show strong reflections in common at 4.6 Å, 8.4 Å and 8.7 Å, and 34.7 Å, indicative of interstrand, intersheet, and proto-filament spacing, respectively (Figure 1.3—Figure Supplement 4). A previous study of 20-29 WT fiber diffraction revealed comparable reflections, which the authors used to formulate a fibril model of 20-29 WT that roughly agrees with our 19-29 S20G atomic structure (69). Our atomic structure and their model differ by a small shift in registration between sheets, allowing for tighter packing in the atomic structure. These results are consistent with earlier findings by Cao and co-workers, who observed that hIAPP-WT fibrils seed hIAPP-S20G fibril formation, thus suggesting a shared fibrillar structure (15).

Although the WT and mutant segments likely form similar structures, the structure of the mutant segment may be more stable. The stability of the mutant segment may stem from the early onset Gly20 mutation, which adopts an unusual geometry ($\varphi = -101.7°$ and $\psi = 107.5°$) that creates a kink in the peptide backbone. To investigate this hypothesis, we generated a model of 19-29 WT consisting of a mated pair of ten-stranded sheets. The model was identical to the 19-29 S20G atomic structure with the exception that we adjusted the backbone torsion angles of Ser20 to comply with the allowed regions of the Ramachandran plot for a non-glycine residue. We compared the energies of the WT and S20G structures after minimization with FoldIt (70). The dry interfaces are nearly identical between the two segments, except near Asn21, where the altered backbone torsion angles break the canonical Asn ladder hydrogen bonding interactions with neighboring Asn21 residues within the sheet and instead, form hydrogen bonds with Ser29 from the opposing sheet. The alteration separates the pair of sheets by approximately 1.5 Å in this region, and therefore the 19-29 S20G structure has a slightly lower energy than 19-29 WT (-590 REU vs. -535 REU).

Segment 15-25 WT forms an arrangement of labile unmated β-sheets

The atomic structure of segment 15-25 WT, also determined by MicroED (Figure 1.2B; Figure 1.4A), shows an arrangement of unmated β-sheets composed of anti-parallel out-of-register β-strands that is uncharacteristic of pathogenic amyloid fibrils (Figure 1.4B). Most pathogenic amyloid fibrils are composed of β-strands that stack perpendicular to the sheet-long axis, but the β-strands in out-of-register structures stack at an angle. Deviation of strands from the fibril perpendicular is a natural consequence of the registration shift implied by out-of-register structures. The out-of-register β-strands are stabilized by extensive hydrogen bonding. Within each sheet, the β-strands form two distinct, unequal interfaces: a stronger interface with twelve hydrogen bonds, and a weaker interface with eight hydrogen bonds (Figure 1.4B). This inequality between interfaces has been observed in previous examples of out-of-register sheets (42,71–73). A view down the “proto-fibril axis” of the crystal shows that the faces of adjacent sheets are wet and overlap only partially (Figure 1.4C); the asymmetric unit contains density for seven ordered water molecules and one thiocyanate molecule. The area buried between adjacent sheets is small (10.7 $Å^2$ per residue) compared to the average steric-zipper (20.1 $Å^2$ per residue). Hence, there is no dry interface between adjacent sheets in the crystal, and the structure seems labile compared to that of 19-29 S20G.

Consistent with our observation of unmated β-sheets in the atomic structure, we observe that 15-25 WT fibrils are relatively weak and reversible compared to 19-29 S20G fibrils, which possess a canonical pathogenic amyloid fibril architecture. Turbidity readings followed by negative-stain EM reveal that 15-25 WT fibrils completely disaggregate in the presence of heat and 1% SDS, but 19-29 S20G fibrils remain intact in up to 2% SDS (Figure 1.4—Figure Supplement 1).

Similar to 19-29 S20G, the 15-25 WT atomic structure reveals curved β-sheets. The sheets possess one of the highest RMSD’s of sheets from planarity for any hIAPP protein segment structure determined to date (Table 1.2, Figure 1.4—Figure Supplement 2).

X-ray fiber diffraction and radial profile analysis of 15-25 WT and 15-25 S20G fibrils indicate they form structures similar to each other (Figure 1.4—Figure Supplement 3). Taken together with the X-ray fiber diffraction data from the 19-29 segments, we conclude that the early onset S20G mutation does not confer a fibril morphology distinguishable from wild-type.

Structural polymorphs elicit different cytotoxic effects

Next we investigated the cytotoxic effects of the spine segments in order to determine if any of them were similarly cytotoxic to full-length hIAPP preparations.

Although the cytotoxic mechanism of hIAPP is not fully understood, several reports show hIAPP induces mitochondrial dysfunction, alters cell metabolism, and initiates activation of pro-apoptotic machinery (74–78). Based on these findings, we tested the cytotoxicity of the spine segments using MTT dye reduction (52,79) and a FRET-based biosensor to assay altered metabolism and pro-apoptotic machinery activation (80), respectively.

Using MTT dye reduction, we observe that the labile 15-25 fibrils are not cytotoxic to HEK293 cells (Figure 1.5A), whereas 19-29 S20G fibrils have comparable cytotoxicity to full-length hIAPP fibrils (Figure 1.5B). To verify the cytotoxic effects of each sample, we examined the morphology of the treated cells under a light microscope. Additionally, in the context of residues 19-29, the S20G segment is significantly more cytotoxic than the WT segment, consistent with parent full-length hIAPP (14,16) (Figure 1.5B). We did not detect any oligomers present in the 15-25 WT or 19-29 S20G fibril samples using the LOC antibody, which detects soluble hIAPP oligomers (Figure 1.5—Figure Supplement 1).

Based on our examination of the insoluble and soluble fractions of the cytotoxic 19-29 S20G sample, we determine that the cytotoxicity of 19-29 S20G mainly resides in its fibrillar form. We tested the cytotoxicity of the total, insoluble and soluble fractions of the 19-29 S20G sample to HEK293 cells using MTT dye reduction. We observe that the insoluble fraction, which contains amyloid fibrils, is similarly cytotoxic to the total (Figure 1.5C), just as we observed with full-length hIAPP (Figure 1.1D, Figure 1.1—Figure Supplement 1B). These results suggest that 19-29 S20G may form the toxic spine of full-length hIAPP.

Further evidence that 19-29 S20G may form the toxic spine of full-length hIAPP comes from our observation that (−)-epigallocatechin gallate (EGCG), a flavanol known to mitigate full-length hIAPP cytotoxicity by preventing hIAPP from forming fibrils (81), also mitigates 19-29 S20G cytotoxicity by preventing it from forming fibrils (Figure 1.5—Figure

Supplement 2B, 2C). We hypothesize that EGCG may mitigate fibril formation of full-length hIAPP and 19-29 S20G by binding to a common site, such as the dry interface of the amyloid spine. A previous study suggested EGCG may mitigate hIAPP fibril formation by binding hIAPP via hydrophobic interactions (82). Indeed, EGCG does not prevent fibril formation of 15-25 WT, which does not possess a dry hydrophobic interface (Figure 1.5—Figure Supplement 2D). In addition, these results further support our conclusion that preparations of segment 19-29 S20G that contain fibrils are cytotoxic.

Next we tested whether the spine segments activate pro-apoptotic machinery using a FRET-based biosensor assay for monitoring caspase-3 activity in real-time (80). In this assay, CHO cells are stably transfected with a construct containing enhanced cyan fluorescent protein (ECFP) and enhanced yellow fluorescent protein (EYFP) fused by a DEVD linker. FRET signal is observed by exciting ECFP at 440 nm. In cells undergoing apoptosis, active caspase-3-like proteases target and cleave the DEVD linker, resulting in loss of FRET signal. Cell viability is measured by monitoring the ratio of 540 nm/480 nm, which reports loss of FRET signal and increased caspase-3 activity.

Using this system, we observe that segment 19-29 S20G elicits the most caspase-dependent cytotoxicity of the spine segments and segments 15-25 are not cytotoxic (Figure 1.5D, 1.5E). Segment 19-29 S20G is not as cytotoxic as full-length hIAPP in this assay, possibly because hIAPP interaction with heparan sulfate proteoglycans (HSPG) is important for apoptosis induction (31), and residues 1-8, which are missing in all of the spine segments, are required for hIAPP binding to HSPG's.

Fibril seeds of 15-25 WT reduce the cytotoxicity of full-length hIAPP

Given that the spine segments seed full-length hIAPP fibril formation and that 19-29 S20G and 15-25 WT fibrils elicit different cytotoxic effects, we investigated whether seeding with either of the spine segments alters hIAPP cytotoxicity. To do this, we prepared seeded hIAPP at 10 μM with 10% monomer equivalent of pre-formed seeds, the same conditions used in the kinetic assay in Figure 1G. For all cytotoxicity assays, we dilute samples 1 to 10 to the concentration specified in culture medium containing pre-plated cells. Thus, we tested the cytotoxicity of seeded hIAPP at 1 μM in order to preserve the conditions of the kinetic assay.

Using MTT dye reduction, we observe that hIAPP seeded with non-toxic 15-25 WT fibrils is less cytotoxic than hIAPP alone, but hIAPP seeded with stable, toxic 19-29 S20G fibrils is similarly cytotoxic to hIAPP alone (Figure 1.6). Likewise, hIAPP seeded with stable, toxic 19-29 S20G fibrils is significantly more cytotoxic than hIAPP seeded with labile, non-toxic 15-25 WT fibrils (Figure 1.6). Seeds alone are not cytotoxic, indicating the cytotoxic effects we observe originate from the interaction of each seed with hIAPP and not the seed alone.

There are two possible explanations for the reduced cytotoxicity of the seeded 15-25 WT sample. First, the 15-25 WT seeds may seed a non-toxic species of full-length hIAPP, or second, the 15-25 WT seeds may interact with full-length hIAPP in some way that reduces its cytotoxicity.

X-ray fiber diffraction and radial profile analysis of the hIAPP fibrils used in the cytotoxicity assay reveal that fibrils formed by seeding with stable, toxic 19-29 S20G fibrils have a slightly tighter packing than fibrils formed by seeding with labile, non-toxic fibrils. hIAPP fibrils formed by seeding with stable, toxic 19-29 S20G fibrils exhibit reflections indicative of shorter equatorial Bragg spacings than hIAPP seeded with labile, non-toxic 15-25 WT fibrils (9.0 Å versus 10 Å) (Figure 1.6—Figure Supplement 1). The tighter packing of these fibrils may explain their enhanced cytotoxicity. Fiber diffraction could not be detected from seeds alone prepared under the same conditions.

DISCUSSION

In 1901, when Dr. Eugene Opie first observed islet amyloid in post-mortem pancreata of T2D patients, he proposed a link between the islet amyloid and T2D (83). Over a century later, multiple studies have shown an unequivocal link between hIAPP aggregation and T2D, but uncertainty remains about which type of hIAPP aggregate contributes to pancreatic β-cell death. Although most recent *in vitro* studies suggest soluble oligomers are the primary type of toxic aggregate, here, we find hIAPP samples that contain fibrils alter pancreatic β-cell metabolism and activate pro-apoptotic caspases.

These findings motivated us to determine the structure of the spine of hIAPP fibrils and elucidate structural features important for hIAPP cytotoxicity. To improve our likelihood of crystallization and structure determination, we selected 4 protein segments that span the spine. We discovered that segment 19-29 S20G forms a pair of β-sheets mated at a dry interface, a structure that shares key features with full-length hIAPP fibrils as described in the following paragraph. What's more, the fibrillar form of 19-29 S20G is cytotoxic. In contrast, segment 15-25 WT forms an unusual arrangement of single, out-of-register β-sheets that are not cytotoxic. The divergence in structure and cytotoxicity of segments 19-29 S20G and 15-25 WT suggests that strong, stable intermolecular interactions are important features of cytotoxic amyloid proteins.

The experiments of this study show that the 19-29 S20G atomic structure recapitulates many of the structural features and cytotoxic properties of hIAPP. First, preparations of 19-29 S20G that contain fibrils are cytotoxic, as is the case for full-length hIAPP. Second, X-ray fiber diffraction calculated from the dry interface of the 19-29 S20G atomic structure shares key features with fiber diffraction collected from full-length hIAPP fibrils. Third, segment 19-29 S20G elicits cytotoxicity by altering cell metabolism and activating pro-apoptotic machinery, mechanisms by which full-length hIAPP fibrils are thought to contribute to pancreatic β-cell death during T2D. Fourth, the early onset S20G mutation confers greater cytotoxicity within segment 19-29 and within full-length hIAPP. Last, EGCG, a flavanol that mitigates full-length hIAPP fibril formation and cytotoxicity, likewise mitigates 19-29 S20G fibril formation and cytotoxicity. These results, taken together with the canonical pathogenic amyloid fibril architecture of segment 19-29 S20G, suggest it represents the toxic amyloid spine of hIAPP.

Our studies begin to provide a framework for understanding which hIAPP fibril polymorphs may contribute to pancreatic β-cell death during T2D. Previous structural studies of hIAPP protein segments (40–42) and full-length hIAPP (46,47,84–87) identified an array of structures with diverse side-chain and sheet arrangements; the 15 hIAPP protein segment structures that overlap the hIAPP amyloid spine belong to 6 different steric-zipper classes (Figure 1.7). These multiple diverse structures suggest there is significant polymorphism within the hIAPP amyloid spine, but exactly which of these polymorphs elicit cytotoxicity was not known. By studying the structures and cytotoxic effects of protein segments in parallel, we identify a cytotoxic hIAPP fibril structure that may contribute to pancreatic β-cell death during T2D. Additionally, our studies suggest that not all hIAPP fibril structures are cytotoxic.

Both atomic structures presented here reveal a new and potentially important observation: curved β-sheets. In the dry interface of the 19-29 S20G atomic structure, the curved β-sheets accommodate the tightly packed hydrophobic core, which includes a bulky phenylalanine, while maintaining high shape complementarity and large buried surface area. Paradoxically, in the 15-25 WT atomic structure, the curved β-sheets appear to have an opposite effect: the curved β-sheets appear to prevent adjacent sheets from associating to form a canonical pathogenic amyloid fibril architecture. In both atomic structures, the effect of the curved β-sheets is dictated by the registry of adjacent β-sheets (Table 1.2, Figure 1.7).

The 15-25 WT atomic structure joins the recently discovered class of out-of-register protein segment structures, which exert disparate cytotoxic effects. Here, we show that 15-25 WT is not cytotoxic but in contrast, the out-of-register protein segment KDWSFY from β2-microglobulin elicits mild cytotoxicity (72). One notable difference between the two structures is that the 15-25 WT structure is formed of single sheets, while the KDWSFY structure is formed of sheets mated by a dry interface. The dry interface of the KDWSFY atomic structure results in a higher solvation energy per strand compared to the 15-25 WT atomic structure (122 cal/mol/strand vs. 19 cal/mol/strand). Given that cytotoxic structures like 19-29 S20G have relatively high solvation energies per strand (279 cal/mol/strand; Table 1.2), this difference may explain the disparate cytotoxic effects of the two out-of-register structures. However, we need more studies of out-of-register protein structures and their cognate cytotoxic effects to definitively make this conclusion. The disparate cytotoxic effects within this structure class lead us to believe that the nature of cytotoxicity is not simply conferred by in-register or out-of-register structures. As many studies have suggested, there may be more than one mechanism of amyloid-related toxicity and the different mechanisms may be catalyzed by different architectures. Alternatively, maybe if additional residues were included, the anti-parallel out-of-register fiber could be stabilized, thereby increasing its toxicity.

Although the 19-29 WT fibrils prepared in this study appear morphologically similar to 19-29 S20G fibrils, the 19-29 WT fibrils are likely polymorphic and may contain some fraction of fibrils that are structurally similar to non-toxic 15-25 WT fibrils. Previous structural studies of segment 20-29 WT fibrils show that it forms an array of polymorphs, some of which are similar to the 15-25 WT atomic structure (67–69,88,89). Structural polymorphism of 19-29 WT fibrils may explain their lower cytotoxicity than 19-29 S20G fibrils, which are homogenous in structure.

These findings, expedited by MicroED, may inform our understanding of hIAPP fibril structures that contribute to pancreatic β-cell death in Type-II Diabetes patients. Going forward, we can use our toxic amyloid spine model as a template for structure-based design in the effort to develop much needed therapeutics that protect against pancreatic β-cell death and disease progression (90,91). In addition, if hIAPP fibrils truly are a major type of toxic aggregate that contributes to T2D, then raising antibodies against hIAPP fibrils may represent a promising strategy for therapeutic development, especially in light of the recent success of preliminary studies with antibodies raised against amyloid-β(92).

MATERIALS AND METHODS

IAPP and protein segments

Human IAPP(1-37)-NH_2 wild-type and mouse IAPP(1-37)NH_2 wild-type were synthesized by Innopep (San Diego, CA) and CS Bio (Menlo Park, CA) and purified to greater than 98% purity. Human and mouse IAPP were prepared by dissolving the lyophilized proteins at 0.25-1 mM in 100% HFIP and leaving them to dissolve for several hours to ensure complete solubility. Next, the HFIP was removed with a CentriVap Concentrator (Labconco, Kansas City, MO). After removal of the HFIP, the peptides were dissolved at 1 mM, 5 mM, or 10 mM in 100% DMSO. The DMSO peptide stocks were diluted 100-fold in filter-sterilized Dulbecco's PBS (Cat. # 14200-075, Life Technologies, Carlsbad, CA). Samples were incubated at room temperature for the designated time periods.

All 4 spine segments were synthesized by GenScript (Piscataway, NJ) and purified to greater than 98% purity. Fibrils were formed by dissolving lyophilized peptide at 1 mM in PBS and 1% DMSO.

Crystallization

15-FLVHSSNNGFA-25 (15-25 WT). 15-25 WT was dissolved at 20 mg/ml in ice-cold, nano-pure water and then spin-filtered. Crystals were grown using the hanging drop vapor diffusion method at 4°C in 0.35 M NaSCN and 35% MPD. Crystals grew within several hours and reached maximum size in a week. 3D crystals only a few hundred nanometers thick grew alongside microcrystals in the same drops.

19-SGNNFGAILSS-29 (19-29 S20G). Microcrystals were grown using the hanging drop vapor diffusion method at 30°C in 0.2M acetate salts and 40% MPD. 3D crystals only a few hundred nanometers thick were grown in batch by dissolving lyophilized peptide at 1 mM in PBS and 1% DMSO without seeding. Crystals grew on the bench top at room temperature in several hours.

MicroED data collection

The procedures for MicroED data collection and processing largely follow published procedures (62,93). Briefly, a 2-3 µl drop of crystals in suspension was deposited onto a Quantifoil holey-carbon EM grid then blotted and vitrified by plunging into liquid ethane using a Vitrobot Mark IV (FEI, Hillsboro, OR). Blotting times and forces were optimized to keep a desired concentration of crystals on the grid and to avoid damaging the crystals. Frozen grids were then either immediately transferred to liquid nitrogen for storage or placed into a Gatan 626 cryo-holder for imaging. Images and diffraction patterns were collected from crystals using an FEG-equipped FEI Tecnai F20 TEM operating at 200 kV and fitted with a bottom mount TVIPS TemCam-F416 CMOS-based camera. Diffraction patterns were recorded by operating the detector in a movie mode termed ‘rolling shutter’ with 2 x 2 pixel binning (61). Exposure times for these images were either 2 or 3 seconds per frame. During each exposure, crystals were continuously unidirectionally rotated within the electron beam at a fixed rate of 0.3 degrees per second, corresponding to a fixed angular wedge of 0.6 or 0.9 degrees per frame.

Crystals that appeared visually undistorted and that were 100-300 nm thick produced the best diffraction. Datasets from individual crystals were merged to improve completeness and redundancy. Each crystal dataset spanned a wedge of reciprocal space ranging from 40-80°. We used a selected area aperture with an illuminating spot size of approximately 1 μm. The geometry detailed above equates to an electron dose rate of less than 0.01 $e^{-}/Å^{2}$ per second being deposited onto our crystals.

Measured diffraction images were converted from TVIPS format into SMV crystallographic format, using in-house software (available for download at http://cryoem.janelia.org/downloads) (62).

We used XDS to index the diffraction images and XSCALE (94) for merging and scaling together datasets originating from different crystals.

For 19-29 S20G, data from 6 crystals were merged to assemble the dataset used for molecular replacement.

For, 15-25 WT, data from 6 crystals were merged to assemble the dataset used for molecular replacement.

Structure determination

19-29 S20G. We determined the structure using molecular replacement. An idealized 7-residue poly-alanine strand led us to our atomic model. The solution was identified using Phaser (95). A dataset merged from 6 crystals was used to identify the initial model, but subsequent rounds of model building and refinement were carried out using a dataset from a single crystal. Free R flags were copied over from the dataset merged from 6 crystals to the single crystal dataset. Subsequent rounds of model building and refinement were carried out using COOT and Phenix, respectively (96,97).

15-25 WT. We determined the structure using molecular replacement. Dozens of search models were used, but an out-of-register β-sheet model led us to our solution. The solution was identified using Phaser (95). Subsequent rounds of model building and refinement were carried out using COOT and Phenix, respectively (96,97). To aid in model building, we used a feature enhanced map (FEM), which sharpens B factors at high resolution (98).

Calculations of the area buried and shape complementarity (SC) were performed with AREAIMOL (99,100) and SC (101–103), respectively.

ThT binding

30 µL of human and mouse IAPP preparations used in the cytotoxicity assays in Figure 1.1 were pipetted into a black-wall 384 well plate and then mixed with 3 µL of 1 mM Thioflavin-T (ThT). Fluorescence was recorded with an excitation wavelength of 444 nm and an emission wavelength of 482 nm.

Dot blot assay

1 µL of each sample generated for cytotoxicity assays in Figure 1.1 and Figure 1.5A and 1.5B were applied to a nitrocellulose membrane (Cat. # 162-0146, BioRad, Hercules, CA). Next, the membrane was blocked in 5% (w/v) nonfat dry milk in PBS-T (T = 0.1% (v/v) Tween-20 (Cat. #BP337-500, Fisher)) for 1 hour at room temperature. After blocking, the membrane was incubated with a 1:100 dilution of LOC polyclonal rabbit serum (Pacific Immunology, Ramona, CA) in 5% (w/v) milk in PBS-T at 4°C overnight. The membrane was washed in PBS-T for 10 minutes 3 times, and then incubated with anti-rabbit secondary antibody (RRID:AB_2307391; Cat. #111-035-144, Jackson ImmunoResearch, West Grove, PA) diluted 1:10,000 in PBS-T for 1 hour at RT. The membrane was washed 3 more times, and then the signal was developed with Clarity™ Western ECL Substrate (Cat. #170-5061, BioRad) and documented with a CCD camera. Exposures ranging from 5 seconds to 5 minutes were collected, but the 5 minute exposure was used in all figures.

Imaging and negative stain transmission electron microscopy

Samples were spotted onto grids (holey or non-holey) and left for 160 to 180 seconds. Remaining liquid was wicked off and grids were left to dry before analyzing. Sample grids were analyzed on the TF20 Electron Microscope (FEI, Hillsboro, OR). Images were collected at 3,500 or 6,000x magnification with an additional 1.4x post-column magnification and recorded using a TIETZ F415MP 16 megapixel CCD camera.

Samples for negative-stain EM were spotted on non-holey carbon-coated grids and left for 160 to 180 seconds. Remaining liquid was wicked off and then 2% uranyl acetate was applied to the grid. After 1 minute, the uranyl acetate was wicked off. The grids were left to dry before analyzing on the T12 Electron Microscope (FEI). Images were collected at 3,200 or 15,000x magnification and recorded using a Gatan 2kX2k CCD camera.

Cell culture

Rin5F cells were purchased from ATCC (RRID:CVCL_2177; Cat. # CRL-2058, Manassas, VA). Cells were cultured in RPMI media (ATCC, Cat. # 30-2001) plus 10% heat-inactivated fetal bovine serum. Cells were cultured at 37°C in a 5% CO_2 incubator. They tested negative for mycoplasma using a MycoAlert PLUS Detection Kit (Cat. #: LT07-701, Lonza, Switzerland) and they were authenticated using Cytochrome C Oxidase 1 (COX1) gene analysis by Laragen (Culver City, CA).

HEK293 c18 cells (hereon referred to as HEK293) were a gift from Carol Eng in the laboratory of Arnold J. Berk, but they were originally purchased from ATCC (RRID:CVCL_6974). Cells were cultured in DMEM media (Cat. # 11965-092, Life Technologies) plus 10% heat-inactivated fetal bovine serum and 1% pen-strep (Life Technologies). Cells were cultured at 37°C in a 5% CO_2 incubator. They tested negative for mycoplasma using a MycoAlert PLUS Detection Kit and they were authenticated using STR profiling (Laragen).

CHO cells were purchased from ATCC (RRID:CVCL_0214; Cat. #: CCL-61). Cells were cultured in RPMI 1640 with 11 mM glucose (Sigma) with 10% FBS, and 1% pen-strep. Cells were cultured at 37°C in a 5% CO_2 incubator. They tested negative for mycoplasma using a PCR-based method and they were authenticated using mRNA analysis.

Spine segment fibril formation

Spine segments were dissolved at 1 mM in PBS with 1% DMSO. Samples were incubated at room temperature for 15 hours or up to one week under quiescent conditions to form fibrils. The presence of fibrils was confirmed with electron microscopy. Fibril samples were diluted appropriately for cell viability assays and fibril formation assays.

Fiber diffraction and radial profile analysis

Fibrils were spun down and washed with water 3 times to remove any salt. Fibrils of spine segments were spun down using a tabletop microfuge. Full-length hIAPP fibrils and spine segment seeds were spun down using an Airfuge® Ultracentrifuge set at 75,000 rpm for 1 hour (Beckman-Coulter, Brea, CA). The samples were concentrated 10x in water and applied between two capillary ends and then the samples were left to dry overnight. Dried fibrils of spine segments and full-length hIAPP in Figure 3D were analyzed with a RIGAKU R-AXIS HTC imaging plate detector using Cu K(alpha) radiation from a FRE+ rotating anode generator with VARIMAX HR confocal optics (Rigaku, Tokyo, Japan). Fiber diffraction from full-length hIAPP fibrils used in Figure 6 was analyzed with an ADSC Q315 CCD detector at the Advanced Photon Source 24-ID-E beamline (Argonne, IL).

Radial profiles were calculated using a program written in-house. The program calculates the average intensity as a function of distance from the beam center.

Thioflavin-T assays

Thioflavin-T (ThT) assays were performed in black 96-well plates (Nunc, Rochester, NY) sealed with UV optical tape. hIAPP and mIAPP were dissolved at 1 mM in 100% HFIP.

The peptides were then diluted 100-fold in 20 mM sodium acetate pH 6.5 and 10 µM ThT. Unsonicated fibril seeds were added at 1 µM monomer equivalent concentration (10% v/v). ThT fluorescence was recorded with excitation and emission of 444 nm and 482 nm, respectively, using a SpectraMax M5 (Molecular Devices, Sunnyvale, CA). Experiments were performed in quadruplicate and readings were recorded every 3 minutes.

Model building and energy analysis of 19-29 WT and 19-29 S20G

To investigate whether 19-29 WT could form a similar structure to 19-29 S20G, we modeled a serine at position 20 in the 19-29 S20G atomic structure. We adjusted the backbone torsion angles so that they fell within the "allowed" regions of the Ramachandran plot for a non-glycine residue (96). We performed energy minimization using FoldIt (RRID:SCR_003788) (70) and compared the energies of the resulting models of 19-29 WT and 19-29 S20G.

Cytotoxicity assays

HEK293 cells and Rin5F cells were plated at 10,000 and 27,000 cells per well in 90 µL, respectively, in clear 96-well plates (Cat. # 3596, Costar, Tewksbury, MA). Cells were allowed to adhere to the plate for 20-24 hours.

For the assay in Figure 1.1, 50 µM full-length IAPP was aged *in vitro* for the designated incubation times. To generate the soluble and insoluble fractions, the "hIAPP 24 h" preparation was centrifuged at 21,000xg for 45 minutes and then the supernatant, which is the soluble fraction, was carefully removed and transferred to a 0.1 µm spin filter tube. Next, the supernatant was filtered and the pelleted material, which is the insoluble fraction, was resuspended in the original total volume.

For the assay in Figure 1.5, 1 mM spine segment and 100 µM full-length IAPP samples were generated by preparing the samples as described previously and then incubating them for 15 hours at room temperature under quiescent conditions. After the incubation period, the spine segments were diluted appropriately.

For all assays, 10 µL of sample was added to cells. By doing this, samples were diluted 1/10 from *in vitro* stocks. Experiments were done in triplicate.

The appropriate statistical test for significance was determined by assessing whether 1). The sample sets had a Gaussian distribution using a D'Agostino-Pearson omnibus normality test and 2). The sample sets had equal variance using a Bartlett's test or F test. For samples with Gaussian distributions and equal variances, we employed an unpaired t-test with equal standard deviations. For samples with Gaussian distributions, but unequal variances, we employed an unpaired t-test with Welch's correction. For samples with non-Gaussian distributions and unequal variances, we employed a Mann-Whitney U-test.

3-(4,5-dimethylthiazol-2-yl)-2,5-diphenyltetrazolium bromide (MTT) dye reduction assay for cell viability

After a 24-hour incubation of samples with cells, 20 µL of Thiazolyl Blue Tetrazolium Bromide MTT dye (Sigma, St. Louis, MO) was added to each well and incubated for 3.5 hours at 37°C under sterile conditions. The MTT dye stock is 5 mg/mL in Dulbecco's PBS. Next, the plate was removed from the incubator and 100 µL of MTT stop solution (Cat. #4101, Promega, Madison, WI) was added to each well. We ensured the MTT crystals were fully dissolved by placing the plates on an orbital shaker (slow speed) for about an hour prior to taking measurements. Alternatively, the MTT assay was stopped by carefully aspirating off the culture media and adding 100 µL of 100% DMSO to each well. Absorbance was measured at 570 nm using a SpectraMax M5. A background reading was recorded at 700 nm and subsequently subtracted from the 570 nm value. Cells treated with vehicle alone (PBS+0.1%DMSO) were designated at 100% viable, and cell viability of all other treatments was calculated accordingly.

For the MTT reduction assay in Figure 1.6, a single data point from the mIAPP sample set was deemed an outlier based on 2 lines of evidence: 1). The data point was identified as an outlier using a Grubb's test ($\alpha = 0.1$) for outliers using the n=9 sample set, and 2). When the sample set is pooled with more data collected for different experiments (n=42), the data point was identified as an outlier using a more stringent Grubb's test ($\alpha = 0.01$).

Caspase-3/7 activation assay

We used the caspase-3/7 GLO assay (Cat. # G8091, Promega, Madison, WI) to detect caspase-3/7 activation. For this assay, Rin5F cells were plated as previously described in white-walled 96-well plates (Cat. # 3917, Costar, Tewksbury, MA). After the designated aging period of each hIAPP preparation, 10 µL of sample was added to cells and thus diluted 1/10 from *in vitro* stocks. Experiments were performed in triplicate. Samples were incubated with cells for 24 hours. Next, cell culture media, caspase-3/7 reagent, and the cells were brought to room temperature. All media was aspirated from wells and then replaced with 25 µL of media and 25 µL of caspase-3/7 reagent and mixed thoroughly. The plate was incubated at room temperature for 30 minutes and then luminescence was measured using a SpectraMax M5. Experimental points were normalized to vehicle-treated cells, which were designated as 100%. Cells treated with 2 µM staurosporine were used as a positive control to ensure the assay kit worked correctly.

FRET-based real-time monitoring of caspase-3 activity

CHO cells were stably transfected with a vector producing EYFP and ECFP connected via a short linker containing the Asp-Glu-Val-Asp (DEVD) sequence targeted by activated caspase-3. The short linker allows fluorescence energy transfer (FRET) to occur between the two fluorophores. During apoptosis activated caspase-3 cleaves the linker resulting in a loss of FRET measured as a reduced 540 nm/480 nm emission ratio.

Cells were plated at 25,000 cells per well in black 96-well optical bottom plates (Nunc, Grand Island, NY) and the assay was performed in Krebs-Ringer (120 mM NaCl, 4.7 mM KCl, 2.5 mM $CaCl_2$, 1.2 mM $MgSO_4$, 0.5 mM KH_2PO_4, pH 7.4) supplemented with 20 mM HEPES and 2 mM glucose (KRHG).

hIAPP peptides (1-37, 15-25 WT and S20G, 19-29 WT and S20G) (final peptide concentration 50 μM in 1% DMSO) were mixed with sonicated, preformed fibrils (seeds) made of the same peptide (corresponding to 166 nM of monomers) and immediately added to the plated cells. FRET was monitored in real-time by measuring emission at 480 nm and 540 nm with 440 nm excitation in a FLUOstar Omega microplate reader (BMG Labtech) over 24 h at 37°C.

SDS sensitivity assay

Fibrils of 15-25 WT and 19-29 S20G at monomer equivalent concentrations were allowed to form for one week to ensure complete fibril formation. The samples were homogenized with vortexing, and then aliquoted to 0.5 mL tubes with equal volumes. Each fibril sample was treated with water or increasing amounts of SDS, and then heated at 55°C for 20 minutes. Next, an aliquot of each sample was transferred to a 384-well plate and turbidity was measured by recording absorbance at 340 nm. Each fibril sample was spotted onto a grid for negative-stain EM to analyze fibril abundance. The experiment was repeated twice, but the results of 1 experiment are shown in Figure 1.4—Figure Supplement 1.

ACKNOWLEDGEMENTS

We thank Dan Anderson for suggesting the use of FEM maps. We thank the Advanced Photon Source (APS) staff for beamline support during collection of fiber diffraction: M. Capel, K. Rajashankar, N. Sukumar, J. Schuermann, I. Kourinov and F. Murphy at NECAT beam lines 24-ID; the UCLA-DOE X-ray Crystallography Core Technology Center, Michael Collazo, and the UCLA-DOE Macromolecular Crystallization Core Technology Center for setting up initial crystallization screens; Ivo Atanasov and the Electron Imaging Center for NanoMachines (EICN) of California NanoSystems Institute (CNSI) at UCLA for the use of their electron microscopes; and the UCLA Statistical Consulting group for guidance on statistical computing. The UCLA-DOE X-ray and Macromolecular and Macromolecular Crystallization Core Technology Centers are supported in part by the Department of Energy grant DE-FC0302ER63421. Use of the Advanced Photon Source is supported by National Institutes of Health grants P41 RR015301 and P41 GM103403 and Department of Energy under Contract DE-AC02-06CH11357. We thank the Cure Alzheimer's Fund, the Swedish Research Council (VR 2015-02297), the Swedish Diabetes Foundation, the Janelia Research Campus visitor program, HHMI, and the National Institutes of Health (NIH) (R01 AG029430) for support.

COMPETING INTERESTS

The authors declare that no competing interests exist.

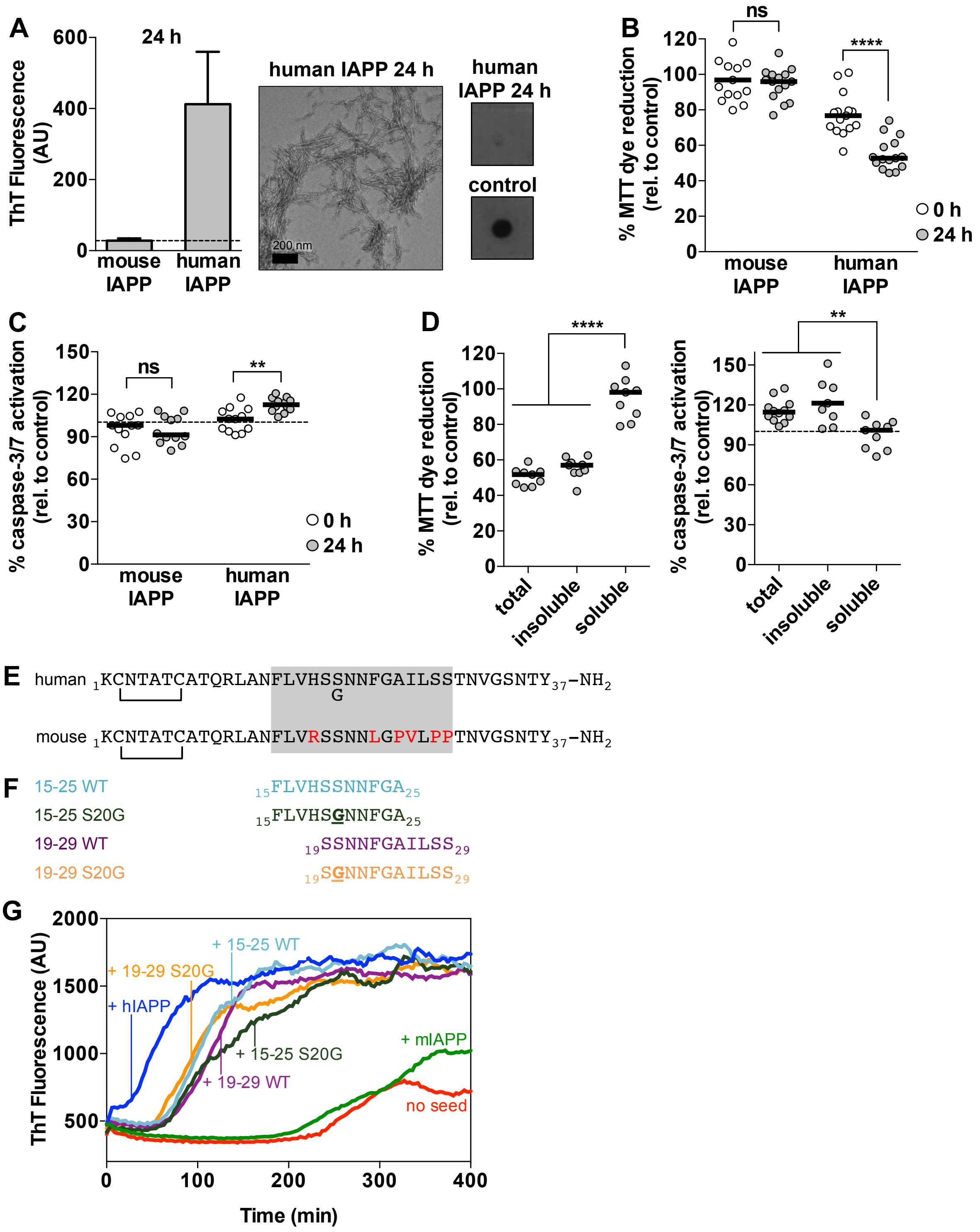

Figure 1.1. Preparations of hIAPP that contain amyloid fibrils are cytotoxic to a rat pancreatic β-cell line. A. Human IAPP (hIAPP) aged for 24 h contains amyloid fibrils and no detectable oligomers. Amyloid fibrils were observed using Thioflavin-

T (ThT) binding and negative-stain electron microscopy (EM). Oligomers were probed using a dot bot assay with the polyclonal anti-oligomer antibody, LOC. hIAPP oligomers were used as the positive control for LOC binding. The dashed line on the ThT binding graph indicates ThT fluorescence of vehicle alone. **B.** and **C.** Human IAPP aged for 24 h is significantly more cytotoxic than human IAPP aged for 0 h. In these experiments, 50 µM human and mouse IAPP were aged for the designated time periods and then they were applied to cells at 5 µM final concentration for 24 hours. Mouse IAPP (mIAPP), which does not form amyloid fibrils, is not cytotoxic regardless of time period of aging. Black horizontal bars indicate the median (n=12-15 across 4-5 biological replicates, each with 3 technical replicates). **B.** Rin5F cells treated with human IAPP aged for 24 h reduce significantly less MTT dye than Rin5F cells treated with human IAPP aged for 0 h (ns=not significant; ****, $p < 0.0001$ using an unpaired t-test with equal standard deviations). **C.** Rin5F cells treated with human IAPP aged for 24 h exhibit significantly higher caspase-3/7 activation than Rin5F cells treated with human IAPP aged for 0 h. Additionally, Rin5F cells treated with human IAPP aged for 24 h exhibit significantly higher caspase-3/7 activation than vehicle-treated cells (***, p=0.0008 using an ordinary one-way ANOVA), but Rin5F cells treated with human IAPP aged for 0 h do not (p=0.4286 using an ordinary one-way ANOVA) (ns=not significant; **, p=0.0011 using an unpaired t-test with equal standard deviations). **D.** The insoluble fraction of human IAPP aged 24 h, which contains amyloid fibrils and no detectable oligomers, contains the cytotoxic species. Cytotoxicity was measured using MTT dye reduction and detection of caspase-3/7 activation (****, $p < 0.0001$; **, $p < 0.0013$; n=9 across 3 biological replicates, each with 3 technical replicates). **E.** Amino acid sequences of human IAPP and mouse IAPP. The location of the early onset familial mutation, S20G, is shown below the human sequence. Red residues in the mouse sequence differ from the human sequence. The amyloid spine of human IAPP and the corresponding region in the mouse sequence is enclosed in the gray box. **F.** Schematic of protein segments that span the amyloid spine, hereon referred to as spine segments, targeted for characterization. **G.** Fibrils of spine segments seed hIAPP fibril formation, suggesting that spine segments embody structural characteristics of full-length hIAPP fibrils. 10 µM hIAPP was seeded with 10% (v/v) monomer equivalent of pre-formed, unsonicated seed of each spine segment. mIAPP, which does not contain amyloid fibrils, does not seed hIAPP fibril formation. Curves show average of 4 technical replicates.

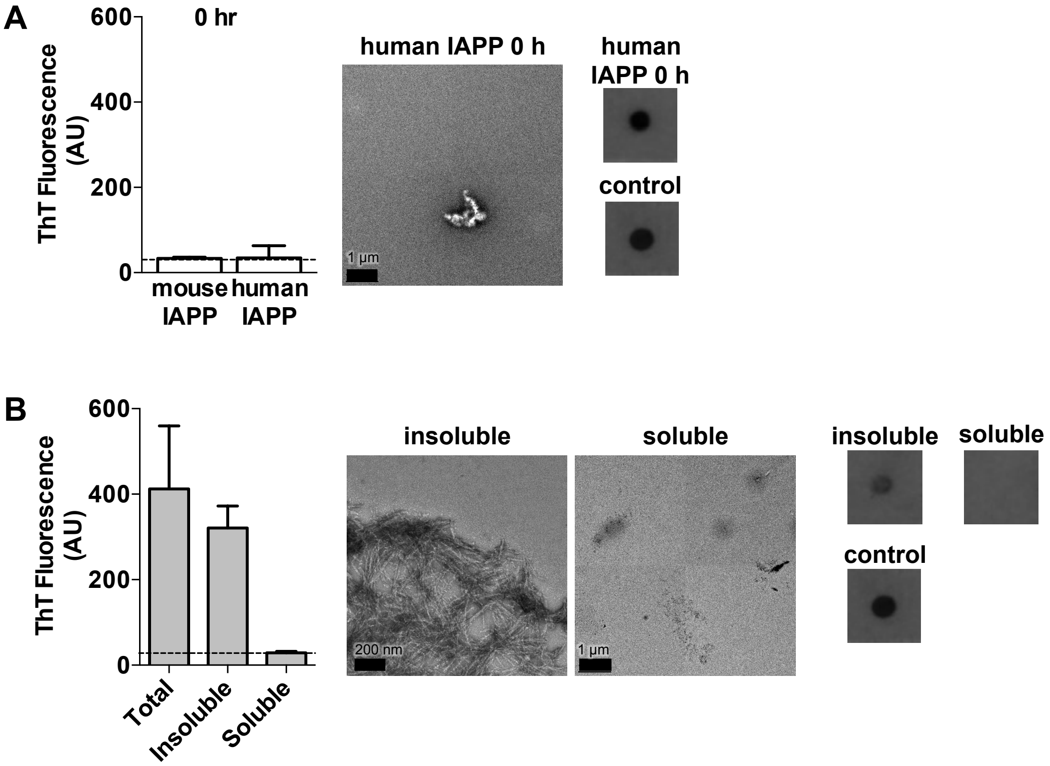

Figure 1.1—Figure Supplement 1. Characterization of hIAPP aged for 0 h and the soluble and insoluble fractions of hIAPP aged for 24 h. A. hIAPP aged for 0 h contains oligomers and no detectable amyloid fibrils as assessed by ThT binding, negative-stain EM and a dot blot assay using the anti-oligomer antibody, LOC. hIAPP oligomers were used as the positive control for LOC binding. **B.** The insoluble fraction of hIAPP aged for 24 h, which contains the cytotoxic species, is composed of amyloid fibrils and no detectable oligomers. The soluble fraction, which is not cytotoxic, contains no detectable amyloid fibrils or oligomers. The dashed line on the ThT binding graphs indicates ThT fluorescence of vehicle alone.

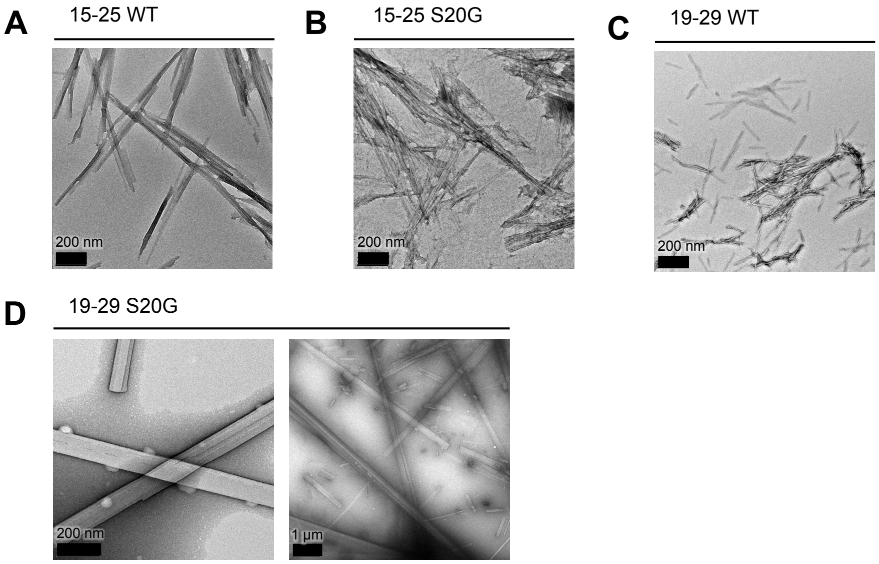

Figure 1.1—Figure Supplement 2. All spine segments form amyloid fibrils or 3D crystals only a few hundred nanometers thick, as observed using negative-stain EM. Fibrils and 3D crystals were formed by dissolving lyophilized protein segments at 1mM in PBS and 1% DMSO and incubating them for one week at room temperature under quiescent conditions. Fibril and crystal formation occurred as quickly as a few hours (19-29 S20G) to as long as overnight (15-25 WT and 15-25 S20G). **A.** 15-25 WT forms striated ribbons. **B.** 15-25 S20G forms striated ribbons. **C.** 19-29 WT forms both striated ribbons and twisted fibrils of varying widths. **D.** 19-29 S20G forms 3D crystals only a few hundred nanometers thick. Right panel scale bar is 1 µm.

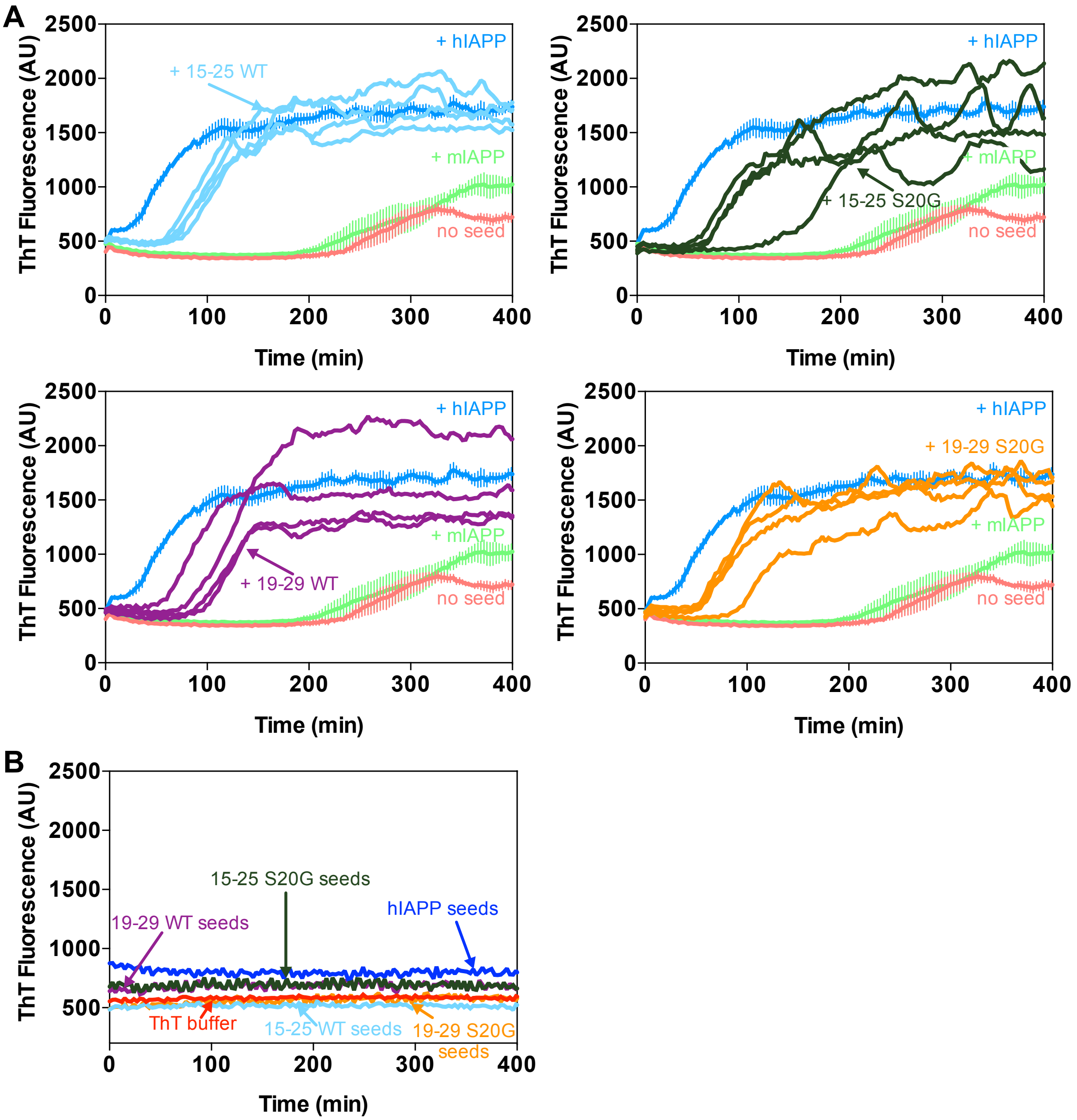

Figure 1.1—Figure Supplement 3. Technical replicates and control samples for ThT assay in Figure 1.1G. A. Fibrils of spine segments seed hIAPP fibril formation. All 4 technical replicates performed in the experiment in Figure 1G are shown. **B.** Seeds of spine segments (1 μM) do not bind Thioflavin-T. The graph shows mean Thioflavin-T fluorescence across 4 technical replicates.

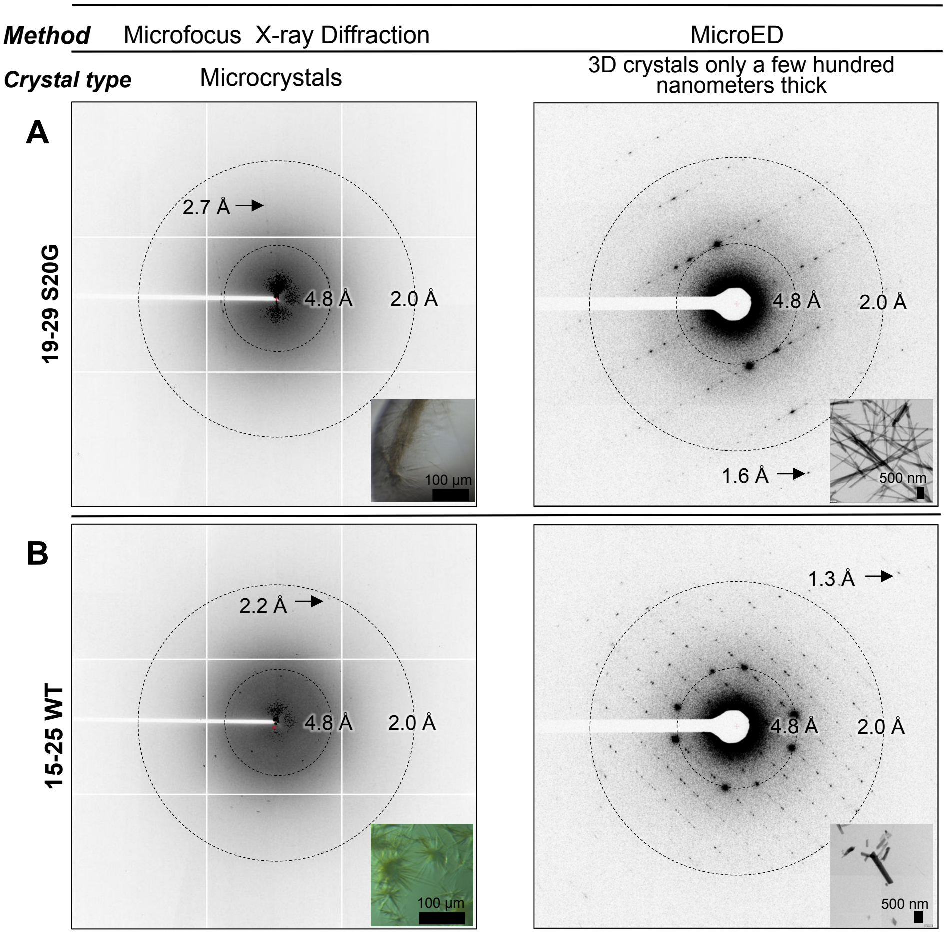

Figure 1.2. 3D crystals only a few hundred nanometers thick diffracted with MicroED show higher resolution Bragg peaks than 10,000 times larger microcrystals diffracted with Microfocus X-rays. A. 3D crystals of 19-29 S20G (right, inset) diffract to 1.6 Å using MicroED, a whole angstrom better resolution than the microcrystals of 19-29 S20G (left, inset). **B.** 3D crystals of 15-25 WT (right, inset) diffract to 1.4 Å using MicroED, whereas microcrystals of 15-25 WT diffract to 2.2 Å using Microfocus X-rays (left, inset).

Table 1.1. Statistics of MicroED data collection and atomic refinement.

Sample	19-29 S20G	15-25 WT
Excitation Voltage (kV)	200	200
Electron Source	field emission gun	field emission gun
Wavelength (Å)	0.0251	0.0251
Total dose per crystal (e^-/ Å^2)	3.425	2.885
Frame rate (frame/s)	0.3-0.5	0.3-0.5
Rotation rate (°/s)	0.3	0.3
# crystals used	6	6
Total angular rotation collected (°)	68	68

Merging Statistics	19-29 S20G	15-25 WT
space group	$P2_12_12_1$	P1
Unit cell dimensions		
a, b, c (Å)	4.78, 18.6, 70.8	11.68, 18.18, 19.93
α, β, γ (°)	90, 90, 90	62.8, 88.9, 87.6
Resolution (Å)	1.9	1.4
R_{merge}	10.6% (15.0%)	19.9% (50%)
# of reflections	1380 (221)	9014 (153)
Unique reflections	548 (115)	2180 (84)
Completeness	83% (65%)	75% (35.3%)
Multiplicity	2.5 (1.9)	4.1 (1.8)
I/σ	5.65 (3.65)	4.33 (1.10)

$CC_{1/2}$ (107)	98.9%	98.5%

Refinement Statistics	19-29 S20G	15-25 WT
Reflections in working set	546	2177
Reflections in test set	53	218
R_{work}[b]	22.75%	22.47%
R_{free}	27.49%	25.90%
RMSD bonds (Å)	0.01	0.008
RMSD angles (°)	1.2	1.2
Ramachandran (%)[c]		
Favored	100	100
Allowed	0	0
Outliers	0	0
PDB ID code	5KNZ	5KO0
EMDB ID code	EMD-8272	EMD-8273

[a] Highest resolution shell shown in parenthesis.

[b] $$Rfactor = 100x \sum \left\| F_{obs} \right| - \left| F_{calc} \right\| / \sum \left| F_{obs} \right|$$

F_{calc} and F_{obs} are the calculated and observed structure factor amplitudes, respectively. R_{work} refers to the R_{factor} for the data utilized in the refinement and R_{free} refers to the R_{factor} for 10% of the reflections randomly chosen that were excluded from the refinement.

[c] Percentage of residues in Ramachandran plot regions were determined using Molprobity (108).

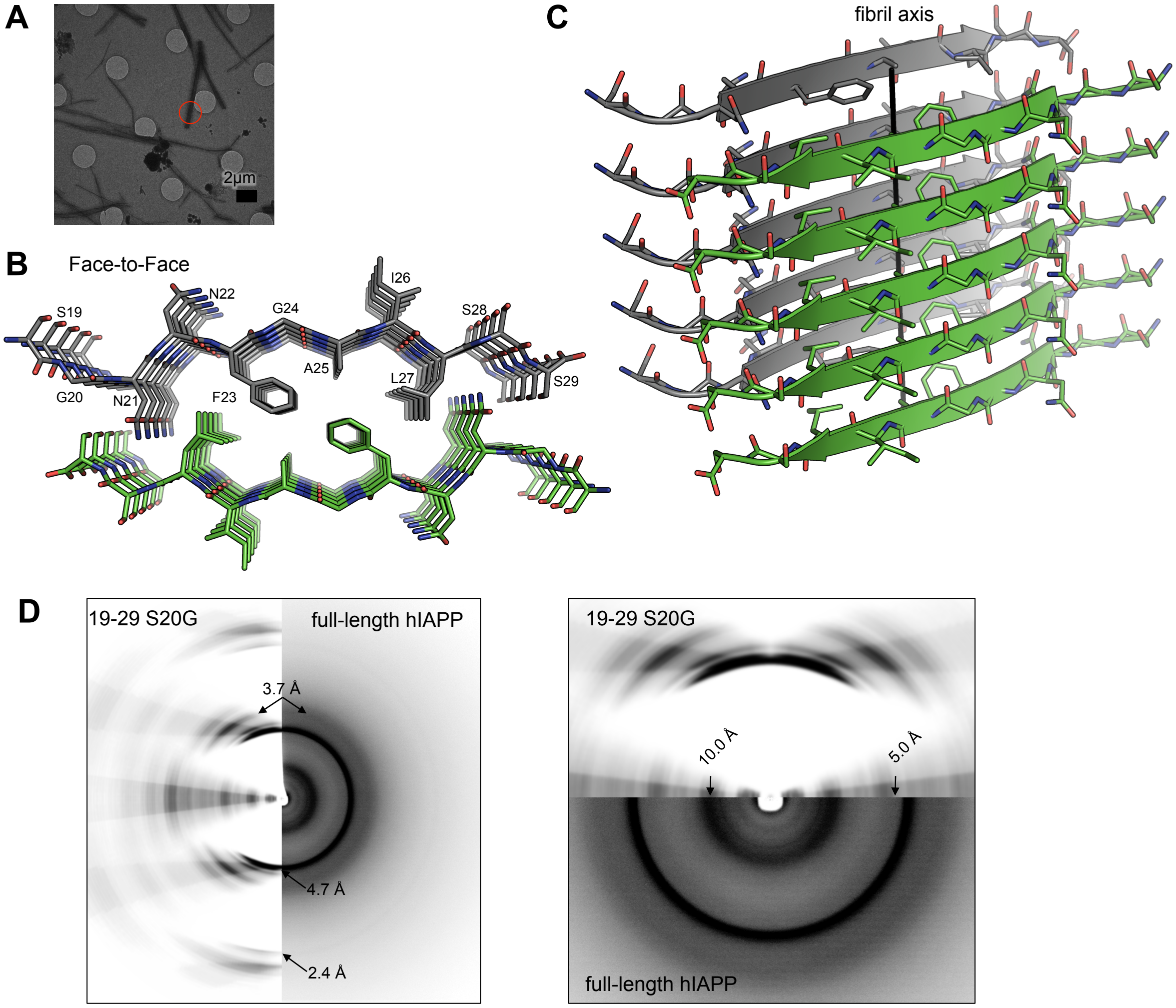

Figure 1.3. The MicroED atomic structure of segment 19-29 S20G reveals pairs of β-sheets mated by a dry interface. A. Electron micrograph of 3D crystals used for data collection. The red circle represents the diameter of the electron beam in diffraction mode. **B.** Pairs of β-sheets are oriented face-to-face and they are tightly mated by a dry interface that excludes water. The dry interface is formed by tightly packed, interdigitating side-chains. This panel shows 5 β-strands or layers along the "a" dimension of the unit cell; the average crystal used for data collection is 10,400 layers long in the "a" dimension. **C.** Orthogonal view of the steric-zipper formed by the dry interface. **D.** The similarity between the fiber diffraction pattern calculated from the structure shown in

Panel C and the fiber diffraction observed from full-length hIAPP fibrils supports the dry interface as a model for the amyloid spine of full-length hIAPP fibrils. Along the meridian (left panel), the dry interface and full-length hIAPP fibrils share reflections at 4.7 Å and and 2.4 Å (black arrows). Additionally, along the off-meridonal, the diffraction patterns share a reflection at 3.7 Å. It is difficult to see the reflection at 2.4 Å in the full-length hIAPP fiber diffraction image, but the reflection is clearly visible in the radial profile in Figure 1.3—Figure Supplement 2. Along the equator (right panel), the dry interface and full-length hIAPP fibrils share reflections at 10.0 Å and 5.0 Å (black arrows). The right panel is magnified 2X to more clearly show the low-resolution reflections along the equator.

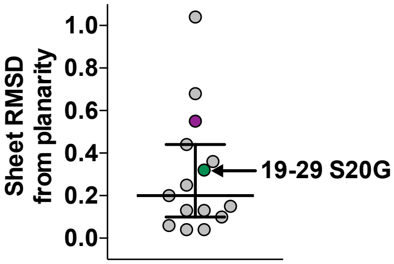

Figure 1.3—Figure Supplement 1. Scatter plot of sheet RMSD from planarity values for all hIAPP protein segment structures determined to date. The values for the 19-29 S20G and 15-25 WT atomic structures are highlighted in green and purple, respectively.

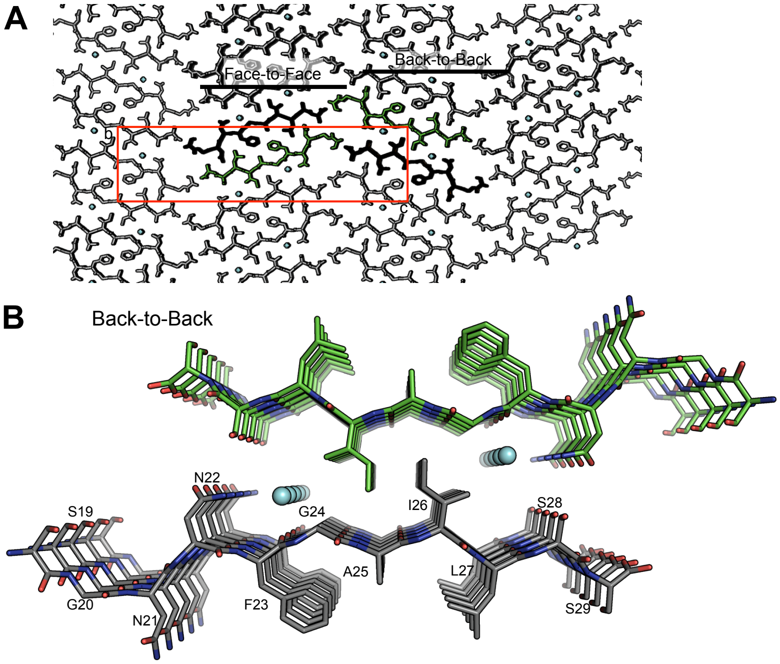

Figure 1.3—Figure Supplement 2. The crystal packing of segment 19-29 S20G reveals a second interface, termed the 'Back-to-Back' or wet interface, which does not form the amyloid spine. The wet interface does not form the amyloid spine because (1) the fiber diffraction pattern calculated from this interface does not match the fiber diffraction pattern collected from full-length hIAPP fibrils, (2) it contains waters, and (3) it possesses less side-chain interdigitation than the dry interface. **A.** View of crystal packing down the "a" dimension of the unit cell reveals the two different interfaces. The unit cell is outlined in red; waters are shown in cyan. **B.** Orthogonal view of the wet interface. The wet interface buries only 153 Å^2 of surface area per strand and it possesses a shape complementarity of 0.64.

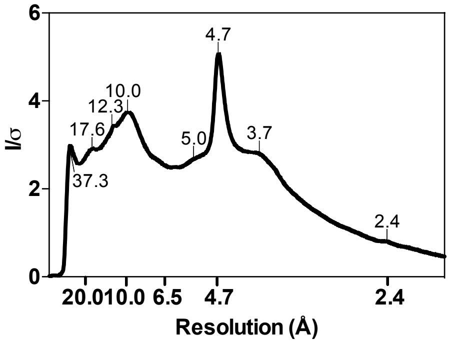

Figure 1.3—Figure Supplement 3. Radial profile calculated from the X-ray diffraction pattern given by cytotoxic full-length hIAPP fibrils. Cytotoxic full-length hIAPP fibrils were prepared under the same conditions as in the cytotoxicity assays. Next, the fibrils were pelleted by centrifugation, washed with water to remove salt, and then applied between two glass capillary tubes as described by Sunde and co-workers (104). The first peak on the left, which occurs at 37.3 Å, may represent a legitimate feature of full-length hIAPP fibrils, but it is too close to the beam stop to definitively makes this conclusion.

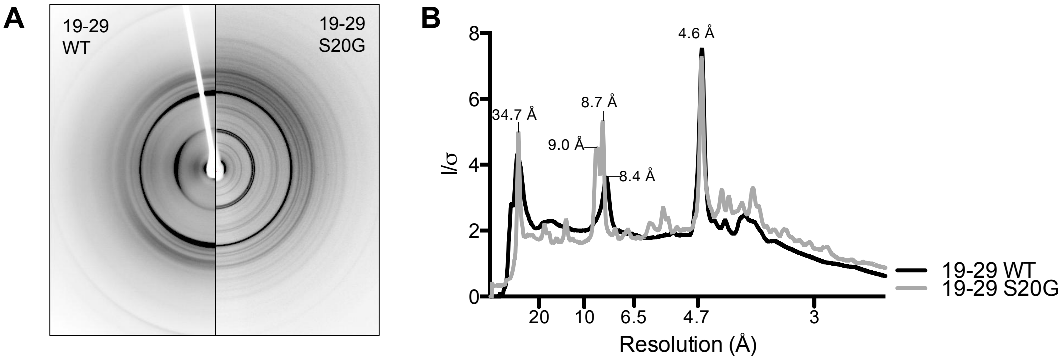

Figure 1.3—Figure Supplement 4. 19-29 WT and S20G have similar fibrillar structures. A. Side-by-side comparison of X-ray diffraction from 19-29 WT fibrils (left) and 19-29 S20G fibrils (right). **B**. Overlaid radial profiles calculated from X-ray fiber diffraction in panel A. 19-29 WT (black) and S20G (gray) fibrils share strong reflections at 4.6 Å, 8.4-9 Å, and 34.7 Å.

Table 1.2. Summary of structural features and biophysical properties of all hIAPP protein segment structures determined to date.

eclipse/staggered^a	registry	references	PDB ID code	zipper symmetry class	sheet symmetry	interface	crystal form	peptide sequence	w
stagg	in	Soriaga et al, J. Phys. Chem. B, 2016	5e5x	2	parallel			ANFLVH	13-18
eclips	in	Wiltzius et al., NSMB 09	3fr1	7	antiparallel			NFLVHS	14-19
eclips	in	Wiltzius et al., NSMB 09	3fth	6	antiparallel			NFLVHSS	14-20
eclips	out	this work	5ko0	6	antiparallel			FLVHSSNNFGA	15-25
eclips	in	Soriaga et al, J. Phys. Chem. B, 2016	5e5z	7	antiparallel			LVHSSN	16-21
stagg	in	Wiltzius et al., NSMB 09	3fpo	4	parallel			HSSNNF	18-23
stagg	in	this work	5knZ	1	parallel	A		SGNNFGAILSS	19-29
stagg	in	this work	5knZ	1	parallel	B		SGNNFGAILSS	19-29
stagg	in	Wiltzius et al. Pro Sci 08	3dgj	1	parallel			NNFGAIL	21-27
stagg	out	Soriaga et al, J. Phys. Chem. B, 2016	5e5v	7	antiparallel			NFGAILS	22-28
stagg	in	Soriaga et al, J. Phys. Chem. B, 2016	5e61	6	antiparallel			FGAILSS	23-29
eclips	in	Wiltzius et al., NSMB 09	3fod	8	antiparallel			AILSST	25-30
stagg	in	Wiltzius et al. Pro Sci 08	3dg1	1	parallel	A	1	SSTNVG	28-33
stagg	in	Wiltzius et al. Pro Sci 08	3dg1	1	parallel	B	1	SSTNVG	28-33
stagg	in	Wiltzius et al., NSMB 09	3ftr	1	parallel	A	2	SSTNVG	28-33
stagg	in	Wiltzius et al., NSMB 09	3ftr	1	parallel	B	2	SSTNVG	28-33
stagg	in	Wiltzius et al., NSMB 09	3ftk	1	parallel		1	NVGSNTY	31-37
stagg	in	Wiltzius et al., NSMB 09	3ftL	1	parallel	A	2	NVGSNTY	31-37
eclips	in	Wiltzius et al., NSMB 09	3ftL	1	parallel	B	2	NVGSNTY	31-37

solvation energy per strand in dry interface cal/mol[e]	maximum sheet-to-sheet distance	mininum sheet-to-sheet distance	standard deviation sheet-to-sheet distance	average sheet-to-sheet distance[d]	Sum of hydropathy values[c]	charge at pH 7	Sheet RMSD from planarity[b]	Sc Coleman	areaburied per residue	areaburied per strand	spg	total residues
189	9.6	8.7	0.31	9.3	0.98	0.1	0.13	0.796	25.2	151.1	$P2_1$	6
139	10.4	10.1	0.13	10.2	0.55	0.1	0.04	0.777	14.9	89.3	$P2_12_12_1$	6
134	11.0	10.5	0.12	10.8	0.36	0.1	0.04	0.537	13.4	94.1	$P2_1$	7
19	13.0	6.6	2.06	9.4	0.29	0.1	0.55	0.664	10.7	118.0	P1	11
130	9.8	9.2	0.36	9.6	-0.05	0.1	0.36	0.473	19.1	114.8	$P2_1$	6
90	8.7	7.7	0.25	8.2	-1.50	0.1	0.06	0.835	21.9	131.5	$P2_1$	6
279	10.1	6.6	1.13	8.8	0.25	0	0.32	0.850	24.1	265.2	$P2_12_12_1$	11
150	11.0	7.5	1.15	8.7	0.25	0	0.32	0.642	13.9	152.8	$P2_12_12_1$	11
141	16.0	4.8	3.85	9.0	0.79	0	1.04	0.902	18.3	128.4	$P2_12_12_1$	7
273	8.4	7.6	0.24	7.8	1.17	0	0.13	0.812	25.8	180.3	P1	7
213	8.3	8.1	0.04	8.2	1.56	0	0.20	0.772	23.3	162.9	P1	7
149	11.7	7.7	0.94	9.8	1.30	0	0.10	0.570	18.6	111.6	$P2_1$	6
0	6.6	5.4	0.41	5.9	-0.33	0	0.25	0.857	21.2	127.2	C2	6
115	11.0	8.3	0.94	9.4	-0.33	0	0.25	0.886	13.7	82.2	C2	6
37	7.3	6.4	0.30	6.9	-0.33	0	0.15	0.806	20.3	121.6	$P2_12_12_1$	6
80	10.4	9.0	0.48	9.5	-0.33	0	0.15	0.801	13.5	80.8	$P2_12_12_1$	6
75	10.0	9.2	0.28	9.7	-0.86	0	0.68	0.868	16.6	116.5	$P2_1$	7
-11	8.8	7.4	0.49	7.9	-0.86	0	0.44	0.712	21.0	147.1	$P2_1$	7
96	10.2	9.0	0.40	9.7	-0.86	0	0.44	0.510	18.1	127.0	$P2_1$	7

[a] Staggered means that the strands from one sheet are translationally offset along the fibril axis with respect to the opposing sheet; eclipsed means there is no offset.

[b] RMSD between 3rd order polynomial fit to sheet coordinates projected down the fibril axis and corresponding to least squares linear fit.

[c] Hydropathy values were calculated from ExPASy Protparam (GRAVY) Kyte and Doolittle values (105).

[d] Sheet-to-sheet distances were calculated by fitting 3rd order polynomial to sheet backbones.

[e] Atomic solvation parameters were obtained from Eisenberg and co-workers (106).

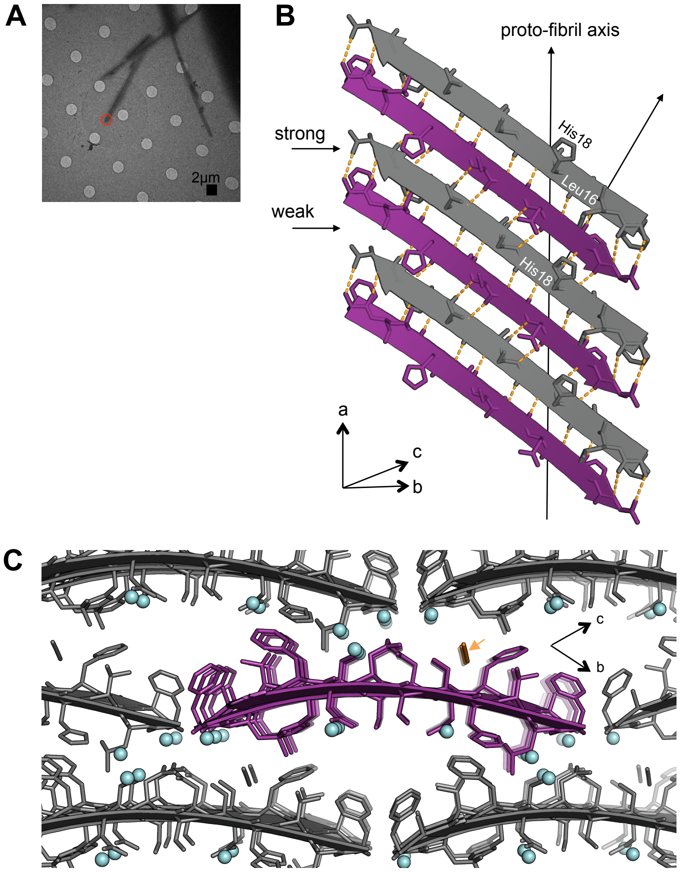

Figure 1.4. Segment 15-25 WT forms an arrangement of unmated β-sheets that is uncharacteristic of pathogenic amyloid fibrils. A. Electron micrograph of 3D crystals used for data collection. The red circle represents the diameter of the electron beam in diffraction mode. **B.** A single β-sheet contains anti-parallel out-of-register β-strands stabilized by two distinct, unequal interfaces: a stronger interface with twelve hydrogen bonds, and a weaker interface with eight hydrogen bonds. The β-strands are out-of-register by 2 residues because Leu16 on the first β-strand is directly above His18 on the third β-strand. **C.** The view down the proto-fibril axis reveals hydrated interfaces between partially overlapping β-sheets. Notice that adjacent β-sheets lack side-chain interdigitation. Water molecules are shown as cyan spheres. The thiocyanate molecule is shown in gold in the central β-sheet and gray in the peripheral β-sheets.

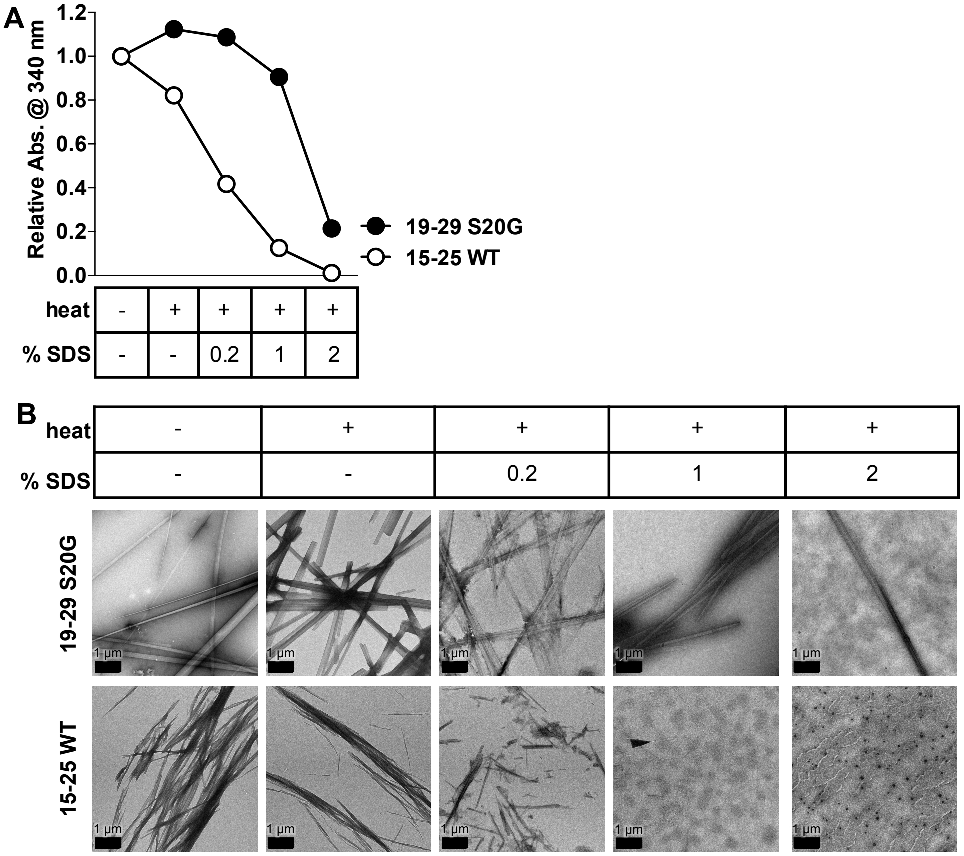

Figure 1.4—Figure Supplement 1. 15-25 WT fibrils are relatively weak and reversible compared to 19-29 S20G fibrils. Equimolar concentrations of 15-25 WT and 19-29 S20G fibrils were treated with increasing amounts of SDS and then heated at 55°C for 20 minutes. **A.** Turbidity measurements of the fibrils treated with heat and increasing amounts of SDS reveal that 15-25 WT fibrils disaggregate more readily than 19-29 S20G fibrils. Turbidity measurements were obtained by recording absorbance at 340 nm. **B.** Negative-stain electron micrographs corroborate the results observed in the turbidity measurements. Scale bars are 1 μm.

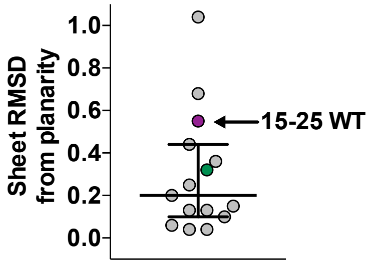

Figure 1.4—Figure Supplement 2. Scatter plot of sheet RMSD from planarity values for all hIAPP protein segment structures determined to date. The values for the 19-29 S20G and 15-25 WT atomic structures are highlighted in green and purple, respectively.

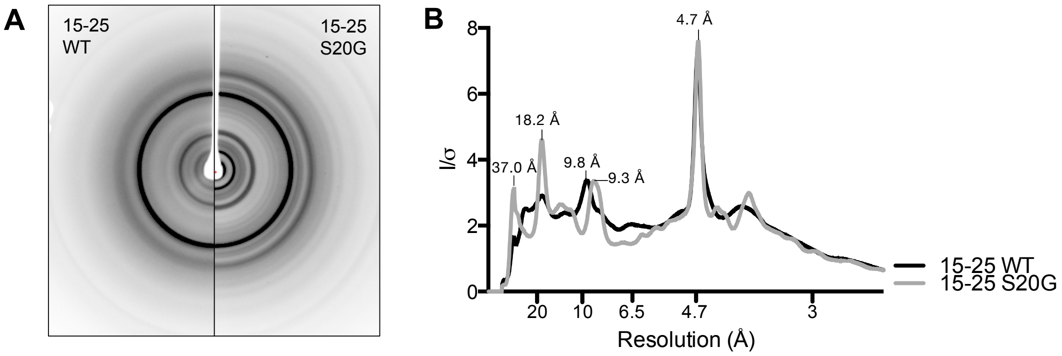

Figure 1.4—Figure Supplement 3. 15-25 WT and S20G have similar fibrillar structures. A. Side-by-side comparison of x-ray diffraction from 15-25 WT fibrils (left) and 15-25 S20G fibrils (right). **B.** Overlaid radial profiles calculated from x-ray fiber diffraction in panel A. 15-25 WT (black) and S20G (gray) fibrils display strong reflections at 4.7 Å, 9.3-9.8 Å, 18.2 Å, and 37.0 Å.

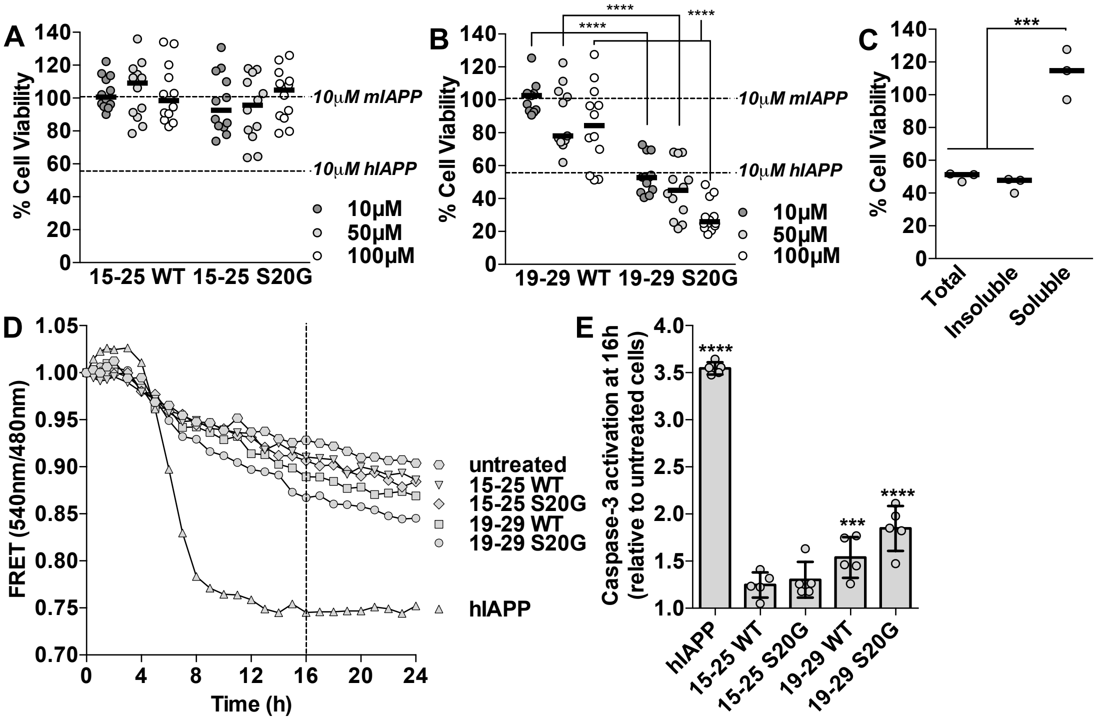

Figure 1.5. Segment 19-29 S20G forms the toxic core of hIAPP and segments 15-25 are not toxic. A. and **B.** Fibrils were formed by incubating the spine segments overnight under quiescent conditions, the same conditions used to prepared full-length hIAPP fibrils. Next, the samples were applied to HEK293 cells at the specified concentrations for 24 hours and then cell viability was quantified using MTT dye reduction. Bars show median cell viability; dashed lines show median cell viability from 10 µM mIAPP and hIAPP. **A.** 15-25 WT and 15-25 S20G fibrils are not toxic compared to full-length hIAPP fibrils (n=12 across 4 biological replicates, each with 3 technical replicates). **B.** 19-29 WT fibrils are mildly cytotoxic and 19-29 S20G fibrils are significantly more cytotoxic than 19-29 WT fibrils (*****, $p < 0.0001$* using a Mann-Whitney U test; n=12 across 4 biological replicates, each with 3 technical replicates). 19-29 S20G fibrils (10 µM) are similarly cytotoxic to full-length hIAPP fibrils at the same concentration (lower dashed line) ($p = 0.09$ using an unpaired t-test with equal standard deviations). **C.** The insoluble fraction of the 50 µM 19-29 S20G cytotoxic preparation contains the cytotoxic species. 19-29 S20G fibrils

were formed overnight at room temperature and then pelleted by centrifugation. The soluble fraction was carefully removed and then filtered to ensure it contained no insoluble material. The insoluble material was resuspended in its original volume. Each sample was applied to HEK293 cells for 24 hours and then cell viability was quantified with MTT dye reduction (***; $p < 0.0002$ using an ordinary one-way ANOVA; n=3 technical replicates) **D.** and **E.** Using a FRET-based biosensor assay for monitoring caspase-3 activity in real-time, 19-29 S20G fibrils elicited the greatest induction of caspase-3 activity, whereas segments 15-25 did not induce caspase-3 activity, consistent with the MTT dye reduction assay results. 50 µM of each spine segment seeded with 166 nM seeds was applied to CHO cells stably transfected with a construct containing ECFP and EYFP fused by a DEVD linker. In non-apoptotic cells, excitation of ECFP results in FRET and EYFP emission at 54 0nm. In apoptotic cells, caspase-3 targets and cleaves at the DEVD site, resulting in loss of FRET signal. Caspase-3 activity is measured by recording fold difference in emission at 540 nm and 480 nm. **D.** Fold difference was recorded over 24 hours. Datapoints represent average fold difference. The dashed line represents the 16-hour mark. **E.** Average levels of caspase-3 activation after a 16-hour incubation relative to untreated cells (***, $p < 0.0002$; ****$p < 0.0001$ using an ordinary one-way ANOVA, Bonferroni correction; n =5 technical replicates)).

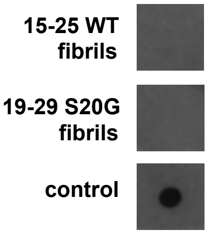

Figure 1.5—Figure Supplement 1. Fibrillar samples of 15-25 WT and 19-29 S20G do not contain detectable amyloid oligomers. Oligomers were probed using a dot bot assay with the polyclonal anti-oligomer antibody, LOC. IAPP oligomers were used as the positive control for LOC binding.

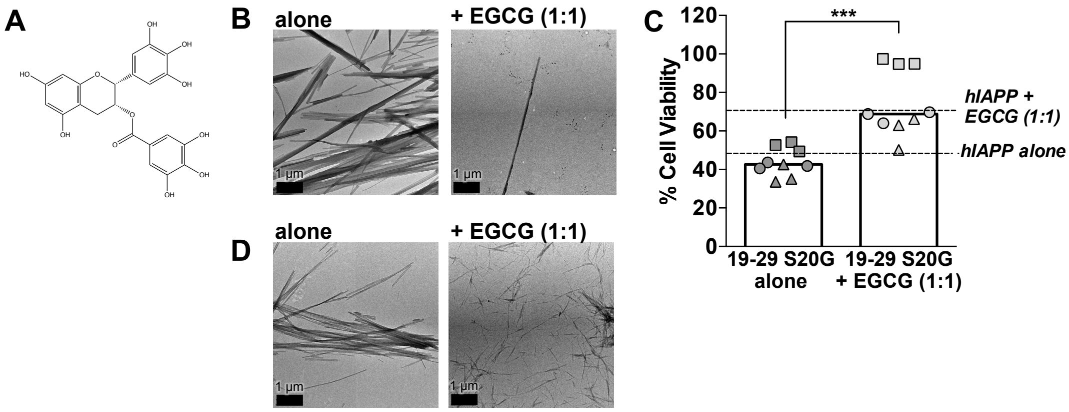

Figure 1.5—Figure Supplement 2. (−)-epigallocatechin gallate (EGCG), a flavanol known to mitigate full-length hIAPP cytotoxicity by preventing it from forming fibrils, likewise mitigates 19-29 S20G cytotoxicity by preventing it from forming fibrils A. Chemical structure of EGCG. **B.** Negative-stain electron micrographs reveal that EGCG mitigates 19-29 S20G fibril formation. 19-29 S20G was incubated overnight at room temperature under quiescent conditions in buffer alone or with equimolar concentration of ECGC. Next, the samples were spotted onto carbon-coated copper grids for negative-stain EM analysis. **C.** EGCG mitigates 19-29 S20G cytotoxicity. Samples were generated as described in panel B and then applied to HEK293 cells and incubated for 24 hours. Cell viability was quantified using MTT dye reduction. Columns indicate median cell viability. Different symbols correspond to values observed in each independent experiment (***; $p = 0.0004$ using a unpaired t-test with Welch's correction for unequal variances; n=9 across 3 biological replicates, each with 3 technical replicates). **D.** Negative-stain EM reveals that EGCG does not mitigate fibril formation of 15-25 WT, a spine segment that does not possess a hydrophobic core. 15-25 WT was incubated for 5 days under shaking conditions with equimolar concentrations of EGCG. Next, the samples were spotted onto carbon-coated copper grids for negative-stain EM.

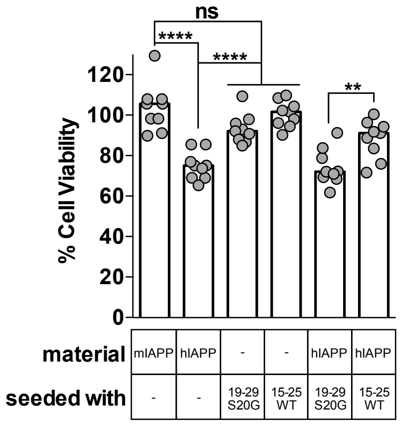

Figure 1.6. Fibril seeds of 15-25 WT reduce the cytotoxicity of full-length hIAPP. In this experiment, we incubated 10 µM hIAPP with or without 10% monomer equivalent of pre-formed seeds overnight under quiescent conditions, the same conditions used to seed full-length hIAPP fibril formation in Figure 1E. Next, we diluted the samples 1 to 10 in culture media containing pre-plated Rin5F cells. Note: the concentration of IAPP used in this experiment is less than the IAPP concentrations used in the cytotoxicity assays in Figures 1 and 5. We did this to preserve the seeding conditions used in the kinetic assay in Figure 1G. 1 µM hIAPP seeded with stable, toxic 19-29 S20G fibrils is more cytotoxic to Rin5F cells than 1 µM hIAPP seeded with labile, non-toxic 15-25 WT fibrils. Columns indicate median cell viability (ns = not significant; **, $p = 0.006$; ****, $p < 0.0001$ using an unpaired t-test with equal standard deviations, n=9 across 3 biological replicates, each with 3 technical replicates). 19-29 S20G seeds and 15-25 WT seeds (100 nM each) are not cytotoxic to Rin5F cells.

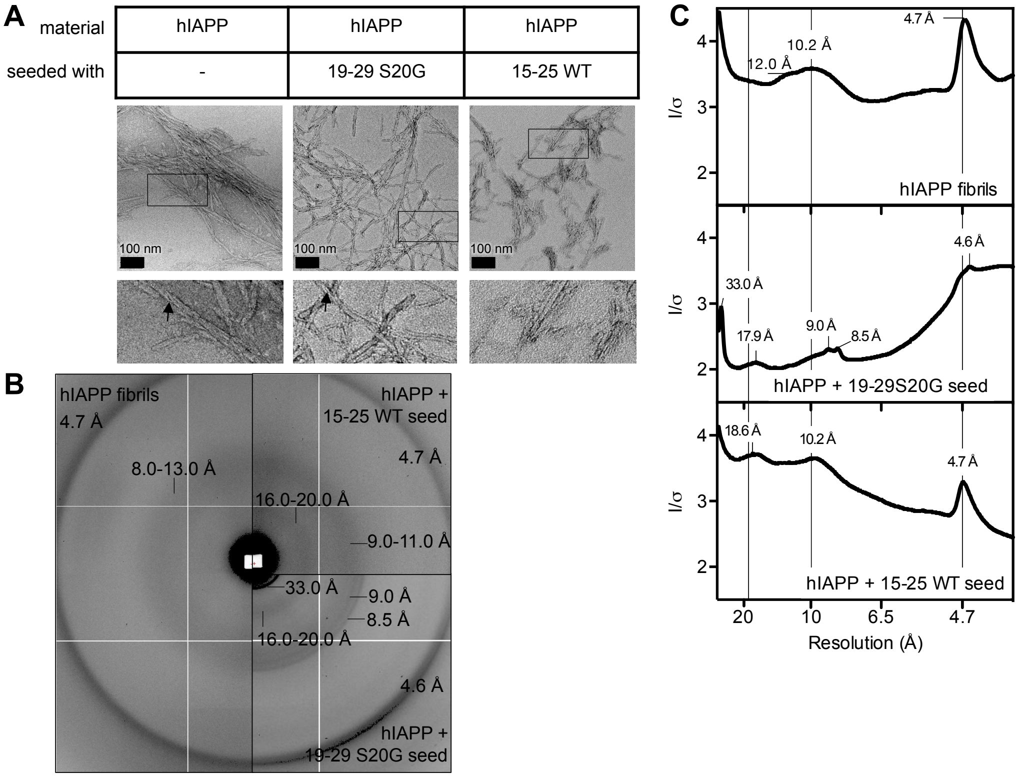

Figure 1.6—Figure Supplement 1. hIAPP fibrils made by seeding with each spine segment have slightly different structural features. A. Negative-stain electron micrographs reveal fibrils made by seeding with each spine segment do not have markedly different morphologies. Unseeded hIAPP forms pre-dominantly striated ribbons of uniform width that bundle together; some fibrils have twists (black arrow head). hIAPP fibrils made by seeding with stable, toxic 19-29S20G fibrils forms striated ribbons of varying widths and some twisted fibrils (black arrow head). hIAPP fibrils made by seeding with labile, non-toxic 15-25 WT fibrils forms striated ribbons that appear slightly thinner than unseeded hIAPP fibrils. **B.** and **C.** X-ray fiber diffraction and radial profile analysis suggest hIAPP fibrils made by seeding with toxic and non-toxic segments have slightly different structures. hIAPP fibrils made by seeding with stable, toxic 19-29 S20G fibrils

display shorter Bragg spacings compared to hIAPP fibrils made by seeding with labile, non-toxic 15-25 WT fibrils. The shorter spacings suggest tighter fibril packing.

$_{8}$ATQRLANFLVHSSNNFGAILSSTNVGSNTY$_{37}$ **G**	Zipper symmetry class	Parallel (//) Or Anti-Parallel (A//)	Registry
ANFLVH	2	//	in
NFLVHS	7	A//	in
NFLVHSS	6	A//	in
FLVHSSNNFGA	6	A//	out
LVHSSN	7	A//	in
HSSNNF	4	//	in
S**G**NNFGAILSS	1	//	in
NNFGAIL	1	//	in
NFGAILS	7	A//	out
FGAILSS	6	A//	in
AILSST	8	A//	in
SSTNVG	1	//	in
NVGSNTY	1	//	in

Figure 1.7. Schematic of structural features of all hIAPP protein segment structures determined to date. Parallel (//) or Anti-parallel (A//) refers to the orientation of β-strands within β-sheets. Registry refers to the translational offset of β-sheets perpendicular to the fiber axis.

REFERENCES

1. Eisenberg D, Jucker M. 2012 The amyloid state of proteins in human diseases. *Cell* **148**:1188–1203. doi:10.1016/j.cell.2012.02.022

2. Westermark P, Wernstedt C, Wilander E, Hayden DW, O'Brien TD, Johnson KH. 1987 Amyloid fibrils in human insulinoma and islets of Langerhans of the diabetic cat are derived from a neuropeptide-like protein also present in normal islet cells. *Proc Natl Acad Sci U S A* **84**:3881–3885. doi:10.1073/pnas.84.11.3881

3. Cooper GJ, Leighton B, Dimitriadis GD, Parry-Billings M, Kowalchuk JM, Howland K, Rothbard JB, Willis AC, Reid KB. 1988 Amylin found in amyloid deposits in human type 2 diabetes mellitus may be a hormone that regulates glycogen metabolism in skeletal muscle. *Proc Natl Acad Sci U S A* **85**:7763–7766.

4. Roberts AN, Leighton B, Todd JA, Cockburn D, Schofield PN, Sutton R, Holt S, Boyd Y, Day AJ, Foot EA, Reid KBM, Cooper GJS. 1989 Molecular and functional characterization of amylin, a peptide associated with type 2 diabetes mellitus. *Proc Natl Acad Sci U S A* **86**:9662–9666. doi:10.1073/pnas.86.24.9662

5. Westermark P, Andersson A, Westermark G. 2011 Islet amyloid polypeptide, islet amyloid, and diabetes mellitus. *Physiol Rev* **91**:795–826. doi:10.1152/physrev.00042.2009

6. Hoppener JWM, Ahren B, Lips CJM. 2000 Islet Amyloid and Type 2 Diabetes Mellitus. *N Engl J Med* **343**:411–419. doi:10.1056/NEJM200008103430607

7. Maloy AL, Longnecker DS, Greenberg ER. 1981 The relation of islet amyloid to the clinical type of diabetes. *Hum Pathol* **12**:917–922.

8. Esapa C, Moffitt JH, Novials A, McNamara CM, Levy JC, Laakso M, Gomis R, Clark A. 2005 Islet amyloid polypeptide gene promoter polymorphisms are not associated with Type 2 diabetes or with the severity of islet amyloidosis. *Biochim Biophys Acta* **1740**:74–78. doi:10.1016/j.bbadis.2005.02.001

9. Jurgens CA, Toukatly MN, Fligner CL, Udayasankar J, Subramanian SL, Zraika S, Aston-Mourney K, Carr DB, Westermark P, Westermark G, Kahn SE, Hull RL. 2011 B-Cell Loss and B-Cell Apoptosis in Human Type 2 Diabetes Are Related To Islet Amyloid Deposition. *Am J Pathol* **178**:2632–40. doi:10.1016/j.ajpath.2011.02.036

10. Nishi M, Chan SJ, Nagamatsu S, Bell GI, Steiner DF. 1989 Conservation of the sequence of islet amyloid polypeptide in five mammals is consistent with its putative role as an islet hormone. *Proc Natl Acad Sci U S A* **86**:5738–5742. doi:10.1073/pnas.86.15.5738

11. Westermark P, Engström U, Johnson K, Westermark G, Betsholtz C. 1990 Islet amyloid polypeptide: pinpointing amino acid residues linked to amyloid fibril formation. *Proc Natl Acad Sci U S A* **87**:5036–40.

12. Verchere CB, D'Alessio D a, Palmiter RD, Weir GC, Bonner-Weir S, Baskin DG, Kahn SE. 1996 Islet amyloid formation associated with hyperglycemia in transgenic mice with pancreatic beta cell expression of human islet amyloid polypeptide. *Proc Natl Acad Sci U S A* **93**:3492–6. doi:10.1073/pnas.93.8.3492

13. Westermark GT, Gebre-Medhin S, Steiner DF, Westermark P. 2000 Islet amyloid development in a mouse strain lacking endogenous islet amyloid polypeptide (IAPP) but expressing human IAPP. *Mol Med* **6**:998–1007. doi:S1528365800209981

14. Sakagashira S, Hiddinga HJ, Tateishi K, Sanke T, Hanabusa T, Nanjo K, Eberhardt NL. 2000 S20G mutant amylin exhibits increased in vitro amyloidogenicity and increased intracellular cytotoxicity compared to wild-type amylin. *Am J Pathol* **157**:2101–9. doi:10.1016/S0002-9440(10)64848-1

15. Cao P, Tu L-H, Abedini A, Levsh O, Akter R, Patsalo V, Schmidt AM, Raleigh DP. 2012 Sensitivity of amyloid formation by human islet amyloid polypeptide to mutations at residue 20. *J Mol Biol* **421**:282–295. doi:10.1016/j.jmb.2011.12.032

16. Meier DT, Entrup L, Templin AT, Hogan MF, Mellati M, Zraika S, Hull RL, Kahn SE. 2016 The S20G substitution in hIAPP is more amyloidogenic and cytotoxic than wild-type hIAPP in mouse islets. *Diabetologia* doi:10.1007/s00125-016-4045-x

17. Sakagashira S, Sanke T, Hanabusa T, Shimomura H, Ohagi S, Kumagaye KY, Nakajima K, Nanjo K. 1996 Missense mutation of amylin gene (S20G) in Japanese NIDDM patients. *Diabetes* **45**:1279–1281.

18. Lee SC, Hashim Y, Li JK, Ko GT, Critchley JA, Cockram CS, Chan JC. 2001 The islet amyloid polypeptide (amylin) gene S20G mutation in Chinese subjects: evidence for associations with type 2 diabetes and cholesterol levels. *Clin Endocrinol (Oxf)* **54**:541–546.

19. Morita S, Sakagashira S, Ueyama M, Shimajiri Y, Furuta M, Sanke T. 2011 Progressive deterioration of insulin secretion in Japanese type 2 diabetic patients in comparison with those who carry the S20G mutation of the islet amyloid polypeptide gene: A long-term follow-up study. *J Diabetes Investig* **2**:287–92. doi:10.1111/j.2040-1124.2011.00102.

20. Lorenzo A, Razzaboni B, Weir GC, Yankner B. 1994 Pancreatic islet cell toxicity of amylin associated with type-2 diabetes mellitus. *Nature* **368**:756–760. doi:10.1038/368756a0

21. Lorenzo A, Yankner B. 1994 Beta-amyloid neurotoxicity requires fibril formation and is inhibited by congo red. *Proc Natl Acad Sci U S A* **91**:12243–12247. doi:10.1073/pnas.91.25.12243

22. Schubert D, Behl C, Lesley R, Brack A, Dargusch R, Sagara Y, Kimura H. 1995 Amyloid peptides are toxic via a common oxidative mechanism. *Proc Natl Acad Sci U S A* **92**:1989–1993. doi:10.1073/pnas.92.6.1989

23. Kapurniotu A. 2001 Amyloidogenicity and cytotoxicity of islet amyloid polypeptide. *Biopolym - Pept Sci Sect* **60**:438–459. doi:10.1002/1097-0282(2001)60:6<438::AID-BIP10182>3.0.CO;2-A

24. O'Brien TD, Butler PC, Kreutter DK, Kane LA, Eberhardt NL. 1995 Human islet amyloid polypeptide expression in COS-1 cells: a model of intracellular amyloidogenesis. *Am J Pathol* **147**:609–616.

25. Hiddinga HJ, Eberhardt NL. 1999 Intracellular amyloidogenesis by human islet amyloid polypeptide induces apoptosis in COS-1 cells. *Am J Pathol* **154**:1077–1088. doi:10.1016/S0002-9440(10)65360-6

26. Janson J, Soeller W, Roche P, Nelson R, Torchia A, Kreutter D, Butler PC. 1996 Spontaneous diabetes mellitus in transgenic mice expressing human islet amyloid polypeptide. *Proc Natl Acad Sci U S A* **93**:7283–7288.

27. Hull RL, Watts MR, Kodama K, Shen Z, Utzschneider KM, Carr DB, Vidal J, Kahn SE. 2005 Genetic background determines the extent of islet amyloid formation in human islet amyloid polypeptide transgenic mice. *Am J Physiol Endocrinol Metab* **289**:703–709. doi:10.1152/ajpendo.00471.2004.

28. Hull RL, Shen Z, Watts MR, Kodama K, Carr DB, Utzschneider KM, Zraika S, Wang F, Kahn SE. 2005 Long-term treatment with rosiglitazone and metformin reduces the extent of, but does not prevent, islet antyloid deposition in mice expressing the gene for human islet antyloid polypeptide. *Diabetes* **54**:2235–2244. doi:10.2337/diabetes.54.7.2235

29. Pilkington EH, Gurzov EN, Kakinen A, Litwak SA, Stanley WJ, Davis TP, Ke PC. 2016 Pancreatic β-Cell membrane fluidity and toxicity induced by human islet amyloid polypeptide species. *Sci Rep* **6**:21274. doi:10.1038/srep21274

30. Schlamadinger DE, Miranker AD. 2014 Fiber-dependent and independent toxicity of islet amyloid polypeptide. *Biophys J* **107**:2559–2566. doi:10.1016/j.bpj.2014.09.047

31. Oskarsson ME, Singh K, Wang J, Vlodavsky I, Li J-P, Westermark G. 2015 Heparan sulfate proteoglycans are important for islet amyloid formation and lslet amyloid polypeptide-induced apoptosis. *J Biol Chem* **290**:15121–15132. doi:10.1074/jbc.M114.631697

32. Meier JJ, Kayed R, Lin CY, Gurlo T, Haataja L, Jayasinghe S, Langen R, Glabe CG, Butler PC. 2006 Inhibition of human IAPP fibril formation does not prevent beta-cell death: evidence for distinct actions of oligomers and fibrils of human IAPP. *Am J Physiol Endocrinol Metab* **291**:1317–1224. doi:10.1152/ajpendo.00082.2006

33. Ritzel RA, Meier JJ, Lin CY, Veldhuis JD, Butler PC. 2007 Human islet amyloid polypeptide oligomers disrupt cell coupling, induce apoptosis, and impair insulin secretion in isolated human islets. *Diabetes* **56**:65–71. doi:10.2337/db06-0734

34. Bram Y, Frydman-Marom A, Yanai I, Gilead S, Shaltiel-Karyo R, Amdursky N, Gazit E. 2014 Apoptosis induced by islet amyloid polypeptide soluble oligomers is neutralized by diabetes-associated specific antibodies. *Sci Rep* **4**:4267. doi:10.1038/srep04267

35. Mukherjee A, Morales-Scheihing D, Butler PC, Soto C. 2015 Type 2 diabetes as a protein misfolding disease. *Trends Mol Med* **21**:439–449. doi:10.1016/S0140-6736(13)62365-X

36. Lin CY, Gurlo T, Kayed R, Butler AE, Haataja L, Glabe CG, Butler PC. 2007 Toxic human islet amyloid polypeptide (h-IAPP) oligomers are intracellular, and vaccination to induce anti-toxic oligomer antibodies does not prevent h-IAPP–Induced beta-cell apoptosis in h-IAPP transgenic mice. *Diabetes* **56**: doi:10.2337/db06-1579.C.-Y.L.

37. Huang C, Lin C, Haataja L, Gurlo T. 2007 High expression rates of human islet amyloid polypeptide induce endoplasmic reticulum stress–mediated β-cell apoptosis, a characteristic of humans with type 2 but not type 1 diabetes. *Diabetes* **56**:2016–2027. doi:10.2337/db07-0197.Ad-hIAPP

38. Haataja L, Gurlo T, Huang CJ, Butler PC. 2008 Islet amyloid in type 2 diabetes, and the toxic oligomer hypothesis. *Endocr Rev* **29**:303–316. doi:10.1210/er.2007-0037

39. Abedini A, Plesner A, Cao P, Ridgway Z, Zhang J, Tu L-H, Middleton CT, Chao B, Sartori D, Meng F, Wang H, Wong AG, Zanni MT, Verchere CB, Raleigh DP, Schmidt AM. 2016 Time-resolved studies define the nature of toxic IAPP intermediates, providing insight for anti-amyloidosis therapeutics. *Elife* **53**:1689–1699. doi:10.7554/eLife.12977

40. Wiltzius JJW, Sievers SA, Sawaya MR, Cascio D, Popov D, Riekel C, Eisenberg D. 2008 Atomic structure of the cross-beta spine of islet amyloid polypeptide (amylin). *Protein Sci* **17**:1467–1474. doi:10.1110/ps.036509.108.

41. Wiltzius JJW, Landau M, Nelson R, Sawaya MR, Apostol MI, Goldschmidt L, Soriaga AB, Cascio D, Rajashankar K, Eisenberg D. 2009 Molecular mechanisms for protein-encoded inheritance. *Nat Struct Mol Biol* **16**:973–978. doi:10.1038/nsmb.1643

42. Soriaga AB, Sangwan S, Macdonald R, Sawaya MR, Eisenberg D. 2015 Crystal structures of IAPP amyloidogenic segments reveal a novel packing motif of out-of-register beta sheets. *J Phys Chem B*[Epub ahead of print]. doi:10.1021/acs.jpcb.5b09981

43. Nelson R, Sawaya MR, Balbirnie M, Madsen AØ, Riekel C, Grothe R, Eisenberg D. 2005 Structure of the cross-beta spine of amyloid-like fibrils. *Nature* **435**:773–778. doi:10.1038/nature03680

44. Sawaya MR, Sambashivan S, Nelson R, Ivanova MI, Sievers SA, Apostol MI, Thompson MJ, Balbirnie M, Wiltzius JJW, McFarlane HT, Madsen AØ, Riekel C, Eisenberg D. 2007 Atomic structures of amyloid cross-β spines reveal varied steric zippers. *Nature* **447**:453–457. doi:10.1038/nature05695

45. Rodriguez JA, Ivanova MI, Sawaya MR, Cascio D, Reyes FE, Shi D, Sangwan S, Guenther EL, Johnson LM, Zhang M, et al. 2015 Structure of the toxic core of α-synuclein from invisible crystals. *Nature* **525**:486–490. doi:10.1038/nature15368

46. Luca S, Yau W-M, Leapman R, Tycko R. 2007 Peptide conformation and supramolecular organization in amylin fibrils: Constraints from solid-state NMR. *Biochemistry* **46**:13505–13522. doi:10.1021/bi701427q

47. Weirich F, Gremer L, Mirecka EA, Schiefer S, Hoyer W, Heise H. 2016 Structural characterization of fibrils from recombinant human islet amyloid polypeptide by solid-state NMR: the central FGAILS segment Is part of the β-Sheet core. *PLoS One* **11**:e0161243. doi:10.1371/journal.pone.0161243

48. Mirecka EA, Feuerstein S, Gremer L, Schröder GF, Stoldt M, Willbold D, Hoyer W. 2016 β -hairpin of islet amyloid polypeptide bound to an aggregation inhibitor. *Sci Rep*1–8. doi:10.1038/srep33474

49. Kayed R, Head E, Sarsoza F, Saing T, Cotman CW, Necula M, Margol L, Wu J, Breydo L, Thompson JL, Rasool S, Gurlo T, Butler P, Glabe CG. 2007 Fibril specific, conformation dependent antibodies recognize a generic epitope common to amyloid fibrils and fibrillar oligomers that is absent in prefibrillar oligomers. *Mol Neurodegener* **2**:18. doi:10.1186/1750-1326-2-18

50. Wu JW, Breydo L, Isas JM, Lee J, Kuznetsov YG, Langen R, Glabe C. 2010 Fibrillar oligomers nucleate the oligomerization of monomeric amyloid-beta but do not seed fibril formation. *J Biol Chem* **285**:6071–6079. doi:10.1074/jbc.M109.069542

51. Gazdar AF, Chick WL, Oie HK, Sims HL, King DL, Weir GC, Lauris V. 1980 Continuous, clonal, insulin- and somatostatin-secreting cell lines established from a transplantable rat islet cell tumor. *Proc Natl Acad Sci U S A* **77**:3519–3523. doi:10.1073/pnas.77.6.3519

52. Mosmann T. 1983 Rapid colorimetric assay for cellular growth and survival: application to proliferation and cytotoxicity assays. *J Immunol Methods* **65**:55–63. doi:10.1016/0022-1759(83)90303-4

53. Liu Y, Peterson DA, Kimura H, Schubert D. 1997 Mechanism of cellular 3- (4,5-dimethylthiazol-2-yl)-2,5- diphenyltetrazolium bromide (MTT) reduction. *J Neurochem* **6**:581–593. doi:10.1046/j.1471-4159.1997.69020581.x

54. Budihardjo I, Oliver H, Lutter M, Luo X, Wang X. 1999 Biochemical pathways of caspase activation during apoptosis. *Annu Rev Cell Dev Biol* **15**:269–290.

55. Moriarty DF, Raleigh DP. 1999 Effects of sequential proline substitutions on amyloid formation by human amylin 20-29. *Biochemistry* **38**:1811–1818. doi:10.1021/bi981658g

56. Goldsbury C, Goldie K, Pellaud J, Seelig J, Frey P, Müller SA, Kistler J, Cooper GJS, Aebi U. 2000 Amyloid fibril formation from full-length and fragments of amylin. *J Struct Biol* **130**:352–362. doi:10.1006/jsbi.2000.4268

57. Tenidis K, Waldner M, Bernhagen J, Fischle W, Bergmann M, Weber M, Merkle ML, Voelter W, Brunner H, Kapurniotu A. 2000 Identification of a penta- and hexapeptide of islet amyloid polypeptide (IAPP) with amyloidogenic and cytotoxic properties. *J Mol Biol* **295**:1055–1071. doi:10.1006/jmbi.1999.3422

58. Wiltzius JJW, Sievers SA, Sawaya MR, Eisenberg D. 2009 Atomic structures of IAPP (amylin) fusions suggest a mechanism for fibrillation and the role of insulin in the process. *Protein Sci* **18**:1521–1530. doi:10.1002/pro.145

59. Shi D, Nannenga BL, Iadanza MG, Gonen T. 2013 Three-dimensional electron crystallography of protein microcrystals. *Elife* **2013**:1–17. doi:10.7554/eLife.01345.001

60. Nannenga BL, Shi D, Hattne J, Reyes FE, Gonen T. 2014 Structure of catalase determined by MicroED. *Elife* **3**:1–11. doi:10.7554/eLife.03600

61. Nannenga BL, Shi D, Leslie AGW, Gonen T. 2014 High-resolution structure determination by continuous-rotation data collection in MicroED. *Nat Methods* **11**:1–5. doi:10.1038/nmeth.3043

62. Hattne J, Reyes FE, Nannenga BL, Shi D, de la Cruz MJ, Leslie AGW, Gonen T. 2015 MicroED data collection and processing. *Acta Crystallogr Sect A Found Adv* **71**:353–360. doi:10.1107/S2053273315010669

63. Liu S, Hattne J, Reyes FE, Sanchez-Martinez S, Jason de la Cruz M, Shi D, Gonen T. 2016 Atomic resolution structure determination by the cryo-EM method MicroED. *Protein Sci* **00**:1–8. doi:10.1002/pro.2989

64. Ivanova MI, Sievers SA, Sawaya MR, Wall JS, Eisenberg D. 2009 Molecular basis for insulin fibril assembly. *Proc Natl Acad Sci U S A* **106**:18990–18995. doi:10.1073/pnas.0910080106

65. Colletier J-P, Laganowsky A, Landau M, Zhao M, Soriaga AB, Goldschmidt L, Flot D, Cascio D, Sawaya MR, Eisenberg D. 2011 Molecular basis for amyloid-polymorphism. *Proc Natl Acad Sci U S A* **108**:16938–16943. doi:10.1073/pnas.1112600108

66. Liu C, Sawaya MR, Eisenberg D. 2010 Beta2-microglobulin forms three-dimensional domain-swapped amyloid fibrils with disulfide linkages. *Nat Struct Mol Biol* **18**:49–55. doi:10.1038/nsmb.1948

67. Griffiths JM, Ashburn TT, Auger M, Costa PR, Griffin RG, Lansbury PT. 1995 Rotational resonance solid-state NMR elucidates a structural model of pancreatic amyloid. *J Am Chem Soc* **117**:3539–3546. doi:10.1021/ja00117a023

68. Jack E, Newsome M, Stockley PG, Radford SE, Middleton DA. 2006 The organization of aromatic side groups in an amyloid fibril probed by solid-state 2 H and 19 F NMR spectroscopy. *J Am Chem Soc* **128**:8098–8099. doi:10.1021/ja0581898

69. Madine J, Jack E, Stockley PG, Radford SE, Serpell LC, Middleton DA. 2008 Structural insights into the polymorphism of amyloid-like fibrils formed by region 20-29 of amylin revealed by solid-state NMR and X-ray fiber diffraction. *J Am Chem Soc* **130**:14990–15001. doi:10.1021/ja802483d

70. Cooper S, Khatib F, Treuille A, Barbero J, Lee J, Beenen M, Leaver-Fay A, Baker D, Popović Z, Players F. 2010 Predicting protein structures with a multiplayer online game. *Nature* **466**:756–760. doi:10.1038/nature09304

71. Laganowsky A, Liu C, Sawaya MR, Whitelegge J, Park J, Zhao M, Pensalfini A, Soriaga AB, Landau M, Teng PK, Cascio D, Glabe CG, Eisenberg D. 2012 Atomic view of a toxic amyloid small oligomer. *Science (80-)* **335**:1228–1231.

72. Liu C, Zhao M, Jiang L, Cheng P-N, Park J, Sawaya MR, Pensalfini A, Gou D, Berk A, Glabe CG, Nowick JS, Eisenberg D. 2012 Out-of-register beta-sheets suggest a pathway to toxic amyloid aggregates. *Proc Natl Acad Sci U S A* **109**:20913–20918. doi:10.1073/pnas.1218792109

73. Yu L, Lee S-J, Yee VC. 2015 Crystal structures of polymorphic prion protein β1 peptides reveal variable steric zipper conformations. *Biochemistry* **54**:3640–8. doi:10.1021/acs.biochem.5b00425

74. Butler AE, Janson J, Bonner-Weir S, Ritzel R, Rizza RA, Butler PC. 2003 Beta-cell deficit and increased beta-cell apoptosis in humans with type 2 diabetes. *Diabetes* **52**:102–110. doi:10.2337/diabetes.52.1.102

75. Mulder H, Ling C. 2009 Mitochondrial dysfunction in pancreatic β-cells in Type 2 Diabetes. *Mol Cell Endocrinol* **297**:34–40. doi:10.1016/j.mce.2008.05.015

76. Zraika S, Hull RL, Verchere CB, Clark A, Potter KJ, Fraser PE, Raleigh DP, Kahn SE. 2010 Toxic oligomers and islet beta cell death: Guilty by association or convicted by circumstantial evidence? *Diabetologia* **53**:1046–1056. doi:10.1007/s00125-010-1671-6

77. Magzoub M, Miranker AD. 2012 Concentration-dependent transitions govern the subcellular localization of islet amyloid polypeptide. *FASEB J* **26**:1228–1238. doi:10.1096/fj.11-194613

78. Tomasello MF, Sinopoli A, Attanasio F, Giuffrida ML, Campagna T, Milardi D, Pappalardo G. 2014 Molecular and cytotoxic properties of hIAPP17-29 and rIAPP17-29 fragments: A comparative study with the respective full-length parent polypeptides. *Eur J Med Chem* **81**:442–455. doi:10.1016/j.ejmech.2014.05.038

79. Liu Y, Schubert D. 1997 Cytotoxic amyloid peptides inhibit cellular 3-(4,5-dimethylthiazol-2-yl)-2,5-diphenyltetrazolium bromide (MTT) reduction by enhancing MTT formazan exocytosis. *J Neurochem* **69**:2285–2293.

80. Paulsson JF, Schultz SW, Köhler M, Leibiger I, Berggren P-O, Westermark GT. 2008 Real-time monitoring of apoptosis by caspase-3-like protease induced FRET reduction triggered by amyloid aggregation. *Exp Diabetes Res* **2008**:1–12. doi:10.1155/2008/865850

81. Meng F, Abedini A, Plesner A, Verchere CB, Raleigh DP. 2010 The Flavanol (-)-epigallocatechin 3-gallate inhibits amyloid formation by islet amyloid polypeptide, disaggregates amyloid fibrils, and protects cultured cells against IAPP-induced toxicity. *Biochemistry* **49**:8127–8133. doi:10.1021/bi100939a

82. Young LM, Saunders JC, Mahood RA, Revill CH, Foster RJ, Tu L-H, Raleigh DP, Radford SE, Ashcroft AE. 2014 Screening and classifying small-molecule inhibitors of amyloid formation using ion mobility spectrometry–mass spectrometry. *Nat Chem* **7**:73–81. doi:10.1038/nchem.2129

83. Opie EL. 1901 The relation of diabetes mellitus to lesions of the pancreas: hyaline degeneration of the islands of Langerhans. *J Exp Med* **5**:527–541.

84. Goldsbury CS, Cooper GJ, Goldie KN, Müller SA, Saafi EL, Gruijters WT, Misur MP, Engel A, Aebi U, Kistler J. 1997 Polymorphic fibrillar assembly of human amylin. *J Struct Biol* **119**:17–27. doi:10.1006/jsbi.1997.3858

85. Kajava A V., Aebi U, Steven AC. 2005 The parallel superpleated beta-structure as a model for amyloid fibrils of human amylin. *J Mol Biol* **348**:247–252. doi:10.1016/j.jmb.2005.02.029

86. Bedrood S, Li Y, Isas JM, Hegde BG, Baxa U, Haworth IS, Langen R. 2012 Fibril structure of human islet amyloid polypeptide. *J Biol Chem* **287**:5235–5241. doi:10.1074/jbc.M111.327817

87. Wineman-Fisher V, Atsmon-Raz Y, Miller Y. 2014 Orientations of Residues along the β - Arch of Self-Assembled Amylin Fibril-Like Structures Lead to Polymorphism. *Biomacromolecules* **16**:156–165. doi:dx.doi.org/10.1021/bm501326y

88. Ashburn TT, Auger M, Lansbury PT. 1992 The structural basis of pancreatic amyloid formation: isotope-edited spectroscopy in the solid state. *J Am Chem Soc*790–791. doi:10.1021/ja00028a073

89. Nielsen JT, Bjerring M, Jeppesen MD, Pedersen RO, Pedersen JM, Hein KL, Vosegaard T, Skrydstrup T, Otzen DE, Nielsen NC. 2009 Unique identification of supramolecular structures in amyloid fibrils by solid-state NMR spectroscopy. *Angew Chemie - Int Ed* **48**:2118–2121. doi:10.1002/anie.200804198

90. Sievers SA, Karanicolas J, Chang HW, Zhao A, Jiang L, Zirafi O, Stevens JT, Münch J, Baker D, Eisenberg D. 2011 Structure-based design of non-natural amino-acid inhibitors of amyloid fibril formation. *Nature* **475**:96–100. doi:10.1038/nature10154

91. Kahn SE, Cooper ME, Del Prato S. 2014 Pathophysiology and treatment of type 2 diabetes: Perspectives on the past, present, and future. *Lancet* **383**:1068–1083. doi:10.1016/S0140-6736(13)62154-6

92. Sevigny J, Chiao P, Bussière T, Weinreb PH, Williams L, Maier M, Dunstan R, Salloway S, Chen T, Ling Y, et al. 2016 The antibody aducanumab reduces Aß plaques in Alzheimer's disease. *Nature* **537**:50–6. doi:10.1038/nature19323

93. Shi D, Nannenga BL, de la Cruz MJ, Liu J, Sawtelle S, Calero G, Reyes FE, Hattne J, Gonen T. 2016 The collection of MicroED data for macromolecular crystallography. *Nat Protoc* **11**:895–904. doi:10.1038/nprot.2016.046

94. Kabsch W. 2010 XDS. *Acta Crystallogr D Biol Crystallogr* **66**:125–32. doi:10.1107/S0907444909047337

95. McCoy AJ. 2007 Solving structures of protein complexes by molecular replacement with Phaser. *Acta Crystallogr D Biol Crystallogr* **63**:32–41. doi:10.1107/S0907444906045975

96. Emsley P, Cowtan K. 2004 Coot: model-building tools for molecular graphics. *Acta Crystallogr D Biol Crystallogr* **60**:2126–32. doi:10.1107/S0907444904019158

97. McCoy AJ, Grosse-Kunstleve RW, Storoni LC, Read RJ. 2005 Likelihood-enhanced fast translation functions. *Acta Crystallogr D Biol Crystallogr* **61**:458–64. doi:10.1107/S0907444905001617

98. Afonine P V, Moriarty NW, Mustyakimov M, Sobolev O V, Terwilliger TC, Turk D, Urzhumtsev A, Adams PD. 2015 FEM: feature-enhanced map. *Acta Crystallogr D Biol Crystallogr* **71**:646–666. doi:10.1107/S1399004714028132

99. Lee B, Richards FM. 1971 The interpretation of protein structures: Estimation of static accessibility. *J Mol Biol* **55**: doi:10.1016/0022-2836(71)90324-X

100. Collaborative Computational Project Number 4. 1994 The CCP4 suite: programs for protein crystallography. *Acta Crystallogr D Biol Crystallogr* **50**:760–763. doi:10.1107/S0907444994003112

101. Connolly ML. 1983 Solvent-accessible surfaces of proteins and nucleic acids. *Science* **221**:709–13. doi:10.1126/science.68779170

102. Richards FM. 1977 Areas, volumes, packing, and protein structure. *Annu Rev Biophys Bioeng* **5**:151–176. doi:10.1146/annurev.bb.06.060177.001055

103. Lawrence MC, Colman PM. 1993 Shape complementarity at protein/protein interfaces. *J Mol Biol* **234**:946–50. doi:10.1006/jmbi.1993.1648

104. Sunde M, Serpell LC, Bartlam M, Fraser PE, Pepys MB, Blake CC. 1997 Common core structure of amyloid fibrils by synchrotron X-ray diffraction. *J Mol Biol* **273**:729–739. doi:10.1006/jmbi.1997.1348

105. Kyte J, Doolittle RF. 1982 A simple method for displaying the hydropathic character of a protein. *J Mol Biol* **157**:105–132. doi:10.1016/0022-2836(82)90515-0

106. Eisenberg DS, Wesson M, Yamashita M. 1989 Interpretation of protein folding and binding with atomic solvation parameters. *Chem Scr* **29A**:217–221.

107. Diederichs K, Karplus P a. 2013 Better models by discarding data? *Acta Crystallogr Sect D* **69**:1215–1222. doi:10.1107/S0907444913001121

108. Chen VB, Arendall WB, Headd JJ, Keedy D a., Immormino RM, Kapral GJ, Murray LW, Richardson JS, Richardson DC. 2010 MolProbity: All-atom structure validation for macromolecular crystallography. *Acta Crystallogr Sect D Biol Crystallogr* **66**:12–21. doi:10.1107/S0907444909042073

CHAPTER 2

Putative models of full-length hIAPP fibrils

INTRODUCTION

Fibrils of human islet amyloid polypeptide (hIAPP) are tightly linked to Type-II Diabetes (T2D) (1,2). They are found in approximately 90% of post-mortem, pancreatic tissue samples taken from T2D patients (3) and their abundance correlates positively with T2D severity (4–6). Despite this tight link to T2D, their precise role in pancreatic ß-cell death, if any, is unclear. Nonetheless, its link to disease necessitates the study of hIAPP fibril structure.

Several studies have generated different full-length hIAPP fibril models using an array of techniques. Although some of the models are very different from one another, they all share a common parallel, in-register ß-sheet structure, with 4.7 Å spacing between ß-strands.

In 2005, Kajava and co-workers proposed a super-pleated ß-sheet fibril model derived from a yeast prion structure (7). The protofibril unit contains one hIAPP molecule that forms three ß-strands in an S-shaped conformation, with minimal side-chain interdigitation between residues on adjacent strands. The units are arranged in parallel to one another along the fibril axis. Of note, no measurements from actual hIAPP fibrils were used to derive this model, except for some fibril width standards from electron micrographs.

In contrast, several groups, including our own, have proposed ß-hairpin fibril models of full-length hIAPP derived using different techniques. Luca and co-workers proposed one model based on mass-per-length (MPL) and solid-state nuclear magnetic resonance (ssNMR) measurements from a relatively homogenous fibril sample with a “striated ribbon” morphology (8). In this model, the protofibril unit contains two hIAPP molecules oriented face-to-face with interdigitation of side-chains, much like the steric zipper structures our group has previously described (9,10). In fact, our group used steric zipper structures of hIAPP 22-NNFGAIL-27 and 28-SSTNVG-33 to derive a similar hIAPP fibril model (11) that agrees with hIAPP fibril diffraction observed by Makin and co-workers (12). A third group used hydrogen exchange protection to derive a fibril model with similar β-sheet secondary structure composition to our group's model, but they did not provide any insight into side-chain arrangements (13). Using electron paramagnetic resonance (EPR) and double electron-electron resonance (DEER), a fourth group proposed yet another β-hairpin fibril model, this one with less β-sheet secondary structure, a left-handed pitch, and minimal side-chain interdigitation (14). Using ssNMR measurements and recombinantly expressed hIAPP, which does not contain the native C-terminal amidation, a fifth group derived a β-hairpin fibril model for hIAPP fibrils with a molten globule-like morphology (15). In this model, 23-FGAIL-27 forms the β-sheet-rich core, while the hIAPP N-terminus is more flexible. The authors further validated their model by demonstrating that hIAPP bound to a designed aggregation inhibitor has a similar structure to their proposed model (16).

Here, we present two more distinct hIAPP fibril models: one novel β-hairpin model generated from ssNMR constraints and atomic structures of hIAPP protein segments previously determined, and a second S-shaped model based on hIAPP's sequence similarity with amyloid-β (Aβ), the protein that forms fibrils associated with Alzheimer's disease (AD).

RESULTS

β-hairpin fibril model

To develop this model, we used ssNMR measurements from Luca and co-workers (8), combined with two previously determined atomic structures of hIAPP protein segments

(11,17). Fibrils of one of these segments, 19-29 S20G, which contains the early onset S20G mutation, was previously shown to be cytotoxic to cultured mammalian cells. The 19-29 S20G atomic structure shows two identical β-strands face-to-face, so we used one strand to model in residues N14-S19 (Figure 2.1B). The second protein segment, 28-33 WT, was used as a template to model in the steric zipper interface between the two β-hairpin protofibrils (Figure 2.1C). Additional features of the model were generated based on ssNMR chemical shifts measured by Luca and co-workers (8).

Similar to previously determined β-hairpin models, the protofibril unit of our model is formed from two C2 symmetry-related hIAPP molecules with β-hairpin structure (Figure 2.1A). The β-strands (8-18 and 23-35) possess tightly interdigitated side-chains, especially surrounding the loop. The loop that connects the β-strands is shorter compared to loops in previously determined β-hairpin models.

This model share similarities and differences with the model proposed by Luca and co-workers (Figure 2.1D). Both models share similar proximities between select amino acid side-chains and backbones, specifically between amino acid side-chains F15 and L27 and backbone pairings between A8-S34, Q10-V32, L12-T30, and N14-S28. Second, residues in both models share an overall similar secondary structure (Figure 2.4). However, the main difference between the two models is the size of the hairpin: in our model, the hairpin is formed between H18 and N22, but the Luca model shows a larger hairpin between H18 and L27. The primary determining factor of the larger hairpin in the Luca model is that F23 was not observed to have strong β-sheet secondary structure. However, more recent measurements of hIAPP fibrils with updated TALOS software for secondary structure predictions indicate that F23 may have β-sheet secondary structure, thus suggesting that our model may be fully compatible with the data from Luca and co-workers (Tycko lab, unpublished data).

Fibril diffraction collected from cytotoxic full-length fibrils is similar to fibril diffraction calculated from our β-hairpin model (Figure 2.2), thus suggesting this model may be a cytotoxic hIAPP fibril structure. The cytotoxicity of this fibrillar preparation was characterized previously (17).

S-shaped homology model

Several lines of evidence point to a link between amyloid-β (Aβ) and hIAPP cross-interaction *in vitro* and *in vivo*. Aβ and hIAPP are 50% similar in sequence (Figure 2.3A), similar segments in both proteins bind to one another (18), and fibrils of hIAPP can cross-seed Aβ fibril formation and vice versa (19). More about the structural similarity between Aβ and hIAPP can be found in Chapter 3. Fibrils of Aβ and hIAPP have been shown to cross-seed in animal models of disease (20,21). Thus, using Aβ fibrils models as templates for hIAPP fibril models is a logical strategy for elucidating structural features of full-length hIAPP fibrils.

We used a ssNMR structure of Aβ1-42 (22) to generate a model of full-length hIAPP fibrils. The Aβ model, derived from over 500 measurements recorded using magic angle spinning (MAS) NMR, shows two Aβ molecules composed of four β-strands that make a double-S-shape. In this model, the two Aβ molecules create a buried interface with two-fold symmetry that contains Q15, L17, L34, and M35. To generate our hIAPP model, we removed the Aβ side-chains and replaced them with their cognate similar hIAPP residues (Figure 2.3B). Next, because the Aβ1-42 had been developed with energy minimization, we likewise performed energy minimization of the hIAPP model using FoldIt.

As expected, the energy-minimized, S-shaped hIAPP model possesses an overall similar fold to its Aβ counterpart, but it is slightly less compact; they share a similar hydrophobic core, but the N and C termini in the hIAPP model are slightly more frayed. In the hIAPP model, hydrophobic residues are buried and polar amino acids are solvent exposed, but the Aβ model possesses four more buried hydrophobic residues, suggesting it may be more stable.

One central question that emerges is whether the interface between two hIAPP molecules would be in the same location as in the Aβ model. It seems equally possible that a second hIAPP molecule could bind on the other side of the fibril and thus generate an interface composed of S20, N21, and F23, thereby burying the hydrophobic F23 instead of leaving it solvent exposed as it is in our current model.

Furthermore, this S-shaped hIAPP fibril model is incompatible with the mouse IAPP (mIAPP) sequence (Figure 2.3D). mIAPP differs from hIAPP by only 6 residues, three of which are β-strand-breaking prolines (23). As a result, mIAPP does not form fibrils and mice do not get T2D. The three prolines fall within the central β-strand of the model and thus would completely disrupt any β-sheet secondary structure. The position of these prolines within a β-strand in the hIAPP model is in contrast to some hIAPP models presented previously (Figure 2.4).

The early onset S20G mutation is located in a loop on the same face as F23, and this location may possibly explain the enhanced fibrillar propensity of hIAPP-S20G. The mutation could generate a kink in the backbone that would allow F23 to point into the already stable hydrophobic core, thus stabilizing it even further. Preliminary energy minimization studies of the hIAPP-S20G fibril model using FoldIt do not support this hypothesis, but it is possible that this program does not sample a large enough conformational space. A more rigorous test of this hypothesis should be done using Molecular Dynamics simulations.

DISCUSSION

Despite the heterogeneity of the hIAPP fibril models presented here and elsewhere, they all exhibit a central theme: parallel in-register β-sheets with significant structural polymorphism between select models (Figure 2.4). Nearly every article that presents these models also cites the polymorphic nature of their fibril samples, thus suggesting that, although a single model is presented in each article, no purely uniform fibril sample exists *in vitro* or possibly *in vivo.* Consistent with the polymorphic nature of hIAPP fibrils, full-length hIAPP has so far resisted crystallization and single-particle cryoEM analysis. Thus, a full, atomic-resolution view of hIAPP fibrils has eluded researchers.

The polymorphic nature of hIAPP fibrils may also explain why some studies report hIAPP fibrils to be cytotoxic and others find them to be totally inert (24,25). Indeed, our own group found that certain structural polymorphs of hIAPP protein segments elicited greater cytotoxicity than others (17). Unfortunately, none of the articles that describe these full-length hIAPP models report on the cytotoxicity of their fibril samples.

There is one strategy that researchers may employ to overcome the polymorphic nature of hIAPP, and in doing so, hopefully uncover a full-length atomic-resolution structure. Using fibril samples taken post-mortem from T2D patients to seed *in vitro* material may create a more homogenous fibril sample. This strategy has been used in previous structural studies of Aβ (8,26). Not only would seeding generate a more homogenous sample, but it should also generate a physiologically relevant hIAPP fibril structure. In addition to studying the structures of these seeded fibrils, it seems equally valuable to investigate whether they elicit cytotoxicity in order for us to better understand whether fibrils are toxic *in vivo.*

MATERIALS AND METHODS

β-hairpin model

We generated this model using ssNMR measurements from Luca and co-workers (8), combined with two previously determined atomic structures of protein segments (11,17). Previously, segment 19-29 S20G (19-SGNNFGAILSS-29) was shown to be cytotoxic to cultured mammalian cells. First, we removed the first three amino acids of 19-29 S20G because they contain the mutant G20, which creates a kink in the backbone that cannot be formed by the wild-type sequence. The backbone and side-chains of one of the strands was used as a template to model in amino acids N14-S19. The second protein segment, 28-33 WT (28-SSTNVG-33), was used as a template to model in the steric zipper interface between the two β-hairpin protofibrils. Additional features of the model were generated based on ssNMR constraints measured by Luca and co-workers (8). Amino acids 8-37 were designated as β-strands based on their ^{13}C secondary chemical shifts measurements. ssNMR constraints between amino acid side-chains F15 and L27 and backbone pairings between A8-S34, Q10-V32, L12-T30, and N14-S28 were also used. Mass-per-length (MPL) measurements of hIAPP fibrils used by Luca and co-workers agree with the size dimensions of our newly developed β-hairpin model.

S-shaped homology model

To generate this model, we took the atomic structure of Aβ1-42 presented by Colvin and co-workers (PDB code: 5KK3) and, using COOT (27), mutated similar amino acids to their cognate amino acids in the hIAPP sequence. Given that the final Aβ1-42 model had been subjected to energy minimization, we likewise performed energy minimization of our new hIAPP model. After performing energy minimization using FoldIt (28), we observed the energy of the model be reduced from +8140 REU to -709 REU. The original Aβ1-42 model possessed a similar energy of -567 REU. We used amino acids 15-42 of the Aβ1-42 model because this was the region that was the most ordered. Thus, our hIAPP model includes residues 10-37 as these are the similar residues to Aβ 15-42.

Fibril diffraction and radial profile analysis

We generally followed our previously published protocol (17). Cytotoxic hIAPP fibrils were formed in PBS and 1% DMSO at room temperature without shaking. Next, the fibrils were pelleted using an Airfuge Ultracentrifuge set at 75,000 rpm for 1 hr (Beckman-Coulter, Brea, CA) and then concentrated 10x in water. The fibrils were pipetted between two siliconized capillary ends (29). Fibril diffraction was collected using a RIGAKU R-AXIS HTC imaging plate detector using Cu K(alpha) radiation from a FRE+ rotating anode generator with VARIMAX HR confocal optics (Rigaku, Tokyo, Japan). Radial profiles of the β-hairpin fibril model were calculated using a program written in-house, which calculates the average intensity as a function of distance from the beam center.

ACKNOWLEDGEMENTS

We thank the Advanced Photon Source (APS) staff for beamline support during collection of fiber diffraction: M. Capel, K. Rajashankar, N. Sukumar, J. Schuermann, I. Kourinov and F. Murphy at NECAT beam lines 24-ID. Also, we thank Robert Tycko for sharing updated secondary structure predictions from TALOS with us.

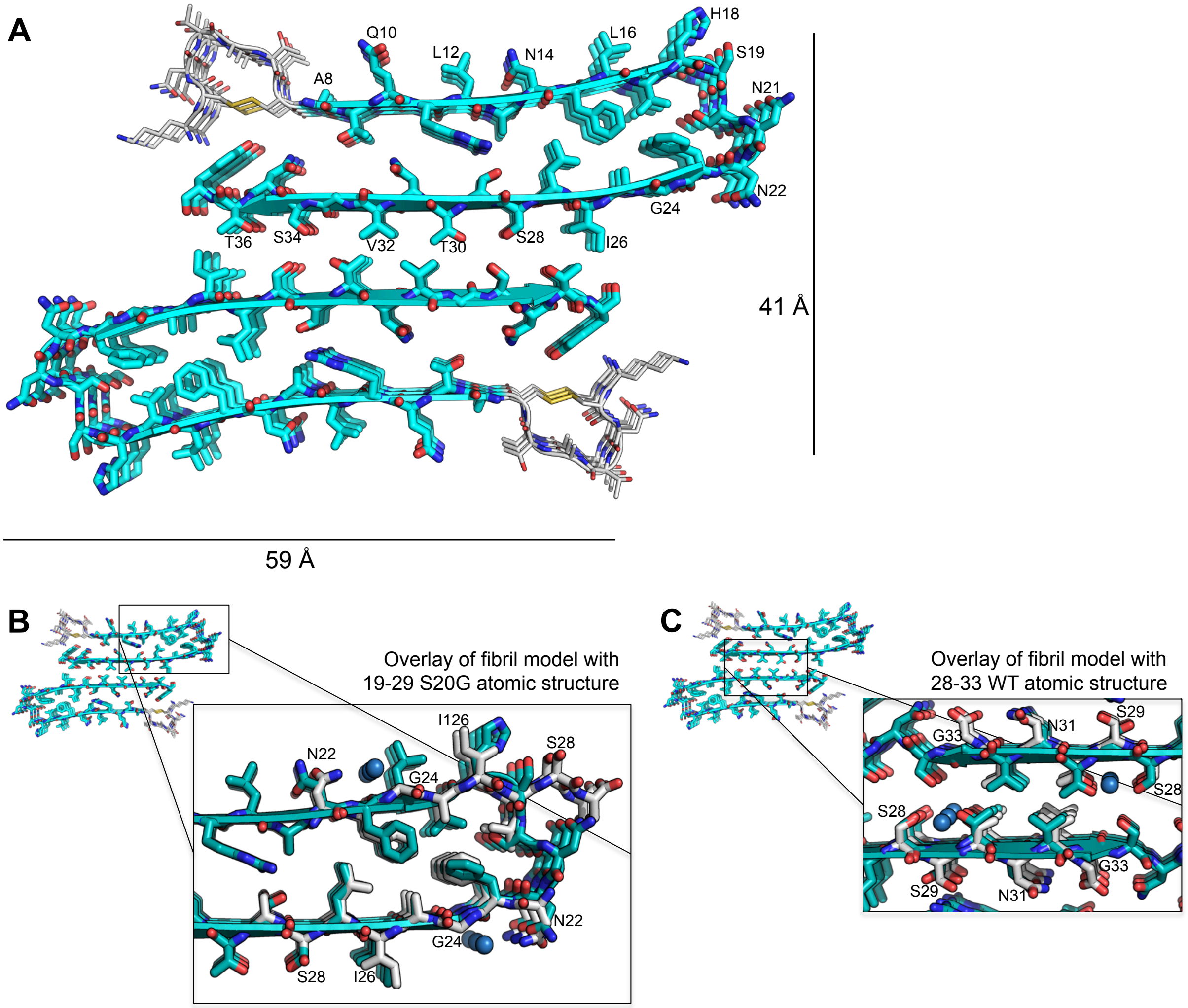

D Overlay of fibril model with Luca *et al* model

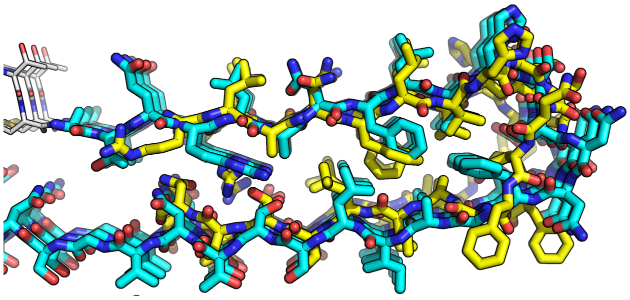

Figure 2.1 β-hairpin model of hIAPP fibrils. A. The model was generated using atomic structures of hIAPP segments (19-29 S20G and 28-33 WT) and select ssNMR constraints (Sidechain pair: F15/L27; Backbone pair: A8/S34, Q10/V32, L12/T30, N14/S28) and MPL measurements recorded by Luca and co-workers. **B.** Atomic structure of 19-29

S20G (white), determined by Krotee and co-workers, overlaid on full-length hIAPP model (cyan). **C.** Atomic structure of 28-33 WT (white), determined by Wiltzius, and co-workers, overlaid on full-length hIAPP model (cyan). **D.** Two layers of β-hairpin structure proposed by Luca and co-workers (yellow) overlaid on hIAPP atomic model (cyan).

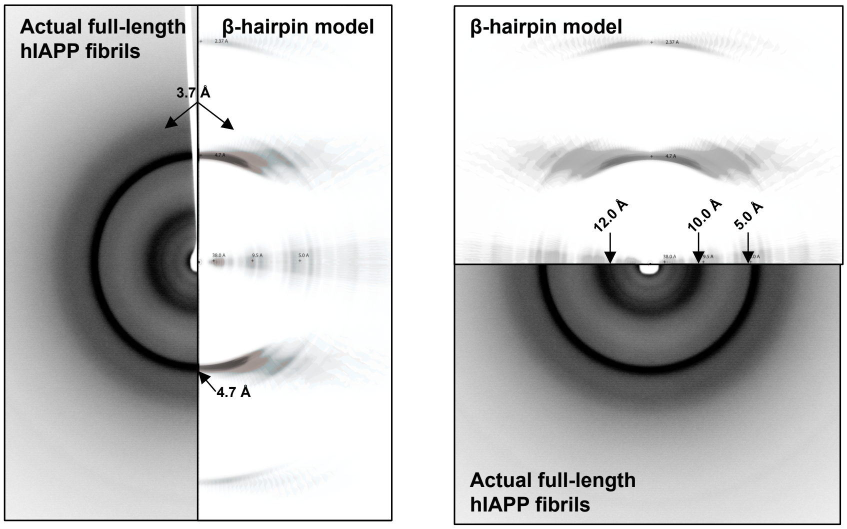

Figure 2.2 Fiber diffraction calculated from the β-hairpin model of hIAPP fibrils is similar to fiber diffraction collected from cytotoxic hIAPP fibrils. The diffraction patterns share reflections at 4.7 Å along the meridian and 3.7 Å along the off-meridian (left panel). Also, the diffraction patterns share reflections at 5.0 Å, 10.0 Å, and 12.0 Å along the equator (right panel).

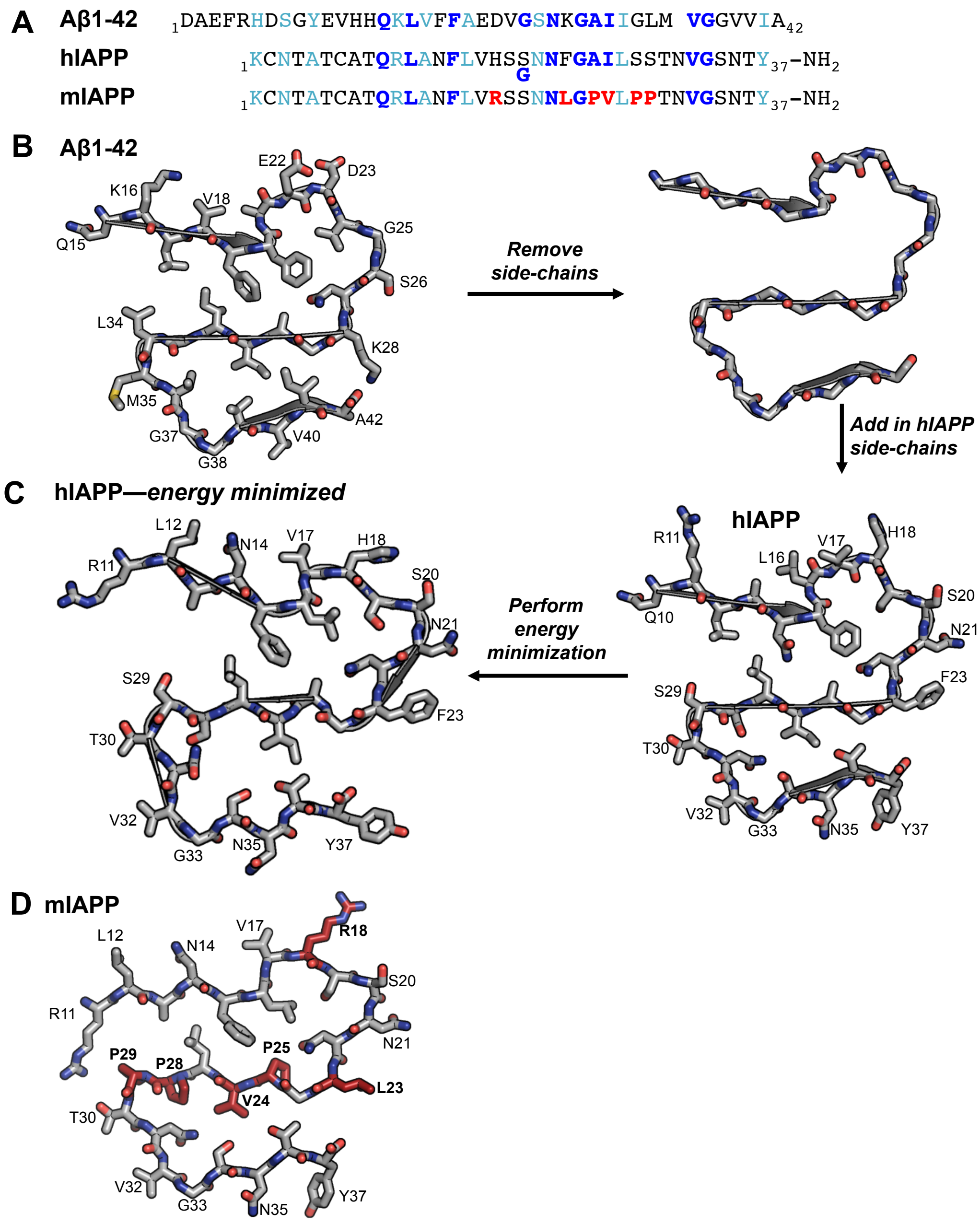

Figure 2.3 S-shaped homology model of hIAPP fibrils. **A.** Sequence alignment of Aβ1-42, hIAPP, and mIAPP; identical and similar residues are highlighted in dark blue and light blue, respectively. Residues unique to mIAPP are highlighted in red. hIAPP is 51% similar and 27% identical to Aβ1-42. The early onset T2D mutation in hIAPP, S20G, is shown below the hIAPP sequence. **B.** Schematic of hIAPP S-shaped homology model

development. We started with the S-shaped Aβ1-42 model proposed by Colvin and co-workers, then we removed the side-chains and added in the appropriate residues from hIAPP (Note: only one Aβ1-42 molecule is shown, but Colvin and co-worked propose that the protofibril unit contains two molecules related by C2 symmetry). Next, the hIAPP model was subjected to energy minimization using FoldIt, to reveal the final structure (**C**). **D.** S-shaped homology model with mouse IAPP (mIAPP) sequence modeled in. Residues of mIAPP that differ from hIAPP are colored red in the model. The three β-strand-breaking prolines of mIAPP—P25, P28, and P29—reside within the central β-strand, thus suggesting that this model is strongly incompatible with the mouse sequence.

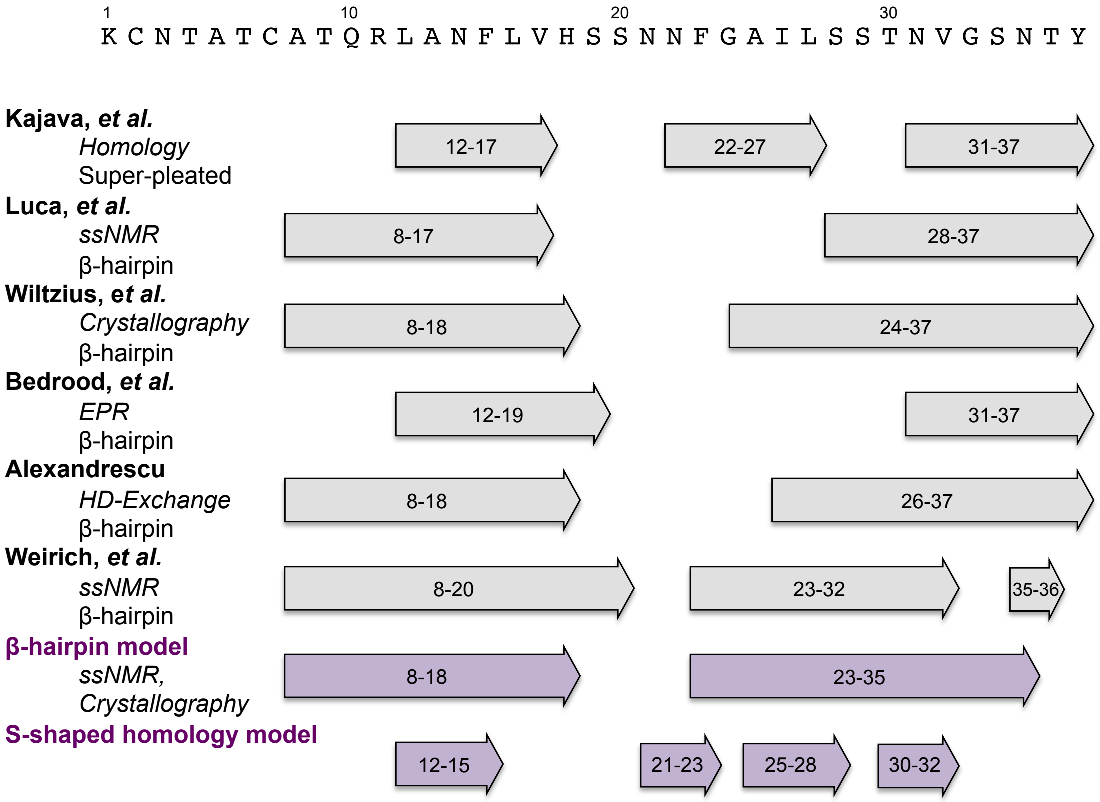

Figure 2.4 Summary of β-sheet secondary structure observed across full-length hIAPP models proposed to date: Kajava, *et al.* (7), Luca, *et al.* (8), Wiltzius, *et al.* (11), Bedrood, *et al.* (14), Alexandrescu (13), and Weirich, *et al.* (15). A short description of the model structure and the method used to generate the model are listed to the left.

REFERENCES

1. Westermark P, Wernstedt C, Wilander E, Hayden DW, O'Brien TD, Johnson KH. 1987 Amyloid fibrils in human insulinoma and islets of Langerhans of the diabetic cat are derived from a neuropeptide-like protein also present in normal islet cells. *Proc Natl Acad Sci U S A* **84**:3881–3885. doi:10.1073/pnas.84.11.3881

2. Cooper GJS, Willis AC, Clark A, Turner RC, Sim RB, Reid KB. 1987 Purification and characterization of a peptide from amyloid-rich pancreases of type 2 diabetic patients. *Proc Natl Acad Sci U S A* **84**:8628–8632. doi:10.1073/pnas.84.23.8628

3. Hoppener JWM, Ahren B, Lips CJM. 2000 Islet Amyloid and Type 2 Diabetes Mellitus. *N Engl J Med* **343**:411–419. doi:10.1056/NEJM200008103430607

4. Maloy AL, Longnecker DS, Greenberg ER. 1981 The relation of islet amyloid to the clinical type of diabetes. *Hum Pathol* **12**:917–922.

5. Esapa C, Moffitt JH, Novials A, McNamara CM, Levy JC, Laakso M, Gomis R, Clark A. 2005 Islet amyloid polypeptide gene promoter polymorphisms are not associated with Type 2 diabetes or with the severity of islet amyloidosis. *Biochim Biophys Acta* **1740**:74–78. doi:10.1016/j.bbadis.2005.02.001

6. Jurgens CA, Toukatly MN, Fligner CL, Udayasankar J, Subramanian SL, Zraika S, Aston-Mourney K, Carr DB, Westermark P, Westermark G, Kahn SE, Hull RL. 2011 Β-Cell Loss and Β-Cell Apoptosis in Human Type 2 Diabetes Are Related To Islet Amyloid Deposition. *Am J Pathol* **178**:2632–40. doi:10.1016/j.ajpath.2011.02.036

7. Kajava A V., Aebi U, Steven AC. 2005 The parallel superpleated beta-structure as a model for amyloid fibrils of human amylin. *J Mol Biol* **348**:247–252. doi:10.1016/j.jmb.2005.02.029

8. Luca S, Yau W-M, Leapman R, Tycko R. 2007 Peptide conformation and supramolecular organization in amylin fibrils: Constraints from solid-state NMR. *Biochemistry* **46**:13505–13522. doi:10.1021/bi701427q

9. Nelson R, Sawaya MR, Balbirnie M, Madsen AØ, Riekel C, Grothe R, Eisenberg D. 2005 Structure of the cross-beta spine of amyloid-like fibrils. *Nature* **435**:773–778. doi:10.1038/nature03680

10. Sawaya MR, Sambashivan S, Nelson R, Ivanova MI, Sievers SA, Apostol MI, Thompson MJ, Balbirnie M, Wiltzius JJW, McFarlane HT, Madsen AØ, Riekel C, Eisenberg D. 2007 Atomic structures of amyloid cross-β spines reveal varied steric zippers. *Nature* **447**:453–457. doi:10.1038/nature05695

11. Wiltzius JJW, Sievers SA, Sawaya MR, Cascio D, Popov D, Riekel C, Eisenberg D. 2008 Atomic structure of the cross-beta spine of islet amyloid polypeptide (amylin). *Protein Sci* **17**:1467–1474. doi:10.1110/ps.036509.108.

12. Makin OS, Serpell LC. 2004 Structural Characterisation of Islet Amyloid Polypeptide Fibrils. *J Mol Biol* **335**:1279–1288. doi:10.1016/j.jmb.2003.11.048

13. Alexandrescu AT. 2013 Amide Proton Solvent Protection in Amylin Fibrils Probed by Quenched Hydrogen Exchange NMR. *PLoS One* **8**: doi:10.1371/journal.pone.0056467

14. Bedrood S, Li Y, Isas JM, Hegde BG, Baxa U, Haworth IS, Langen R. 2012 Fibril structure of human islet amyloid polypeptide. *J Biol Chem* **287**:5235–5241. doi:10.1074/jbc.M111.327817

15. Weirich F, Gremer L, Mirecka EA, Schiefer S, Hoyer W, Heise H. 2016 Structural characterization of fibrils from recombinant human islet amyloid polypeptide by solid-state NMR: the central FGAILS segment Is part of the β-Sheet core. *PLoS One* **11**:e0161243. doi:10.1371/journal.pone.0161243

16. Mirecka EA, Feuerstein S, Gremer L, Schröder GF, Stoldt M, Willbold D, Hoyer W. 2016 β -hairpin of islet amyloid polypeptide bound to an aggregation inhibitor. *Sci Rep*1–8. doi:10.1038/srep33474

17. Krotee P, Rodriguez JA, Sawaya MR, Cascio D, Reyes FE, Shi D, Hattne J, Nannenga BL, Oskarsson ME, Philipp S, Griner S, Jiang L, Glabe CG, Westermark GT, Gonen T, Eisenberg DS. 2017 Atomic Structures of Fibrillar Segments of hIAPP Suggest Tightly Mated β-Sheets Are Important for Cytotoxicity. *Elife* **6**:e19273. doi:10.7554/eLife.19273

18. Andreetto E, Malideli E, Yan L, Kracklauer M, Farbiarz K, Tatarek-nossol M, Rammes G, Prade E, Neumüller T, Caporale A, Spanopoulou A, Bakou M, Reif B, Kapurniotu A. Supporting Information A Hot-Segment-Based Approach for the Design of Cross-Amyloid Interaction Surface Mimics as Inhibitors of Amyloid Self-Assembly.

19. O'Nuallain B, Williams AD, Westermark P, Wetzel R. 2004 Seeding Specificity in Amyloid Growth Induced by Heterologous Fibrils. *J Biol Chem* **279**:17490–17499. doi:10.1074/jbc.M311300200

20. Oskarsson ME, Paulsson JF, Schultz SW, Ingelsson M, Westermark P, Westermark G. 2015 In Vivo Seeding and Cross-Seeding of Localized Amyloidosis. *Am J Pathol* **185**:834–846. doi:10.1016/j.ajpath.2014.11.016

21. Moreno-Gonzalez I, Edwards III G, Salvadores N, Shahnawaz M, Diaz-Espinoza R, Soto C. 2017 Molecular interaction between type 2 diabetes and Alzheimer's disease through cross-seeding of protein misfolding. *Mol Psychiatry* doi:10.1038/mp.2016.230

22. Colvin MT, Silvers R, Ni QZ, Can T V., Sergeyev I, Rosay M, Donovan KJ, Michael B, Wall J, Linse S, Griffin RG. 2016 Atomic Resolution Structure of Monomorphic A??42 Amyloid Fibrils. *J Am Chem Soc* **138**:9663–9674. doi:10.1021/jacs.6b05129

23. Nishi M, Chan SJ, Nagamatsu S, Bell GI, Steiner DF. 1989 Conservation of the sequence of islet amyloid polypeptide in five mammals is consistent with its putative role as an islet hormone. *Proc Natl Acad Sci U S A* **86**:5738–5742. doi:10.1073/pnas.86.15.5738

24. Abedini A, Plesner A, Cao P, Ridgway Z, Zhang J, Tu L-H, Middleton CT, Chao B, Sartori D, Meng F, Wang H, Wong AG, Zanni MT, Verchere CB, Raleigh DP, Schmidt AM. 2016 Time-resolved studies define the nature of toxic IAPP intermediates, providing insight for anti-amyloidosis therapeutics. *Elife* **53**:1689–1699. doi:10.7554/eLife.12977

25. Schlamadinger DE, Miranker AD. 2014 Fiber-dependent and independent toxicity of islet amyloid polypeptide. *Biophys J* **107**:2559–2566. doi:10.1016/j.bpj.2014.09.047

26. Qiang W, Yau W-M, Lu J-X, Collinge J, Tycko R. 2017 Structural variation in amyloid-β fibrils from Alzheimer's disease clinical subtypes. *Nature* **541**:217–221. doi:10.1038/nature20814

27. Emsley P, Cowtan K. 2004 Coot: model-building tools for molecular graphics. *Acta Crystallogr D Biol Crystallogr* **60**:2126–32. doi:10.1107/S0907444904019158

28. Cooper S, Khatib F, Treuille A, Barbero J, Lee J, Beenen M, Leaver-Fay A, Baker D, Popović Z, Players F. 2010 Predicting protein structures with a multiplayer online game. *Nature* **466**:756–760. doi:10.1038/nature09304

29. Sunde M, Serpell LC, Bartlam M, Fraser PE, Pepys MB, Blake CC. 1997 Common core structure of amyloid fibrils by synchrotron X-ray diffraction. *J Mol Biol* **273**:729–739. doi:10.1006/jmbi.1997.1348

CHAPTER 3

Common fibrillar spines of amyloid-β and hIAPP revealed by MicroED and inhibitors developed using structure-based design

INTRODUCTION

Amyloid fibrils, formed from the aggregation of specific proteins, are associated with pathogenesis in a variety of incurable, and largely untreatable, diseases. These fibrils all appear morphologically similar and share β-sheet rich structures, which normally stack along the fibril axis. Such fibrils give a cross-β diffraction pattern when they are aligned and analyzed with a X-ray beam (1,2). Two of the most common of these amyloid diseases are Alzheimer's disease (AD) and Type-II diabetes (T2D). In AD, extracellular amyloid fibrils that form senile plaques are primarily composed of amyloid-β (Aβ), a peptide of 39-42 residues in length. In T2D, amyloid fibrils are primarily composed of human islet amyloid polypeptide (hIAPP), a 37-residue peptide hormone (3,4).

Although the deposits of the fibrils are predominantly of a single protein in each disease, they can contain more than one protein, which has led some to hypothesize that amyloid proteins may make cross-sequence interactions and self-assemble (5). For example, in AD, Aβ has been reported to form soluble complexes with tau (6), as well as co-deposit with alpha-synuclein (7) and transthyretin (8). In contrast, in T2D, hIAPP aggregation is inhibited by binding to insulin (9,10). Recently, hIAPP has been identified to co-deposit with Aβ in senile plaques found in AD patient-derived samples (11).

The molecular basis for cross-sequence interactions and self-assembly of Aβ and hIAPP has been examined *in vitro*. Both peptides are natively unfolded, but contain hydrophobic regions that are highly aggregation prone. They share a high degree of sequence similarity, being 50% similar and 25% identical (Figure 3.1A), with sequence segments important for self-assembly displaying the most similarity (12). Protein segments of Aβ and hIAPP with the highest degrees of similarity appear to be important for hetero-assembly formation as well, and are capable of binding to one another with high affinity (13,14). Aβ and IAPP appear to interact not only in their native unfolded states, but they can also interact once aggregated. Aβ fibrils seed hIAPP fibril formation *in vitro*, suggesting the 3D fibril structure of Aβ is able to template hIAPP fibril formation, possibly by conferring a similar structural motif (15). Supporting this idea that the underlying structures of the fibrils are similar, a recent study describes a peptide-based inhibitor that mitigates fibril formation and cytotoxicity of both Aβ and hIAPP (16).

These observations suggest that the proteins may also interact *in vivo,* and thus have been investigated in more pre-clinical disease models. One study showed that islet amyloid formed in hIAPP transgenic mice upon injection with either Aβ or hIAPP fibril seeds (11). Moreover, a recent study observed a similar cross-seeding effect when Aβ transgenic mice were injected with hIAPP seeds (17). Beyond model systems, clinical observations have reported a correlation in increased risk for AD in T2D patients and vice versa (18–20), but clear cause of the increased risk has not been identified. Some studies suggest AD and T2D are connected by heightened stress and cholesterol levels, while others propose that cross-amyloid interactions, or cross-seeding, connect the diseases (21). This has led some to hypothesize that drugs used to treat T2D may be effective treatments for AD (22). If the underlying connection between AD and T2D is cross-seeding, then fibrillar structures of Aβ and hIAPP may provide a path for the development of therapeutics using structure-based design, which target both diseases.

Here, we examine the fibrillar structures of Aβ and hIAPP by focusing on 2 11-residue, fibril-forming protein segments with 64% sequence identity; we call the segments Aβ 24-34 WT and hIAPP 19-29 S20G, which harbors a familial mutation implicated in early onset T2D (Figure 3.1B) (23–25). In addition to high identity, these sequences appear to be important for fibril formation and accompanying toxicity of their respective full-length proteins. The Aβ 24-34 WT segment is integral to the core in all of the various models of full length Aβ fibrils (26–29). Additionally, short protein segments spanning residues 27-32 and 29-34 of Aβ crystallize in steric zipper arrangements (30). Computational predictions identify Aβ 24-34 WT as a minimal segment able to oligomerize (31,32); indeed, it contains residues necessary for oligomerization and formation of toxic species (33–35). Previously, we demonstrated that fibrils formed from the hIAPP 19-29 S20G segment are near toxic to that of full-length hIAPP and comprise the spine of the mature fibrils (36). Through atomic structures of these cytotoxic fibrillary segments, we provide atomic-resolution evidence for similar Aβ and hIAPP fibrillar structures. By testing peptide-based inhibitors developed using structure-based design from one structure, we demonstrate that inhibitors appear to target both of these segments in their parent full-length proteins and thus show dual efficacy.

RESULTS

Atomic structure of Aβ 24-34 WT determined using MicroED

Like the 11-residue segments of previously determined amyloid structures (36,37), Aβ 24-34 WT crystallized as microcrystals only a few hundred nanometers thick (Figure 3.2A). This crystal size is ideal for Micro-Electron Diffraction (MicroED), a diffraction mode method of cryo-electron microscopy (cryoEM), as the low dose electrons interact strongly with matter and are able to produce diffraction patterns similar to X-ray crystallography (38–41).

The structure of Aß 24-34 WT forms a typical class I steric-zipper, with pairs of parallel in-register ß-sheets (Figure 3.2B). The side-chains interdigitate to form two dry interfaces (Figure 3.2—Figure Supplement 1). Interface A buries almost 210 Å^2 of solvent-accessible surface area per strand with a shape complementarity of 0.62, with Ala30, Ile32 and Leu34 stabilizing the core. Additionally, this interface is capped by hydrogen bonding of Lys28 to the carboxy-terminus of the paired sheet. Interface B buries 256 Å^2 of solvent-accessible surface area and has a shape complementarity of 0.85, with Asn27, Gly29 and Ile31 stabilizing this interface. A kink in the backbone at Gly25 causes Val24 and Gly33 to contribute to this interface, with Val24 packing into the space provided by the lack of side-chain at Gly33. This kink also positions the terminal residues of the opposing chains together, facilitating hydrogen bonding, a motif that was previously seen in the atomic structure of the NACore of α-synuclein (37).

We see similarities in reflections collected from fibril diffraction of Aß1-42 and our crystallized segment. Both share reflections at 4.7 Å and 2.4 Å, indicative of the spacing of stacked ß-sheets, and a set of reflections around 3.7 Å (Figure 3.2C). The diffraction pattern of Aß 24-34 WT has two strong lower resolution rings of 8.6 Å and 7.4 Å, pertaining to the distance between the sheets in Interface A and B, respectively. The Aß1-42 diffraction pattern has a wide band of unresolved low resolution reflections centered around 10 Å, which is most likely caused by the structural heterogeneity seen in full-length fibrils. These distances indicate that Interface A, being more widely spaced, is more likely the interface that is similar to the spine of the full-length fibrils. Furthermore, residues stabilizing Interface A are in agreement with ß-turn-ß ssNMR structures of Aß1-40 and

Aβ1-42, which have residues Ala30, Ile32 and Leu34 positioned in the fibril interface (26,28).

Segment Aβ 24-34 WT is cytotoxic

Given that full-length Aβ is known to be cytotoxic (42), we next aimed to determine if Aβ 24-34 WT is likewise cytotoxic. To investigate the cytotoxicity of Aβ 24-34 WT, we assessed the effects of the soluble and fibrillar forms of the protein segment on Neuro-2a (N2a) cells, a mouse neuroblastoma cell line (43). We measured cytotoxicity using MTT dye reduction (44,45) and we measured pro-apoptotic caspase activation using a fluorescent marker for caspase activity.

Using MTT dye reduction, we observe that soluble Aβ 24-34 WT is mildly cytotoxic at high concentrations, but its fibrillar form is significantly more cytotoxic (Figure 3.3A). Aβ 24-34 WT is not as cytotoxic as full-length Aβ 1-42, possibly because Aβ 24-34 WT lacks other residues that are important for cytotoxicity, particularly Met35, which is an important contributor to the potent cytotoxicity of Aβ 25-35 (46,47). Additionally, we observe that fibrillar Aβ 24-34 WT activates pro-apoptotic caspases, but to a lesser degree than full-length Aβ 1-42 at similar concentrations (Figure 3.3B, Figure 3.3—Figure Supplement 1D).

The insoluble fraction of the Aβ 24-34 WT fibrillar sample is cytotoxic, while the soluble fractions are not, thus suggesting that fibrils are the cytotoxic species in our studies (Figure 3.3B). However, it is plausible that some undetectable population of highly toxic oligomers that associate with fibrils causes the cytotoxicity of the insoluble fraction.

Additionally, we observe that fibrils of the toxic spine from hIAPP, hIAPP 19-29 S20G, are slightly more cytotoxic than Aβ 24-34 WT to the same cell line (Figure 3.3—Figure Supplement 1B).

The spines of Aβ and hIAPP are structurally similar

The similarity in sequence between segments Aβ 24-34 WT and hIAPP 19-29 S20G motivated us to compare their atomic structures. We had previously determined the atomic structure of hIAPP 19-29 S20G (36), a spine segment of hIAPP that shares 64% sequence similarity with Aβ 24-34 WT (Figure 3.1B), also using MicroED data.

For both segments, the packing of the crystal reveals two interfaces termed Interface A and Interface B (Figure 3.4A). For hIAPP 19-29 S20G, Interface A is likely the primary interface because it excludes waters and fibril diffraction calculated from this interface best matches diffraction collected from full-length hIAPP fibrils. Its Interface B contains waters and lower shape complementarity.

After performing a structural overlay of Aβ 24-34 WT onto hIAPP 19-29 S20G using LSQKAB, we observe that their A Interfaces are the most similar; their backbones possess a low RMSD of 0.96 Å (Figure 3.4A). The backbones of Interfaces B possess a higher RMSD of 2.11 Å. Although the backbones of this interface do not align as well, the interface is stabilized by almost identical residues. The residues flanking this interface, deviating from β-sheet secondary structure to form favorable crystal packing contacts, as well as a water coordinated to Asn22 in hIAPP 19-29 S20G may account for the increased backbone RMSD. Indeed, these segments, which share similar sequences, possess equally similar structures.

However, a closer look at the segment overlay of the A Interfaces reveals a paradox. Although the backbones of the interfaces agree well and the sequences of the segments are very similar, their identical side-chains do not align and, instead, are shifted by two residues (Figure 3.4B). As a result, the alanine residues that occupy the cores of the interfaces, Ala30 in Aβ 24-34 WT and Ala25 in hIAPP 19-29 S20G, overlay with Phe23 and Ile32 in the hIAPP and Aβ atomic structures, respectively. The leucines in the cores of each of the two interfaces, which are not corresponding residues in the sequence alignment, almost perfectly overlay.

Additionally, the mated sheets in each of the two atomic structures differ in the number of residues that stabilize Interface A. 10 of the 11 residues of hIAPP 19-29 S20G form Interface A, while the same interface of the Aβ 24-34 WT structure is composed of only 6 of the 11 residues (Figure 3.4B). In the Aβ 24-34 WT atomic structure, the main driver of the reduced overlap between sheets appears to be Lys28, which hydrogen bonds to the carboxy terminus of the adjacent strand in the mated sheet. As these atomic structures form the spines of their parent full-length proteins and are so similar, we postulated that they could facilitate cross-seeding of amyloid fibril formation. Unsurprisingly, both Aβ 24-34 WT and hIAPP 19-29 S20G fibrils seed full-length Aβ 1-42 and hIAPP fibril formation near to the efficiency of their cognate full-length protein (Figure 3.4C, D). These results suggest that perhaps peptide-based inhibitors of fibril formation, developed for hIAPP using the 19-29 S0G atomic structure, may likewise target Aβ.

Development of inhibitors using structure-based design against hIAPP 19-29 S20G

We sought to develop peptide-based inhibitors of hIAPP fibril formation. To this end, we used the hIAPP 19-29 S20G atomic structure as a scaffold for structure-based design of the inhibitors and we used a Rosetta-based design strategy and workflow similar to Sievers, *et al.* (Figure 3.5A). Our laboratory has used similar strategies to develop peptide-based inhibitors that reduce fibril formation of amyloid proteins tau, p53, and transthyretin, which are implicated in tauopathies, various cancers, and familial amyloid polyneuropathy (FAP), respectively (48–50). We performed multiple rounds of design that produced approximately 50 peptide sequences, about a dozen of which were effective at reducing hIAPP 19-29 S20G fibril formation and cytotoxicity (Table 3.3; Figure 3.5—Figure Supplement 1).

We chose to focus on 2 D-form peptide sequences because of their potential *in vivo* stability (Miller et al. 1995), which may be important during downstream clinical testing (Figure 3.5B, C). These designs, abbreviated p14 and p15, reduce fibril formation of the design target, hIAPP 19-29 S20G (Figure 3.5D) at equimolar concentrations, while their cognate negative controls do not. Consistent with previous findings, reducing fibril formation likewise reduces the cytotoxicity of hIAPP 19-29 S20G to HEK293 cells (Figure 3.5E).

The peptide-based inhibitors are specific for the design target; they do not reduce aggregation of three other amyloid proteins, transthyretin, tau, and α-synuclein (Figure 5—Figure Supplement 3).

Cross-amyloid efficiency of inhibitors

Given the structural and sequence similarity between the two atomic structures and their ability to cross-seed, we aimed to determine whether the inhibitors, developed using the hIAPP 19-29 S20G atomic structure, were effective against both full-length hIAPP and full-length Aβ.

Using ThT fluorescence, we observe that p14 and p15 reduce fibril formation of full-length hIAPP, but their cognate negative control peptides (p16 and p17, respectively) do not (Figure 3.6A). 48 hours into the ThT fluorescence assay in Figure 3.6A, the experiment was paused and aliquots were taken for negative-stain TEM. Negative-stain TEM analysis confirmed the reduction of fibrils in hIAPP samples incubated with p14 and p15. Instead, these samples contained small fibrillar aggregates and amorphous aggregates (Figure 3.6B). As expected, hIAPP samples incubated with negative control peptides contained abundant fibrils.

Consistent with our observation of reduced fibrils, we observe that p14 and p15 reduce cytotoxicity of full-length hIAPP, but their cognate negative control peptides do not (Figure 3.6C). We tested the cytotoxicity of the samples to Rin5F cells, a rat pancreatic β-cell line, and we quantified cytotoxicity using MTT dye reduction. Other inhibitor designs also reduce the cytotoxicity of full-length hIAPP to Rin5F cells (Figure 3.6—Figure Supplement 3).

Next, we tested whether the same inhibitors, designed against hIAPP 19-29 S20G, reduce fibril formation and cytotoxicity of full-length Aβ 1-42. We observe that p14 and p15 reduce cytotoxicity of Aβ 1-42 to N2a cells (Figure 3.6D), but neither p14 nor p15 appear to reduce Aβ 1-42 fibril formation (Figure 3.6—Figure Supplement 1). To investigate whether the peptide inhibitors reduce the formation of some other cytotoxic Aβ 1-42 assemblies, we probed samples with 31 different conformational antibodies. Three monoclonal antibodies, mOC 88, mOC 3, and mOC 22 showed markedly reduced binding to Aβ 1-42 incubated with either p14 or p15 (Figure 3.6E, Figure 3.6—Figure Supplement 2). We observed no reduction in binding to Aβ 1-42 incubated with negative control peptides. Although not much is known about the conformations of Aβ that these antibodies recognize, one previous study showed that mOC 3 and mOC 22 bind to Aβ plaques in AD patient-derived brain tissue and also bind to hIAPP fibrils formed *in vitro* (51).

DISCUSSION

Aβ and hIAPP, implicated in AD and T2D, respectively, have been linked for over a decade, but the underlying cause of the link has not been fully clear. Previous studies point to their similar sequences and their abilities to cross-seed *in vivo* and *in vitro* as the underlying cause (11,13,17,52). Here, through atomic structures determined using MicroED and designed inhibitors with cross-amyloid efficacy, we provide evidence that indicates these proteins are further linked by spines with similar fibrillar structures.

Although the spines of Aß and hIAPP are similar in sequence and structure, their structural similarity does not necessarily correlate with regions of increased sequence identity; this is particularly true for the 'A' Interfaces of the two segments. This observation that sequence similarity is not the only determinant of cross-seeding efficiency has been described previously for immunoglobulin (Ig) light chains, polyglutamine tracts, and ß-2 microglobulin, all of which seed Aß 1-40 fibril formation *in vitro* (15), and this is especially true for the amyloid-like prion proteins Sup35p, Ure2p, and Rnq1p (53). Nevertheless, the efficiency with which Aß 24-34 WT and hIAPP 19-29 S20G fibrils seed both Aß 1-42 and hIAPP fibril formation suggests that their common structures are important for cross-seeding.

We further support the hypothesis that Aß 1-42 and hIAPP are linked by their similar fibrillar structures by showing that peptide inhibitors, designed against 'Interface A' of the hIAPP 19-29 S20G atomic structure, reduce cytotoxicity of both full-length hIAPP and Aß 1-42. These peptide inhibitors appear to reduce hIAPP cytotoxicity to rat pancreatic ß-cells by reducing fibril formation. In contrast, these inhibitors appear to reduce Aß 1-42 cytotoxicity to mouse neuroblastoma cells by some mechanism other than fibril formation reduction. The inhibitors may reduce Aß 1-42 fibril formation at an interface structurally similar to 'Interface A,' but another fibril-forming interface remains uninhibited and thus fibril formation persists. For example, Aß 16-KLVFFA-21, a known core segment of Aß fibrils (54), may drive fibril formation even in the presence of inhibitor.

In order to determine how Aß 24-34 WT and hIAPP 19-29 S20G may cross-seed, we generated models of all eight possible hetero-assemblies. Next, using Rosetta, we assessed their propensities to form by evaluating their energies and shape complementarities. The hetero-assembly modeled onto the backbone of 'Interface B' of the hIAPP 19-29 S20G atomic structure possesses the highest shape complementarity (Sc) of all the models at 0.66 (Figure 4.7). Its Sc score and Rosetta Energy score are comparable to that of the homo-assemblies containing 'Interface B', suggesting that this hetero-assembly model may be a *bona fide* structure.

This hetero-assembly model, taken together with the effects of the inhibitors on hIAPP and Aβ1-42 fibril formation and cytotoxicity, lead us to postulate that different fibrillar interfaces may be important for cytotoxicity and cross-seeding. Recall that the inhibitors were designed to target 'Interface A' of the hIAPP 19-29 S20G atomic structure. Indeed, these inhibitors reduce fibril formation and cytotoxicity of full-length hIAPP, likely by targeting a similar interface in the full-length protein and preventing it from forming. In contrast, these inhibitors do not reduce fibril formation of Aβ1-42, but they do reduce its cytotoxicity. Thus, it seems plausible that these inhibitors target and reduce the formation of interfaces similar to 'Interface A' in both full-length proteins and that 'Interface A' may be important for cytotoxicity of both proteins. The good fit of the hetero-assembly model in Figure 5.7 suggests that 'Interface B' is important for cross-seeding.

Our hypothesis regarding the functions of the different interfaces may also explain our dot blot results of Aβ1-42 incubated with the inhibitors. Conformation-specific antibodies mOC 88, mOC 3, and mOC 22, all of which show a marked reduction in binding to Aβ1-42 incubated with inhibitors, may recognize a structural motif, or epitope, similar to 'Interface A.' Indeed, a previous study showed that mOC 3 and mOC 22 recognize epitopes shared between Aβ and hIAPP fibrils (51). Alternatively, the fact that for Aβ 1-42, the inhibitors do not reduce cytotoxicity by reducing fibril formation suggests that perhaps the inhibitors are targeting smaller cytotoxic aggregates and preventing them from forming. Indeed, these observations align with the most common view in the field, which is that smaller Aβ 1-42 aggregates, like soluble oligomers, are the cytotoxic species (55). Therefore, it seems possible that these smaller Aβ 1-42 aggregates may share common structural epitopes with hIAPP fibrils, which we previously showed alter cell metabolism and activate pro-apoptotic caspases (36). Additionally, this conclusion agrees with studies from Glabe and co-workers who showed that monoclonal antibodies can recognize identical structural epitopes on both fibrils and oligomers (51,56). This interpretation engenders an intriguing notion: perhaps it is structural epitopes and not necessarily particular assemblies that are responsible for cross-seeding.

We postulate that this structural epitope, represented as 'Interface A' of Aβ 24-34 WT, is a previously unobserved conformation from any previous models of full-length Aβ fibrils. Aβ 24-34 WT atomic structure reveals residues 26-34 in an extended β-strand conformation, whereas in the β-turn-β fibril models, residues 26-29 compose the flexible loop region connecting adjacent β-strands (26,57). In more recent ssNMR structures of Aβ 1-42, where it forms a S-shaped conformation, residues 24-34 encompass 2 short β-strands from 26–28 and 30–32 (27,29). However, in this structure, these two short strands have a significant kink between them at Gly29. Furthermore, atomic structures of shorter six to eight-residue protein segments derived from Aβ reveal even more possible conformations within residues 24-34 (Table 3.2) (30). Despite our model differing from previous structures, the ability of Aβ 24-34 WT microcrystals to seed full length Aβ indicates that it is a conformation compatible with the aggregation pathway.

The fibrillar structures presented here contain structural motifs important for cytotoxicity and cross-seeding of their parent full-length proteins. We identify two extensive interfaces that are similar in both atomic structures. Interface A appears to convey cytotoxicity and can be targeted in both full-length proteins by inhibitors designed from Interface A of IAPP 19-29 S20G. Interface B is stabilized by almost identical residues in both structures, and serves as a model for hetero-assembly, which may also explain the co-deposition of their parent full-length proteins into fibrils *in vitro* and *in vivo*. Going forward, we need more structural studies of fibrils derived from patient samples in order to determine whether exposed cross-seeding interfaces may be an effective target to limit the initiation of additional amyloid aggregation. Perhaps these inhibitors may be optimized to generate potentially relevant therapeutics for two, as of now, incurable diseases.

MATERIALS AND METHODS

Peptides and protein purification

Candidate inhibitors were custom made and purchased from Innopep (San Diego, CA). For studies with the design target, 19-29 S20G, lyophilized candidate inhibitors were dissolved at 1mM in PBS and 1% DMSO. For studies with full-length hIAPP and Aβ1-42, lyophilized candidate inhibitors were dissolved at 10mM in 100% DMSO. 10mM stocks were diluted as necessary. All stocks were stored frozen at -20°C.

Human IAPP1-37NH$_2$ (hIAPP) was purchased for Innopep (San Diego, CA). Mouse IAPP1-37NH$_2$ (mIAPP) was purchased from CS Bio (Menlo Park, CA). Peptides were prepared by dissolving lyophilized peptide in 100% 1,1,1,3,3,3-Hexafluoro-2-propanol (HFIP) at 250µM for 2 hours. Next, the sample was spin-filtered and then HFIP was removed with a CentriVap Concentrator (Labconco, Kansas City, MO). After removal of the HFIP, the peptides were dissolved at 1mM or 10mM in 100% DMSO (IAPP alone) or 100% DMSO solutions containing 1mM or 10mM inhibitor. The DMSO peptide stocks were diluted 100-fold in filter-sterilized Dulbecco's PBS (Cat. # 14200-075, Life Technologies, Carlsbad, CA).

Recombinant amyloid-beta peptide cloning and expression

Aβ was cloned and purified similar o the methods described in Lagonowsky et al. Aβ was PCR amplified using Phusion high-fidelity DNA polymerase (New England Biolabs, Ipswich, MA), using an N-terminal primer containing a SacI restriction and TEV protease site, and a C-terminal primer containing a stop codon and XhoI restriction site and purified with QIAquick PCR Purification kit (Qiagen, Valencia, CA). The PCR product and p15-MBP were digested with XhoI and SacI according to manufacturer's protocol (New England Biolabs, Ipswich, MA). Digested vector products were purified as above. A ligation mixture was performed using a Quick Ligation kit (New England Biolabs, Ipswich, MA) according to manufacturer protocol and transformed into *E. coli* cell line TOP10 (Invitrogen, Carlsbad, CA). Several colonies were grown overnight, and plasmids containing the synthetic Aβ gene were purified using QIAprep Spin Miniprep Kit (Qiagen, Valencia, CA). The final construct p15-MBP-Aβ was sequenced prior to transformation into *E. coli* expression cell line BL21 (DE3) gold cells (Agilent Technologies, Santa Clara, CA).

A single colony was inoculated into 100 mL LB Miller broth (Fisher Scientific, Pittsburgh, PA) supplemented with 100 µg/mL ampicillin (Fisher Scientific, Pittsburgh, PA) and grown overnight at 37℃. One liter of LB Miller supplemented with 100 µg/mL ampicillin in 2L shaker flasks was inoculated with 15 mL of overnight culture and grown at 37℃ until the culture reached an OD600 ~0.6-0.8 using a BioPhotometer UV/VIS Photometer (Eppendorf, Westbury, NY). The cells were induced with IPTG (Isopropyl β–D-1-thiogalactopyranoside) at a final concentration of 1 mM, and grown for 3-4 hours at 37℃. Cells were harvested by centrifugation at 5,000 x g for 10 minutes at 4℃. The cell pellet was frozen and stored at -80℃.

The cell pellet was thawed on ice and re-suspended in buffer A (50 mM sodium phosphate, 0.3 M sodium chloride, 20 mM imidazole, pH 8.0) at 120 mL per 3L of culture volume and lysed by sonication. Crude cell lysate was clarified by centrifugation at 15,000 x g for 30 minutes at 4℃. The clarified cell lysate was filtered through a 0.45 µm syringe filtration device (HPF Millex-HV, Millipore, Billerica, MA) before loading onto 2 5mL HisTrap-HP columns (GE Healthcare, Piscataway, NJ). The HisTrap-HP column was washed with five column volumes of buffer A and then washed in five column volumes of 10% buffer B (50 mM sodium phosphate, 0.3 M sodium chloride, 500 mM imidazole, pH 8.0). Protein eluted was eluted in 3 column volumes of 100% buffer B. The pooled sample diluted to less than 10mg/ml and was loaded into 6,000-8,00 MWCO tubing (Fisher Scientific, Pittsburgh, PA), and dialyzed against buffer C (25 mM Tris pH 8.0, 20 mM imidazole, 100 mM sodium chloride) at 4℃ for 4 hours, changing buffer after 2 hours. The dialyzed sample was pooled and 1/50 volume of TEV protease stock was added. The TEV protease reaction was incubated overnight at 4℃ before loading over a 5mL HisTrap-HP column equilibrated in buffer A. The flow through was collected, containing the recombinant Aβ peptide. Pooled recombinant Aβ peptide was 0.22 µm filtered (Steriflip, Millipore, Billerica, MA) and further purified by reverse phase high performance liquid chromatography (RP-HPLC) on a 2.2 x 25 cm Vydac 208TP52 column at 80 ℃ equilibrated in buffer RA (0.1% trifluroacetic acid (TFA)/water) and eluted over a linear gradient from 15% to 50% buffer RB (Acetonitrile/0.1% TFA) in 59 minutes at a flow rate of 10 mL/min. Absorbance at 220nm and 280nm were recorded using a Waters 2487 dual ʎ absorbance detector (Waters, Milford, MA). Peak fractions containing peptide were assessed for purity by MALDI-TOF mass spectrometry (Voyager-DE-STR, Applied Biosystems, Carlsbad, CA). Pooled fractions were frozen in liquid nitrogen and lyophilized. Dried peptide powders were stored in desiccant jars at -20 ℃.

Crystallization

24-VGSNKGAIIGL-34 (24-34). 24-34 was dissolved at 7.5 mg/ml in 25 mM citric acid pH 4.0 and 5% DMSO. Micro crystals were grown in batch at 37°C, shaking. Crystals grew within 2 days to a maximum of 1 week.

MicroED data collection

The procedures for MicroED data collection and processing largely follow published procedures (38,58). Briefly, a 2-3 µL drop of crystals in suspension was deposited onto a Quantifoil holey-carbon EM grid then blotted and vitrified by plunging into liquid ethane using a Vitrobot Mark IV (FEI, Hillsboro, OR). Blotting times and forces were optimized to keep a desired concentration of crystals on the grid and to avoid damaging the crystals. Frozen grids were then either immediately transferred to liquid nitrogen for storage or placed into a Gatan 626 cryo-holder for imaging. Images and diffraction patterns were collected from crystals using an FEG-equipped FEI Tecnai F20 TEM operating at 200 kV and fitted with a bottom mount TVIPS TemCam-F416 CMOS-based camera. Diffraction patterns were recorded by operating the detector in a movie mode termed 'rolling shutter' with 2 x 2 pixel binning (40). Exposure times for these images were either 2 or 3 seconds per frame. During each exposure, crystals were continuously unidirectionally rotated within the electron beam at a fixed rate of 0.3 degrees per second, corresponding to a fixed angular wedge of 0.6 or 0.9 degrees per frame.

Crystals that appeared visually undistorted and that were 100-300 nm thick produced the best diffraction. Datasets from individual crystals were merged to improve completeness and redundancy. Each crystal dataset spanned a wedge of reciprocal space ranging from 40-80°. We used a selected area aperture with an illuminating spot size of approximately 1 μm. The geometry detailed above equates to an electron dose rate of less than 0.01 $e^{-}/Å^{2}$ per second being deposited onto our crystals.

Measured diffraction images were converted from TVIPS format into SMV crystallographic format, using in-house software (available for download at http://cryoem.janelia.org/downloads).

We used XDS to index the diffraction images and XSCALE (59) for merging and scaling together datasets originating from five different crystals.

Structure determination

We determined the structure of 24-24 using molecular replacement. An idealized 10-residue peptide strand with the sequence GAAGAIIGA led us to our atomic model. The solution was identified using Phaser (60). Subsequent rounds of model building and refinement were carried out using COOT and Phenix, respectively (61,62). Electron scattering factors were used for refinement. Calculations of the area buried and shape complementarity (SC) were performed with AREAIMOL (63,64)) and SC (65–67), respectively.

Fibril diffraction

Fibrils of Aß 1-42 or microcrystals of 24-34 were spun down and washed with water three times to remove any salt using a tabletop microfuge. The samples were concentrated 20x in water and applied between two capillary ends and then the samples were left to dry overnight. Fibrils were analyzed with a RIGAKU R-AXIS HTC imaging plate detector using Cu K(alpha) radiation from a FRE+ rotating anode generator with VARIMAX HR confocal optics (Rigaku, Tokyo, Japan). Radial profiles were calculated using a program written in-house. The program calculates the average intensity as a function of distance from the beam center.

Atomic structure overlay

A structural overlay of Aß 24-34 WT onto hIAPP 19-29 S20G was performed using LSQKAB from the CCP4 Suite (68). We calculated room mean square deviation of main chains.

Computational structure-based design

Computational designs were carried out using the RosettaDesign software as described previously (49). The atomic structure of the 19-SGNNFGAILSS-29 hIAPP segment was used as a starting template for computational design. An extended L-peptide (or D-peptide, seven to nine residues) was first placed at either top or bottom of the starting template of hIAPP 19-29 S20G atomic structure. The design procedure then built side-chain rotamers of all residues onto the nine-residue peptide backbone placed at growing end of fibril. The optimal set of rotamers was identified as those that minimize an energy function containing a Lennard-Jones potential, an orientation-dependent hydrogen bond potential, a solvation term, amino acid-dependent reference energies, and a statistical torsional potential that depends on the backbone and side-chain dihedral angles. Area buried and shape complementarity calculations were performed with areaimol and sc, respectively, from the CCP4 suite of crystallographic programs (63). The solubility of each peptide was evaluated by hydropathy index (69) and its aggregation propensity was calculated by self-stacking score (Jiang *et al*, unpublished data). The designed peptides were selected based on calculated binding energy of top or bottom binding mode, shape complementarity and peptide solubility. Each structural model of selected peptides went through human inspection using Pymol, where those peptides with sequence redundancy and less binding interactions were omitted. Finally, select peptides were synthesized and tested experimentally.

Testing of candidate inhibitors with design target

To test whether the candidate inhibitors prevent fibril formation of the design target, 19-29 S20G, we dissolved the lyophilized 19-29 S20G peptide at 1 mM in PBS and 1% DMSO or in an equimolar solution of candidate inhibitor in PBS and 1% DMSO. Samples were incubated for 6 hours to 15 hours at room temperature under quiescent conditions. Fibril abundance was checked using electron microscopy.
Next, the samples were applied to pre-plated HEK293 cells for 24 hours, and then cell viability was measured using MTT dye reduction.

Transmission electron microscopy

Samples were spotted onto non-holey grids and left for 160 to 180 seconds. Remaining liquid was wicked off and then left to dry before analyzing. Samples for negative-stain TEM were treated with 2% uranyl acetate after sample was wicked off the grid. After 1 minute, the uranyl acetate was wicked off. The grids were analyzed on the T12 Electron Microscope (FEI, Hillsboro, OR). Images were collected at 3,200 or 15,000x magnification and recorded using a Gatan 2kX2k CCD camera.

Thioflavin-T (ThT) kinetic assays

Thioflavin-T (ThT) assays with hIAPP were performed in black 384-well plates (Nunc, Rochester, NY) sealed with UV optical tape. hIAPP1-37NH_2 and mIAPP1-37NH_2 were prepared as described. The total reaction volume was 50 µL per well. ThT fluorescence was recorded with excitation and emission of 444 nm and 482 nm, respectively, using a Varioskan Flash (Thermo Fisher Scientific, Grand Island, NY). Experiments were performed at 25°C without shaking in triplicate and readings were recorded every 5 minutes.

For the seeding assays in Figure 4, 1 mM of hIAPP1-37NH_2 in 100% DMSO was diluted 1 to 100 in 0.1 M NaOAc pH 6.5 containing 10% monomer-equivalent seed and 10µM ThT. Seeds of Aβ, Aβ 24-34 WT, and hIAPP 19-29 S20G were sonicated for five minutes prior to addition; seeds of hIAPP were not sonicated.

For the inhibition assays in Figure 6, 1 mM of hIAPP1-37NH_2 in 100% DMSO was diluted 1 to 100 in PBS buffer containing 10 µM ThT. Stocks of each inhibitor were diluted 1 to 100 in the same manner.

ThT assays with Aβ were performed as above with the following exceptions. 1 mM of Aβ in 100% DMSO was diluted 1 to 100 in 25 µM Thioflavin-T and PBS. For seeding experiments, fibril or microcrystal seeds were added at 10% monomer equivalent concentration. Seeds of Aβ and Aβ 24-34 WT were sonicated for five minutes prior to addition; seeds of hIAPP and 19-29 S20G were not sonicated. Inhibitors were added at the specified concentration by diluting 10 mM stocks in 100% DMSO 1 to 100 in 25 µM Thioflavin-T and PBS. The total reaction volume was 180µL per well; experiments were performed in black 96-well plates. Experiments were performed at 37°C without shaking in triplicate and readings were recorded every 5 minutes.

Cell culture

HEK293 cells were a gift from Carol Eng in the laboratory of Arnold J. Berk at UCLA. Cells were cultured in DMEM media (Cat. # 11965-092, Life Technologies) plus 10%

heat-inactivated fetal bovine serum and 1% pen-strep (Life Technologies). Cells were cultured at 37°C in 5% CO_2 incubator.

Rin5F cells were purchased from ATCC (Cat. # CRL-2058, Manassas, VA). Cells were cultured in RPMI media (ATCC, Cat. # 30-2001) plus 10% heat-inactivated fetal bovine serum. Cells were cultured at 37°C in a 5% CO_2 incubator.

Nuero2a (N2a) cells were a gift from the Pop Wongpalee in the laboratory of Douglas Black at UCLA. Cells were cultured in MEM media (Cat. # 11095-080, Life Technologies) plus 10% heat-inactivated fetal bovine serum and 1% pen-strep (Life Technologies). Cells were cultured at 37°C in 5% CO_2 incubator.

3-(4,5-dimethylthiazol-2-yl)-2,5-diphenyltetrazolium bromide (MTT) dye reduction assay for cell viability

HEK293 cells, Rin5F cells, and N2a cells were plated at 10,000, 27,000, and 15,000 cells per well in 90 µL, respectively, in clear 96-well plates (Cat. # 3596, Costar, Tewksbury, MA). Cells were allowed to adhere to the plate for 20-24 hours. For cell assays with Aβ 24-34 WT, fibrillar samples were incubated for at least 4 days and soluble samples were freshly dissolved and then applied to N2a cells. For cell assays with the design target, hIAPP 19-29 S20G, samples were incubated with or without inhibitors for 6-15 hours and then applied to HEK293 cells. For cell assays with full-length hIAPP, samples were incubated with or without inhibitors for 15 hours to 1 week and then applied to Rin5F cells. For cell assays with Aβ1-42, samples were incubated with or without inhibitors for 6 hours at 37°C and then applied to N2a cells. 10 µL of sample was added to cells. By doing this, samples were diluted 1/10 from *in vitro* stocks. Experiments were done in triplicate.

After a 24-hour incubation, 20 µL of Thiazolyl Blue Tetrazolium Bromide MTT dye (Sigma, St. Louis, MO) was added to each well and incubated for 3.5 hours at 37°C under sterile conditions. The MTT dye stock is 5 mg/mL in Dulbecco's PBS. Next, the plate was removed from the incubator and the MTT assay was stopped by carefully aspirating off the culture media and adding 100 µL of 100% DMSO to each well. Absorbance was measured at 570 nm using a SpectraMax M5. A background reading was recorded at 700 nm and subsequently subtracted from the 570 nm value. Cells treated with vehicle alone (PBS+0.1%DMSO) were designated at 100% viable, and cell viability of all other treatments was calculated accordingly.

We determined the appropriate statistical test for significance by assessing whether 1). The sample sets had a Gaussian distribution using a D'Agostino-Pearson omnibus normality test and 2). The sample sets had equal variance using a Bartlett's test or F test. For samples with Gaussian distributions and equal variances, we employed an unpaired t-test with equal standard deviations. For samples with Gaussian distributions, but unequal variances, we employed an unpaired t-test with Welch's correction. For samples with non-Gaussian distributions and unequal variances, we employed a Mann-Whitney U-test.

Detection of caspase-3/7

N2a cells were plated at 7,200 cells per well in black-walled 96 well plates (Cat. # 3603, Costar) and treated as described in the previous section. After a 24 hour treatment, cell media was aspirated and then 100 µL of 2 µM Nexcelom ViaStain Live Caspase 3/7 in PBS (Cat. # CSK-V0003-1, Nexcelom Bioscience LLC, Lawrence, MA) was added to each well. The stain was incubated with cells at 37°C for 30 minutes, and then the cells were imaged using a Celigo Image Cytometer (Nexcelom Biosciences) and a Zeiss fluorescent microscope. Cells treated with 2 µM staurosporine were used as a positive control for caspase activation.

Aggregation inhibition assay with transthyretin (TTR)

The TTR aggregation and immunoblot assays largely follow the protocol described in Saelices, *et al.* (48). TTR was aggregated at 1 mg/ml in 10 mM sodium acetate (pH 4.3), 100 mM KCl, 10 mM EDTA under quiescent conditions at 37 °C for a maximum of 4 days. TTR was aggregated in the presence and absence of peptide inhibitors at a ratio of 1:10 (TTR monomer:inhibitor). On each day of aggregation, absorbance at 400 nm was recorded to measure sample turbidity. On the final day of aggregation, the concentration of the insoluble fraction was measured. To do this, we first spun down 100 µL of sample at 13,000 rpm for 30 min. Next, the pellet was washed with fresh buffer and spun again and then re-spun. The pellet was dissolved in 6 M guanidine chloride, and then absorbance was measured at 295 nm. Absorbance was used to calculate the concentration of the insoluble fraction. Additionally, TTR aggregation on the final day was measured using dot blot analysis as described (70) using the SuperSignal West HisProbe™ kit following the manufacturer's instructions (Thermo Scientific). The insoluble fraction of the samples after 4 days of incubation was dotted onto nitrocellulose membranes (0.2 µm; BioRad). A dilution ratio of 1:10,000 was used for the HisProbe.

Aggregation inhibition assay with tau

We used a construct of tau called K18 that contains only the 4 repeat domains of the full-length protein. Peptide inhibitors were tested by shaking 25 µM K18 in a 96-well plate at 700 rpm in PBS buffer (pH 7.4) with 40 µM ThT and 2 mM DTT. 0.5 mg/ml heparin and a two-fold molar excess of inhibitor were added. Inhibitors were diluted to the appropriate concentration from 10 mM stocks in 100% DMSO. ThT fluorescence was measured using a FLUOstar Omega plate reader with excitation and emission wavelengths of 440 and 480 nm, respectively. Averaged curves were generated from triplicate measurements.

Aggregation inhibition assay with α-synuclein

α-synuclein was expressed and purified as described previously in Rodriguez, *et al* (37) with the following exceptions to the expression protocol. An overnight starter culture was grown in 15 mL instead of 100 mL, 7 mL of which was used to inoculate 1 L culture flasks. After induction, cells were allowed to grow for 3-4 hours at 34°C instead of 4-6 hours at 30 °C. Cells were then harvested by centrifuging at 5,000 x g.

ThT assays with α-synuclein were performed in black 96-well plates (Nunc, Rochester, NY) sealed with UV optical tape. The total reaction volume was 180 µL per well. ThT fluorescence was recorded with excitation and emission of 444 nm and 482 nm, respectively, using a Varioskan Flash (Thermo Fisher Scientific, Grand Island, NY). Experiments were performed at 37°C, shaking at 600 rpm with a teflon bead, in triplicate and readings were recorded every 15 minutes. α-synuclein at 105 µM in PBS was diluted to a final concentration of 50 µM in 25 µM Thioflavin-T and PBS. Inhibitors were added at the specified concentration by diluting 10 mM stocks in 100% DMSO 1 to 40 in the same manner. Thus, inhibitors were tested at 5:1 molar excess of α-synuclein.

Hetero-Assembly Model

Energies and structures for the hetero-assembly models were calculated using the 3D profile method (71). Using Rosetta, the sequences of Aβ 24-34 WT and hIAPP 19-29 S20G were “threaded” onto three template backbone structures: the Aβ 24-34 WT backbone, the hIAPP 19-29 S20G fiber backbone, and an idealized beta-sheet fiber backbone. The distance between the beta-sheets of each of these threaded structures was varied by 10 Å, in increments of 0.25 Å and the shift along the stand axis was 20 Å, also by 0.25 Å increments. Each of the structures was scored by Rosetta Energy, buried surface area, and shape complementarity (72). Hetero-assembly models containing the ‘A’ Interfaces of the atomic structures scored so poorly (contained positive digits) that we deemed them unlikely to form and thus the models were not shown.

ACKNOWLEDGEMENTS

We thank Dan Anderson for general support in the laboratory and Jeannette Bowler for providing purified α-synuclein for our aggregation inhibition studies. We thank the UCLA-DOE X-ray Crystallography Core Technology Center, Michael Collazo, and the UCLA-DOE Macromolecular Crystallization Core Technology Center for setting up initial crystallization screens; and Ivo Atanasov and the Electron Imaging Center for NanoMachines (EICN) of California NanoSystems Institute (CNSI) at UCLA for the use of their electron microscopes. The UCLA-DOE X-ray and Macromolecular and Macromolecular Crystallization Core Technology Centers are supported in part by the Department of Energy grant DE-FC0302ER63421. We thank the Janelia Research Campus visitor program, HHMI, and the National Institutes of Health (NIH) (R01 AG029430) for support.

COMPETING INTERESTS

The authors declare that no competing interests exist.

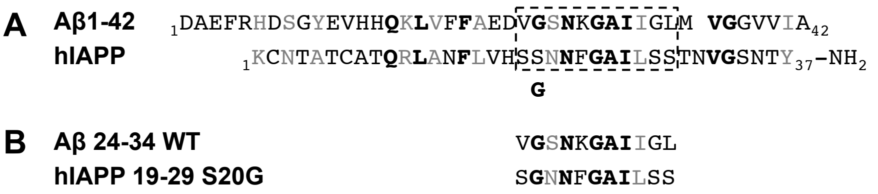

Figure 3.1. Alignment of amyloid-β1-42 (Aβ1-42) and hIAPP sequences and protein segments. Identical residues are highlighted in bold font and similar residues are highlighted in gray. **A.** Alignment of Aβ1-42 and hIAPP sequences reveals that hIAPP is 51% similar and 27% identical to Aβ1-42. The early onset Type-II Diabetes mutation in hIAPP, S20G, is shown below the hIAPP sequence. The amyloid spines of Aβ1-42 and hIAPP are encapsulated in the box with dotted lines. hIAPP-S20G was used to calculate sequence homology to Aβ1-42. **B.** Alignment of the spines of Aβ1-42 and hIAPP, Aβ 24-34 WT and hIAPP 19-29 S20G, respectively, reveals that they are 64% similar are 45% identical.

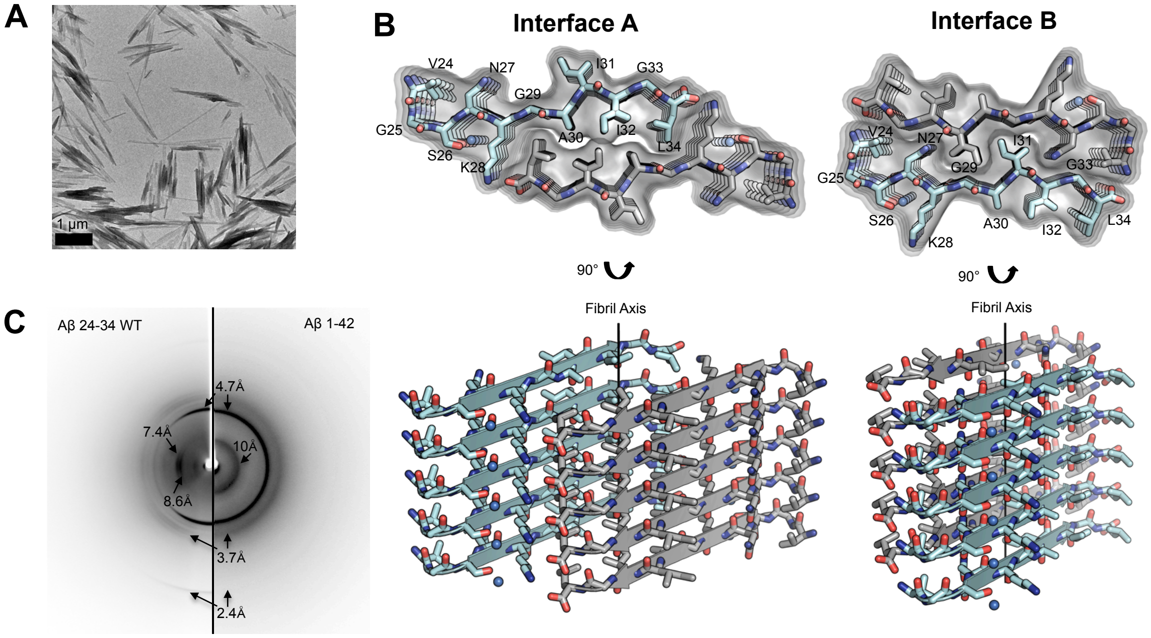

Figure 3.2. MicroED structure of segment Aβ 24–34 WT from microcrystals. **A**. Electron micrograph of 3D crystals used for data collection. **B**. The crystal structure reveals tightly mated pairs of β-sheets. The side-chains interdigitate to form two extensive dry interfaces, termed Interface A and Interface B, with a surface displayed in grey. Beneath, the structures are rotated 90° to show the orthogonal view of each interface. The sheets are related by a 2_1 fibril axis, shown in black. **C**. Comparison of the fibril diffraction of aligned Aβ 24-34 WT microcrystals and Aβ 1-42. Both share a strong reflection around 4.7 Å and a weaker reflection at 2.4 Å. Additionally, the two have a broad reflection around 3.7 Å. Aβ 24-34 WT has two distinct reflections at 8.6 Å and 7.4 Å, pertaining to the distance between sheets in each interface, while Aβ1-42 has a broad reflection around 10 Å.

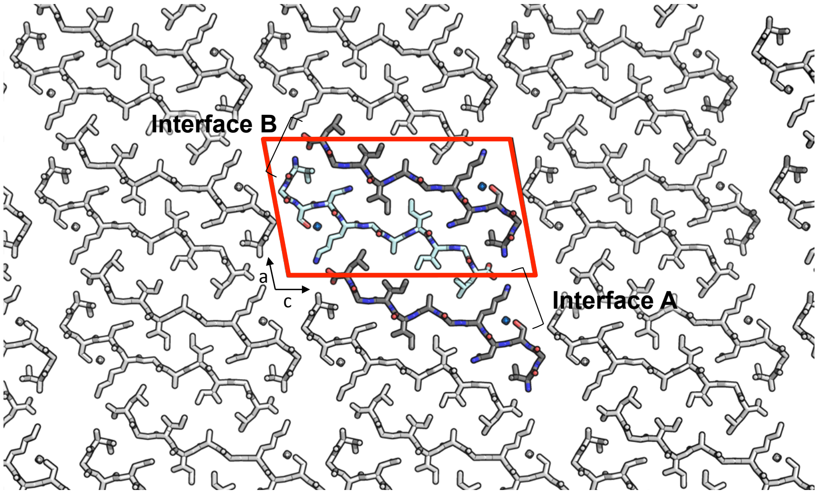

Figure 3.2—Figure Supplement 1. Crystal packing of the Aβ 24–34 WT atomic structure reveals two interfaces. View down the b dimension of the unit cell, which is highlighted in red.

Table 3.1. Statistics of MicroED data collection and atomic refinement.

Sample	**VGSNKGAIIGL**
Excitation Voltage (kV)	200
Electron Source	field emission gun
Wavelength (Å)	0.0251
Total dose per crystal (e^{-}/ Å^{2})	3.4
Frame rate (frame/s)	0.3–0.5
Rotation rate (°/s)	0.3
# crystals used	5
Total angular rotation collected (°)	
Merging Statistics	
space group	$P2_1$
Unit cell dimensions	
a, b, c (Å)	18.78, 4.73, 33.47
α, β, γ (°)	90, 100.02, 90
Resolution (Å)	1.42 (1.49-1.42)
R_{merge}	22.2% (49.6%)
# of reflections	5843
Unique reflections	1129 (84)
Completeness	85.5% (47.5%)
Multiplicity	
I/σ	4.88 (1.09)
$CC_{1/2}$ (73)	98% (45.2%)

Refinement Statistics	
Reflections in working set	1014
Reflections in test set	113
R_{work}[†]	23.4%
R_{free}	29.4%
RMSD bonds (Å)	0.016
RMSD angles (°)	1.838
Ramachandran (%)[‡]	
Favored	
Allowed	0
Outliers	0
PDB ID code	
EMDB ID code	

*Highest resolution shell shown in parenthesis.

[†] Rfactor=100x∑||Fobs|−|Fcalc||/∑|Fobs|Rfactor=100x∑||Fobs|−|Fcalc||/∑|Fobs|

F_{calc} and F_{obs} are the calculated and observed structure factor amplitudes, respectively. R_{work} refers to the R_{factor} for the data utilized in the refinement and R_{free} refers to the R_{factor} for 10% of the reflections randomly chosen that were excluded from the refinement.

[‡] Percentage of residues in Ramachandran plot regions were determined using Molprobity (74).

Table 3.2. Summary of structural features and biophysical properties of all amyloid-ß protein segment structures determined to date.

registry	eclipse/ staggered	total residues	spg	areaburied per strand	areaburied per residue	Sc Coleman	N-to-C distance/ total residues	charge at pH 7	Sum of hydropathy values	average sheet-to-sheet distance	standard deviation sheet-to-sheet distance	mininum sheet-to-sheet distance	maximum sheet-to-sheet distance	solvation energy per strand in dry interface cal/mol
out	n/a	6	$P3_121$	171.0	28.5	0.760	2.90	-0.8	-1.23	n/a	n/a	n/a	n/a	n/a
in	eclips	6	$P2_12_12$	113.8	19.0	0.780	3.31	-0.8	-1.23	11.0	0.73	9.8	12.8	97
in	stagg	4	C2	105.7	26.4	0.608	3.29	0	1.73	9.1	0.08	9.0	9.3	-70
in	eclips	6	$P2_12_12_1$	113.4	18.9	0.576	3.34	1	1.92	10.2	0.20	9.9	10.7	163
in	eclips	6	C2	130.5	21.8	0.541	3.45	1	1.92	10.3	0.21	9.7	10.6	113
in	eclips	6	C2	134.8	22.5	0.662	3.45	1	1.92	10.0	0.38	9.4	11.0	256
in	eclips	6	$P2_12_12_1$	114.1	19.0	0.553	3.36	1	1.92	10.5	0.25	10.1	11.1	158
in	eclips	6	P1	54.8	9.1	0.574	3.38	1	1.92	13.4	1.55	10.4	16.5	50
out	eclips	11	$P2_1$	289.5	26.3	0.746	3.11	0	0.68	8.8	0.99	5.2	10.1	219
in	stagg	11	$P2_1$	257.6	23.4	0.852	2.88	1	0.86	7.3	0.25	6.6	7.7	190
in	stagg	11	$P2_1$	209.8	19.1	0.621	2.88	1	0.86	9.2	0.91	6.7	10.6	153
in	stagg	6	$P2_1$	175.7	29.3	0.864	3.28	1	0.50	6.7	0.19	6.2	7.0	136
in	stagg	6	$P2_1$	176.2	29.4	0.920	3.28	1	0.50	7.9	0.24	7.3	8.2	96
in	stagg	6	P1	66.3	11.1	0.750	2.89	0	2.30	11.2	0.31	10.9	12.3	94
in	stagg	6	P1	165.9	27.7	0.725	3.45	0	2.68	7.9	0.08	7.7	8.0	213
in	stagg	6	P1	91.7	15.3	0.763	3.43	0	2.28	7.0	0.27	6.6	7.9	140
in	stagg	6	$P2_1$	103.3	17.2	0.821	3.08	0	2.28	7.2	0.63	6.1	8.6	144
in	stagg	8	P1	168.6	21.1	0.511	3.32	0	2.50	7.7	0.55	6.8	9.5	222
in	stagg	8	$P2_1$	170.5	21.3	0.571	3.30	0	2.50	7.8	0.70	6.7	9.7	239
in	stagg	6	$P2_12_12$	114.5	19.1	0.889	3.24	0	2.32	8.4	0.44	7.6	9.2	169
in	stagg	3	P1	55.8	18.6	0.796	3.22	0	3.50	9.5	0.61	8.3	10.8	108
in	stagg	6	$P2_1$	98.1	16.4	0.548	3.32	-2	0.87	9.1	0.37	8.6	10.3	82

residue range	peptide sequence	crystal form	inter-face	sheet symmetry	zipper sym-metry class	PDB or CSD ID code	references
09-14	GYEVHH	1		parallel	corkscr		Angela Soriaga thesis
09-14	GYEVHH	2		parallel	1		this work
16-19	ace-KLVF			parallel	1		this work
16-21	KLVFFA	1		antiparallel	7	2y2a	Colletier et al. 2011
16-21	KLVFFA	2	A	antiparallel	7	3ow9	Colletier et al. 2011
16-21	KLVFFA	2	B	antiparallel	7	3ow9	Colletier et al. 2011
16-21	KLVFFA	3		antiparallel	7	2y29	Colletier et al. 2011
16-21	KLVFFA-ORG			antiparallel	8	3ovj	Landau et al., 2011
16-26	KLVFFAENVGS			antiparallel	7		this work
24-34	VGSNKGAIIGL		A	parallel	1		this work
24-34	VGSNKGAIIGL		B	parallel	1		this work
27-32	NKGAII		A	parallel	1	3q2x	Colletier et al. 2011
27-32	NKGAII		B	parallel	1	3q2x	Colletier et al. 2011
29-34	GAIIGL			antiparallel	6	3pzz	Colletier et al. 2011
30-35	AIIGLM			parallel	2	2y3j	Colletier et al. 2011
35-40	MVGGVV	1		antiparallel	8	2ona	Sawaya et al. Nature 07
35-40	MVGGVV	2		antiparallel	8	2okz	Sawaya et al. Nature 07
35-42	MVGGVVIA	1		parallel	2	2y3k	Colletier et al. 2011
35-42	MVGGVVIA	2		antiparallel	7	2y3L	Colletier et al. 2011
37-42	GGVVIA			parallel	4	2onv	Sawaya et al. Nature 07
40-42	VIA			antiparallel	5	XEPZAU	Ray et al, Chem. Comm. 06
63-68	GVVEVD			parallel	2		Jacques Philippe Colletier

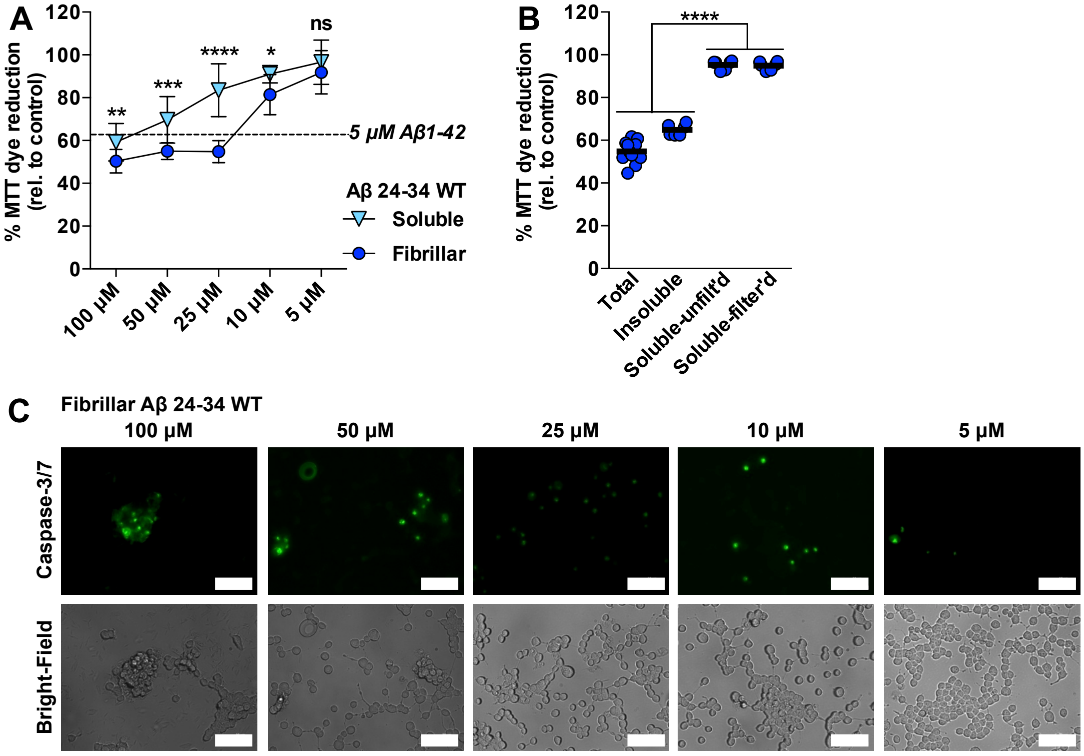

Figure 3.3. Aβ 24-34 WT is cytotoxic to N2a cells, a mouse neuroblastoma cell line. A. The cytotoxicity of Aβ 24-34 WT mainly resides in its fibrillar form (dark blue), but its soluble form is also somewhat cytotoxic (light blue). Samples were diluted to the appropriate concentration and then further diluted 1:10 in media containing pre-plated cells to the concentration specified. **B.** The insoluble fraction of the 25 µM fibrillar sample, which contains fibrils, is cytotoxic, further confirming that fibrils or some type of oligomer that tightly associates with fibrils is the cytotoxic species. The insoluble fraction was isolated by centrifuging the fibrillar sample for 1 h using a tabletop centrifuge, and then aspirating off the soluble fraction. Then, the insoluble fraction was resuspended in fresh buffer at its original volume. The 'soluble-filtered' fraction was filtered with a 0.1 µm spin filter while the 'soluble-unfiltered' fraction was not. For **A** and **B**, cytotoxicity was quantified using MTT dye reduction. Points and bars show mean with one standard deviation (n = 6-12; ns = not significant; *, $p < 0.05$; **, $p < 0.01$; ***, $p < 0.001$; ****, $p <$

0.0001 using a unpaired t-test with equal standard deviations). **C.** The fibrillar form of Aß 24-34 WT is associated with increased pro-apoptotic caspase-3/7 activation. Cells were treated as described previously, and then caspase-3/7 activity was visualized using a fluorescence-based probe for caspase activity. Cells were imaged using a Zeiss fluorescent microscope. Scale bars are 50 microns.

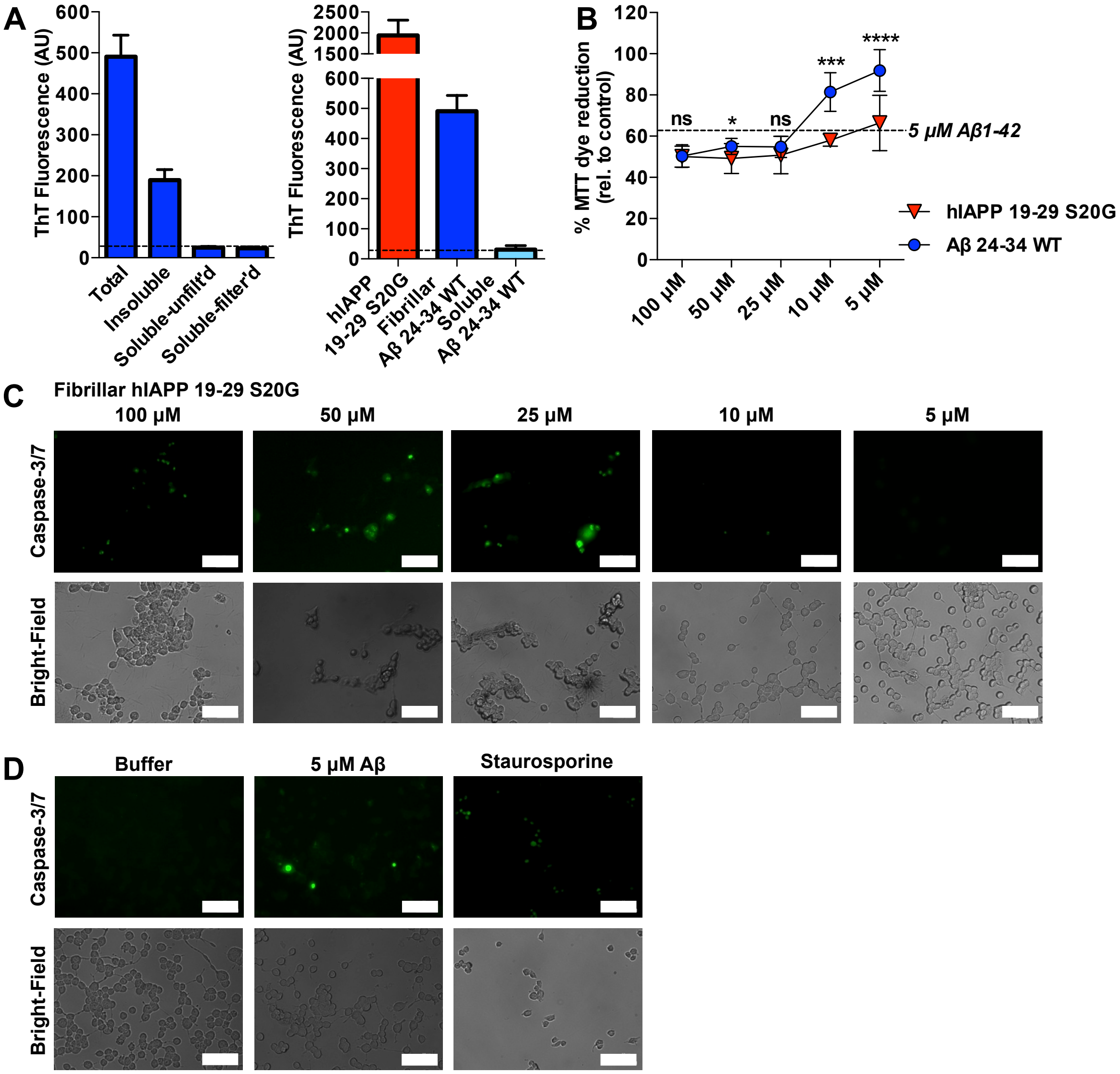

Figure 3.3—Figure Supplement 1. Fibrillar forms of Aβ 24-34 WT and hIAPP 19-29 S20G are cytotoxic to N2a cells. A. Samples of Aβ 24-34 WT and hIAPP 19-29 S20G that contain fibrils show high Thioflavin-T (ThT) fluorescence, while soluble samples show very low fluorescence. The dashed lines on both graphs represent fluorescence from buffer alone. **B.** hIAPP 19-29 S20G is more cytotoxic than Aβ 24-34 WT at select concentrations. Cytotoxicity was quantified using MTT dye reduction. Points show mean with one standard deviation (*n* = 12; ns = not significant; *, $p < 0.05$; ***, $p < 0.001$; ****, $p < 0.0001$ using a unpaired t-test with equal standard deviations). **C.** hIAPP 19-29 S20G

activates pro-apoptotic caspases. Cells were imaged using a Zeiss fluorescent microscope.

D. Images of cells treated with negative and positive controls and then stained for caspase-3/7 activity. Scale bars are 50 microns.

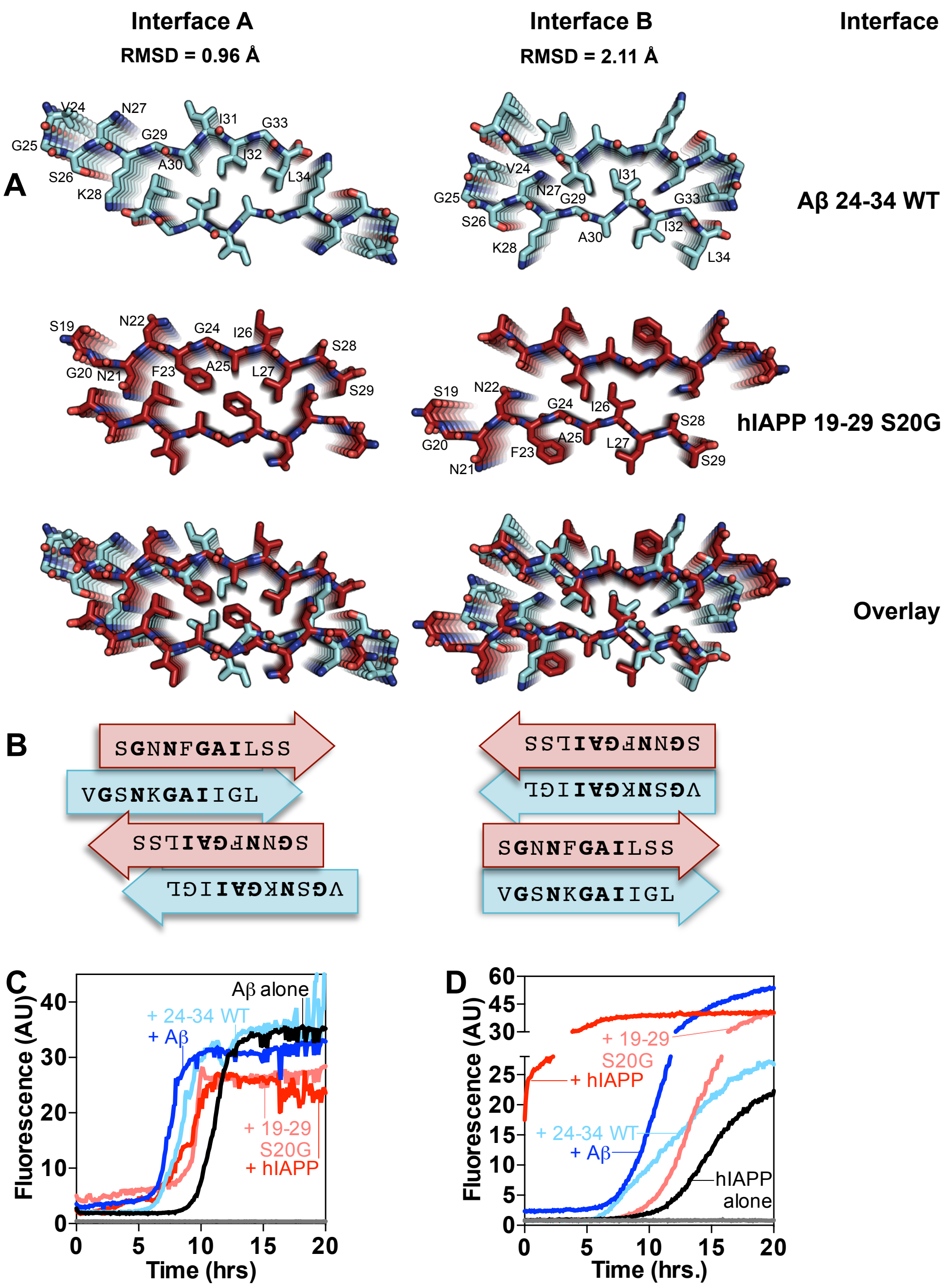

Figure 3.4. The spines of Aβ 24-34 WT and hIAPP 19-29 S20G are structurally similar. A. The crystal packing reveals two interfaces: Interface A and Interface B. The backbones of Interface A (left) differ from each other by 0.96 Å, while the backbones of Interface B (right) differ from each other by 2.11 Å. RMSD values were calculated using LSQKAB. **B.** Schematic of how atomic structures overlap reveals that mated sheets

composing Interface A are shifted by two residues and possess different degrees of overlap. Identical residues are highlighted in bold. **C.** Seeds of Aβ 24-34 WT and hIAPP 19-29 S20G seed full-length Aβ 1-42 fibril formation near to the efficiency of their parent full-length proteins, suggesting the segments share similar structures to full-length Aβ 1-42 fibrils. **D.** Likewise, seeds of Aβ 24-34 WT and hIAPP 19-29 S20G seed full-length hIAPP fibril formation near to the efficiency of their parent full-length proteins. For **C** and **D**, 10 μM Aβ 1-42 or hIAPP was seeded with 10% (v/v) monomer equivalent of pre-formed seed of each protein or protein segment. Fluorescence of buffer alone is show in gray. Lines show average of three technical replicates.

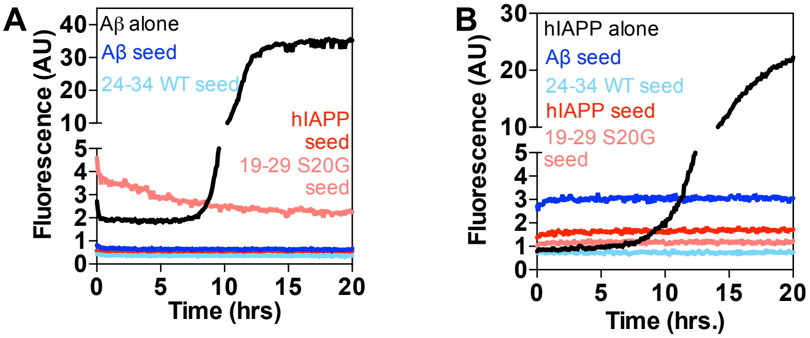

Figure 3.4—Figure Supplement 1. Seeds used in the ThT assay in Figure 3.4 do not bind ThT. A. Seeds in conditions used for Aβ ThT assay. **B.** Seeds in conditions used for hIAPP ThT assay.

Table 3.3. Summary of designed peptide inhibitors and their properties.

Peptide Name	Sequence	MW (g/mol)	Hydropathy Index	Self-Stacking Propensity	Binding Energy (Top)	Binding Energy (Bottom)	SC (Top)	SC (Bottom)	SA Buried (Top)	SA Buried (Bottom)
p1	NFKmAImLH	869.6	2.3	-13.184	-31.734	-31.051	0.708	0.753	552	564
p4	NFWAKLN	891.5	-3.4	-9.3	-33.4	-32.7	0.8	0.81	614	590
p6	TFYATLH	851.4	2.5	-11.9	-30.5	-29.6	0.7	0.78	547	579
p8	NLGPVLP	707.9	4.7	-6.196	-10.536	-10.625	0.682	0.613	531	534
p11	AcNFEAYLHS-NH_2	979.1	-3.1	-11.782	-33.449	-31.004	0.837	0.759	580	565
p12	AcTFYAELYS-NH_2	992.1	1.6	-10.06	-27.862	-30.093	0.684	0.765	564	572
p13	AcHFNELYNS-NH_2	1022.1	-8.4	-12.148	-24.92	-27.122	0.703	0.73	503	515
p14	D-NFEAYLH	893.0	-3.1	-11.782	-26.444	-26.575	0.672	0.701	539	478
p15	D-ELFAHYN	893.0	-3.1	-11.404	-30.454	-18.686	0.652	0.644	586	534
p16 (-)	D-NAEAALH	724.8	4	-8.928	-22.887	-20.944	0.583	0.564	460	431
p17 (-)	D-ELAAHAN	724.8	4	-9.118	-25.142	-20.122	0.574	0.773	499	381
p21	NNFYAELYSS	1206.4	-1.2	-11.588	-29.438	-30.683	0.698	0.753	580	570
p22	AcNNFYAELYSS-NH_2	1247.5	-1.2	-11.588	-29.438	-30.745	0.697	0.765	582	564
p23	NFRmAImLHS	984.5	1.7	-9.692	-31.739	-30.996	0.696	0.761	563	563
p24	D-NNFKAILSS	992.5	5.5	-14.326	-27.803	-23.709	0.649	0.724	513	444

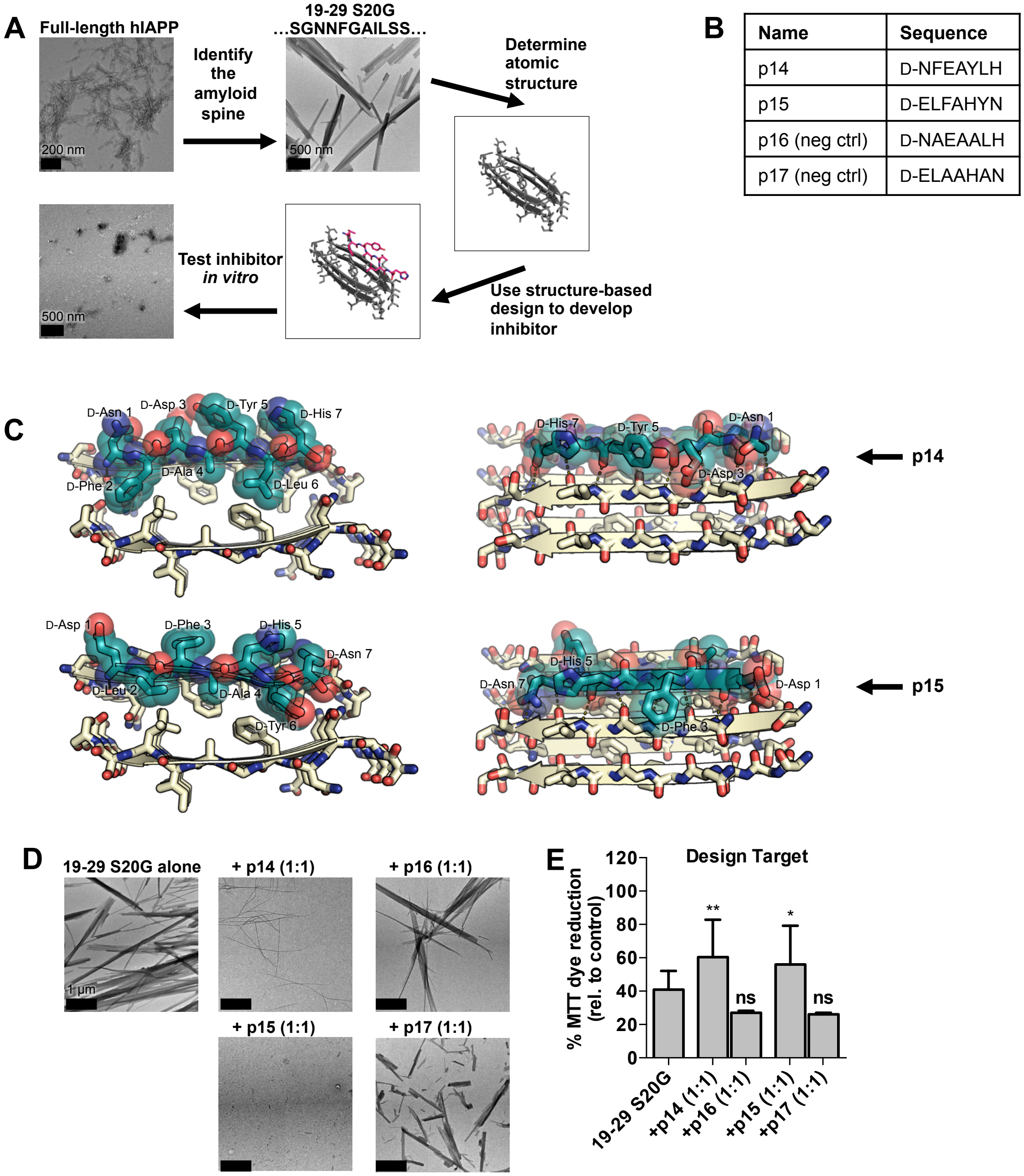

Name	Sequence
p14	D-NFEAYLH
p15	D-ELFAHYN
p16 (neg ctrl)	D-NAEAALH
p17 (neg ctrl)	D-ELAAHAN

Figure 3.5. Development of inhibitors using structure-based design against hIAPP 19-29 S20G. A. Schematic of structure-based design process using Rosetta. Segment hIAPP 19-29 S20G, which forms the toxic spine of hIAPP, was used as the design target. Schematic is based on the one used in Sievers, *et al.* **B.** Overview of primary peptide inhibitors used in this study and their sequences. Peptides p16 and p17 are the negative controls for peptide inhibitors p14 and p15, respectively. **C.** Models of peptide inhibitors

p14 and p15 (dark teal) bound to the design target, hIAPP 19-29 S20G (ivory). The side-chains of the peptide inhibitors form hydrophobic interactions with the core of hIAPP 19-29 S20G. Additionally, the peptide inhibitors form favorable hydrogen bonding along the peptide backbone (left panel). **D.** Designed peptide inhibitors, p14 and p15, reduce fibril formation of the design target, hIAPP 19-29 S20G, but negative control peptides do not. 1 mM hIAPP 19-29 S20G was incubated with equimolar concentrations of each inhibitor overnight under quiescent conditions. Fibril abundance was evaluated using TEM. Images were captured at 3,200x. Scale bars are one micron. **E.** Peptide inhibitors reduce cytotoxicity of the design target, hIAPP 19-29 S20G, but negative control peptides do not. Samples were prepared as described in panel **D** and then applied to HEK293 cells at 10 µM final concentration for 24 hours. Cytotoxicity was quantified using MTT dye reduction. Columns show mean with one standard deviation (n = 3-6; ns = not significant; **, p = 0.0014; *, p = 0.0118 using an ordinary one-way ANOVA).

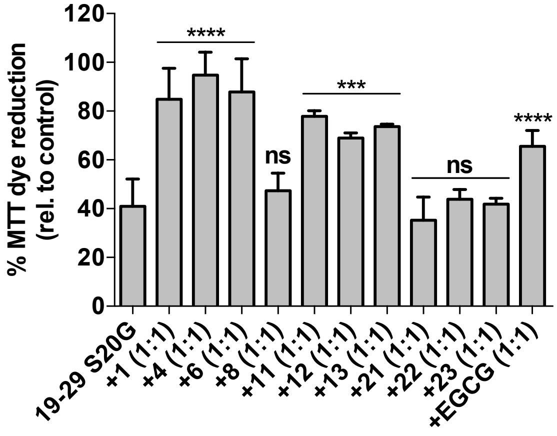

Figure 3.5—Figure Supplement 1. Other inhibitors developed with structure-based design against the hIAPP 19-29 S20G structure also reduce cytotoxicity of hIAPP 19-29 S20G. 1 mM hIAPP 19-29 S20G was incubated with equimolar concentrations of each inhibitor overnight under quiescent conditions. Samples were prepared as described in Figure 3.5D and then applied to HEK293 cells at 10 μM final concentration for 24 hours. Cytotoxicity was quantified using MTT dye reduction. EGCG, a flavanol know to mitigate hIAPP 19-29 S20G cytotoxicity by reducing fibril formation, was used as a positive control. Columns show mean with one standard deviation (n = 3-9; ns = not significant; ***, $p < 0.0005$; ****, $p < 0.0001$ using an ordinary one-way ANOVA).

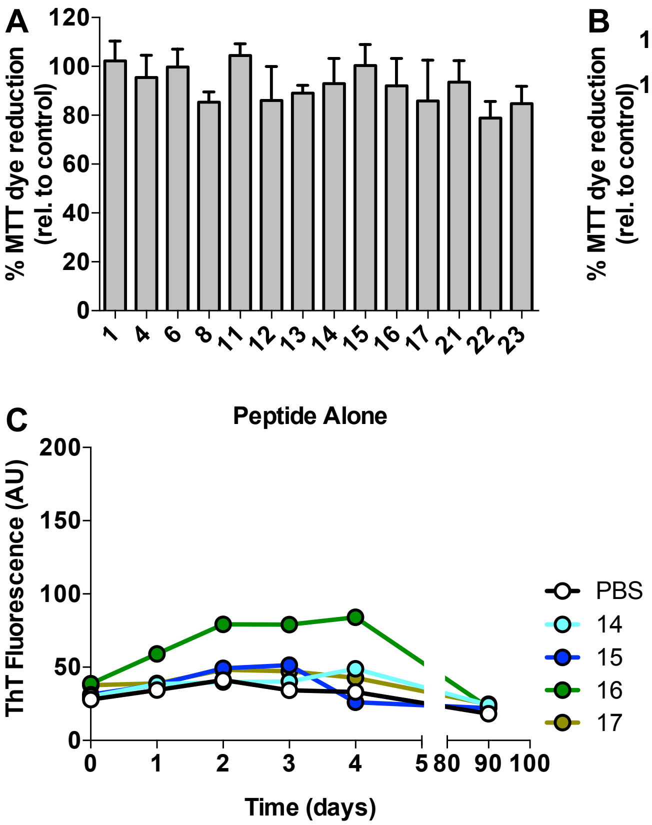

Figure 3.5—Figure Supplement 2. Inhibitors are not cytotoxic and they do not form fibrils. 1-10 μM of each inhibitor was applied to Rin5F cells (**A**) or N2a cells (**B**) for 24 hours and then cytotoxicity was quantified using MTT dye reduction. **C.** Inhibitors alone do not form fibrils as assessed with Thioflavin-T (ThT) binding. 100 μM of each inhibitor was incubated with 100 μM ThT at 25 °C under quiescent conditions.

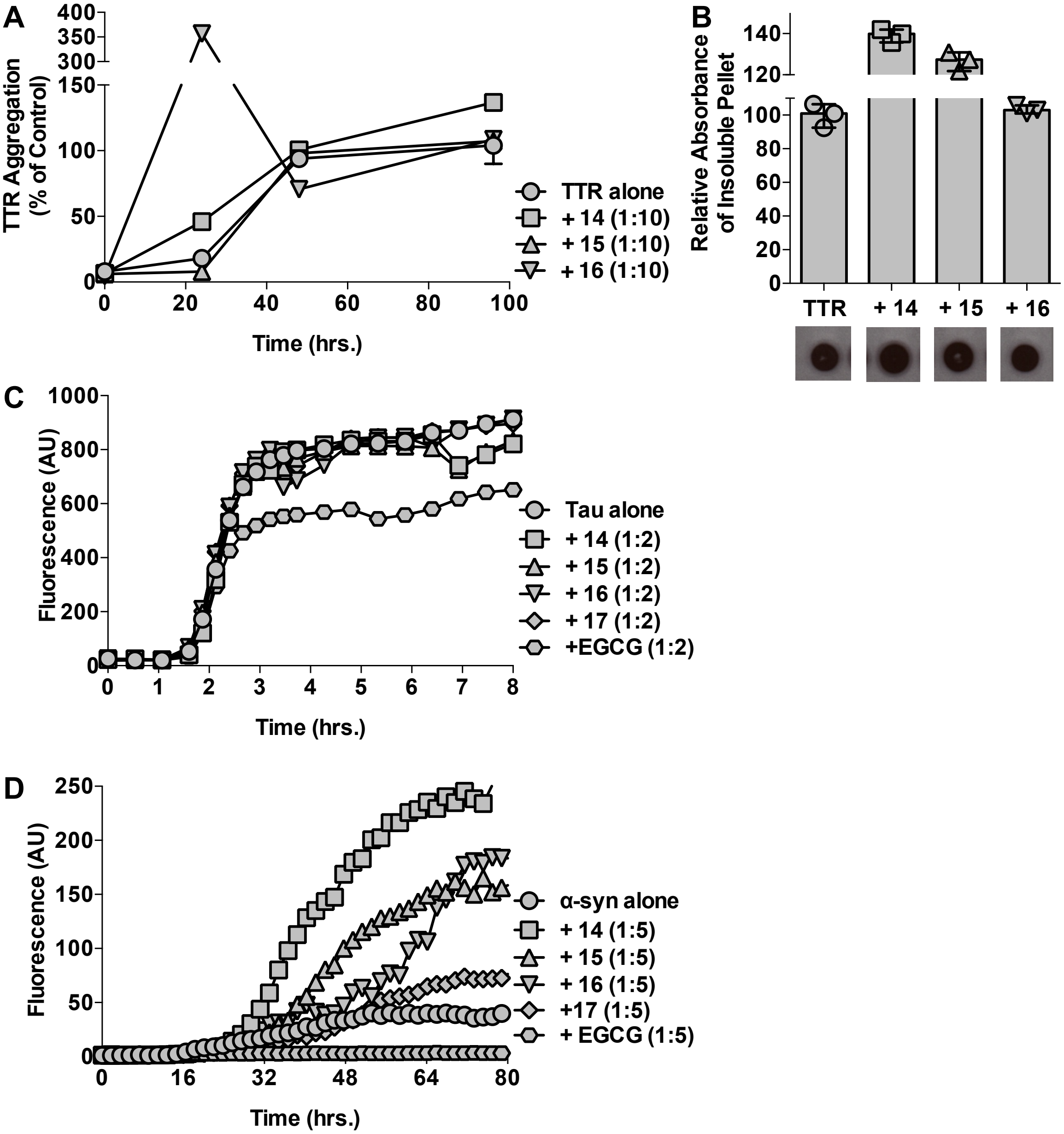

Figure 3.5—Figure Supplement 3. Peptide inhibitors p14 and p15 are specific for the design target and they do not reduce fibril formation of three other amyloid proteins. A. and **B.** Peptide inhibitors, p14 and p15, and negative control peptide p16, do not reduce TTR fibril formation. **A.** TTR fibril formation was monitored by measuring absorbance at 400 nm over a 4-day period. Points were normalized to the average of TTR alone at day 4. Individual points show median with range across triplicates.

Most of the range bars are the same size or smaller than the symbols in the graph. **B.** On day 4 of the TTR aggregation assay, the insoluble fractions of the reactions were isolated with centrifugation and then dissolved in guanidinium hydrochloride. Next, the dissolved insoluble fraction was quantified by measuring absorbance at 280 nm, and by dot blot analysis with an anti-His antibody (the transthyretin protein used in these studies contained a N-terminal His-tag). Graph shows median with range. **C.** Peptides p14, p15, p16, and p17 do not reduce fibril formation of the K18 tau construct. K18 contains only the four repeat domains of the full-length protein. Small molecule epigallocatechin-3-gallate (EGCG), a known inhibitor of K18 fibril formation (75), slightly reduces fibril formation. Lines show average of 3 replicates. **D.** Peptides p14, p15, p16, and p17 do not reduce fibril formation of α-synuclein. EGCG was used as a positive control for fibril inhibition (76). Lines show average of 3 replicates.

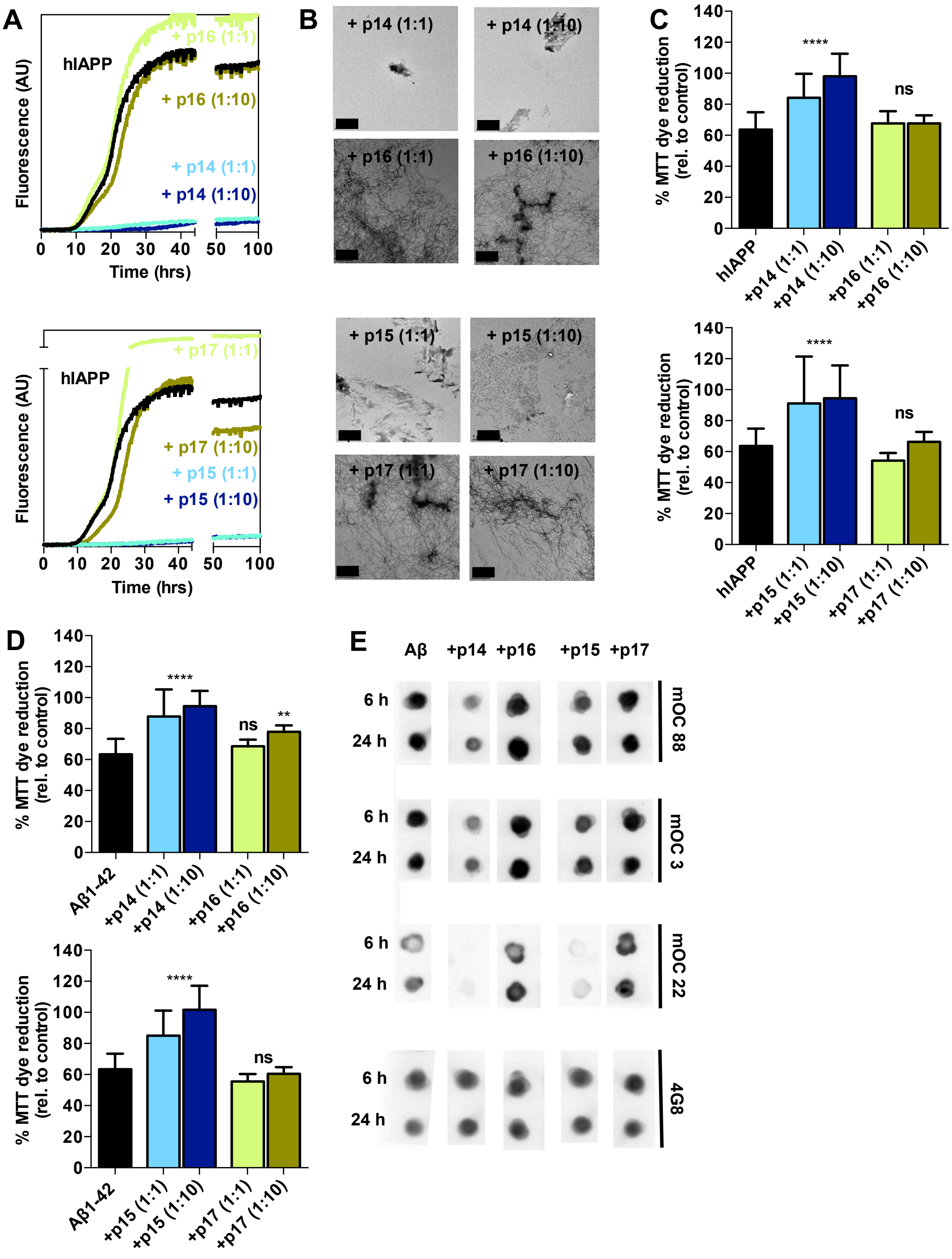

Figure 3.6. Cross-amyloid efficacy of inhibitors developed with structure-based design against hIAPP 19-29 S20G. A. Peptide inhibitors p14 and p15 reduce fibril formation of full-length hIAPP, while negative control peptides p16 and p17 do not. 10

μM hIAPP was incubated with 1:1 or 1:10 molar ratio of each inhibitor under quiescent conditions. Fibril formation was monitored using Thioflavin-T (ThT) fluorescence. Lines show the average of three technical replicates. **B.** Negative-stain TEM analysis confirms the results of the ThT assays in Figure 6A. 45 hours into the ThT assay, the experiment was paused and samples were extracted for TEM analysis. After samples were extracted, the assay was resumed for 3 more days. **C.** Peptide inhibitors reduce cytotoxicity of full-length hIAPP. 10 μM hIAPP was incubated alone or with the designated concentration of peptide inhibitor overnight under quiescent conditions and then diluted 1:10 with pre-plated Rin5F cells, a rat pancreatic β-cell line. Cytotoxicity was quantified using MTT dye reduction. Bars show mean with one standard deviation (n = 3-9; ns = not significant; ****, $p < 0.0001$ using an ordinary one-way ANOVA). **D.** Peptide inhibitors reduce the cytotoxicity of Aβ1-42, while negative control peptides do not. 10 μM Aβ1-42 was incubated alone or with 10-fold molar excess of each peptide for 6 hours and then diluted 1:10 with pre-plated N2a cells. Cytotoxicity was quantified using MTT dye reduction. Bars represent mean with one standard deviation (n = 3-9; ns = not significant; ****, $p < 0.0001$ using an ordinary one-way ANOVA). **E.** Peptide inhibitors reduce the formation of Aβ1-42 assemblies recognized by conformational monoclonal antibodies, while negative control peptides do not. 10 μM Aβ1-42 was incubated alone (left-most column) or with 10-fold molar excess of each peptide-based inhibitor. Aliquots of the reaction were tested for antibody-binding at 6 h and 24 h. Binding to 4G8, a monoclonal antibody specific for residues 17-24 in the linearized Aβ sequence, was used to confirm equal loading of sample onto membranes.

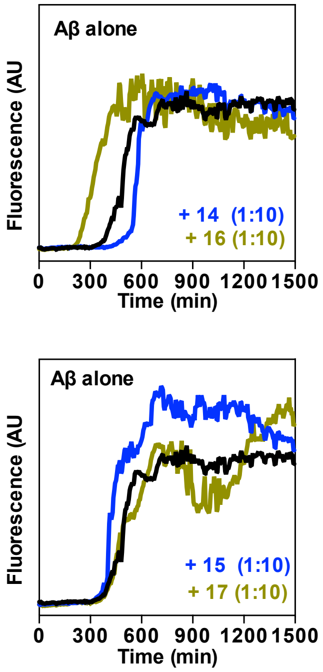

Figure 3.6—Figure Supplement 1. Peptide inhibitors do not reduce Aβ1-42 fibril formation as assessed with ThT fluorescence.

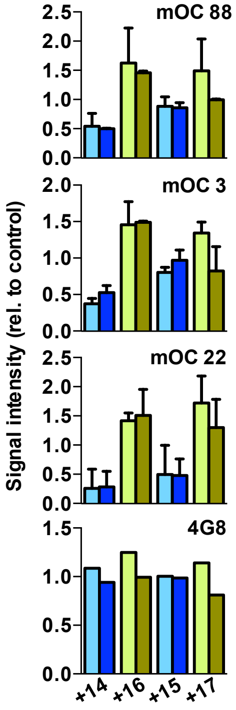

Figure 3.6—Figure Supplement 2. Quantification of antibody-binding experiments show peptide-based inhibitors reduce the formation of Aß1-42 assemblies recognized by certain conformational monoclonal antibodies, while negative control peptides do not. Signal intensity was normalized relative to Aß1-42 alone at that time-point. The light-colored bars represent the 6 h reactions while the dark-colored bars represent the 24 h reaction.

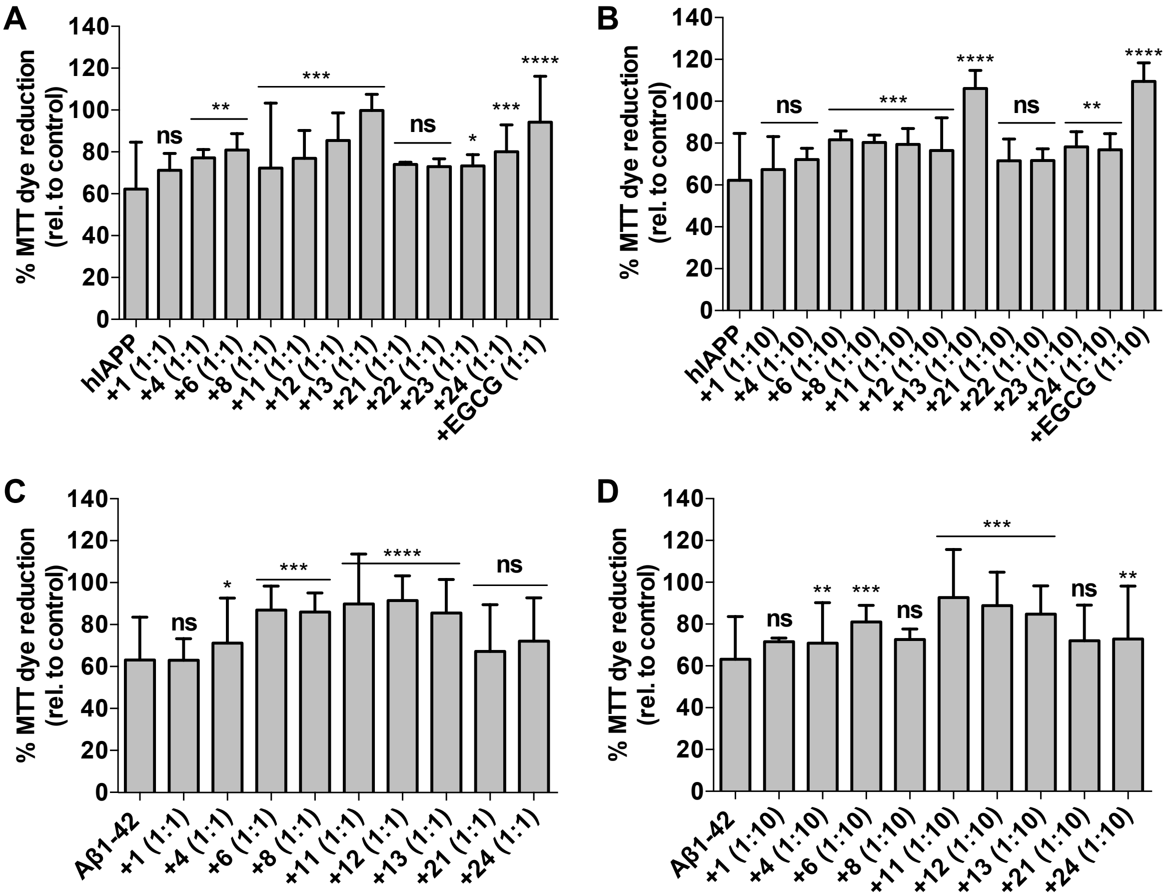

E

	1	4	6	8	11	12	13	14	15	21	22	23	24
hIAPP	X	✓	✓	✓	✓	✓	✓	✓	✓	X	X	✓	✓
Aβ1-42	X	✓	✓	✓	✓	✓	✓	✓	✓	X	-	-	X

Figure 3.6—Figure Supplement 3. Other peptide-based inhibitors developed against hIAPP 19-29 S20G reduce cytotoxicity of full-length hIAPP (A and B) and Aβ1-42 (C and D) to Rin5F and N2a cells, respectively. Cytotoxicity was quantified using MTT dye reduction. **E.** Summary of efficacies of peptide inhibitors on reduction of cytotoxicity described in this study.

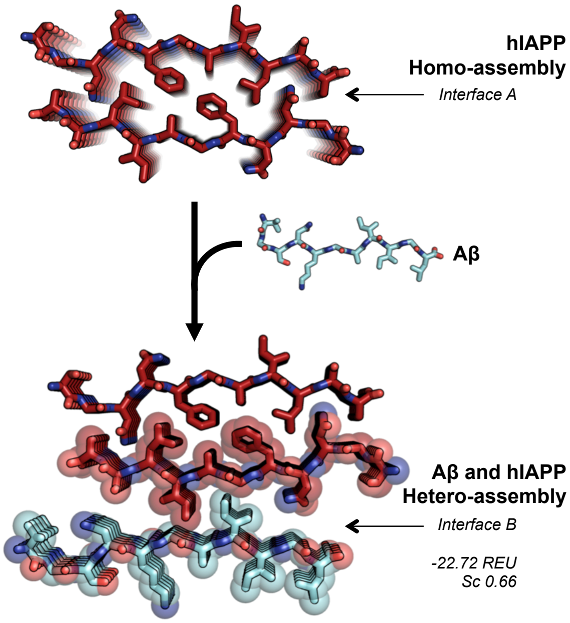

Figure 3.7. Model of an Aβ 24-34 WT and hIAPP 19-29 S20G hetero-assembly, which may explain how full-length Aβ and hIAPP cross-seed. The interface of the hetero-assembly model is highlighted with transparent spheres representing van der Waals radii. The model was generated from the backbone of Interface B of the hIAPP 19-29 S20G atomic structure using Rosetta. Its Rosetta Energy and shape complementarity scores are shown to its right. These scores are comparable to the Interface B homo-assemblies (Aβ 24-34 WT: -19.4 REU, Sc 0.85; hIAPP 19-29 S20G: -35.09, 0.72). Our results with the peptide inhibitors suggest that Interface A may be important for cytotoxicity.

REFERENCES

1. Eisenberg D, Jucker M. 2012 The amyloid state of proteins in human diseases. *Cell* **148**:1188–1203. doi:10.1016/j.cell.2012.02.022

2. Sunde M, Serpell LC, Bartlam M, Fraser PE, Pepys MB, Blake CC. 1997 Common core structure of amyloid fibrils by synchrotron X-ray diffraction. *J Mol Biol* **273**:729–739. doi:10.1006/jmbi.1997.1348

3. Cooper GJS, Willis AC, Clark A, Turner RC, Sim RB, Reid KB. 1987 Purification and characterization of a peptide from amyloid-rich pancreases of type 2 diabetic patients. *Proc Natl Acad Sci U S A* **84**:8628–8632. doi:10.1073/pnas.84.23.8628

4. Westermark P, Wernstedt C, Wilander E, Hayden DW, O'Brien TD, Johnson KH. 1987 Amyloid fibrils in human insulinoma and islets of Langerhans of the diabetic cat are derived from a neuropeptide-like protein also present in normal islet cells. *Proc Natl Acad Sci U S A* **84**:3881–3885. doi:10.1073/pnas.84.11.3881

5. Morales R, Moreno-Gonzalez I, Soto C. 2013 Cross-Seeding of Misfolded Proteins: Implications for Etiology and Pathogenesis of Protein Misfolding Diseases. *PLoS Pathog* **9**:1–4. doi:10.1371/journal.ppat.1003537

6. Guo J-P, Arai T, Miklossy J, McGeer PL. 2006 Abeta and tau form soluble complexes that may promote self aggregation of both into the insoluble forms observed in Alzheimer's disease. *Proc Natl Acad Sci U S A* **103**:1953–8. doi:10.1073/pnas.0509386103

7. Uéda K, Fukushima H, Masliah E, Xia Y, Iwai a, Yoshimoto M, Otero D a, Kondo J, Ihara Y, Saitoh T. 1993 Molecular cloning of cDNA encoding an unrecognized component of amyloid in Alzheimer disease. *Proc Natl Acad Sci U S A* **90**:11282–11286. doi:10.1073/pnas.90.23.11282

8. Buxbaum JN, Ye Z, Reixach N, Friske L, Levy C, Das P, Golde T, Masliah E, Roberts AR, Bartfai T. 2008 Transthyretin protects Alzheimer's mice from the behavioral and biochemical effects of Abeta toxicity. *Proc Natl Acad Sci U S A* **105**:2681–2686. doi:10.1073/pnas.0712197105

9. Westermark P, Li ZC, Westermark GT, Leckström A, Steiner DF. 1996 Effects of beta cell granule components on human islet amyloid polypeptide fibril formation. *FEBS Lett* **379**:203–6. doi:10.1006/bbrc.1997.7014

10. Wiltzius JJW, Sievers SA, Sawaya MR, Eisenberg D. 2009 Atomic structures of IAPP (amylin) fusions suggest a mechanism for fibrillation and the role of insulin in the process. *Protein Sci* **18**:1521–1530. doi:10.1002/pro.145

11. Oskarsson ME, Paulsson JF, Schultz SW, Ingelsson M, Westermark P, Westermark G. 2015 In Vivo Seeding and Cross-Seeding of Localized Amyloidosis. *Am J Pathol* **185**:834–846. doi:10.1016/j.ajpath.2014.11.016

12. Kapurniotu A. 2001 Amyloidogenicity and cytotoxicity of islet amyloid polypeptide. *Biopolym - Pept Sci Sect* **60**:438–459. doi:10.1002/1097-0282(2001)60:6<438::AID-BIP10182>3.0.CO;2-A

13. Andreetto E, Yan L-M, Tatarek-Nossol M, Velkova A, Frank R, Kapurniotu A. 2010 Identification of hot regions of the A??-IAPP Interaction interface as high-affinity binding sites in both cross- and self-association. *Angew Chemie - Int Ed* **49**:3081–3085. doi:10.1002/anie.200904902

14. Hu R, Zhang M, Chen H, Jiang B, Zheng J. 2015 Cross-Seeding Interaction between β-Amyloid and Human Islet Amyloid Polypeptide. *ACS Chem Neurosci* doi:10.1021/acschemneuro.5b00192

15. O'Nuallain B, Williams AD, Westermark P, Wetzel R. 2004 Seeding Specificity in Amyloid Growth Induced by Heterologous Fibrils. *J Biol Chem* **279**:17490–17499. doi:10.1074/jbc.M311300200

16. Andreetto E, Malideli E, Yan L-M, Kracklauer M, Farbiarz K, Tatarek-Nossol M, Rammes G, Prade E, Neumüller T, Caporale A, Spanopoulou A, Bakou M, Reif B, Kapurniotu A. 2015 A Hot-Segment-Based Approach for the Design of Cross-Amyloid Interaction Surface Mimics as Inhibitors of Amyloid Self-Assembly. *Angew Chemie Int Ed*n/a–n/a. doi:10.1002/anie.201504973

17. Moreno-Gonzalez I, Edwards III G, Salvadores N, Shahnawaz M, Diaz-Espinoza R, Soto C. 2017 Molecular interaction between type 2 diabetes and Alzheimer's disease through cross-seeding of protein misfolding. *Mol Psychiatry* doi:10.1038/mp.2016.230

18. Janson J, Laedtke T, Parisi JE, O'Brien P, Petersen RC, Butler PC. 2004 Increased risk of type 2 diabetes in Alzheimer disease. *Diabetes* **53**:474–481. doi:10.2337/diabetes.53.2.474

19. Miklossy J, Qing H, Radenovic A, Kis A, Vileno B, L??szl?? F, Miller L, Martins RN, Waeber G, Mooser V, Bosman F, Khalili K, Darbinian N, McGeer PL. 2010 Beta amyloid and hyperphosphorylated tau deposits in the pancreas in type 2 diabetes. *Neurobiol Aging* **31**:1503–1515. doi:10.1016/j.neurobiolaging.2008.08.019

20. Peila R, Rodriguez BL, Launer LJ. 2002 Type 2 Diabetes, APOE Gene, and the Risk for Dementia and Related Pathologies. *Diabetes* **51**:1256 –1262. doi:10.2337/diabetes.51.4.1256

21. Mukherjee A, Morales-Scheihing D, Butler PC, Soto C. 2015 Type 2 diabetes as a protein misfolding disease. *Trends Mol Med* **21**:439–449. doi:10.1016/S0140-6736(13)62365-X

22. Akter K, Lanza E a., Martin S a., Myronyuk N, Rua M, Raffa RB. 2011 Diabetes mellitus and Alzheimer's disease: Shared pathology and treatment? *Br J Clin Pharmacol* **71**:365–376. doi:10.1111/j.1365-2125.2010.03830.x

23. Lee SC, Hashim Y, Li JK, Ko GT, Critchley JA, Cockram CS, Chan JC. 2001 The islet amyloid polypeptide (amylin) gene S20G mutation in Chinese subjects: evidence for associations with type 2 diabetes and cholesterol levels. *Clin Endocrinol (Oxf)* **54**:541–546.

24. Morita S, Sakagashira S, Ueyama M, Shimajiri Y, Furuta M, Sanke T. 2011 Progressive deterioration of insulin secretion in Japanese type 2 diabetic patients in comparison with those who carry the S20G mutation of the islet amyloid polypeptide gene: A long-term follow-up study. *J Diabetes Investig* **2**:287–92. doi:10.1111/j.2040-1124.2011.00102.

25. Sakagashira S, Sanke T, Hanabusa T, Shimomura H, Ohagi S, Kumagaye KY, Nakajima K, Nanjo K. 1996 Missense mutation of amylin gene (S20G) in Japanese NIDDM patients. *Diabetes* **45**:1279–1281.

26. Lührs T, Ritter C, Adrian M, Riek-Loher D, Bohrmann B, Döbeli H, Schubert D, Riek R. 2005 3D structure of Alzheimer's amyloid-beta(1-42) fibrils. *Proc Natl Acad Sci U S A* **102**:17342–17347. doi:10.1073/pnas.0506723102

27. Wälti MA, Ravotti F, Arai H, Glabe CG, Wall JS, Böckmann A, Güntert P, Meier BH, Riek R. 2016 Atomic-resolution structure of a disease-relevant Aβ(1-42) amyloid fibril. *Proc Natl Acad Sci U S A* **113**:E4976–84. doi:10.1073/pnas.1600749113

28. Scheidt HA, Morgado I, Rothemund S, Huster D. 2012 Dynamics of amyloid ?? fibrils revealed by solid-state NMR. *J Biol Chem* **287**:2017–2021. doi:10.1074/jbc.M111.308619

29. Colvin MT, Silvers R, Ni QZ, Can T V., Sergeyev I, Rosay M, Donovan KJ, Michael B, Wall J, Linse S, Griffin RG. 2016 Atomic Resolution Structure of Monomorphic A??42 Amyloid Fibrils. *J Am Chem Soc* **138**:9663–9674. doi:10.1021/jacs.6b05129

30. Colletier J-P, Laganowsky A, Landau M, Zhao M, Soriaga AB, Goldschmidt L, Flot D, Cascio D, Sawaya MR, Eisenberg D. 2011 Molecular basis for amyloid-polymorphism. *Proc Natl Acad Sci* **108**:16938–16943. doi:10.1073/pnas.1112600108

31. Do TD, LaPointe NE, Nelson R, Krotee P, Hayden EY, Ulrich B, Quan S, Feinstein SC, Teplow DB, Eisenberg D, Shea J-E, Bowers MT. 2016 Amyloid β-Protein C-terminal Fragments: Formation of Cylindrins and β-barrels. *J Am Chem Soc* **138**:jacs.549–557. doi:10.1021/jacs.5b09536

32. Laganowsky A, Liu C, Sawaya MR, Whitelegge J, Park J, Zhao M, Pensalfini A, Soriaga AB, Landau M, Teng PK, Cascio D, Glabe CG, Eisenberg D. 2012 Atomic View of a Toxic Amyloid Small Oligomer. *Science* **335**:1228–1231. doi:10.1126/science.1213151

33. Fonte V, Dostal V, Roberts CM, Gonzales P, Lacor P, Magrane J, Dingwell N, Fan EY, Silverman M a, Stein GH, Link CD. 2011 A glycine zipper motif mediates the

formation of toxic β-amyloid oligomers in vitro and in vivo. *Mol Neurodegener* **6**:61. doi:10.1186/1750-1326-6-61

34. Harmeier A, Wozny C, Rost BR, Munter L-M, Hua H, Georgiev O, Beyermann M, Hildebrand PW, Weise C, Schaffner W, Schmitz D, Multhaup G. 2009 Role of amyloid-beta glycine 33 in oligomerization, toxicity, and neuronal plasticity. *J Neurosci* **29**:7582–7590. doi:10.1523/JNEUROSCI.1336-09.2009

35. Kanski J, Varadarajan S, Aksenova M, Butterfield DA. 2002 Role of glycine-33 and methionine-35 in Alzheimer's amyloid β-peptide 1-42-associated oxidative stress and neurotoxicity. *Biochim Biophys Acta - Mol Basis Dis* **1586**:190–198. doi:10.1016/S0925-4439(01)00097-7

36. Krotee P, Rodriguez JA, Sawaya MR, Cascio D, Reyes FE, Shi D, Hattne J, Nannenga BL, Oskarsson ME, Philipp S, Griner S, Jiang L, Glabe CG, Westermark GT, Gonen T, Eisenberg DS. 2017 Atomic Structures of Fibrillar Segments of hIAPP Suggest Tightly Mated β-Sheets Are Important for Cytotoxicity. *Elife* **6**:e19273. doi:10.7554/eLife.19273

37. Rodriguez JA, Ivanova MI, Sawaya MR, Cascio D, Reyes FE, Shi D, Sangwan S, Guenther EL, Johnson LM, Zhang M, et al. 2015 Structure of the toxic core of α-synuclein from invisible crystals. *Nature* **525**:486–490. doi:10.1038/nature15368

38. Hattne J, Reyes FE, Nannenga BL, Shi D, de la Cruz MJ, Leslie AGW, Gonen T. 2015 MicroED data collection and processing. *Acta Crystallogr Sect A Found Adv* **71**:353–360. doi:10.1107/S2053273315010669

39. Liu S, Hattne J, Reyes FE, Sanchez-Martinez S, Jason de la Cruz M, Shi D, Gonen T. 2016 Atomic resolution structure determination by the cryo-EM method MicroED. *Protein Sci* **00**:1–8. doi:10.1002/pro.2989

40. Nannenga BL, Shi D, Leslie AGW, Gonen T. 2014 High-resolution structure determination by continuous-rotation data collection in MicroED. *Nat Methods* **11**:1–5. doi:10.1038/nmeth.3043

41. Shi D, Nannenga BL, Iadanza MG, Gonen T. 2013 Three-dimensional electron crystallography of protein microcrystals. *Elife* **2013**:1–17. doi:10.7554/eLife.01345.001

42. Lorenzo a, Yankner B a. 1996 Amyloid fibril toxicity in Alzheimer's disease and diabetes. *Ann N Y Acad Sci* **777**:89–95. doi:10.1111/j.1749-6632.1996.tb34406.x

43. Olmsted JB, Carlson K, Klebe R, Ruddle F, Rosenbaum J. 1970 Isolation of microtubule protein from cultured mouse neuroblastoma cells. *Proc Natl Acad Sci U S A* **65**:129–136. doi:10.1073/pnas.65.1.129

44. Mosmann T. 1983 Rapid colorimetric assay for cellular growth and survival: application to proliferation and cytotoxicity assays. *J Immunol Methods* **65**:55–63. doi:10.1016/0022-1759(83)90303-4

45. Liu Y, Peterson DA, Kimura H, Schubert D. 1997 Mechanism of cellular 3- (4,5-dimethylthiazol-2-yl)-2,5- diphenyltetrazolium bromide (MTT) reduction. *J Neurochem* **6**:581–593. doi:10.1046/j.1471-4159.1997.69020581.x

46. Pike C, Walencewicz-Wasserman A, Kosmoski J, Cribbs D, Glabe C, Cotman C. 1995 Structure-activity analyses of beta-amyloid peptides: contributions of the beta 25-35 region to aggregation and neurotoxicity. *J Neurochem* **6**:253–265.

47. Yankner BA, Duffy LK, Kirschner DA. 1990 Neurotrophic and neurotoxic effects of amyloid beta protein: reversal by tachykinin neuropeptides. *Science* **250**:279–82. Available at: http://www.ncbi.nlm.nih.gov/pubmed/2218531 [Accessed February 19, 2017]

48. Saelices L, Johnson LM, Liang WY, Sawaya MR, Cascio D, Ruchala P, Whitelegge J, Jiang L, Riek R, Eisenberg DS. 2015 Uncovering the mechanism of aggregation of human transthyretin. *J Biol Chem* **290**:28932–28943. doi:10.1074/jbc.M115.659912

49. Sievers SA, Karanicolas J, Chang HW, Zhao A, Jiang L, Zirafi O, Stevens JT, Münch J, Baker D, Eisenberg D. 2011 Structure-based design of non-natural amino-acid inhibitors of amyloid fibril formation. *Nature* **475**:96–100. doi:10.1038/nature10154

50. Soragni A, Janzen DM, Johnson LM, Lindgren AG, Thai-Quynh Nguyen A, Tiourin E, Soriaga AB, Lu J, Jiang L, Faull KF, Pellegrini M, Memarzadeh S, Eisenberg DS. 2016 A Designed Inhibitor of p53 Aggregation Rescues p53 Tumor Suppression in Ovarian Carcinomas. *Cancer Cell* **29**:90–103. doi:10.1016/j.ccell.2015.12.002

51. Hatami A, Albay R, Monjazeb S, Milton S, Glabe C. 2014 Monoclonal antibodies against A??42 fibrils distinguish multiple aggregation state polymorphisms in vitro and in Alzheimer disease brain. *J Biol Chem* **289**:32131–32143. doi:10.1074/jbc.M114.594846

52. Morales R, Duran-Aniotz C, Diaz-Espinoza R, Camacho M V, Soto C. 2012 Protein misfolding cyclic amplification of infectious prions. *Nat Protoc* **7**:1397–1409. doi:10.1038/nprot.2012.067

53. Ross CD, McCarty BR, Hamilton M, Ben-Hur A, Ross ED. 2009 A promiscuous prion: Efficient induction of [URE3] prion formation by heterologous prion domains. *Genetics* **183**:929–940. doi:10.1534/genetics.109.109322

54. Tjernberg LO, Näslund J, Lindqvist F, Johansson J, Karlström a R, Thyberg J, Terenius L, Nordstedt C. 1996 Arrest of beta-amyloid fibril formation by a pentapeptide ligand. *J Biol Chem* **271**:8545–8548. doi:10.1074/jbc.271.15.8545

55. Hardy J, Selkoe DJ. 2002 The Amyloid Hypothesis of Alzheimer's Disease: Progress and Problems on the Road to Therapeutics. *Science* **297**:353–356. doi:10.1126/science.1072994

56. Wu JW, Breydo L, Isas JM, Lee J, Kuznetsov YG, Langen R, Glabe C. 2010 Fibrillar oligomers nucleate the oligomerization of monomeric amyloid-beta but do not seed fibril formation. *J Biol Chem* **285**:6071–6079. doi:10.1074/jbc.M109.069542

57. Qiang W, Yau W-M, Luo Y, Mattson MP, Tycko R. 2012 Antiparallel -sheet architecture in Iowa-mutant -amyloid fibrils. *Proc Natl Acad Sci* **109**:4443–4448. doi:10.1073/pnas.1111305109

58. Shi D, Nannenga BL, de la Cruz MJ, Liu J, Sawtelle S, Calero G, Reyes FE, Hattne J, Gonen T. 2016 The collection of MicroED data for macromolecular crystallography. *Nat Protoc* **11**:895–904. doi:10.1038/nprot.2016.046

59. Kabsch W. 2010 XDS. *Acta Crystallogr D Biol Crystallogr* **66**:125–32. doi:10.1107/S0907444909047337

60. McCoy AJ. 2007 Solving structures of protein complexes by molecular replacement with Phaser. *Acta Crystallogr D Biol Crystallogr* **63**:32–41. doi:10.1107/S0907444906045975

61. Emsley P, Cowtan K. 2004 Coot: model-building tools for molecular graphics. *Acta Crystallogr D Biol Crystallogr* **60**:2126–32. doi:10.1107/S0907444904019158

62. McCoy AJ, Grosse-Kunstleve RW, Storoni LC, Read RJ. 2005 Likelihood-enhanced fast translation functions. *Acta Crystallogr D Biol Crystallogr* **61**:458–64. doi:10.1107/S0907444905001617

63. Collaborative Computational Project Number 4. 1994 The CCP4 suite: programs for protein crystallography. *Acta Crystallogr D Biol Crystallogr* **50**:760–763. doi:10.1107/S0907444994003112

64. Lee B, Richards FM. 1971 The interpretation of protein structures: estimation of static accessibility. *J Mol Biol* **55**:379–400.

65. Connolly ML. 1983 Solvent-accessible surfaces of proteins and nucleic acids. *Science* **221**:709–13. doi:10.1126/science.68779170

66. Lawrence MC, Colman PM. 1993 Shape complementarity at protein-protein interfaces. *J Mol Biol* **93**:946–950. doi:10.1002/bip.360340711

67. Richards FM. 1977 Areas, volumes, packing, and protein structure. *Annu Rev Biophys Bioeng* **5**:151–176. doi:10.1146/annurev.bb.06.060177.001055

68. Kabsch W. 1976 A solution for the best rotation to relate two sets of vectors. *Acta Crystallogr Sect A* **32**:922–923. doi:10.1107/S0567739476001873

69. Kyte J, Doolittle RF. 1982 A simple method for displaying the hydropathic character of a protein. *J Mol Biol* **157**:105–132. doi:10.1016/0022-2836(82)90515-0

70. Kayed R, Head E, Sarsoza F, Saing T, Cotman CW, Necula M, Margol L, Wu J, Breydo L, Thompson JL, Rasool S, Gurlo T, Butler P, Glabe CG. 2007 Fibril specific, conformation dependent antibodies recognize a generic epitope common to amyloid fibrils and fibrillar oligomers that is absent in prefibrillar oligomers. *Mol Neurodegener* **2**:18. doi:10.1186/1750-1326-2-18

71. Thompson MJ, Sievers SA, Karanicolas J, Ivanova MI, Baker D, Eisenberg D. 2006 The 3D profile method for identifying fibril-forming segments of proteins. *Proc Natl Acad Sci U S A* **103**:4074–4078. Available at: http://eutils.ncbi.nlm.nih.gov/entrez/eutils/elink.fcgi?dbfrom=pubmed&id=16537487&retmode=ref&cmd=prlinks

72. Kuhlman B, Dantas G, Ireton GC, Varani G, Stoddard BL, Baker D. 2003 Design of a Novel Globular Protein Fold with Atomic-Level Accuracy. *Science (80-)* **302**:1364–1368. doi:10.1126/science.1089427

73. Diederichs K, Karplus P a. 2013 Better models by discarding data? *Acta Crystallogr Sect D* **69**:1215–1222. doi:10.1107/S0907444913001121

74. Chen VB, Arendall WB, Headd JJ, Keedy D a., Immormino RM, Kapral GJ, Murray LW, Richardson JS, Richardson DC. 2010 MolProbity: All-atom structure validation for macromolecular crystallography. *Acta Crystallogr Sect D Biol Crystallogr* **66**:12–21. doi:10.1107/S0907444909042073

75. Wobst HJ, Sharma A, Diamond MI, Wanker EE, Bieschke J. 2015 The green tea polyphenol (−)-epigallocatechin gallate prevents the aggregation of tau protein into toxic oligomers at substoichiometric ratios. *FEBS Lett* **589**:77–83. doi:10.1016/j.febslet.2014.11.026

76. Bieschke J, Russ J, Friedrich RP, Ehrnhoefer DE, Wobst H, Neugebauer K, Wanker EE. 2010 EGCG remodels mature alpha-synuclein and amyloid-beta fibrils and reduces cellular toxicity. *Proc Natl Acad Sci U S A* **107**:7710–5. doi:10.1073/pnas.0910723107

CHAPTER 4

Amyloid β-protein C-terminal segments: formation of cylindrins and β-barrels

INTRODUCTION

Structure-neurotoxicity relationships among Aβ oligomers have been the subject of intense research efforts. Some Aβ oligomers have been found to be precursors of the classical 10 nm-diameter amyloid fibrils (1–5), while others form independently of fibril formation. Although fibril formation is a defining feature of many devastating diseases including Alzheimer's, Parkinson's and type II diabetes, multiple lines of evidence indicate that oligomers likely are the most important toxic agents (6–9). Of note, a variety of amyloid proteins and peptides with different primary structures form oligomers with similar quaternary structures (8,10). These structures are more stable than their monomeric and smaller oligomeric precursors, but less stable than their ultimate fibrillar products (11,12). From a structure-function perspective, toxic oligomers would be predicted to have relatively well-organized structures that interact with cellular membranes, receptors, or other proteins. Recently, a novel class of oligomer structure, the cylindrin, was defined (13). Cylindrins contain six single β-strands arranged near-vertically around a central axis, thus forming a cylinder. Computational studies predict that larger cylindrins are possible, but evidence for these remains lacking (14).

To date, the most detailed structural findings have come from studies of amyloid oligomers in stable, homogeneous populations (13,15–17). X-ray crystallographic studies were the first to reveal the three-dimensional structures of oligomers and fibrils (18–22), including those of a model peptides from αB-crystallin (13) and prion (20). These peptides were found to form cylindrins. The success of those studies was highly dependent on the availability of homogeneous, stable oligomers. However, for many biologically-relevant amyloid proteins, it remains quite challenging to perform the same kind of experiment for two reasons: (a) the extremely high aggregation propensity of many of these proteins, which produces polydisperse aggregates (13), and (b) the existence of multiple conformational states for oligomers of identical molecular weight (23). In addition, X-ray crystallographic analyses often yield data only on a dominant conformational state, and thus a complete definition of the oligomer conformational space is not possible.

Many of these experimental difficulties can be overcome by mass spectrometry (MS). The maturation of MS in recent years and has led to significant advancements in studies of protein structure-function relationships, especially in the area of protein assembly and aggregation (23–29). Native ion-mobility mass spectrometry (IM-MS) offers an additional dimension of measure, in that it allows a variety of oligomers to be separated not only by their mass to charge ratios (*m/z*), as in basic MS, but also by their sizes and shapes. With IM-MS, the overall structure of a specific oligomer can be captured through means of cross-section measurement, which can then be directly compared with structures obtained using other experimental techniques or theoretical calculations (24,25,30–32). Here, we have applied IM-MS, in combination with transmission electron microscopy (TEM), atomic force microscopy (AFM), and computational modeling, to investigate possible cylindrin formation by protein segments derived from Aβ. We examine three overlapping segments: Aβ(24-34), Aβ(25-35), and Aβ(26-36). The Aβ(25-35) segment is known to exist in the brain and is cytotoxic (33,34). The other two segments were predicted to be compatible with the cylindrin structure. In addition, we examined tandem-repeat versions of each segment, in which two copies of the same segment are connected head-to-tail by a di-glycine (GG) linker. This linking strategy was used successfully with cylindrin-forming segments of αB-crystallin (13). The tandem-repeat peptides of Aß are annotated as GG(24-34), GG(25-35) and GG(26-36). Scheme 4.1 shows the sequences of full length Aß(1-42) and of the three single-repeat peptide segments used in this study.

RESULTS

Imaging data indicate different aggregation characteristics for similar Aß segments

We examined the aggregation characteristics of the six peptides by AFM and TEM (Figure 4.1 and Supplementary Figures 4.3-4.6). All peptides formed fibrils after a 24-hour incubation except Aß(24-34), which did not form fibrils observable by microscopy even after one week (Figure 4.1A). The weaker aggregation propensity of Aß(24-34) is consistent with previous studies by Pike et al. and Hou et al. showing that methionine M35 is crucial for fibril formation (24,33,35). However, as described in Chapter 3, Aß(24-34) forms microcrystals when incubated for a week at approximately 5 times higher concentration.

On the other hand, GG(24-34) formed short fibrils after a week-long incubation in water (Figure 4.1E) and fibrils with a striated ribbon morphology when incubated in PBS (Supplementary Figure 4.3). We observed a variety of aggregate morphologies for GG(26-36) (Figure 4.1F), including a mix of elongated twisted fibrils, short fibrils, non-fibrillar aggregates, and ring-like structures. A comparison of microtubule samples to GG(26-36) samples reveals some of the short GG(26-36) fibrils share a similar morphology (see Supplementary Figure 4.5, blue arrows). Similar results were observed from the set of AFM images (see Supplementary Figure 4.6) with Aß(25-35) forming the most fibrils out of the two single-repeat peptides while all three tandem repeat peptides show abundant fibrils and non-amyloid aggregates.

Overall, the microscopy data suggest that these peptides have different aggregation characteristics, in which Aβ(24-34) and Aβ(26-36) form less regular fibrils. The effect of the GG linker also varies. Our Thioflavin-T assays indicate that both Aβ(24-34) and Aβ(26-36) have weaker aggregation propensities than Aβ(25-35). On the other hand, the same experiments reveal that GG(26-36) is the most aggregation-prone tandem-repeat out of the three, followed by GG(25-35), and GG(24-34) remains the weakest (see Supplementary Figure 4.8).

The Aβ segments and tandem GG repeats form stoichiometric oligomers with similar cross-sections

We next turned to IM-MS to investigate oligomer structure and stiochiometry. All mass spectral data reported here are of the six peptides in water. Ammonium acetate buffer (an ESI-friendly solvent) yielded similar charge state distributions and aggregate morphologies (see Supplementary Figure 4.9 and 4.10 for TEM and AFM images obtained in buffer conditions), but the signals for oligomer peaks were less intense and the arrival time distributions (ATDs) were less resolved than in water.

Figure 4.2 shows the mass spectra of the six peptides obtained from the high-resolution instrument I. The major peaks are $n/z = 1/2$ and $1/1$ (n is the oligomer size and z is the charge) for the single-repeat Aβ peptides (Figure 4.2A-C), and 1/3 and 1/2 for their GG tandem-repeat versions (Figure 4.2F). The ATDs of the $n/z = 1/1$ peaks of the single-repeat Aβ peptides are shown in Figure 4.3A-C (ATDs of other peaks are shown in Supplementary Figure 4.11). The ATDs of $n/z = 1/1$ peaks are complicated with multiple features and require a combination of simulations and use of the isotropic model to assign each feature. The isotropic model assumes the oligomer grows isotropically in all directions, and that its cross-section σ_n can be predicted using the equation $\sigma_n = \sigma_1 \times n^{2/3}$ where σ_1 is the monomer cross-section and n is the oligomer size. For oligomers with the same n/z the oligomer with highest *n* travels fastest through the cell because the charge increases linearly with *n* but the cross-section more slowly. For example, a dimer with 2 charges will travel through the cell faster than a monomer with one charge since the summed cross-section of 2 monomers is greater than the cross-section of the dimer (36). However, among oligomers of the same order *n*, compact species appear at shorter drift times than extended or elongated ones. For instrument I, when the ATD features are well-resolved and separated as they are here, it is likely that the features correspond to oligomers of different order, rather than different conformations of the same order *n*.

The assignment of features in the Aβ(25-35) ATD (*n/z* = 1/1, 1101 *m/z*; Figure 4.3B) is representative of the process we followed for each sample. The feature with the longest arrival time should be either a monomer or a small oligomer. If assigned as a monomer, the arrival time indicates a cross-section of 204 Å^2, which is significantly too small. Our previous work (23,37) shows that the smallest Aβ(25-35) monomer should have a cross-section of about 250 Å^2. In this work, IM-MS experiments (Supplementary Figure 4.11) and T-REMD simulations (Supplementary Figure 4.12) show the monomer has a cross-section in the 260 to 280 Å^2 range. Hence, we assigned this feature as a dimer.

We assigned the next feature as a trimer because the cross-section is too small for a dimer. The two partially resolved features at immediately shorter times are also trimers. The next feature, near 70 ms, is therefore the tetramer. We assigned the feature at the shortest time as a hexamer (*n/z* = +6/6), rather than a pentamer (*n/z* = +5/5), based on the trend in the spacing between each pair of features. As we move from dimer to trimer to tetramer, the spacing between features decreases, since adding a monomer adds a proportionately smaller volume as oligomers get larger. However, the spacing increases between the tetramer peak and the shortest time peak, indicating an oligomer larger than a pentamer.

Using the same analysis, we assigned all of the features in the ATDs of Aβ(24-34) and Aβ(26-36) (Figure 4.3A and C). In the Aβ(24-34) ATD (*n/z* = 1/1, 1069 *m/z*, Figure 4.3A), the feature near 75 ms is missing. We note that the cross-sections of dimer, trimer, tetramer, and hexamer species are similar among all three Aβ segments, as are the spacings between their features in the ATDs (Table 4.2, Figure 4.3A-C).

The ATDs of the tandem-repeat GG peptides (Figure 4.3D-F) were less challenging to assign. These ATDs of species with *n/z* = 1/2 have oligomers whose number of charges per Aβ repeat are identical to the species of *n/z* = 1/1 of single-repeat Aβ. We assigned the features near 80 ms to be monomers whose cross-sections are comparable to the dimers of single-repeat Aβ peptides. The middle features are thus dimers, whose cross-sections correlate with those of the single-repeat tetramers (see Table 4.2). The remaining features are assigned as trimers, having cross-sections comparable to single-repeat hexamers. Taken together, these cross-section data suggest that the GG linkers do not significantly affect the quaternary structures of the oligomers. In summary, ion-mobility experiments by instrument I suggest that all of the three Aβ segments can form hexamers, whereas GG tandem-repeats populate trimers.

Of note, size exclusion chromatography (SEC) reveals that GG(24-34) forms a trimer (Supplementary Figure 4.13). Furthermore, this trimer is recognized by the oligomer-specific antibody, A11, while fibrils of the same segment are not recognized by A11. Since GG(25-35) and GG(26-36) are significantly less soluble than GG(24-34), GG(25-35) and GG(26-36) oligomers could not be resolved with SEC. Therefore, we did not pursue these methods to characterize their oligomeric forms. However, IM-MS data on both these peptides strongly support the notion that both segments are capable of forming trimers of tandem-repeat Aβ segments.

The cross-sections of Aβ-segment hexamers and tandem-repeat GG trimers agree with cylindrin model structures

In order to determine whether the observed single-repeat Aβ hexamers and GG tandem-repeat trimers could be cylindrins, we made cylindrin models of all six peptides and then calculated their cross-sections. Beginning with the X-ray crystal structures of the αB-crystallin cylindrin hexamer and tandem GG trimer (PDB ID 3SGO and 3SGR) (13), we substituted the side-chains to match each of the six Aβ constructs using Swiss-PDB (http://www.expasy.org/spdbv/) (38,39). This modeling was followed by MD relaxation using the GROMACS package (40,41), to allow the side chains to structurally equilibrate. The final structures are shown in Figure 4.4. Because it is challenging to calculate accurate cross-sections for such complex structures, we used two methods: the trajectory (TJ) method available from the Mobcal package (42,43) and the projected superposition approximation (PSA) method (44,45) (http://luschka.bic.ucsb.edu:8080/WebPSA/). The calculated cross-sections agree reasonably well with each other and with the experimental cross-sections (Table 4.3), especially given the approximate nature of the theoretical structures. We note that the experimental cross-sections of the single-repeat Aβ hexamers and GG tandem-repeat trimers are smaller than the β-sheet-like hexamers ($\sigma > 1098$ Å^2) that were previously observed for the uncapped Aβ(25-35) peptide (23).

The models shown in Figure 4.4 highlight some differences among the peptides. The cylindrins of Aβ(25-35) and GG(25-35) contain less β-secondary structure than other four models due to the lysine residues being positioned inside the cavity. In Aβ(24-34), Aβ(26-36), GG(24-34), and GG(26-36), Asn and Ile are the only two amino acids of each chain that participate in forming the cylindrin core. As a result, the cylindrin core of these four peptides are dry (hydrophobic) whereas those of Aβ(25-35) and GG(25-35) are amphipathic.

Injection energy studies reveal octamers and dodecamers

To verify the existence of single-repeat Aβ hexamers and GG tandem-repeat trimers, we collected IM-MS data on instrument II. Instrument II is better at generating low-charge-state oligomers than instrument I, and thus large oligomers can often be detected. Figure 4.5 shows the n-ESI mass spectra of Aβ(24-34) and GG(24-34) in water obtained from instrument II. The mass spectra of the other peptides are shown in Supplementary Figure 4.16.

One major difference between the mass spectra in Figures 4.2 and 4.5 (and Supplementary Figure 4.16) is the presence of low charge state species ($z < n$) whose ATDs can be recorded using instrument II. Due to the difference in construction, the same oligomers generated from ESI can have different charge states when sprayed from instruments I and II (i.e., large ions generated from instrument II tend to have lower charge states than the same ions generated by instrument I). The mass spectrum of Aβ(24-34) (Figure 4.5A) shows the presence of n/z = 3/2 (1604 *m/z*) and 4/3 (1427 *m/z*) while that of its GG version shows n/z = 2/3 (1644 *m/z*) and 3/4 (1462 *m/z*). It is important to note the species of Aβ(24-34) oligomers having n/z = 3/2 have approximately 0.67 charge per Aβ(24-34) repeat, which is the same as the species of GG(24-34) having n/z = 3/4. Similarly, the n/z = 4/3 species of Aβ(24-34) contains 0.75 charge per Aβ(24-34) repeat, as does the n/z = 2/3 species of GG(24-34). The ATDs are given in Figure 4.6. The overall ATDs of the species with the same charge per Aβ(24-34) are similar, indicating similar oligomer formation in both cases, consistent with the data obtained from instrument I.

A second difference between the data obtained from the two instruments is the ATDs of n/z = 1/1 of Aβ(24-34) (Figure 4.6A) and n/z = 1/2 of GG(24-34) (Figure 4.6D). The largest oligomers detected from these ATDs are only Aβ(24-34) and GG(24-34) dimers. Larger oligomers are not detected at these charge states. However, a hexamer and a dodecamer of Aβ(24-34) are observed at 1604 *m/z* (Figure 4.6C). Similarly, an octamer and another dodecamer are observed at 1427 *m/z*. These large oligomers (i.e., the shorter time features in the ATDs) dissociate into trimers and tetramers, respectively, at high injection voltages (see bottom panels of Figure 4.6).

Similar results were obtained for the GG(24-34) where oligomers as large as hexamers (i.e. stoichiometrically equivalent to an Aß(24-34) dodecamer) are found in the ATDs (see also Supplementary Figure 4.17). The cross-sections of the Aß(24-34) hexamer (σ_{exp} = 1050 Å^2) and octamer (σ_{exp} = 1340 Å^2) are very similar to the cross-sections of the GG(24-34) trimer (σ_{exp} = 1054 Å^2) and tetramer (σ_{exp} = 1343 Å^2). The cross-sections measured on instrument II for the hexamers are somewhat larger than those measured on the more accurate instrument I. Nevertheless, the charge state distributions in the mass spectra and injection studies unambiguously support the presence of hexamer, octamer and dodecamer of Aß(24-34) as well as trimer, tetramer and hexamer of GG(24-34). Large oligomers are also found in the Aß(25-35), Aß(26-36) and their tandem GG versions (see Supplementary Figures 4.18 and 4.19).

A minor, but interesting difference between the data obtained from the two instruments is that the ATD peaks in instrument II appear to better fit the expected single species line width than in instrument I. Since instrument II provides a less gentle condition than instrument I, several metastable structures could be annealed into fewer families of structures during the ion-trapping and injection process.

Segment Aß(21-30) may form stable oligomers

In addition to the three segments described previously, we studied a fourth segment, termed Aß(21-30), and its cognate tandem repeat (Figure 4.7A). This segment is only 10 residues in length, but still contains a central glycine residue like the other segments. It contains three charged residues and thus, is far more soluble than the other segments, which only contain one charged residue.

Consistent with the high solubility of Aβ(21-30), we observe that its cognate tandem repeat GG (21-30) does not form fibrils under the same conditions as the other segments (Figure 4.7B), but it does form oligomers with different stoichoimetries. Like GG(24-34), GG(21-30) elutes as a trimer using SEC and is recognized by A11 (Figure 4.7C).

The mass spectra of Aβ(21-30) and GG(21-30) reveal several major peaks. For Aβ(21-30), we observe namely a sodiated peak of [1+1Na]/2 at 506 m/z (with a less intense, parent peak of n/z 1/1 at 495 m/z), another sodiated peak of n/z [2+1Na]/3 at 667 m/z, and a peak of n/z 1/1 at 988 m/z (Figure 4.7D). Although the experiments are carried out in positive mode ESI, in addition to the presence of sodiated peaks, the monomer cross sections of Aβ(21-30) show no significant difference from those obtained in negative mode ESI (i.e., from this work σ (z = +1) = 219 Å^2, σ (z = +2) = 230 Å^2, and from Murray et al (46) σ (z = -1) = 227 Å^2, σ (theory) = 231 Å^2). For the tandem repeat GG(21-30), two major peaks are observed at 677 m/z (n/z 1/3) and 1016 m/z (n/z 1/2), and two minor peaks at 1219 m/z (n/z 3/5) and 1355 m/z (n/z 2/3). The presence of the peak at 1219 m/z suggests the presence of a hexamer (i.e., the cross-section would be too small if it is assigned as a trimer). The hexamer cross-section is σ = 798 Å^2, which is smaller than the hexamer cylindrin of single strand Aβ(21-30) (σ = 876 Å^2), indicating that the hexamer of Aβ(21-30) is not a cylindrin. However, in light of the SEC and dot blot data, it may form some other oligomer with anti-parallel β-strands.

For Aβ(21-30), the arrival time distributions (ATDs) of the last peak of n/z 1/1 contain multiple species, including monomer and oligomers (Figure 4.7E). The experimental cross-sections obtained from all ATD peaks (including those from the ATDs of n/z 1/1) are compared to those of two structural models: Riek's NMR model of full-length Aβ(1-42) fibrils (47) and Eisenberg's X-ray model of Aβ(16-35) fibrils (48). The theoretical structures of Aβ(21-30) oligomers were extracted from these models, in which Riek's model describes Aβ(21-30) oligomers composed of β-strands, whereas Aβ(21-30) monomers in

Eisenberg's model are turn-like structures, which is similar to what has been found in the Tycko's NMR model of Aβ(1-40) (49). The experimental cross sections show a better match to the Eisenberg's X-ray model, which is also consistent to previous simulations and experimental data indicating that Aβ(21-30) adopts turn-like structure by itself and also in the context of longer fragments (Figure 4.7E, lower panel) (46,49–51).

Cylindrical octamer of amyloid peptides can be formed from anti-parallel β-sheet with a high shear number

Low charge state species observed in instrument II unambiguously support the presence of octamers of the single-repeat Aβ segments (Figure 4.6). In order to elucidate the structure of octamers, a standard MD simulation was performed starting with a pre-built out-of-register (triclinic) antiparallel Aβ(25-35) β-sheet (octamer) (see Figure 4.8 for the starting structure). Of the three single repeat peptides, Aβ(25-35) is more biologically active than either Aβ(24-34) or Aβ(26-36) (33). Furthermore, Aβ(25-35) shows a similar fibril morphology to the full-length protein for both single- and tandem-repeat versions (23,33,34). This peptide also forms the highest populations of octamers and GG tandem-repeat tetramers. Of note, the simulation demonstrates that the cylindrins/β-barrels can be formed from out-of-register β-sheets. Some snapshots obtained from the simulation are shown in Figure 4.8.

There is abundant evidence suggesting that in-register β-sheets are the architecture of the cores of amyloid fibrils (52). Thus the formation of such a β-sheet should favor the formation of amyloid fibrils, rather than a cylindrin, although a cylindrin may have a lower free energy than a β-sheet in general according to Laganowsky et al (13). They also show that unrolling of a cylindrin hexamer yields an antiparallel β-sheet with the shear number S = 6 (i.e., a measure of the stagger of the strands within the sheet) (53) and the mean slope of strands to the central axis of the barrel of 35°. However, we show here by MD simulation that a triclinic antiparallel β-sheet with higher shear number ($S \geq 8$) can fold into a β-barrel that resembles a large cylindrin. A cylindrin can be considered a specific type of β-barrel that exists for small oligomers. These cylindrins and β-barrels can become toxic agents mainly by interacting with cell membranes as proposed by other research groups (54–56). The cross-section obtained from the TJ method is 1355 Å^2 and that from the PSA method is 1205 Å^2, which is very similar to Aβ(25-35) octamer (σ_{exp} = 1320 Å^2) and GG(25-35) tetramer (σ_{exp} = 1314 Å^2) obtained from instrument II.

DISCUSSION

A central question in the assembly of amyloid systems is whether or not there exists a common oligomeric structure, or family of structures, responsible for disease initiation in these systems. This is a very difficult question to address since oligomers in amyloid systems exist in a dynamic and evolving environment that resists study by standard structural methods. Two systems have, however, been shown recently to allow crystal growth and subsequent X-ray analysis of protein segments: The αB-Crystallin and human prion protein amyloid systems (13,20). In both cases cylindrical, hexameric, β-strand structures were observed and, in the case of αB-Crystallin, named a cylindrin (13). However, due to the heterogeneous and dynamic nature of most amyloid systems in solution, it is very difficult to apply these methods broadly to investigate whether cylindrin type structures are common or only occur in select systems. Here we have chosen to apply ion mobility based mass spectrometry, high-level molecular dynamics simulations, and a variety of supporting techniques to this difficult but important problem. IM-MS has been shown to successfully obtain both oligomer distributions and structures in a number of amyloid systems (23,25) and hence is an ideal technique to apply to this problem.

In this paper we have chosen to study three peptide segments of the amyloid β-protein Aβ42 responsible for Alzheimer's disease: Aβ(25–35) and its two nearest neighbors Aβ(24–34) and Aβ(26–36). Aβ(25–35) was chosen as it is known to both exist in the brain and to be cytotoxic while Aβ(24–34) and Aβ(26–36) fulfill known sequence requirements for possible cylindrin formation. We also studied the GG tandem repeats of all three peptides in order to be consistent with the earlier study of the αB-Crystallin segment. The IM-MS data reveal the existence of hexamers in the aggregation cascades of all single-stranded Aβ segments used in this study. The GG linker connecting two Aβ segments head-to-tail stabilizes the GG tandem-repeat trimer, which is the stoichiometric equivalent of a single-repeat Aβ hexamer. Some important conclusions can be drawn from these data:

(1) The experimental cross-sections of the Aβ segment hexamers and the GG tandem-repeats agree with each other and with the cross-sections of cylindrin model structures constructed from the experimental X-ray crystal structure of αB-crystallin peptide. This result suggests that cylindrin formation may be a common event in amyloid systems although further research is needed to verify this suggestion.

(2) The Aβ-segment octamers and corresponding GG tandem-repeat tetramers are also observed. The majority of these structures have cross-sections similar to a β-barrel obtained from the folding of a triclinic anti-parallel β-sheet with a high shear number.

(3) The formation of these cylindrin and β-barrel structures requires a specific kind of β-sheet. Due to a relatively low population *in vitro*, it is difficult for conventional techniques to isolate and characterize these oligomers. IM-MS provides a new approach to search for cylindrin and barrel-like oligomers.

Finally, the results presented here provide important new evidence for structures that may be involved in amyloid disease initiation. However, more research is needed to determine how widespread cylindrin/β-barrel structures are, whether these structures are always toxic, and if they are toxic, what is the mechanism involved.

MATERIALS AND METHODS

Prediction of cylindrin-compatible Aβ segments.

Using ROSETTADESIGN (www.rosettacommons.org), the sequence of Aβ was threaded onto the backbone structure of the hexameric αB-crystallin cylindrin (PDB ID 3SGO). After side-chain repacking, the energy of each 11-residue stretch of Aβ (in the cylindrin conformation) was calculated. C-terminal segments Aβ(24-34), Aβ(28-38) and Aβ(32-42) scored well, that is, they had energies that were lower than that of the native cylindrin sequence (Table 4.1). Each of these segments contains a glycine at position 6, which allows space for packing side chains of the adjacent internal site, position 4. Indeed, mutating glycines in this region to bulky tryptophan residues significantly reduces the cytotoxicity of Aβ1-42 to Neuro-2a cells (Supplementary Figure 4.1). Further manual predictions of cylindrin-compatible segments were made based on having a pattern of internal glycines adjacent to aliphatic residues. Specifically, sequences containing an aliphatic residue at position 6, with glycines at positions 4 and 8, were predicted to have favorable internal packing. Sequences matching this pattern include Aβ(26-36) and Aβ(30-40). In the present work, we chose to study the predicted cylindrin-compatible Aβ(24-34) and Aβ(26-36) segments, the closely related Aβ(25-35) segment, and the GG-linked tandem-repeats of these three segments.

Table 4.1. Sequences and ROSETTADESIGN energies of 11-residue cylindrin-compatible segments.

Protein Segment	Sequence	Rosetta Energy Units
αB crystallin cylindrin	KVKVLGDVIEV	-166.00
Aβ(24-34)	VGSNKGAIIGL	-199.00
Aβ(26-36)	SNKGAIIGLMV	n/a
Aβ(28-38)	KGAIIGLMVGG	-217.88
Aβ(30-40)	AIIGLMVGGVV	n/a
Aβ(32-42)	IGLMVGGVVIA	-205.81

Peptides

All peptides were synthesized by FMOC (N-(9-fluorenyl)methoxycarbonyl) chemistry with acetylated N-termini and amidated C-termini. Dried peptides were dissolved in water or in 20 mM ammonium acetate, pH 7.0, to the final concentration of 50-100 μM. The samples were incubated at room temperature for 24 hours to one week.

Recombinant expression and purification of tandem-repeat constructs

In addition to the synthetic forms of the GG-linked tandem-repeat peptides, we also used recombinantly expressed forms. The recombinant forms were used for the size exclusion chromatography (SEC) and dot blot studies, in addition to other biochemical studies not included in the published article. The recombinant expression largely followed the protocol from Laganowsky, *et al.* (13).

The DNA sequences of the tandem-repeats were generated using PCR-based gene synthesis. Primers were designed using DNA Works. The PCR product was cloned into a pET15-MBP expression vector between Sac1 and Xho1 restriction sites. The construct encodes a 6xHis-tagged maltose-binding protein (MBP) followed by a tobacco etch virus (TEV) protease cleavage site and the tandem-repeat (TR) (Supplementary Figure 4.2A). The plasmid was transformed into BL21 (DE3) Gold cells for plasmid amplification and recombinant expression.

For recombinant expression, a single colony was used to inoculate a 100 mL starter culture, which was allowed to grow overnight in the presence of ampicillin. The following day, 75 mL of the culture was used to inoculate three 1 L flasks of LB and ampicillin. The E. Coli was grown to OD_{600} 0.7 and then induced with 0.5 mM IPTG for 4 hours at 32°C. Next, the E. Coli were pelleted with centrifugation and washed pellets were stored at -20°C until needed.

For purification, the pellets were thawed and resuspended in 20 mL of Native Wash buffer (50 mM Sodium Phosphate pH 8, 300 mM NaCl, 20 mM imidazole) and then 400 µL of HALT protease inhibitor cocktail was added. The resuspended pellet was sonicated for 3 minutes (5 seconds on, 2 seconds off) with the temperature probe set to 18°C. Next, the lysate was centrifuged at 15,500 rpm for 30 minutes at 4°C. The supernatant was then filtered and applied to a 2x 5 mL HisTrap-HP column (GE Healthcare). The column was washed with three column volumes of Native Wash buffer, at then the MBP-fusion was eluted in a steep gradient into Native Elution buffer (50 mM Sodium Phosphate pH 8, 300 mM NaCl, 500 mM imidazole) (Supplementary Figure 4.2B).

The fractions that contained the MBP-fusion protein were pooled at then dialyzed into TEV cleavage buffer (20 mM tris pH 8, 150 mM NaCl, 20 mM imidazole) for 2 hours at room temperature. A stock of His-tagged TEV protease (3 mg/mL) was added to the MBP-fusion at 1:50 (v:v). Aliquots of the reaction were taken intermittently to monitor the level of TEV cleavage (Supplementary Figure 4.2C). After the reaction was complete, the solution was passed over the 2x 5 mL HisTrap-HP column to separate the MBP and TEV from the tandem-repeat, which came out in the flow-through (Supplementary Figure 4.2C).

Last, the tandem-repeat was further purified by reverse phase high performance liquid chromatography (RP-HPLC) on a heated 2.2 x 25 cm Vydac 214TP101522 column equilibrated in buffer A (0.1% trifluroacetic acid (TFA)/water) and eluted over a linear gradient from 0% to 100% buffer B (Acetonitrile/0.1% TFA) in 40 minutes at a flow rate of 9 mL/min. Absorbance at 220 nm and 280 nm were recorded using a Waters 2487 dual λ absorbance detector (Waters, Milford, MA) (Supplementary Figure 4.2D). We assessed the purity of collected fractions using MALDI-TOF mass spectrometry (Voyager-DE-STR, Applied Biosystems, Carlsbad, CA). Pure pooled fractions were frozen in liquid nitrogen and lyophilized. Dried peptide powders were stored in desiccant jars at -20°C.

Ion-mobility mass spectrometry

In IM-MS, species at the m/z (m = mass, z = charge) with either different conformations or different n/z (n = oligomer number, or number of monomer subunits) can be separated by measuring arrival time distributions (ATDs). In these experiments, ions are generated from solution by nano-electrospray ionization (n-ESI), captured by an ion funnel and then pulsed, via a 'drift voltage', into a drift cell filled with helium gas. Species with larger charge are 'pushed' harder by the drift voltage and fly faster than species with smaller charge. In contrast, species having the same charge state but a larger shape will collide with helium atoms more frequently, and be slowed to a greater degree, than species with smaller shape. Upon exiting the drift cell, the species of interest are selected by a mass analyzer (at a specific m/z value) and passed on to the detector. The ATDs of these species (at a specific m/z value) are measured with the pulse occurring at time $t = 0$ and the arrival at the detector occurring at time t_A. By measuring ATDs at different pressure-to-drift-voltage ratios (*P/V*), mobility K_0 can be measured (57), and the cross-section σ can be calculated (see Eq. 4.1) (58). These cross-section values are independent of instrumental parameters and can be compared with cross-sections generated from theoretical structures.

$$\sigma \approx \frac{3q}{16N}\left(\frac{2\pi}{\mu k_B T}\right)^{\frac{1}{2}}\frac{1}{K_0} \ (Eq. 4.1)$$

Here, N is the buffer gas number density, μ is the reduced mass of the collision system (ion + helium), k_B is Boltzmann's factor and T is the drift cell temperature. The flux of ions exiting the drift tube can be calculated. It is assumed that the ion packet takes the form of a periodic delta function and the flux is given by Eq. 4.2.

$$\varphi(0,z,t) = \frac{s \cdot a \cdot e^{-\alpha t}}{4(\pi D_L t)^{1/2}} \cdot \left(v_d + \frac{z}{t}\right) \cdot \left[1 - e^{\left(-r_0{}^2/_{4D_T t}\right)}\right] \cdot e^{\left(-(z-v_d t)^2/_{4D_{L}t}\right)} \ (Eq. 4.2)$$

Where z is the distance the ion travels, r_0 is the radius of the intial ion packet, a is the area of the exit aperture, D_L and D_T are the longitudinal and transverse diffusion coefficients, s is the initial ion density and α is the loss of ions due to the reactions in the drift tube (57). The line shape generated from Eq. 4.2 would correspond to that of an ion packet composed of a single ion conformation. Experiment line shapes broader than this limit indicate more than one conformation is generating the experimental peak.

Here we use two different IM-MS instruments with somewhat different capabilities, for reasons described below:

Instrument I. This lab-built instrument (59) consists of an n-ESI source, an ion funnel, a 200-cm-long drift cell, and a quadrupole mass filter. The long drift cell allows for good separation of oligomers of different sizes.

Instrument II. This instrument is similar to instrument I, except with a shorter, 5.0-cm-long drift cell (60). The injection voltages on this instrument can be manually controlled, so it is possible to perform injection energy studies on this instrument. In brief, by gradually increasing the injection energy applied to the ions, larger, less-stable oligomers can be broken apart into smaller, more-stable oligomers (36). This method is useful in determining the oligomer-charge ratios (*n/z*) of features in the ATDs that contain multiple peaks. In addition, this instrument can detect oligomers with lower charge states than instrument I, which is useful for a more-detailed investigation of large oligomers and their conformations.

Microscopy

Atomic force microscopy (AFM) and transmission electron microscopy (TEM) images were collected for peptide samples incubated in water. Detailed descriptions of these techniques have been given previously. To prepare Aß peptides for TEM, a drop of sample (no fixation) was placed on a 300-mesh Formvar/carbon-coated copper grid (Electron Microscopy Sciences) and allowed to absorb for 1.5 min. After this time, excess sample was wicked away, and the grid was rinsed with deionized water and then negatively stained with 2% uranyl acetate (Ted Pella) for 1 min. Microtubule samples were prepared similarly, except that they were fixed with 0.2% glutaraldehyde prior to placement on 200-mesh grids, grids were coated with 1 mg/mL cytochrome C prior to the deionized water rinse, and stained with 1.5% uranyl acetate for 20 s. All grids were viewed on a JEOL-1230 TEM microscope at 80 kV. An ORCA camera and AMT Image Capture Software (version 5.24) was used to acquire digital images.

For time course TEM experiment in sodium phosphate buffer (20mM, pH = 7), peptides were imaged at t = 0 and t = 144 h. At each time point, 10 µL of peptide (20 µM), was spotted onto a carbon-coated Formvar grid (Electron Microscopy Sciences, Hatfield, PA) and incubated for 2 min. The droplet then was displaced with an equal volume of 1% (w/v) filtered (0.2 µM) uranyl acetate in water (Electron Microscopy Sciences). This solution was wicked off and then the grid was air-dried. Sample grids were examined using a JEOL 1200

EX transmission electron microscope with an accelerating voltage of 80 kV. Digital images were analyzed with ImageJ 1.43r, using the "measure tool" to calculate dimensions.

AFM images were collected using an Asylum MFP-3D-SA system (Asylum Research, Santa Barbara, CA). A silicon cantilever (MikroMasch NSC-15) with nominal resonant frequency of 325 kHz and spring constant of 40 N/m was employed in tapping mode. The cantilever was tuned to the resonant frequency at a voltage of 1 V, corresponding to a ~50 nm free amplitude. An amplitude set point ratio (R/R0) of 75–80% was used to achieve optimal height tracking as well as to keep the tip in attractive mode (phase >90°). All images were collected at 1 Hz using 512 × 512 scan points. Images were processed using Igor Pro software and were modified by masking fibrils and then applying a first-order flatten to the height and phase images ("Magic Mask" in MFP3D software). No further image modification was used.

Microtubule Preparation

Purified tubulin (15 µM) and tau (0.5 µM) were incubated for 60 min at 37°C in 80 mM Pipes, pH 6.8, 1 mM EGTA, 1 mM MgSO4, 0.1% B-mercaptoethanol, and 1 mM GTP.

Gel-filtration/size exclusion chromatography

Aβ segments were analyzed with Size Exclusion Chromatography (SEC) using a Superdex 30/100 peptide column (GE Biosciences). Lyophilized peptide was dissolved in Amyloid Buffer (15 0mM HEPES pH 7.4 and 150 mM NaCl) at 5 mg/mL. The dissolved peptide was filtered with a 0.1 µm spin filter, and then 500 µL was injected onto the column. The experiment was performed using an AKTA (GE Life Sciences) at 4°C. We used a flow rate of 0.3 mL/min in Amyloid Buffer. Absorbance was monitored at 220 nm.

Dot blot assay

Oligomeric preparations of Aβ peptides were made by dissolving lyophilized peptide at 5mg/mL in Amyloid Buffer, and then filtered with a 0.1 µm spin filter. Fibrillar preparations of Aβ peptides were made by resuspending lyophilized peptide at 20 µM in Amyloid Buffer. Fibrillar samples were shaken at 37°C for several days and fibrillation was detected by monitoring Thioflavin-T (ThT) fluorescence. 2 µL of each sample was gently spotted onto a nitrocellulose membrane and left to dry. The membrane was blocked with 10% milk in TBS-T, and probed with A11 antibody (1:500 in 5% milk in TBS-T, Millipore). The membrane was washed with TBS-T three times, and then probed using an anti-rabbit IgG antibody (BioRad). The membrane was washed three times with TBS-T. The signal was developed using a SuperSignal kit (ThermoScientific) and exposed to film for 5 minutes.

Thioflavin-T (ThT) Assay

Peptides were dissolved in 1, 1, 1, 3, 3, 3-hexafluoroisopropanol (HFIP) at 4°C, at a concentration of 500 µM, and then sonicated for 5 min at room temperature (22.5 °C) in a bath sonicator (Branson Model 1510, Danbury, CT). The tubes containing the peptide solutions were then incubated at room temperature for 30 min and left uncovered in a fume hood overnight to evaporate. Following this overnight incubation, complete removal of HFIP was effected by vacuum evaporation for 1 h in a Speed-Vac concentrator (Thermo Scientific, Savant SPD121P). For ThT experiments, the peptide films were solvated with a 1:4.5:4:5 (v/v) mixture of 60 mM NaOH:Milli-Q water:22.2 mM sodium phosphate, pH 7.4. The peptide solution then was sonicated for 1 minute to yield a final peptide concentration of 25 µM in 10 mM sodium phosphate, pH 7.4. ThT assays were done by co-incubation of peptides (20 µM final concentration) with ThT (60 µM final concentration) at 37 °C in 96-well microtiter plates (Thermo Scientific, Rochester, NY) with 160 rpm orbital shaking. Fluorescence intensities (Synergy HT fluorometer; BioTek, Beijing, China) were measured immediately after sample preparation and then periodically for up to two weeks thereafter.

Excitation and emission wavelengths were 420 and 485 nm, respectively, with slit widths of 10 nm in each case. At least three independent experiments were done for each sample. GraphPad Prism was used for graphing and analysis.

Molecular dynamics (MD)

All simulations utilized explicit solvent and the OPLS-AA force field.4-6 OPLS-AA is considered a suitable force field for Aß peptide simulations (61). Larini and Shea have used this force field for the simulations of the free terminal Aß(25-35) oligomers (37). The initial conformation was solvated in a TIP3P water box (62). Negatively charged Cl atoms were added to neutralize the overall charges of the peptides. All simulations were carried out using the GROMACS-4.5.5 software (40,41). During the simulations, covalent bonds in the water molecules were held constant using the SETTLE algorithm (63). Intra-peptide bonds involving hydrogen atoms were constrained according to LINCS protocol (64) allowing a 2 fs simulation time step. Non-bonded Lennard-Jones interactions had a 12 A° cut-off. Neighbor lists for the non-bonded interactions were updated every 10 simulation steps. Electrostatic interactions were included using the particle mesh Ewald (PME) approach (65,66). Temperature was controlled by the Nose- Hoover algorithm16 with a 0.1 ps time constant.

Replica exchange molecular dynamics (REMD)

The simulations started with random conformations in which the peptides were capped using N-terminal acetylation and C-terminal amidation. Preliminary simulations were performed for 5 to 10 ns in NPT ensemble to preequilibrate the box volume. Another 5 to 10 ns of equilibration in NVT ensemble at T = 300 K followed. The temperature range was from 280 K to 420 K, increasing exponentially. The temperature scheme was sufficiently broad to allow conformations to quickly escape local minima at high temperature without possibility of chirality conversion. In the first stage, the replicas were run at the different temperatures without any exchange for 5 ns. The production run followed with attempted exchanges happening every 3 ps. The exchange rate was 25-30%. The production run continued for 300 ns, where the first 100 ns were considered as additional equilibrium and the last 200 ns were used for analysis.

Standard molecular dynamics (MD)

Standard MD simulation was performed to examine the folding of anti-parallel free terminal Aß(25-35) ß-sheet in which every consecutive peptide chain was continuously shifted by two residues in order to obtain a high shear number (i.e., triclinic ß- sheet) (54). The initial structure was solvated in 2460 nm^3 cubic water box with additional counter ions to neutralize the charge. System minimization was performed in NPT ensemble for 3 ns, followed by 42 ns of NVT simulation to observe the folding of the initial structure into a ß-barrel.

Circular dichroism (CD) spectroscopy

CD spectra of peptides were acquired immediately after sample preparation and following 16, 44, 68, 82, 104, 130, and 144 h of incubation. 20 µM of each peptide was incubated in 1 mm path length quartz cuvettes (Hellma, Forest Hills, NY) at 37°C. CD spectra were acquired with a J-810 spectropolarimeter (JASCO, Tokyo, Japan). Spectra were recorded at 22°C from 195–260 nm at 0.2 nm resolution with a scan rate of 100 nm/min. Ten scans were acquired and averaged for each sample.

Modeling of Aß(25-35) steric zippers

In order to obtain the steric zipper model of Aß(25-35), the residues 22 to 24 in each peptide strand within the steric zipper of Aß(22-35) (48) were manually removed. The acetylated and amidated termini were added to each strand by first adding a glycine to each zwitterionic terminus using the Swiss PDB viewer program. Atom coordinates of the glycine backbone were then used to construct the acetyl (ACE) and amide (NHE) residues using the tleap module available in the Amber 12 package. Finally, the structure was subjected to a short minimization.

3-(4,5-dimethylthiazol-2-yl)-2,5-diphenyltetrazolium bromide (MTT) dye reduction assay for cell viability

Nuero2a (N2a) cells were a gift from the Pop Wongpalee in the laboratory of Douglas Black at UCLA. Cells were cultured in MEM media (Cat. # 11095-080, Life Technologies) plus 10% heat-inactivated fetal bovine serum and 1% pen-strep (Life Technologies). Cells were cultured at 37°C in 5% CO_2 incubator.

N2a cells were plated at 20,000 cells per well in 90 µL in clear 96-well plates (Cat. # 3596, Costar, Tewksbury, MA) and allowed to adhere to the plate overnight. The next day, Aβ samples were diluted appropriately and then 10 µL of sample was applied to N2a cells at specified concentrations.. By doing this, samples were diluted 1/10 from *in vitro* stocks. Experiments were done in triplicate. After a 24-hour incubation, 20 µL of Thiazolyl Blue Tetrazolium Bromide MTT dye (Sigma, St. Louis, MO) was added to each well and incubated for 3.5 hours at 37°C under sterile conditions. The MTT dye stock is 5 mg/mL in Dulbecco's PBS. Next, the plate was removed from the incubator and the MTT assay was stopped by carefully aspirating off the culture media and adding 100 µL of 100% DMSO to each well. Absorbance was measured at 570 nm using a SpectraMax M5. A background reading was recorded at 700 nm and subsequently subtracted from the 570 nm value. Cells treated with vehicle alone (PBS+0.1%DMSO) were designated at 100% viable, and cell viability of all other treatments was calculated accordingly.

ACKNOWLEDGEMENTS

The authors thank Dr. Nicholas Economou and Prof. Steven Buratto at UCSB for the microscopy data and Ms. Margaret Condron at UCLA for synthesizing the peptides. We gratefully acknowledge support from the National Science Foundation grant CHE-1301032 for personnel support, the Air Force Office of Scientific Research grant FA9550-11-0113 for instrumental support, and the National Institutes of Health grant 1RO1AG047116-01 for material support and partial personal support. We acknowledge support from the Center for Scientific Computing from the CNSI and MRL: an NSF MRSEC (DMR-1121053) and NSF CNS-0960316.

COMPETING INTERESTS

The authors declare no competing financial interest.

metal-binding CHC

Aβ(1-42): DAEFRHDSGYEVHHQKLVFFAEDVGSNKGAIIGLMVGGVVIA
Aβ(24-34): Ac-VGSNKGAIIGL-NH$_2$
Aβ(25-35): Ac-GSNKGAIIGLM-NH$_2$
Aβ(26-36): Ac-SNKGAIIGLMV-NH$_2$

GG(24-34): **Aβ(24-34)-GG-Aβ(24-34)**
GG(25-35): **Aβ(25-35)-GG-Aβ(25-35)**
GG(26-36): **Aβ(26-36)-GG-Aβ(26-36)**

Scheme 4.1. Primary structures of Aβ(1-42), Aβ(24-34), Aβ(25-35), Aβ(26-36) and their tandem repeats. The postulated metal-binding region and the central hydrophobic core are annotated. The sequence common to all three peptides is colored red. Methionine in the peptide segments is colored green.

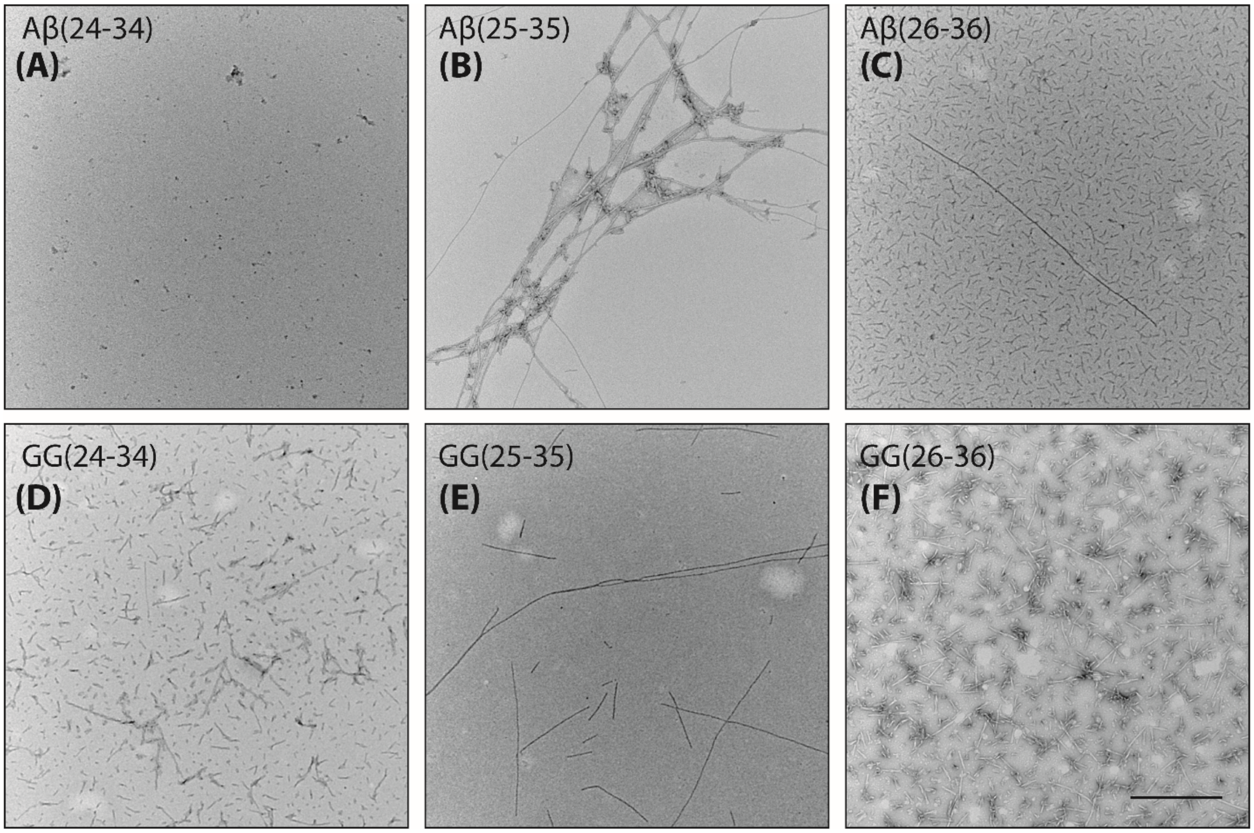

Figure 4.1. Representative TEM images of peptides incubated at 150 μM in water for one week. The scale bar is 100 nm.

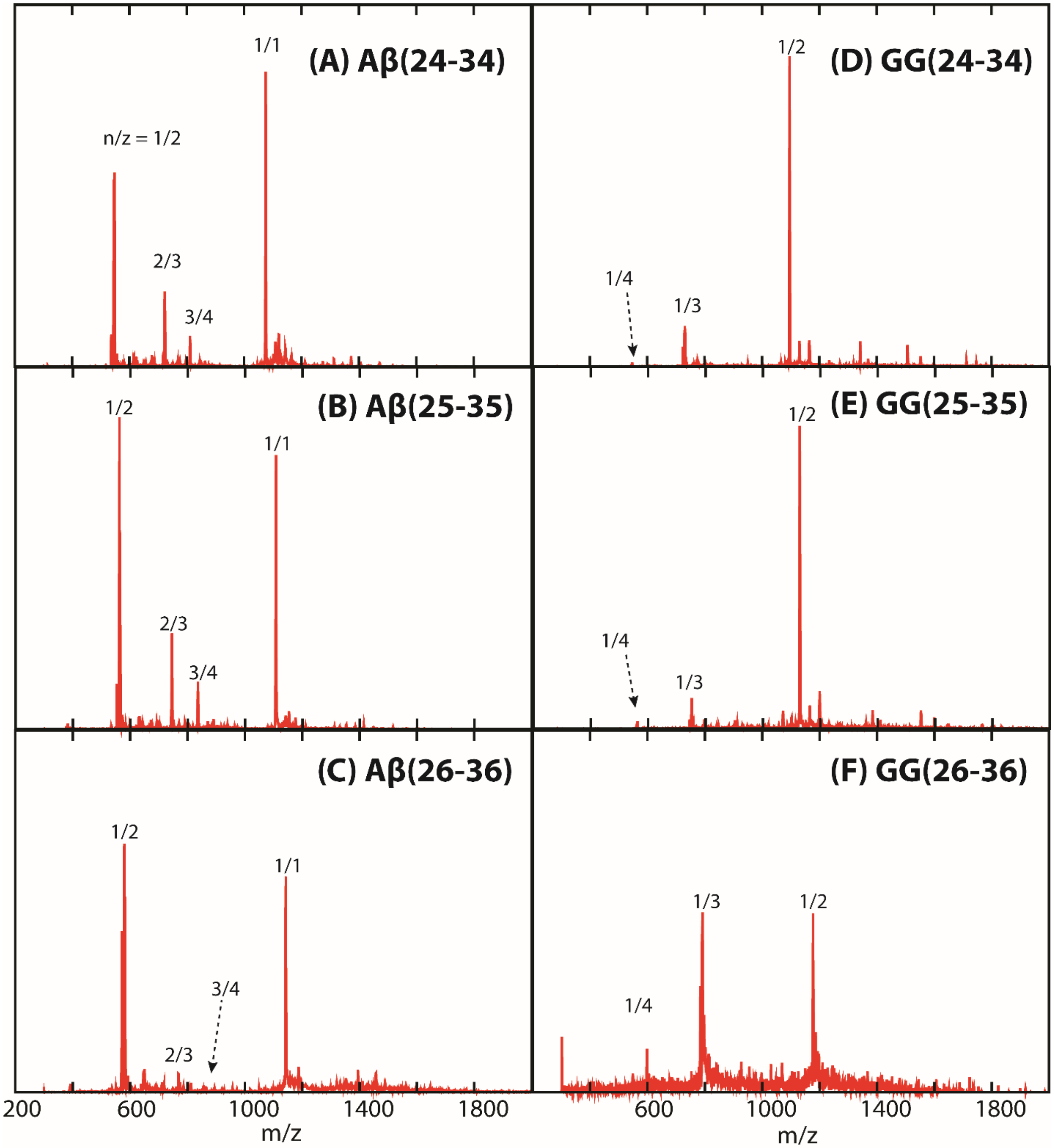

Figure 4.2. n-ESI-quadrupole mass spectra of Aβ(24-34), Aβ(25-35), Aβ(26-36) and their GG tandem repeats. Each mass spectral peak is annotated with an *n/z* ratio where *n* is oligomer size or order and *z* is charge. We used a peptide concentration of 100 μM for these studies.

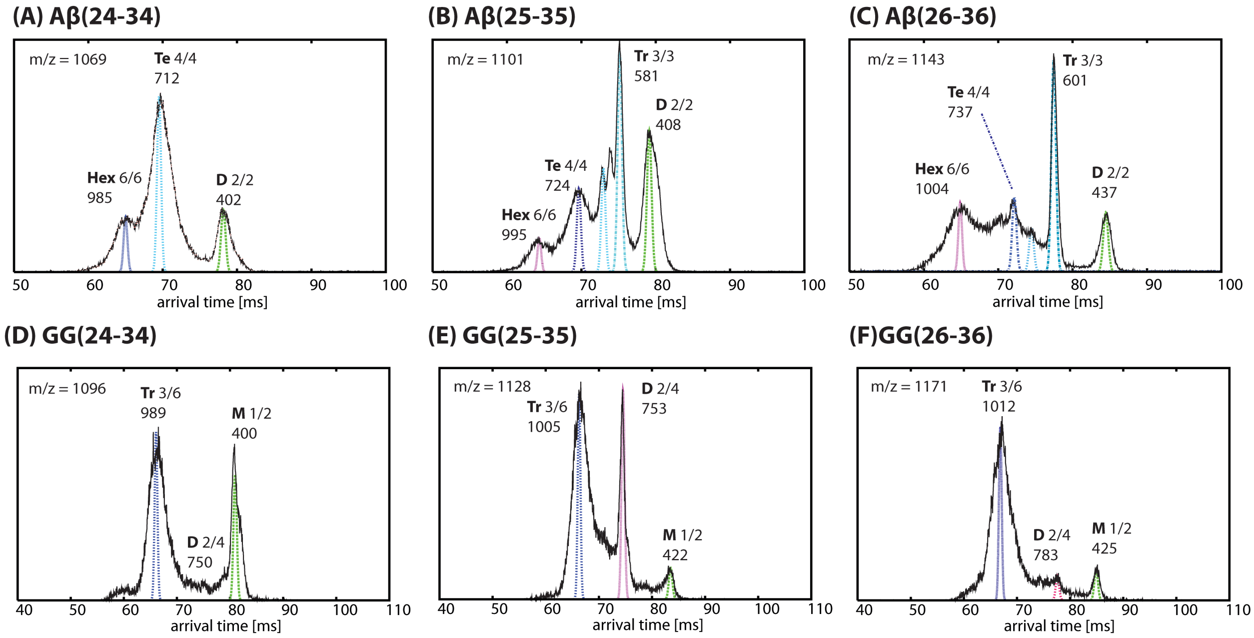

Figure 4.3. Representative arrival time distributions (ATDs) of the natural charge state (one charge per monomer) peaks of Aβ(24-34), Aβ(25-35), Aβ(26-36) and their GG versions obtained from instrument I. Each feature is labeled with oligomer size (M = monomer, D = dimer, Tr = trimer, Te = tetramer, Hex = hexamer), *n/z* ratio and experimental cross-section σ in Å^2. The narrow dashed lines are the peak shapes predicted for a single conformer of the cross-sections given in the Figure. The ATD features are broader than the predicted shape for a single conformer, suggesting there are multiple families of structures with similar cross-sections. The cross-sections listed above the peaks and in the Table 4.2 are of these dotted line peaks. We used a peptide concentration of 100 μM for these studies.

Table 4.2. Experimental cross-sections (σ, Å^2) of single-repeat Aβ and GG tandem-repeat oligomers.

Oligomer	Aβ(24-34)	Oligomer	GG(24-34)
Dimer	402	Monomer	400
Tetramer	712	Dimer	750
Hexamer	985	Trimer	989
Oligomer	Aβ(25-35)	Oligomer	GG(25-35)
Dimer	408	Monomer	422
Tetramer	724	Dimer	753
Hexamer	995	Trimer	1005
Oligomer	Aβ(26-36)	Oligomer	GG(26-36)
Dimer	437	Monomer	425
Tetramer	737	Dimer	782
Hexamer	1004	Trimer	1012

Table 4.3. Experimental and theoretical cylindrin cross-sections (σ, Å^2) of the hexamers of Aβ(24-34), Aβ(25-35) and Aβ(26-36) and the trimers of GG(24-34), GG(25-35) and GG(26-36). The cross-section data are from instrument I. The theoretical cross-sections were calculated using the trajectory (TJ) (42,43) and the projected superposition approximation (PSA) (44,48) methods.

Peptide	Aβ(24-34)	Aβ(25-35)	Aβ(26-36)	GG(24-34)	GG(25-35)	GG(26-36)
σ_{EXP} (Å^2)	985	995	1004	989	1005	1012
σ_{TJ} (Å^2)	1038	1041	1074	1058	1067	1101
σ_{PSA} (Å^2)	901	949	942	938	974	965

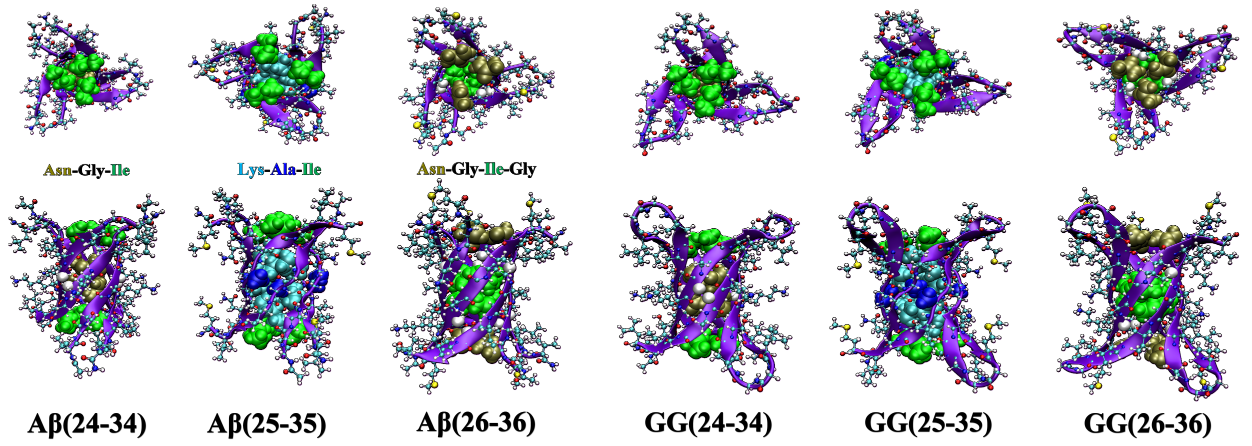

Figure 4.4. Cylindrin models of single-repeat Aβ hexamers and tandem-repeat GG trimers. Each peptide chain is shown as a violet β-strand. The side chains inside the cylindrin cavities are shown in space filling representation in green.

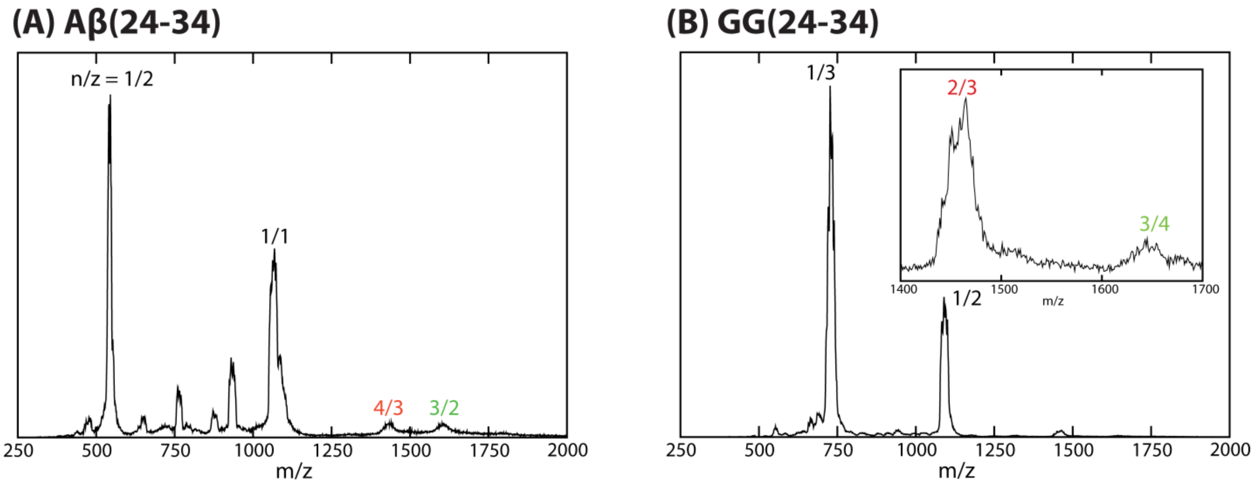

Figure 4.5. n-ESI-quadrupole mass spectra of **(A)** Aβ(24-34) and **(B)** GG(24-34). Each mass spectral peak is annotated with *n/z* ratio where *n* is oligomer size and *z* is charge. The peptide concentration is 50 μM.

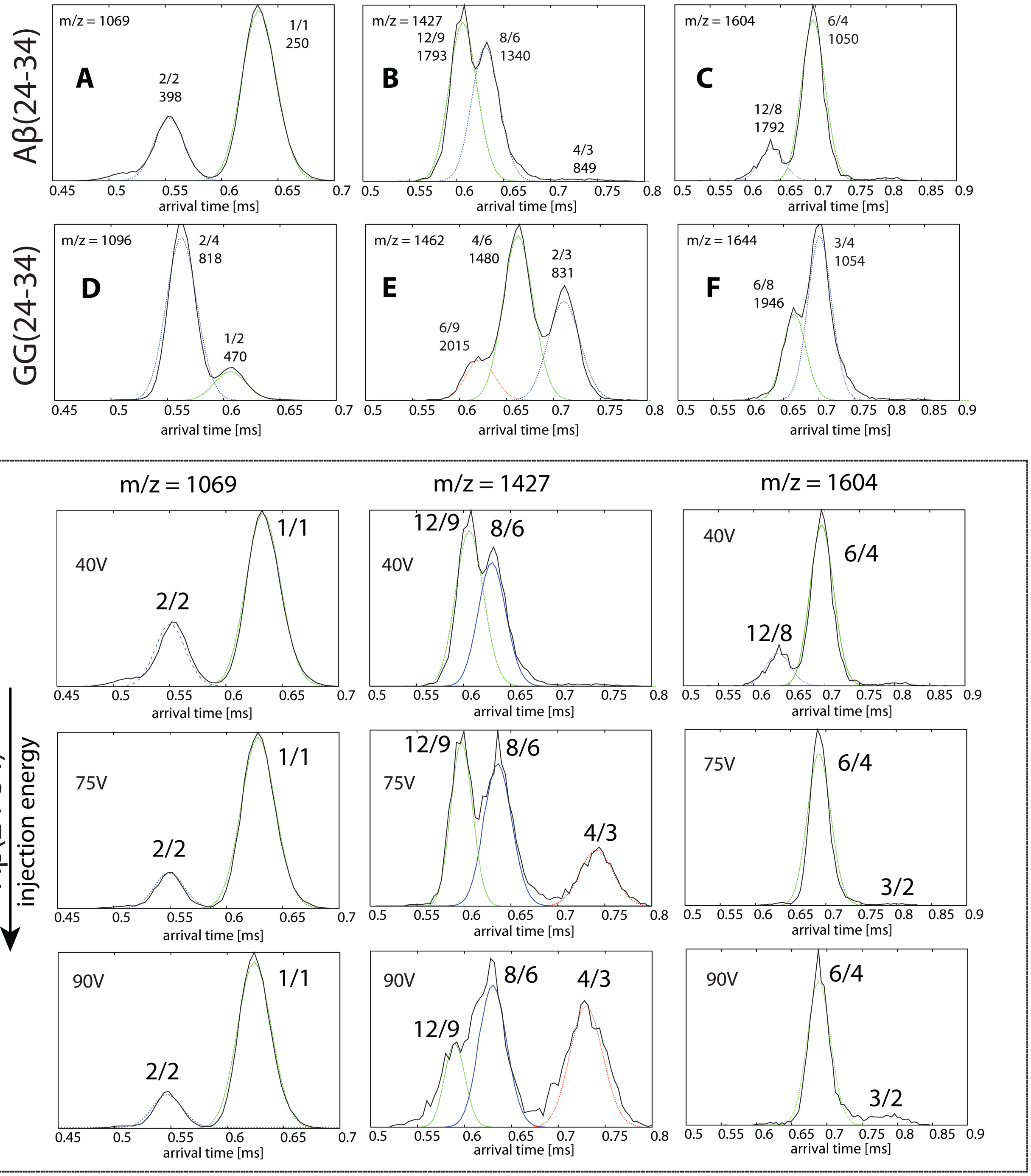

Figure 4.6. (Top panel) Representative arrival time distributions (ATDs) of the *n/z* = 1/1, 4/3 and 3/2 peaks of Aβ(24-34), and 1/2, 2/3 and 3/4 of its GG tandem version. The features in the ATDs of the low charge state peaks are assigned based on injection energy studies. Each feature is annotated with *n/z* ratio and experimental cross-section σ in Å^2. The narrow

dashed lines are the peak shapes predicted for a single conformer of the cross-sections given in the Figure. The peptide concentration is 50 μM. (Bottom panel, in box) Representative ATDs illustrating the injection energy studies for Aβ(24-34).

A **Aβ1-42** 1-DAEFRHDSGYEVHHQKLVFFAEDVGSNKGAIIGLMVGGVVIA-42

Aβ21-30 Ac-AEDVGSNKGA-NH_2
GG(21-30): Aβ21-30-GG-Aβ21-30

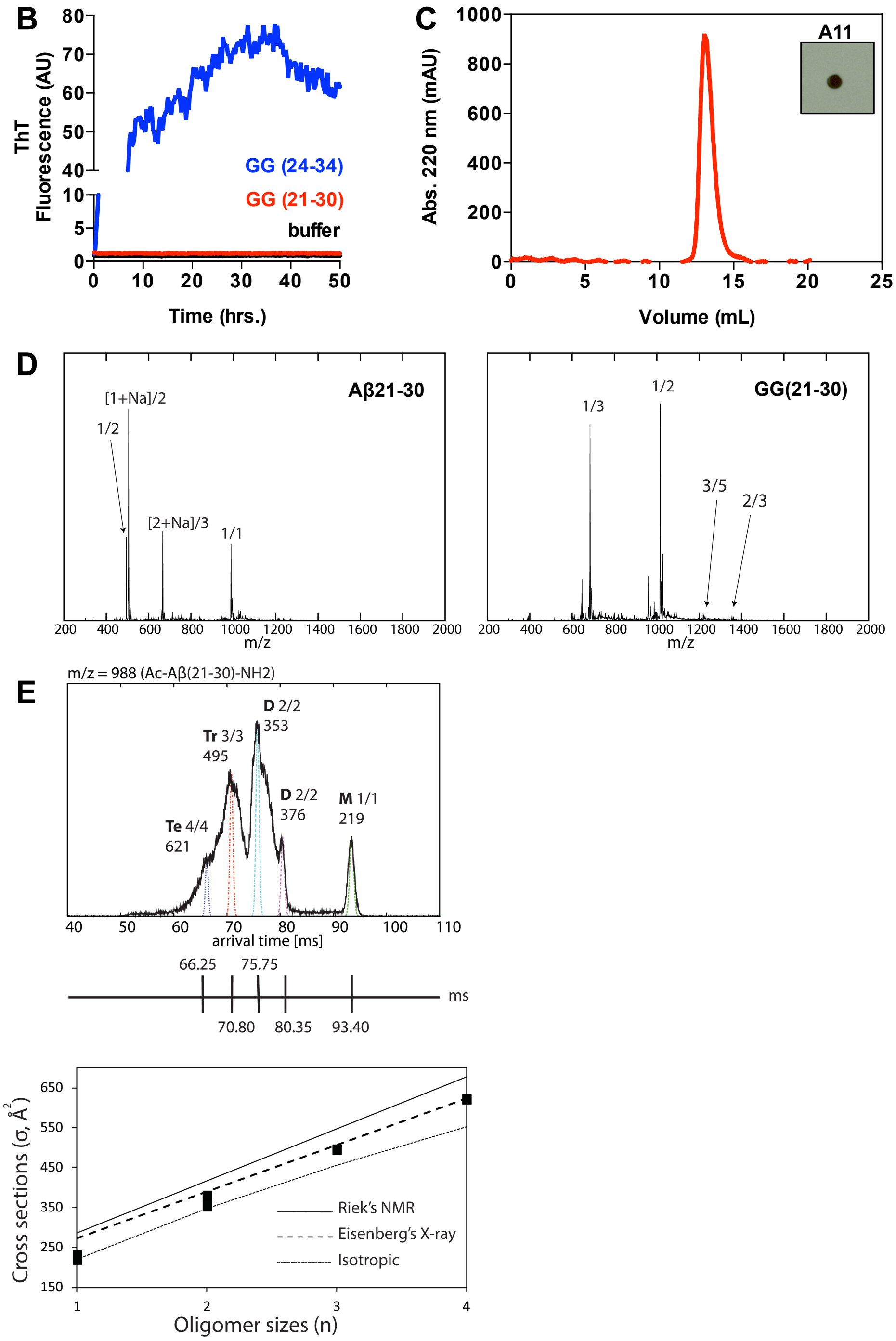

Figure 4.7. Segment Aβ(21-30) may form stable oligomers. A. Schematic illustrating where the sequence of Aβ(21-30) falls within the sequence of full-length Aβ 1-

42. GG(21-30) refers to its cognate tandem repeat. **B.** GG(21-30) does not form fibrils under the same conditions as the other segments. The fibril formation propensity of GG(24-34) is shown as a positive control. **C.** GG(21-30) forms an A11-positive oligomer (inset) than elutes as a trimer using size exclusion chromatography (SEC). **D.** The mass spectra of Aß(21-30) and GG(21-30) at 250 μM in water. **E.** The representative ATD of 988 m/z with features annotated by n/z values and the experimental cross sections (top). The experimental cross sections are compared to three theoretical models as described in the text (bottom).

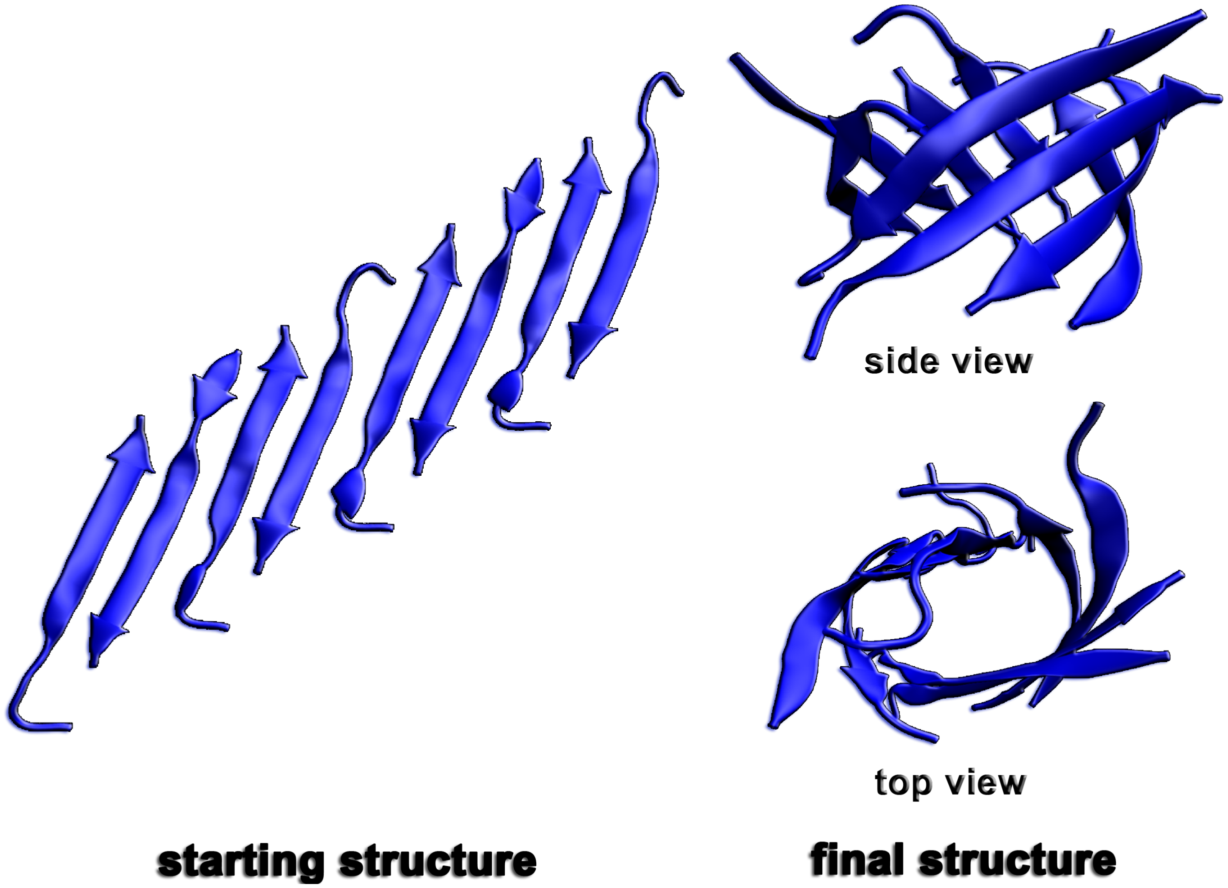

Figure 4.8. Initial and final structures of Aβ(25-35) octamers obtained from standard explicit solvent MD simulation.

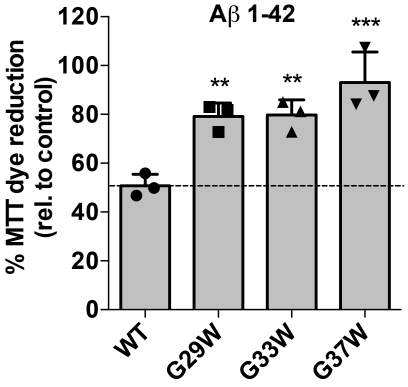

Supplementary Figure 4.1. Mutating glycines in the cylindrin-predicted region of Aβ 1-42 to tryptophans reduces Aβ 1-42 cytotoxicity to Neuro-2a cells, a mouse neuroblastoma cell line. Each sample of **Aβ** 1-42 was added to cells at 0.5 μM final concentration and cytotoxicity was quantified using MTT dye reduction. Dashed line shows mean cytotoxicity of **Aβ** 1-42 wild-type (WT) (*n* = 3; **, $p < 0.01$; ***, $p < 0.001$ using an ordinary one-way ANOVA).

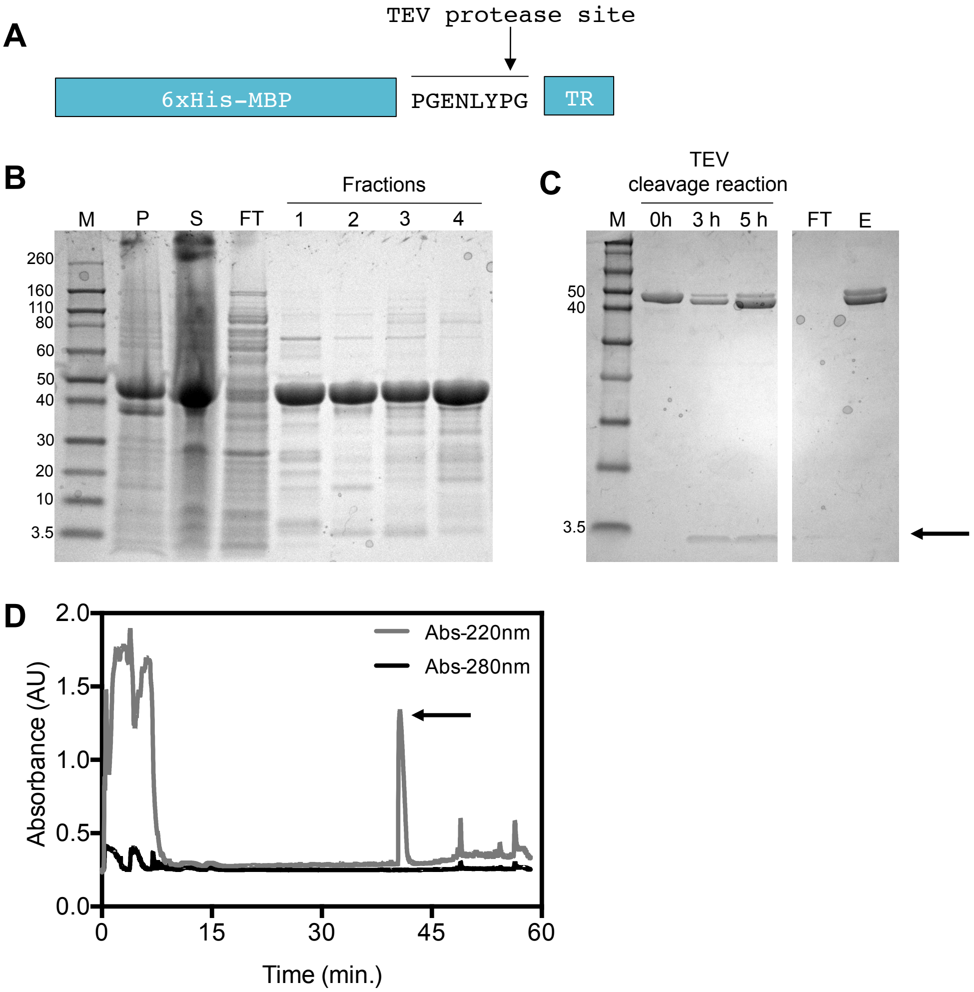

Supplementary Figure 4.2. Recombinant expression and purification of tandem-repeat constructs. A. Cartoon of designed protein construct. A DNA sequence encoding a 6x-His-tagged maltose-binding protein (6x-His MBP) with a C-terminal TEV cleavage site was ligated next to a DNA sequence encoding the tandem-repeat (TR). After protein expression and preliminary purification, the TR was removed from the MBP with TEV cleavage, leaving a N-terminal glycine on the TR. **B.—D.** show steps from purification of GG (24-34) purification, even though all tandem-repeats were purified in an identical manner. **B.** Representative gel of samples from steps of preliminary protein purification. Although some of the protein was insoluble, most of it was soluble. (P = pellet; S =

supernatant; FT = flow-through from nickel (Ni) column; Fractions 1-4 = fractions from Ni column purification. All were pooled and used for subsequent purification.) **C.** Representative gel of products from TEV cleavage reaction. After 5 hours at room temperature, the reaction was mostly complete and thus stopped. The reaction was then flowed over a Ni column and the flow-through (FT), which contains the TR, was collected. The eluate (E) contains the MBP-fusion and TEV protease. Arrows indicate cleaved TR. **D.** Representative chromatogram of reverse-phase HPLC purification of the TR. Arrow points to peak of TR.

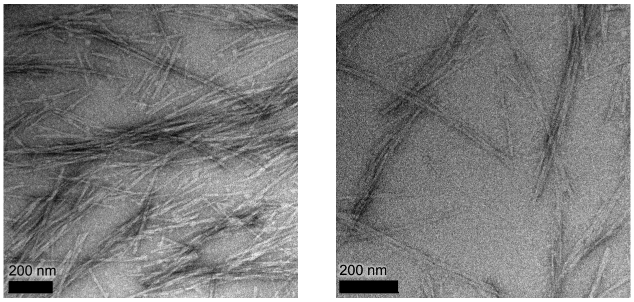

Supplementary Figure 4.3. Electron micrographs of fibrils of GG(24-34) formed after a week-long incubation in PBS. Scale bars are 200 nm.

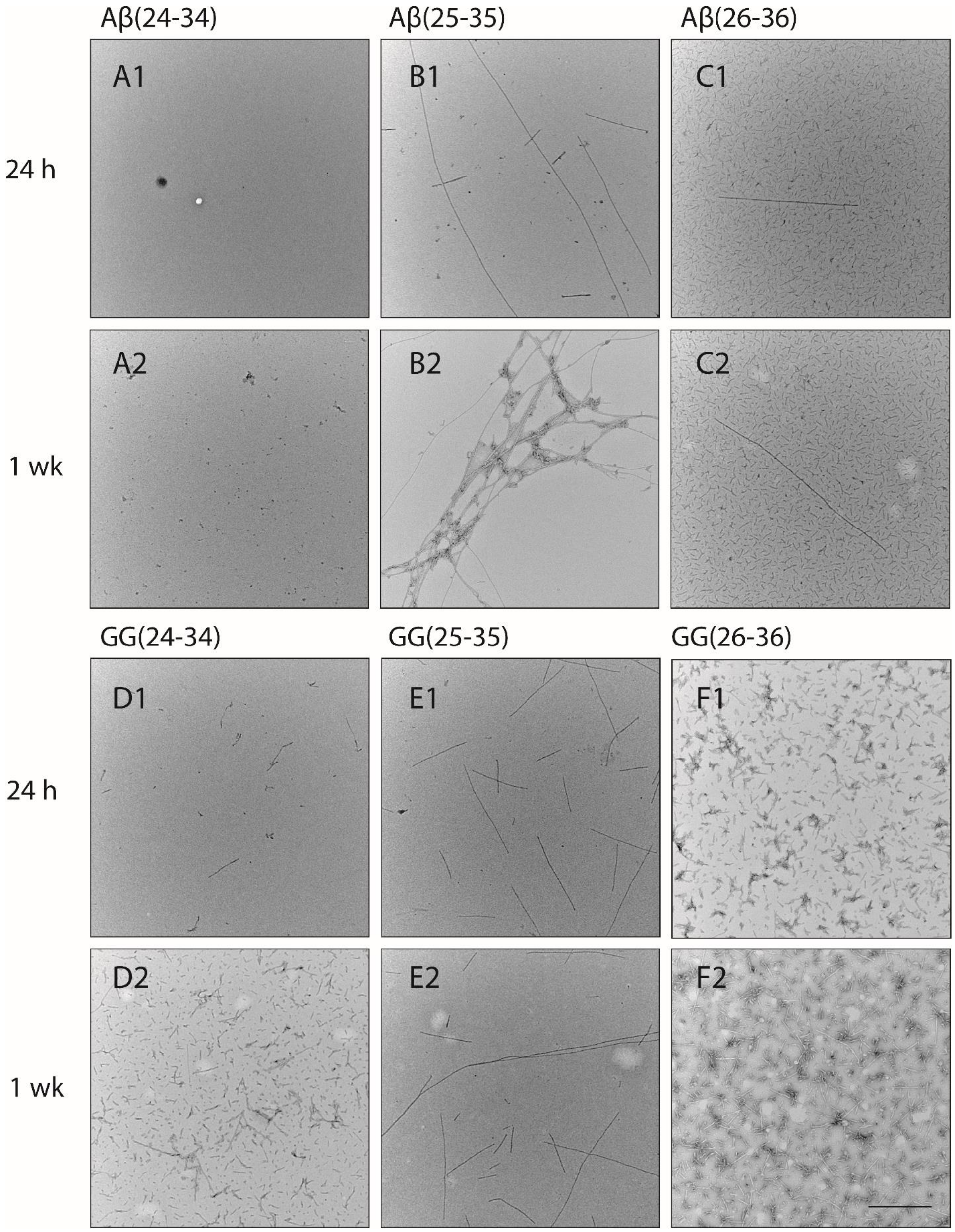

Supplementary Figure 4.4. Time-course TEM images of the Aβ segments and GG tandem repeats after 24- hour and one-week incubation in water at room temperature. The TEM images of Aβ(24- 34) show many small aggregates only after one-week incubation (**A1** and **A2**). Aβ(25-35) shows a high aggregation propensity as fibrils appear at 24 hours (**B1**) and persist, elongating into mature fibrils after one week (**B2**). Aβ(26-36) shows a combination of mostly short fibrils and some long fibrils at 24 hours

(**C1**), which remains unchanged over one week (**C2**). The GG linker increases the aggregation propensity of Aβ(24-34), as GG(24-34) forms short fibrils at 24 hours (**D1**) and continues to populate more fibrils at the later time point (**D2**). GG(25-35) shows a similar behavior to the single stranded version (**E1** and **E2**). The GG linker also changes the aggregation propensity of Aβ(26-36), as GG(26-36) now shows a combination of fibrils and shorter structures with morphologies similar to part of a microtubule as the dominant species (Figure 4.1 and Figure 4.2; see also Supplementary Figure 4.2 and main text for more discussion).

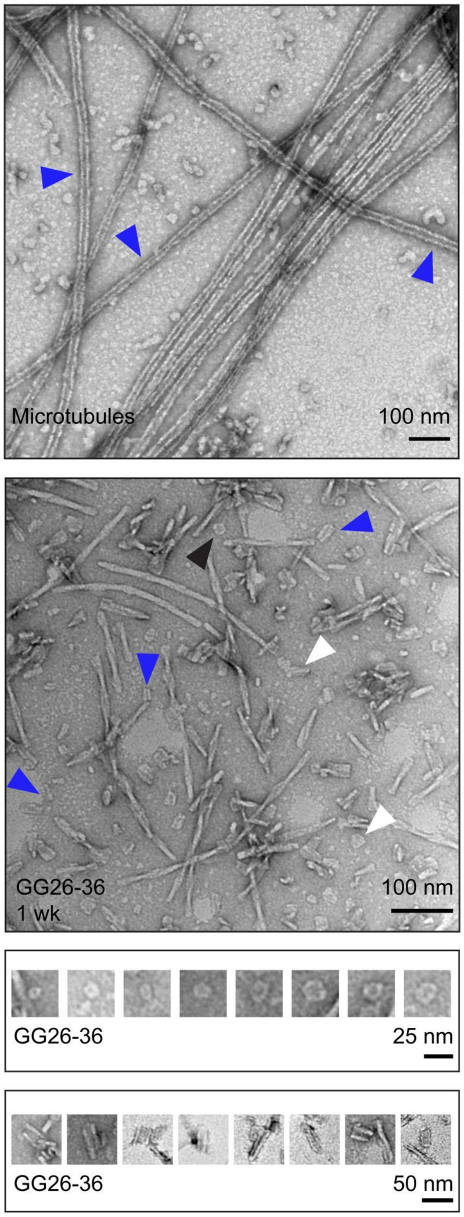

Supplementary Figure 4.5. Representative TEM images of GG(26-36) and microtubules. Individual microtubules in the top panel (blue arrows) show a characteristic striped appearance corresponding to alternating areas of low- and high-electron density, as a result of being hollow tubular structures. Short aggregates of GG(26-36) (blue arrows in the bottom panel) have a similar striped morphology, suggesting that they too may be hollow or have a low electron density core. Non-fibrillar striated aggregates (white arrows) and elongated, twisted fibers are also apparent.

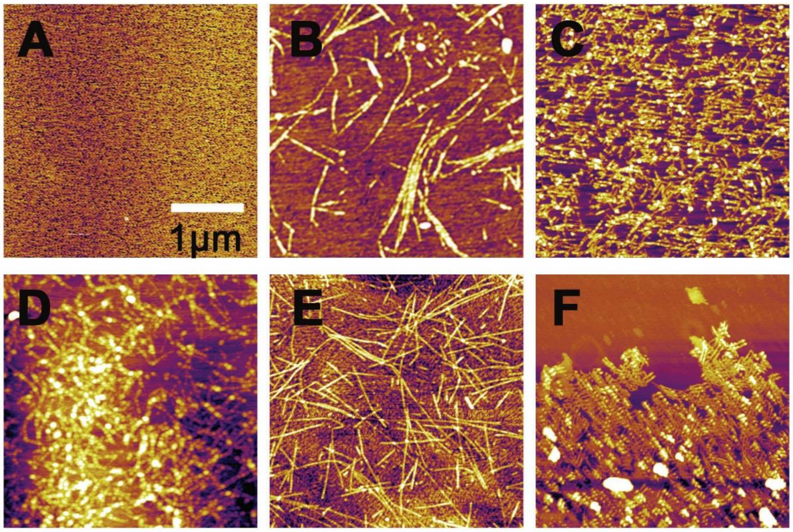

Supplementary Figure 4.6. Representative AFM images of the six peptides (A) Aβ(24-34), **(B)** Aβ(25-35), **(C)** Aβ(26-36), **(D)** GG(24-34), **(E)** GG(25-35) and **(F)** GG(26-36) after 24-h incubation in water. The AFM data are consistent with the TEM images. The peptide concentrations are 100-150 μM.

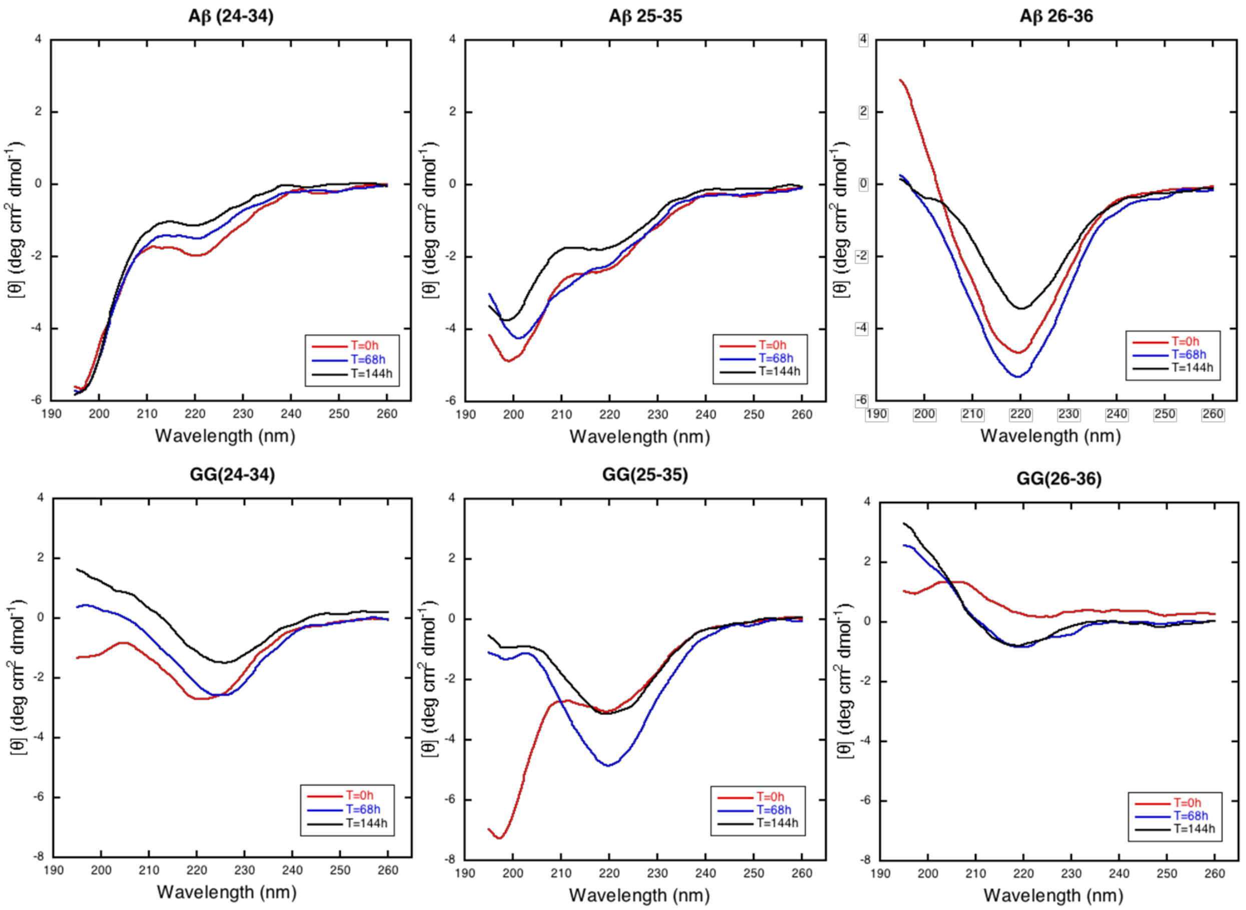

Supplementary Figure 4.7. Circular Dichroism of Aβ segments and tandem repeats. CD spectra are shown for Aβ(24-34), Aβ(25-35), Aβ(26-36), and GG(24-34), GG(25-35), and GG(26-36) at t = 0, 68, and 144 h. Circular dichroism spectroscopy (CD) was used to monitor peptide secondary structure during 6 days of incubation. Aβ(24-34) displayed molar ellipticity minima $[\Theta]_m$ at ≈ 195 and ≈ 221 nm, characteristics of statistical coil (SC) secondary structure. SC-type spectra were observed during the entire observation period. Similar spectra were observed for the Aβ(25-25) peptide. In contrast, the initial spectrum produced by Aβ(26-36) displayed a single $[\Theta]_m$ ≈ 220 nm. This spectral shape remained relatively constant, although $|[\Theta]|$ decreased over time, likely due to decreased protein concentration within the illuminated volume of the cuvette that can arise if aggregation occurs. "All β-sheet" proteins typically produce a $[\Theta]_m \approx 215$ nm, thus the shift of the minimum of Aβ(26-36) to ≈ 220 nm suggests the presence of mixed α/β structure, or possibly not typical β-sheet structure.

Each of the tandem peptides exhibited spectra consistent with non-SC structures. Tandem GG(24-34) displayed an initial $[\Theta]_m \approx 220$ nm. As the incubation proceeded, this minimum shifted to higher wavelengths, ending at ≈ 225 nm. The initial and later spectral shapes indicated that the tandem GG(24-34) peptide was structured, likely possessing mixed α/β elements. Tandem GG(25-35) initially displayed a prominent $[\Theta]_m \approx 197$ nm, but with a second minimum at ≈ 220 nm, indicating that although this peptide was largely SC in structure, some non-SC elements were present. These non-SC elements predominated by 16 h of incubation (data not shown). Pure β-structure produces spectra with a $[\Theta]_m$ at the apex of a parabola. The spectral asymmetry observed adjacent to the $[\Theta]_m$ of the tandem GG(25-35) peptide suggests that it, like tandem GG(24-34), possessed mixed α/β elements. The spectrum of GG(26-36) was similar to that of the GG(25-35) tandem repeat, though with a lower $|[\Theta]|$. As described above, the lower signal is indicative of a lower peptide concentration in the illuminated volume.

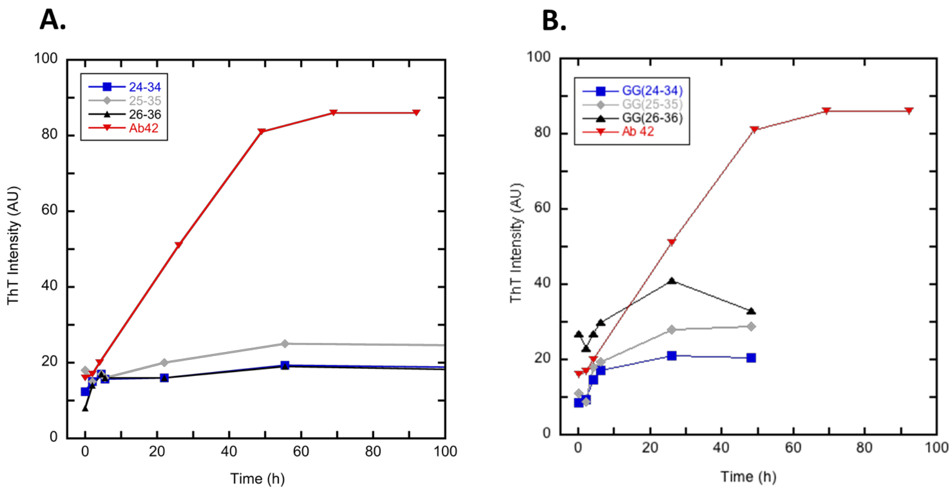

Supplementary Figure 4.8. Thioflavin T (ThT) fluorescence of Aβ peptides and tandem repeats compared to Aβ42. Thioflavin T intensity was used to measure the amount of aggregation in 20 μM peptides. **(A)** Aβ(24-34), Aβ(25-35), and Aβ(26-36) compared to Aβ42. **(B)** Tandem repeats GG(24- 34), GG(25-35), and GG(26-36) compared to Aβ42.

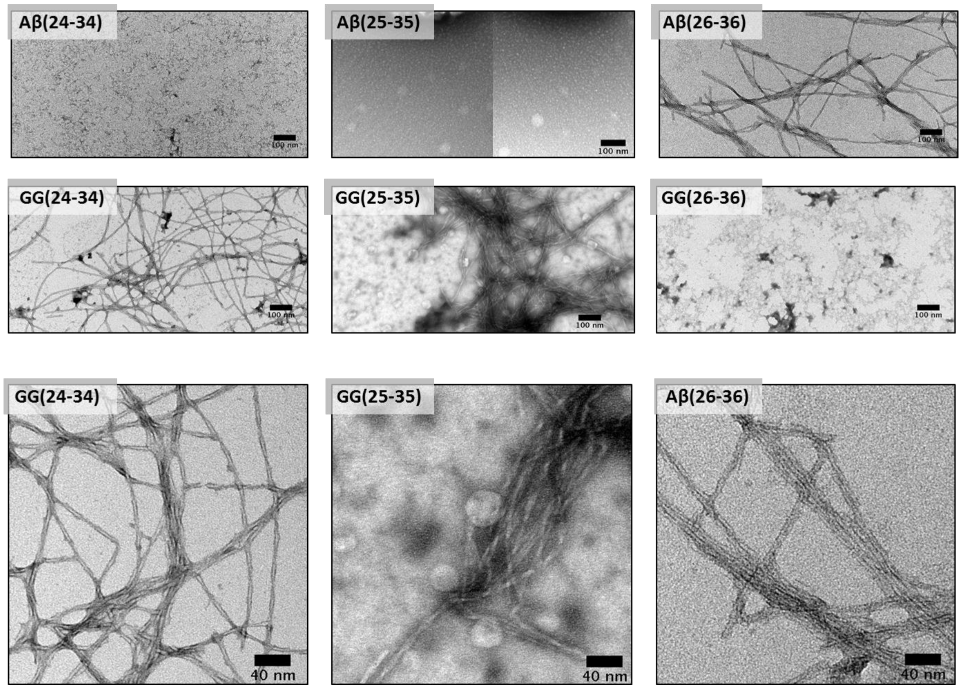

Supplementary Figure 4.9. Negative stain transmission electron microscopy (TEM) of Aβ segments and tandem repeats in sodium phosphate buffer. Electron micrographs are shown at t = 144 h for Aβ(24-34), Aβ(25-35), Aβ(26-36), and GG(24-34), GG(25-35), and GG(26-36). Scale bars in the top row of figures are 100 nm. The image of Aβ(25-35) is a composite of two different regions of the same grid. Scale bars are 40 nm.

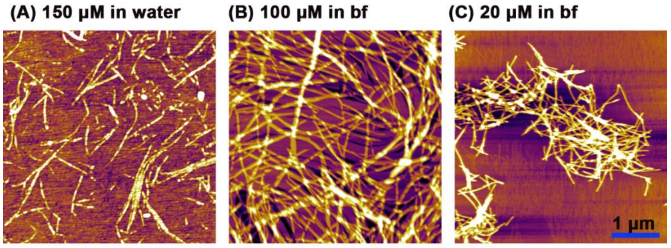

Supplementary Figure 4.10. Comparison of Aβ(25-35) fibril morphologies observed under different buffer conditions and peptide concentrations. **(A)** Aβ(25-35) at 150 µM in water, Aβ(25-35) in 20 mM ammonium acetate buffer (20 mM, pH = 7) at **(B)** 100 µM and **(C)** 20 µM.

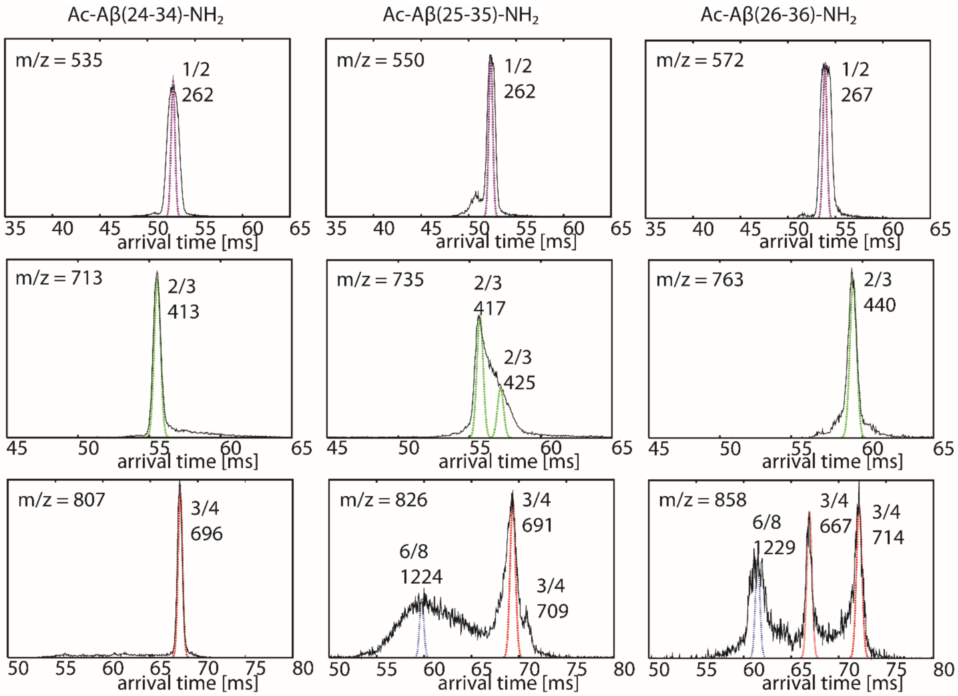

Supplementary Figure 4.11. Representative ATDs of n/z = 1/2 (top), 2/3 (middle) and 3/4 (bottom). Each feature is annotated with an n/z and an experimental cross-section (σ, Å2). Ion-mobility experiments on the monomer peaks at n/z = 1/2 yield the monomer cross-sections of the single-repeat Aβ peptides. These values help to assign the features in the ATDs at n/z = 1/1 as elaborated in the main text. Aβ(26-36) also forms larger oligomers at n/z = 2/3 and 3/4 as compared to the other two segments. However, the n/z = 2/3 and 3/4 mass spectral peaks are very minor compared with n/z = 1/2 and 1/1. The narrow dashed lines are the peak shapes predicted for a single conformer of the cross-sections given in the Figure.

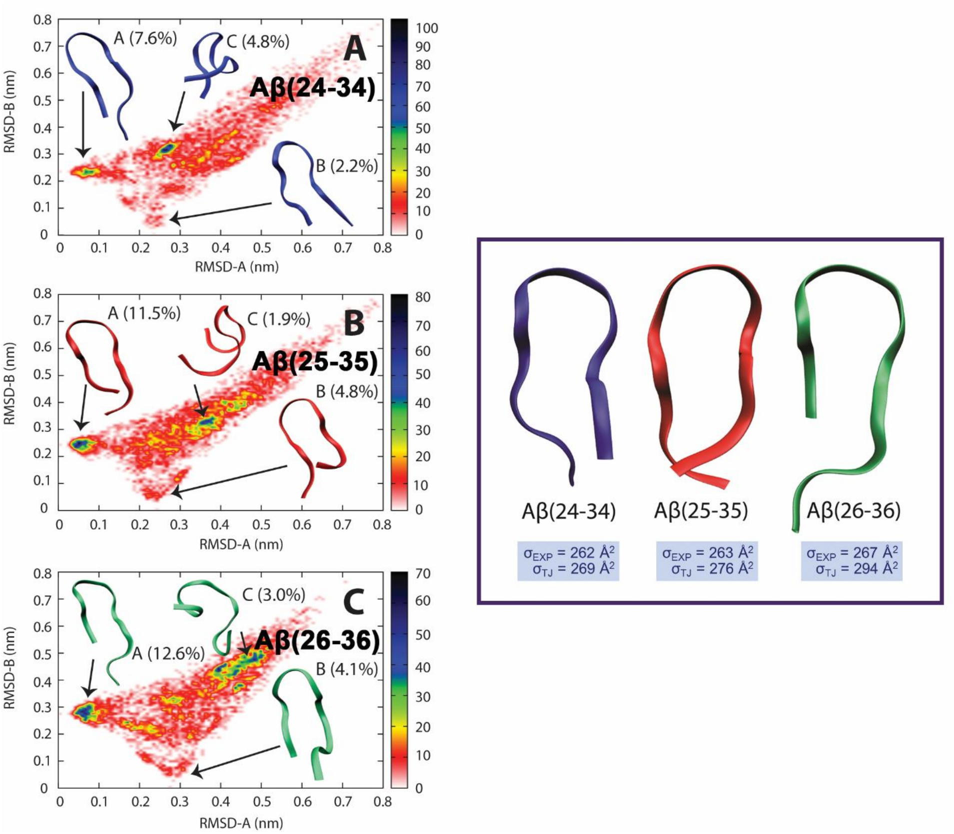

Supplementary Figure 4.12. (Left) Probability of finding a particular conformation of the backbone within monomers **(A)** Aβ(24-34), **(B)** Aβ(25-35) and **(C)** Aβ(26-36). The x-axis of the plot is root- mean squared deviation from the most populous cluster, and the y-axis is the distance between Cα backbone atoms of Lysine 4 and Isoleucine 7. (Right) Dominant β-hairpins of the Aβ peptides are asymmetric for Aβ(24-34) and Aβ(26-36) and symmetric for Aβ(25-35).

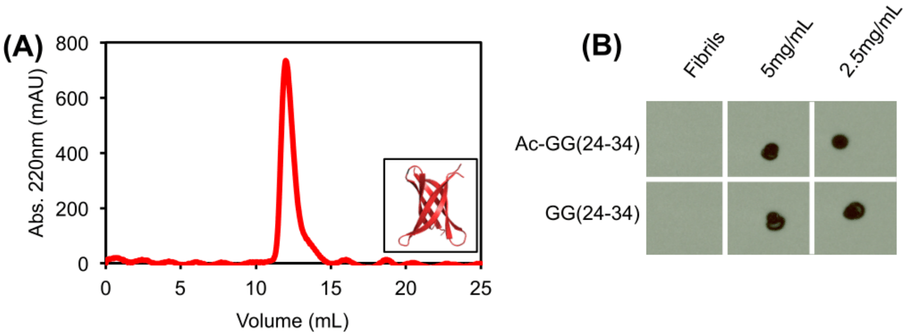

Supplementary Figure 4.13. GG(24-34) forms a hexameric oligomer. (A). Size Exclusion Chromatography using a Superdex Peptide 10/300 GL column reveals that GG(24-34) forms a trimer. Given that GG(24-34) is composed of a tandem repeat of the Aβ(24-34) sequence, it appears to form a trimer of dimers. This stoichiometry is identical to the cylindrin structure observed for αB crystallin (inset). **(B).** The polycloncal oligomer-specific antibody, A11, recognizes GG(24-34). A11 also recognizes the N-terminally acetylated form of the peptide (Ac-GG(24-34)). Fibrils formed by GG(24-34) and Ac-GG(24-34) are not recognized by A11.

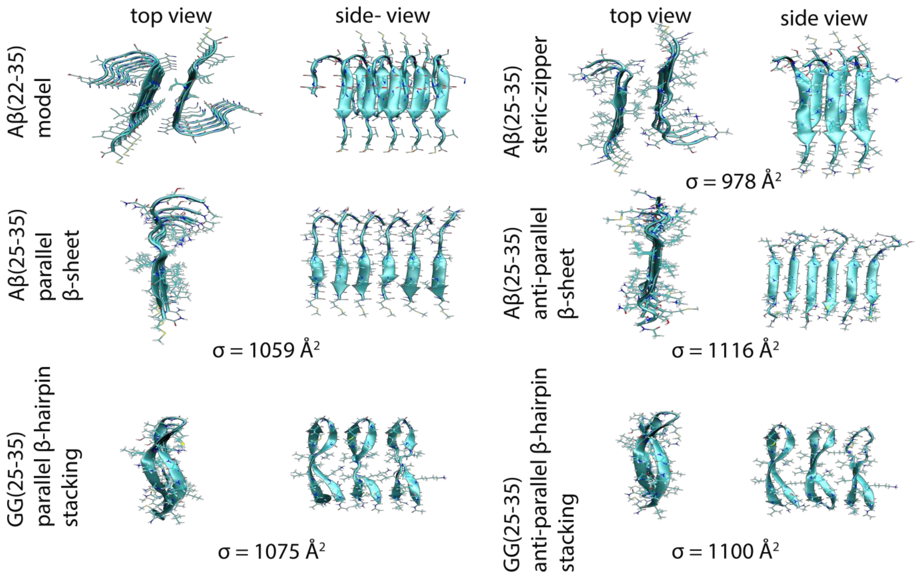

Supplementary Figure 4.14. Model structures of zwitterionic terminal Aβ(22-35) steric zipper, capped terminal Aβ(25-35) steric zipper and β-sheets, and parallel/anti-parallel stacking of GG(25- 35) β-hairpins. All structures were minimized in vacuum to mimic the dehydration process before theoretical cross-section calculations.

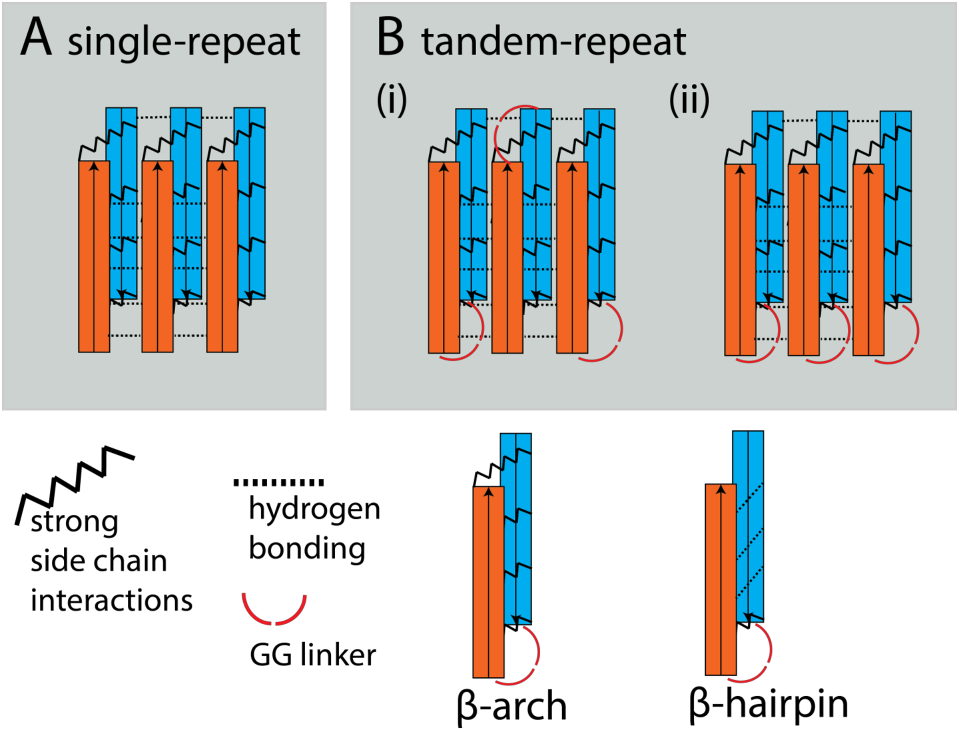

Supplementary Figure 4.15. Cartoon representations of (**A**) single-repeat Aß steric zipper, and (**B**) tandem- repeat steric zippers. The steric zippers are stabilized by hydrogen bonds within each layers and strong side chain interactions between two mating sheets.

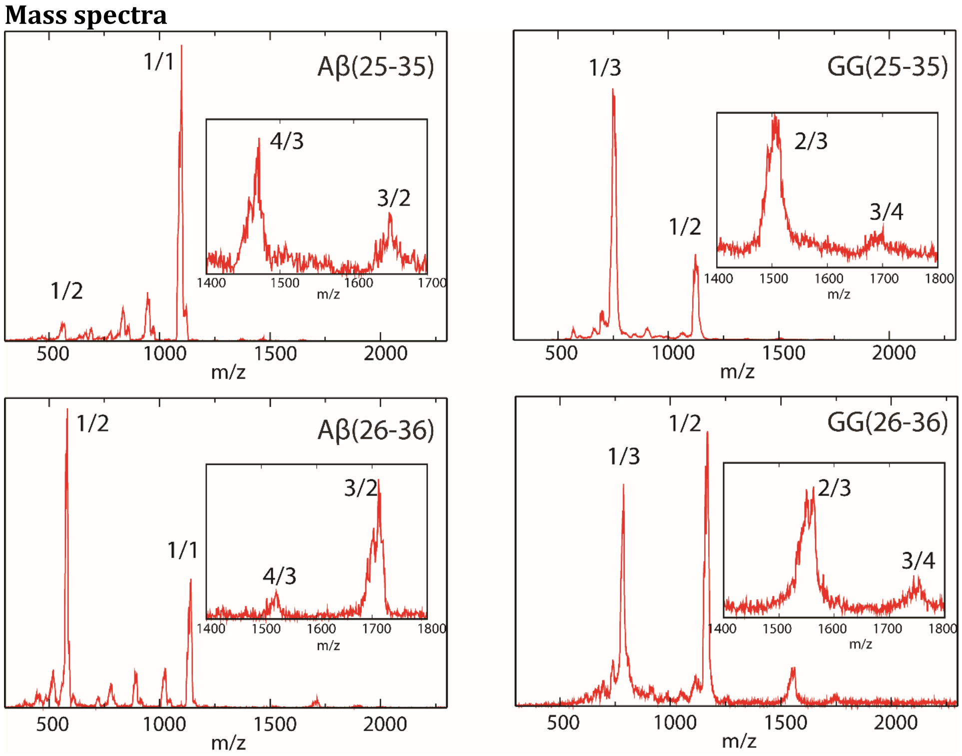

Supplementary Figure 4.16. n-ESI mass spectra of the three Aβ segments and GG tandem repeats obtained from instrument II. Each mass spectral peak is annotated with n/z ratio where n is the oligomer number and z is the charge.

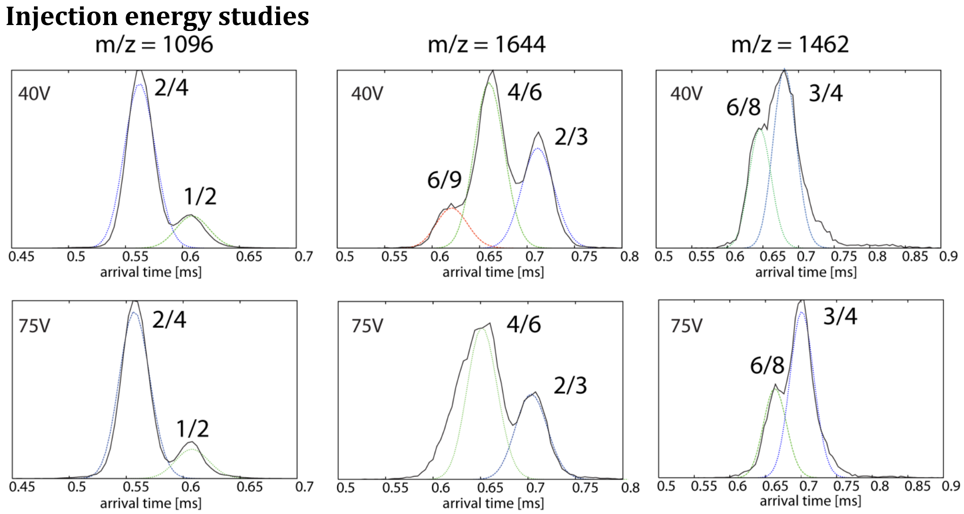

Supplementary Figure 4.17. Representative ATDs of the mass spectral peaks at 1096 m/z (left panels), 1644 m/z (middle panels), and 1462 m/z (right panels) of GG(24-34) obtained at two different injection voltages using instrument II. At high injection energy, the features corresponding to the large oligomers (e.g., n/z = 6/9 at m/z = 1644 and n/z = 6/8 at 1462 m/z) decrease in intensity, suggesting that they dissociate into smaller oligomers. The narrow dashed lines are the peak shapes predicted for a single conformer of the cross-sections given in the Figure.

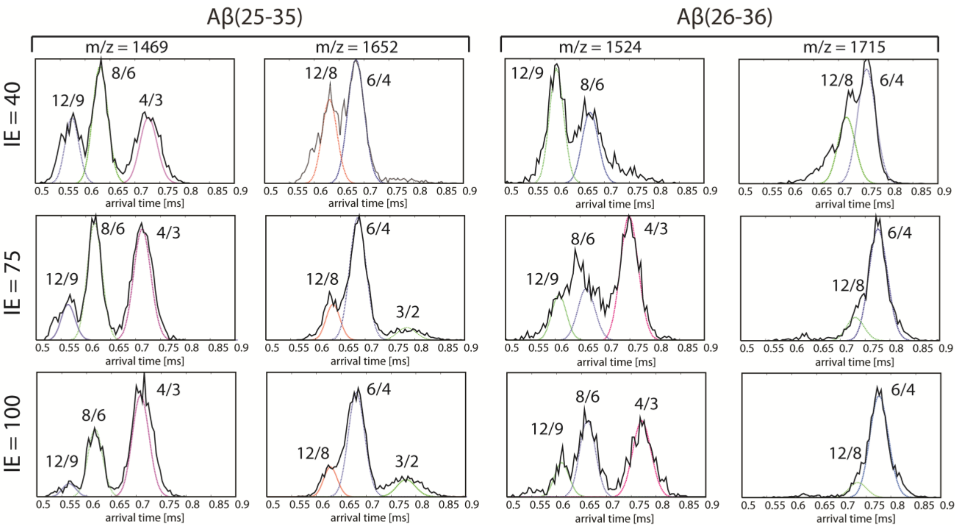

Supplementary Figure 4.18. Representative ATDs of the mass spectral peaks of n/z = 4/3 at 1469 m/z and 1524 m/z of Aβ(25-35) and Aβ(26-36), respectively. Injection energy studies confirm the presence of large oligomers up to n = 12 in both Aβ(25-35) and Aβ(26-36) systems similar to the case of Aβ(24-34) discussed in the main text. At high injection energy, the large oligomers (e.g., n = 12/8 and 12/9) dissociate into smaller oligomers (e.g., n/z = 4/3 and 3/2). The narrow dashed lines are the peak shapes predicted for a single conformer of the cross-sections given in the Figure.

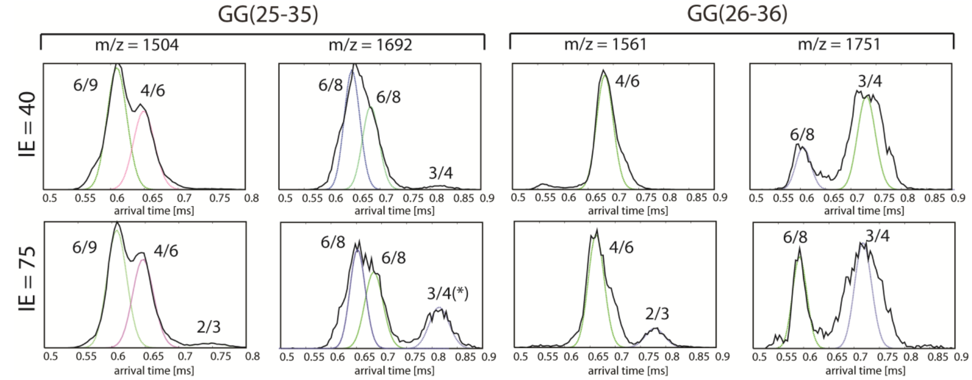

Supplementary Figure 4.19. Representative ATDs of the mass spectral peaks of n/z = 4/3 and 2/3 at 1561 m/z and 1751 m/z of GG(25-35) and GG(26-36), respectively. At high injection energy, large oligomers (e.g., n/z = 6/8 and 4/6) dissociate into smaller oligomers (e.g., n/z = 3/4 and 2/3). The narrow dashed lines are the peak shapes predicted for a single conformer of the cross-sections given in the Figure.

Supplementary Table 4.1. Averaged collision cross-sections of single-repeat Aβ and tandem-repeat GG peptide segments obtained using Instrument II.

n	***z***	**Aβ(24-34)**	***n***	***z***	**GG(24-34)**
4	3	849	2	3	831
6	4	1050	3	4	1054
8	6	1340	4	6	1480
12	8	1792	6	8	1946
12	9	1793	6	9	2015
n	***z***	**Aβ(25-35)**	***n***	***z***	**GG(25-35)**
4	3	852	2	3	n/a
6	4	1037	3	4	1059
8	6	1320	4	6	1426
12	8	1808	6	8	1905
12	9	1830	6	9	1971
n	***z***	**Aβ(26-36)**	***n***	***z***	**GG(26-36)**
4	3	n/a	2	3	n/a
6	4	1192	3	4	1125
8	6	1470	4	6	1516
12	8	2136	6	8	1884
12	9	2200	6	9	n/a

In comparison to Instrument I, the cross-sections of single-repeat Aβ tetramers, hexamers and tandem-repeat GG trimers and tetramers are at most +5% larger. At n = 12, the difference in cross-section between single- and tandem-repeat oligomers is noticeable. One possible explanation is that each peptide takes on different aggregation pathway (after n = 8), as supported by the microscopy and CD data present above and in the main text. As a result, some peptides form extended structures with large cross-sections (e.g., GG(24-34), GG(25-35)) whereas others form more compact structures (e.g., GG(26-36)).

REFERENCES

1. Hardy J, Selkoe DJ. 2002 The Amyloid Hypothesis of Alzheimer's Disease: Progress and Problems on the Road to Therapeutics. *Science* **297**:353–356. doi:10.1126/science.1072994

2. Chiti F, Dobson CM. 2006 Protein Misfolding, Functional Amyloid, and Human Disease. *Annu Rev Biochem* **75**:333–366. doi:10.1146/annurev.biochem.75.101304.123901

3. Chiti F, Dobson CM. 2009 Amyloid formation by globular proteins under native conditions. *Nat Chem Biol* **5**:15–22. doi:10.1038/nchembio.131

4. Eisenberg D, Nelson R, Sawaya MR, Balbirnie M, Sambashivan S, Ivanova MI, Madsen AØ, Riekel C. 2006 The Structural Biology of Protein Aggregation Diseases: Fundamental Questions and Some Answers. *Acc Chem Res* **39**:568–575.

5. Murphy RM. 2002 Peptide aggregation in neurodegenerative disease. *Annu Rev Biomed Eng* **4**:155–74. doi:10.1146/annurev.bioeng.4.092801.094202

6. Caughey B, Lansbury PT. 2003 Protofibrils, pores, fibrils, and neurodegeneration: separating the responsible protein aggregates from the innocent bystanders. *Annu Rev Neurosci* **26**:267–98. doi:10.1146/annurev.neuro.26.010302.081142

7. Xue W-F, Hellewell a. L, Gosal WS, Homans SW, Hewitt EW, Radford SE. 2009 Fibril Fragmentation Enhances Amyloid Cytotoxicity. *J Biol Chem* **284**:34272–34282. doi:10.1074/jbc.M109.049809

8. Kayed R, Head E, Thompson JL, McIntire TM, Milton SC, Cotman CW, Glabe CG. 2003 Common Structure of Soluble Amyloid Oligomers Implies Common Mechanism of Pathogenesis. *Science* **300**:486–489. doi:10.1126/science.1079469

9. Glabe CG. 2008 Structural Classification of Toxic Amyloid Oligomers. *J Biol Chem* **283**:29639–29643. doi:10.1074/jbc.R800016200

10. Krishnan R, Goodman JL, Mukhopadhyay S, Pacheco CD, Lemke E a., Deniz a. a., Lindquist S. 2012 Conserved features of intermediates in amyloid assembly determine their benign or toxic states. *Proc Natl Acad Sci* **109**:11172–11177. doi:10.1073/pnas.1209527109

11. Kodali R, Wetzel R. 2007 Polymorphism in the intermediates and products of amyloid assembly. *Curr Opin Struct Biol* **17**:48–57.

12. Do T, LaPointe NE, Sangwan S, Teplow DB, Feinstein SC, Sawaya MR, Eisenberg DS, Bowers MT. 2014 Factors That Drive Peptide Assembly from Native to Amyloid Structures: Experimental and Theoretical Analysis of [Leu-5]-Enkephalin Mutants. *J Phys Chem B* **118**:7247–7256.

13. Laganowsky A, Liu C, Sawaya MR, Whitelegge J, Park J, Zhao M, Pensalfini A, Soriaga AB, Landau M, Teng PK, Cascio D, Glabe CG, Eisenberg D. 2012 Atomic View of a Toxic Amyloid Small Oligomer. *Science* **335**:1228–1231. doi:10.1126/science.1213151

14. DeSimone A, Derreumaux P. 2010 Low molecular weight oligomers of amyloid peptides display beta-barrel conformations: a replica exchange molecular dynamics study in explicit solvent. *J Phys Chem B* **132**:165103.

15. Liu C, Zhao M, Jiang L, Cheng P-N, Park J, Sawaya MR, Pensalfini A, Gou D, Berk A, Glabe CG, Nowick JS, Eisenberg D. 2012 Out-of-register beta-sheets suggest a pathway to toxic amyloid aggregates. *Proc Natl Acad Sci U S A* **109**:20913–20918. doi:10.1073/pnas.1218792109

16. Gu L, Liu C, Stroud J, Ngo S, Jiang L, Guo Z. 2014 Antiparallel triple-strand architecture for prefibrillar Aβ42 oligomers. *J Biol Chem* **289**:27300–27013.

17. Morgado I, Wieligmann K, Bereza M, Ronicke R, Meinhardt K, Annamalai K, Baumann M, Wacker J, Hortschansky P, Malesvic M, et al. 2012 Molecular basis of β-amyloid oligomer recognition with a conformational antibody fragment. *Proc Natl Acad Sci* **109**:12503–12508.

18. Nelson R, Sawaya MR, Balbirnie M, Madsen AØ, Riekel C, Grothe R, Eisenberg D. 2005 Structure of the cross-beta spine of amyloid-like fibrils. *Nature* **435**:773–778. doi:10.1038/nature03680

19. Sawaya MR, Sambashivan S, Nelson R, Ivanova MI, Sievers SA, Apostol MI, Thompson MJ, Balbirnie M, Wiltzius JJW, McFarlane HT, Madsen AØ, Riekel C, Eisenberg D. 2007 Atomic structures of amyloid cross-β spines reveal varied steric zippers. *Nature* **447**:453–457. doi:10.1038/nature05695

20. Apostol MI, Perry K, Surewicz WK. 2013 Crystal structure of a human prion protein fragment reveals a motif for oligomer formation. *J Am Chem Soc* **135**:10202–10205. doi:10.1021/ja403001q

21. Pham J, Chim N, Goulding C, Nowick JS. 2013 Structures of oligomers of a peptide from β-amyloid. *J Am Chem Soc* **135**:12460–12467.

22. Spencer R, Li H, Nowick JS. 2014 X-ray crystallographic structures of trimers and higher-order oligomeric assemblies of a peptide derived from Aβ(17-36). *J Am Chem Soc* **136**:5595–5598.

23. Bleiholder C, Do TD, Wu C, Economou N, Bernstein S, Buratto S, Shea J-E, Bowers MT. 2013 Ion mobility spectrometry reveals the mechanism of amyloid formation of Aβ(25-35) and its modulation by inhibitors at the molecular level: epigallocatechin gallate and scyllo-inositol. *J Am Chem Soc* **135**:16926–16937.

24. Berstein S, Dupuis N, Lazo N, Wyttenbach T, Condron M, Bitan G, Teplow DB, Shea J-E, Ruotolo BT, Robinson C V, Bowers MT. 2009 Amyloid-β protein oligomerization and the importance of tetramers and dodecamers in the aetiology of Alzheimer's disease. *Nat Chem* **1**:326–331.

25. Bleiholder C, Dupuis N, Wyttenbach T, Bowers MT. 2011 Ion mobility-mass spectrometry reveals a conformational conversion from random assembly to β-sheet in amyloid fibril formation. *Nat Chem* **3**:172–177.

26. Uetrecht C, Versluis C, Watts N, Roos W, Wuite G, Wingfield P, Steven A, Heck A. 2008 High-resolution mass spectrometry of viral assemblies: molecular composition and stability of dimorphic hepatitis B virus capsids. *Proc Natl Acad Sci* **105**:9216–9220.

27. Pierson E, Keifer D, Selzer L, Lee L, Contino N, Wang J, Zlotnick A, Jarrold M. 2014 Detection of late intermediates in virus capsid assembly by charge detection mass spectrometry. *J Am Chem Soc* **136**:3536–3541.

28. Laganowsky A, Reading E, Allison T, Ulmschneider M, Degiacomi M, Baldwin A, Robinson C V. 2014 Membrane proteins bind lipids selectively to modulate their structure and function. *Nature* **510**:172–175.

29. Benesch J, Ruotolo BT. 2011 Mass spectrometry: come of age for structural and dynamical biology. *Curr Opin Struct Biol* **21**:641–649.

30. Susa A, Wu C, Bernstein S, Dupuis N, Wang H, Raleigh DP, Shea J-E, Bowers MT. 2014 Defining the molecular basis of amyloid inhibitors: human islet amyloid polypeptide-insulin interactions. *J Am Chem Soc* **136**:12912–12919.

31. Shi L, Holliday A, Shi H, Zhu F, Ewing M, Russell D, Clemmer D. 2014 Characterizing intermediates along the transition from polyproline I to polyproline II using ion mobility spectrometry-mass spectrometry. *J Am Chem Soc* **136**:12702–12711.

32. Wyttenbach T, Pierson N, Clemmer D, Bowers MT. 2014 Ion mobility analysis of molecular dynamics. *Annu Rev Phys Chem* **65**:175–196.

33. Pike C, Walencewicz-Wasserman A, Kosmoski J, Cribbs D, Glabe C, Cotman C. 1995 Structure-activity analyses of beta-amyloid peptides: contributions of the beta 25-35 region to aggregation and neurotoxicity. *J Neurochem* **6**:253–265.

34. Kubo T, Nishimura S, Kumagae Y, Kaneko I. 2002 In vivo conversion of racemized beta-amyloid ([D-Ser 26]A beta 1-40) to truncated and toxic fragments ([D-Ser 26]A beta 25-35/40) and fragment presence in the brains of Alzheimer's patients. *J Neurosci Res* **70**:474–483.

35. Hou L, Kang I, Marchant RE, Zagorski MG. 2002 Methionine 35 Oxidation Reduces Fibril Assembly of the Amyloid Abeta-(1– 42) Peptide of Alzheimer's Disease*. *J Biol Chem* doi:10.1074/jbc.C200338200

36. Bernstein S, Wyttenbach, Baumketner A, Shea J-E, Bitan G, Teplow DB, Bowers MT. 2005 Amyloid β-Protein: Monomer Structure and Early Aggregation States of Aβ42 and Its Pro19 Alloform. *J Am Chem Soc* doi:10.1021/JA044531P

37. Larini L, Shea J-E. 2012 Role of β-hairpin formation in aggregation: the self-assembly of the amyloid-β(25-35) peptide. *Biophys J* **103**:576–86. doi:10.1016/j.bpj.2012.06.027

38. Guex N, Peitsch MC. 1997 SWISS-MODEL and the Swiss-Pdb Viewer: An environment for comparative protein modeling. *Electrophoresis* **18**:2714–2723. doi:10.1002/elps.1150181505

39. Johansson MU, Zoete V, Michielin O, Guex N. 2012 Defining and searching for structural motifs using DeepView/Swiss-PdbViewer. *BMC Bioinformatics* **13**:173. doi:10.1186/1471-2105-13-173

40. Hess B, Kutzner C, van der Spoel D, Lindahl E. 2008 GROMACS 4: Algorithms for Highly Efficient, Load-Balanced, and Scalable Molecular Simulation. *J Chem Theory Comput* **4**:435–47. doi:10.1021/ct700301q

41. Van Der Spoel D, Lindahl E, Hess B, Groenhof G, Mark AE, Berendsen HJC. 2005 GROMACS: fast, flexible, and free. *J Comput Chem* **26**:1701–18. doi:10.1002/jcc.20291

42. Shvartsburg AA, Jarrold MF. 1996 An exact hard-spheres scattering model for the mobilities of polyatomic ions. *Chem Phys Lett* **261**:86–91. doi:10.1016/0009-2614(96)00941-4

43. Mesleh M, Hunter J, Shvartsburg A, Schatz C, Jarrold M. 1996 Structural Information from Ion Mobility Measurements: Effects of the Long-Range Potential. doi:10.1021/JP961623V

44. Bleiholder C, Wyttenbach T, Bowers MT. 2011 A novel projection approximation algorithm for the fast and accurate computation of molecular collision cross sections (I). Method. *Int J Mass Spectrom* **308**:1–10. doi:10.1016/j.ijms.2011.06.014

45. Bleiholder C, Contreras S, Bowers MT. 2013 A novel projection approximation algorithm for the fast and accurate computation of molecular collision cross sections (IV). Application to polypeptides. *Int J Mass Spectrom* **354**:275–280. doi:10.1016/j.ijms.2013.06.011

46. Murray MM, Krone MG, Bernstein SL, Baumketner A, Condron MM, Lazo ND, Teplow DB, Wyttenbach T, Shea J-E, Bowers MT. 2009 Amyloid β-Protein:

Experiment and Theory on the 21−30 Fragment. *J Phys Chem B* **113**:6041–6046. doi:10.1021/jp808384x

47. Lührs T, Ritter C, Adrian M, Riek-Loher D, Bohrmann B, Döbeli H, Schubert D, Riek R. 2005 3D structure of Alzheimer’s amyloid-beta(1-42) fibrils. *Proc Natl Acad Sci U S A* **102**:17342–17347. doi:10.1073/pnas.0506723102

48. Colletier J-P, Laganowsky A, Landau M, Zhao M, Soriaga AB, Goldschmidt L, Flot D, Cascio D, Sawaya MR, Eisenberg D. 2011 Molecular basis for amyloid-beta polymorphism. *Proc Natl Acad Sci U S A* **108**:16938–43. doi:10.1073/pnas.1112600108

49. Petkova AT, Leapman RD, Guo Z, Yau W-M, Mattson MP, Tycko R. 2005 Self-Propagating, Molecular-Level Polymorphism in Alzheimer’s -Amyloid Fibrils. *Science (80-)* **307**:262–265. doi:10.1126/science.1105850

50. Baumketner A, Shea J-E. 2007 The Structure of the Alzheimer Amyloid β 10-35 Peptide Probed through Replica-Exchange Molecular Dynamics Simulations in Explicit Solvent. *J Mol Biol* **366**:275–285. doi:10.1016/j.jmb.2006.11.015

51. Borreguero JM, Urbanc B, Lazo ND, Buldyrev S V, Teplow DB, Stanley HE. 2005 Folding events in the 21-30 region of amyloid beta-protein (Abeta) studied in silico. *Proc Natl Acad Sci U S A* **102**:6015–6020. doi:10.1073/pnas.0502006102

52. Do TD, Kincannon WM, Bowers MT. 2015 Phenylalanine Oligomers and Fibrils: The Mechanism of Assembly and the Importance of Tetramers and Counterions. *J Am Chem Soc* **137**:10080–10083. doi:10.1021/jacs.5b05482

53. Groveman BR, Dolan MA, Taubner LM, Kraus A, Wickner RB, Caughey B. 2014 Parallel In-register Intermolecular -Sheet Architectures for Prion-seeded Prion Protein (PrP) Amyloids. *J Biol Chem* **289**:24129–24142. doi:10.1074/jbc.M114.578344

54. Murzin AG, Lesk AM, Chothia C. 1994 Principles determining the structure of beta-sheet barrels in proteins. II. The observed structures. *J Mol Biol* **236**:1382–400. Available at: http://www.ncbi.nlm.nih.gov/pubmed/8126727 [Accessed March 28, 2017]

55. Jang H, Arce FT, Ramachandran S, Capone R, Azimova R, Kagan BL, Nussinov R, Lal R. 2010 Truncated beta-amyloid peptide channels provide an alternative mechanism for Alzheimer’s Disease and Down syndrome. *Proc Natl Acad Sci U S A* **107**:6538–6543. doi:10.1073/pnas.0914251107

56. Chang Z, Luo Y, Zhang Y, Wei G. 2011 Interactions of Aβ25−35 β-Barrel-like Oligomers with Anionic Lipid Bilayer and Resulting Membrane Leakage: An All-Atom Molecular Dynamics Study. *J Phys Chem B* **115**:1165–1174. doi:10.1021/jp107558e

57. Gidden J, Ferzoco A, Baker E, Bowers M. 2004 Duplex formation and the onset of helicity in poly d(CG)n oligonucleotides in a solvent-free environment. *J Am Chem Soc* **126**:15132–15140.

58. Mason E. 1988 *Transport Properties of Ions in Gases*. 99th ed. , ed. J. W. and Sons (1988).

59. Kemper P, Dupuis N, Bowers MT. 2009 A new, higher resolution, ion mobility mass spectrometer. *Int J Mass Spectrom* **287**:46–57.

60. Wyttenbach T, Kemper P, Bowers MT. 2001 Design of a new electrospray ion mobility mass spectrometer. *Int J Mass Spectrom* **212**:13–23.

61. Sgourakis NG, Merced-Serrano M, Boutsidis C, Drineas P, Du Z, Wang C, Garcia AE. 2011 Atomic-Level Characterization of the Ensemble of the Aβ(1–42) Monomer in Water Using Unbiased Molecular Dynamics Simulations and Spectral Algorithms. *J Mol Biol* **405**:570–583. doi:10.1016/j.jmb.2010.10.015

62. Jorgensen WL, Chandrasekhar J, Madura JD, Impey RW, Klein ML. 1983 Comparison of simple potential functions for simulating liquid water. *J Chem Phys* **79**:926–935. doi:10.1063/1.445869

63. Miyamoto S, Kollman PA. 1992 Settle: An analytical version of the SHAKE and RATTLE algorithm for rigid water models. *J Comput Chem* **13**:952–962. doi:10.1002/jcc.540130805

64. Hess B, Bekker H, Berendsen HJC, Fraaije JGEM. 1997 LINCS: A linear constraint solver for molecular simulations. *J Comput Chem* **18**:1463–1472. doi:10.1002/(SICI)1096-987X(199709)18:12<1463::AID-JCC4>3.0.CO;2-H

65. Darden T, York D, Pedersen L. 1993 Particle mesh Ewald: An $N\cdot\log(N)$ method for Ewald sums in large systems. *J Chem Phys* **98**:10089–10092. doi:10.1063/1.464397

66. Essmann U, Perera L, Berkowitz ML, Darden T, Lee H, Pedersen LG. 2005 A smooth particle mesh Ewald method. *J Phys Chem B* **103**:8577–8593. Available at: https://www.unc.edu/~perera/PAPERS/JChemPhys_1995_103_8577.pdf [Accessed March 28, 2017]

CHAPTER 5

Multistage optimization of non-natural amino-acid inhibitors of tau fibril formation

INTRODUCTION

The hallmark of amyloid diseases, such as Alzheimer's and Parkinson's disease, is the presence of amyloid fibrils in tissues (1). The core of most amyloid fibrils is composed of a cross-β arrangement of proteins, where extended peptide chains align perpendicular to the fibril axis in β-sheets (2,3). The two layers of β-sheets are tightly mated by a dehydrated interface termed a 'steric zipper' (4,5). Amyloid fibril formation, or the fibrils themselves, may contribute to cellular dysfunction during disease, thus, molecules that target and block fibril formation are attractive potential therapeutics.

There are several classes of therapeutic molecules that target amyloid fibrils or the process of fibril formation with different modes of action (6,7). One class encompasses small molecules that increase the thermodynamic stability of natively-folded proteins, termed pharmacological chaperones. These molecules target the earliest molecular events in the fibril formation process, as loss of native structure precedes amyloid fibril formation (8–10). Some of these compounds have proven effective at delaying fibril formation *in vitro* and reducing disease symptoms in clinical trials (11,12). A second class of compounds, which includes EGCG and other polyphenols, prevent amyloid fibril formation both *in vitro* and *in vivo*, but by an unknown mechanism and without specificity to their desired targets (13,14). Their lack of defined mechanism and specificity make these molecules unattractive potential therapeutics. A third class of compounds was designed to bind and stabilize pre-existing amyloid fibrils. The designed compounds were derived from atomic structures of molecules bound to steric zippers (15). This strategy is an effort to prevent amyloid fibril growth by blocking two of the kinetic events associated with enhanced cytotoxicity *in vitro*: fibril breakage and secondary nucleation of oligomers on fibril surfaces (16,17). These compounds prevent amyloid-related toxicity without disrupting fibril formation (18).

Our group developed yet another design strategy that uses the atomic structures of steric zippers as design templates for the development of peptide-based inhibitors (1,6). The designed peptide-based inhibitors are intended to cap the ends of amyloid fibrils and thus prevent new monomers from binding to the fibrils. Once the fibril ends are protected from association of new monomers, amyloid fibril formation kinetics are delayed or terminated (19–21). Our design strategy has a unique advantage in that it combines the detailed structural characteristics of the amyloid core, with the latest computational techniques for structure-based design. What is more, this design strategy holds the promise of very few off-target effects. In some cases, modifications of the peptide backbone such as macrocyclization (22), N-methylation (23,24), and O-acylation (25) have been added to designs in order to enhance the fibril-capping efficacy of the inhibitors.

Despite the specificity promised by these designed peptide-based inhibitors, identifying potently effective designs can take extensive experimental validation. Computational protein design methods generate a large number of false-positive decoys, which mandate laborious biochemical validation before true hits are identified. Indeed, a previous study that details peptide-based inhibitors of tau fibril formation went through several false-positive decoys before identifying true hits (19). Thus a rational post-design step would help ensure the validity of a designed inhibitor before biochemical validation. Identifying atomic structures of amyloid fibrils bound to their designed inhibitors could be one such validation tool, but the innate heterogeneity of amyloid fibril structure impedes this process.

Here, we aim to overcome these challenges by expanding our novel design method for peptide-based inhibitors, which we use to develop D-peptide inhibitors of tau fibril formation. Tau forms amyloid fibrils that accumulate as neurofibrillary tangles in Alzheimer's disease as well as a class of neurodegenerative diseases called tauopathies (26). Our method combines computational structure-based design using the Rosetta program suite with molecular dynamics (MD) simulations using the CHARMM program package (Figure 5.1). First, we show that the primary binding mode for previously designed D-peptide inhibitors of tau fibril formation is at the top or bottom of the steric zipper, or fibril. Second, we demonstrate that the computed binding free energy of the D-peptide inhibitors from MD simulations provides a quantitative prediction of the efficacy of the designs during experimental validation. By iterating over the computational structure-based design and the MD simulations steps, we developed two new D-peptide inhibitors, which reduce tau fibril formation *in vitro*. In addition, we utilized our new method to optimize a previously designed D-peptide inhibitor. Detailed analysis of the MD simulations of the designed D-peptide inhibitors bound to fibrils reveals common features of the most effective D-peptide inhibitors.

RESULTS

Development of a new MD simulation method to assess D-peptide inhibitor binding to tau fibrils

In an effort to improve our likelihood of designing effective D-peptide inhibitors, we sought to develop a new system for examining their efficacies *in silico* using MD simulations (27). Previously, MD simulations have been used to guide the design of novel inhibitors (28,29). The method is particularly useful for calculating the free energy of the binding (ΔG_{bind}) of designed inhibitors, as ΔG_{bind} values are an indicator of the efficacy of competitive inhibitors (30). The simulation, however, is challenging because the calculation of ΔG_{bind} mandates sampling of both bound and unbound states of the designed peptide to the target molecule. For our studies, we used four layers of the atomic structure of protein segment VQIVYK as the tau fibril (5), which we hereon refer to as the VQIVYK fibril. In order to improve the sampling efficiency, we employed an advanced simulation method known as conformational flooding (CF) (31). Contrary to umbrella sampling (US), where successive restraining potentials guide efficient sampling of otherwise rarely sampled regions of the reaction coordinate, the CF algorithm flattens the free energy surface by boosting the energy of regions of the energy landscape where the free energy is minimized. Previously the algorithm was used to study the conformational free energy landscape of a short peptide system (32). Herein, we refer to the new method as the replica exchange-conformational flooding (REX-CF) algorithm.

First, we demonstrated that REX-CF MD simulations reveal how a single VQIVYK molecule binds to the top or the bottom of the VQIVYK fibril. Figure 5.2 (a) shows the free energy profile of the single VQIVYK molecule adjacent to the VQIVYK fibril as a function of the distance between the centers of mass of the VQIVYK fibril and the single molecule. The free energy profile has two minima that correspond to two binding sites available to the single molecule on the fibril (Figure 5.2 (a)). The lowest minimum ($G(r = 14\ \text{Å}) = -8.0\ \text{kcal/mol}$) accounts for two grooves where the peptide interacts with opposing β-sheets, which we term “groove-ends” (Figure 5.2 (b); Supplementary Figure 5.2) After MD simulations were finished, we carried out structural cluster analysis in order to identify similar conformations at minima in the potential of mean force (PMF) profile. As shown in Figure 5.2 (b), the analysis confirms the majority of single VQIVYK molecules are located on the top or the bottom of the fibril. The lowest energy conformations possess 4 to 6 backbone hydrogen bonds between the designed D-peptide and the VQIVYK fibril. Ramachandran plot analysis of the bound inhibitors show a preference for extended β-sheet secondary structure, except for terminal residues, which prefer a turn conformation (Supplementary Figure 5.3). In some cases, D-peptides bound to sides of the VQIVYK fibril (Supplementary Figure 5.4), but the binding energy of these interactions was approximately 3-4 kcal/mol higher than the lowest energy binding modes. This higher binding energy indicates 150-fold weaker binding than to the grooved-ends of fibrils. Moreover, the orientation and the hydrogen bonding pattern of the single VQIVYK molecule resembles those of the other VQIVYK molecules within the fibril structure. These findings suggest that REX-CF MD simulations accurately capture how VQIVYK molecules are added to the ends of the VQIVYK fibril.

Next we investigated the energetics and binding modes of previously characterized D-peptide inhibitors to the VQIVYK fibril. The inhibitors that proved to be effective *in vitro*, D-TLKIVW and D-TWKLVL, have two distinct minima in the PMF profile (Figure 5.2 (a)). The locations of the minima are similar to the location of the four possible binding sites of VQIVYK molecule to the fibril (Supplementary Figure 5.2). The binding affinities of D-TLKIVW and D-TWKLVL to the VQIVYK fibril are lower than for a single VQIVYK molecule ($G_{min} \leq -8.0$ kcal/mol). The binding modes with the lowest energies occupy the grooved-ends on the VQIVYK fibril (Figure 5.3 (a) and (b)). In contrast, the PMF profiles of D-DYYFEF and D-DYYFEK, which do not inhibit VQIVYK fibril formation *in vitro*, show weaker binding affinity ($G_{min} > -8.0$ kcal/mol) to the VQIVYK fibril than the single VQIVYK molecule. Fig 5.2 (a) inset shows the correlation between the calculated binding affinity and the observed delay in fibril formation with *in vitro* testing. The correlation shown in the plot demonstrates that designed D-peptides with stronger binding affinities are better inhibitors *in vitro*.

Next, we used MD simulations to determine whether the designed D-peptides prevent the addition of VQIVYK molecules to fibril ends through competitive inhibition. To do this, we bound D-TLKIVW inhibitor to the grooved-end of either the top or the bottom of the VQIVYK fibril. Then, we computed the binding energy profile of a single VQIVYK molecule interacting with the VQIVYK fibril. The D-TLKIVW inhibitor was restrained to the bound conformation using additional harmonic potentials. The PMF profile of VQIVYK monomer shows that the binding energy of the VQIVYK monomer is reduced from -8.0 kcal/mol to -3.0 to -4.5 kcal/mol, when interacting with the bound D-TLKIVW inhibitor. The change in binding energies correspond to an increment in dissociation constant (k_d) from 0.5 μM to ~6 mM (33). This observation suggests that the binding of the D-peptide inhibitor reduces the propensity of a VQIVYK monomer to interact with the ends of the VQIVYK fibril and that two of the successful inhibitors, D-TLKIVW and D-TWKLVL, are competitive inhibitors of VQIVYK fibril formation.

Furthermore, we observe that REX-CF MD simulations can be used as a predictor of the efficacy of D-peptide inhibitors at delaying VQIVYK fibril formation. Table 5.1 summarizes predicted binding affinities of the D-peptide inhibitors and their efficacies *in vitro*. The calculated binding affinity of D-TLKIVW, an effective inhibitor, is -8.8 kcal/mol, which qualitatively agrees with the value reported previously (-7.4 kcal/mol) (19). D-peptides with scrambled sequences of effective inhibitors (i.e, D-LKTWIV, D-TIKWVL, and D-TIWKVL), a point mutant of the most effective inhibitor (D-TAKIVW), and the L-form of an effective inhibitor, all of which do not inhibit VQIVYK fibril formation *in vitro* (Supplementary Figure 5.6), likewise possess poor predicted binding affinity to the VQIVYK fibril. Taken together, these results suggest that the potency of a designed inhibitor is dependent upon its amino acid sequence, which allows for specific interactions with the VQIVYK fibril. These observations strengthen our hypothesis that a successfully designed D-peptide inhibitor is a competitive inhibitor of VQIVYK fibril formation, which occupies the same binding site as a single VQIVYK molecule.

Design of new D-peptide inhibitors for tau fibril formation

After demonstrating the effectiveness of MD simulations as a post-Rosetta Design screening method for known effective D-peptide inhibitors, we designed several new D-peptide inhibitors for tau fibril formation using this same protocol. First, we generated hundreds of hexameric D-peptide sequences using Rosetta Design while considering multiplicity of possible orientations of the D-peptides on the top or the bottom of the VQIVYK fibril. We selected the D-peptides in the top 10% of the Rosetta scoring system as well as those with maximum backbone hydrogen bonds to the adjacent VQIVYK molecule for further characterization. These selected sequences were subjected to REX-CF MD simulation to validate their quality of design. Representative snapshots from the MD simulations reveal that the new designs bind to the grooved-ends of the VQIVYK fibril, just like D-TLKIVW and D-TWKLVL (Figure 5.3 (c) and (d) and Table 5.1). We deemed these new D-peptides, D-WVFKIS and D-WKIVIT, to be of top quality by REX-CF and subjected them to *in vitro* testing.

Designed D-peptides specifically bind VQIVYK fibrils

In order to determine whether the newly designed D-peptides specifically bind to VQIVYK fibrils, we carried out NMR binding assays of D-WVFKIS and three negative controls: D-LKTWIV, D-TAKWIV, and L-TLKIVW. For these experiments, we incubated 4 mM VQIVYK fibrils with 100 μM D-peptide and then quantified the remaining percentage of D-peptide in solution. Lower percentages of peptide in solution indicate more specific binding to fibrils. For the negative controls, we observe a larger percentage of peptides in solution relative to the effective D-peptides (Figure 5.4 (b)), thus indicating low binding affinities of the negative controls to fibrils. D-WVFKIS bound VQIVYK fibrils almost as strongly as our original effective D-peptide design, D-TLKIVW. These results suggest that our novel MD simulation technique identified promising D-peptide inhibitors of tau fibril formation.

Designed D-peptides effectively delay tau fibril formation *in vitro*

Next, we tested whether the newly designed D-peptides, D-WKIVIT and D-WVFKIS, reduce fibril formation of three tau constructs *in vitro* (Figure 5.4 (a)). We monitored tau fibril formation by measuring Thioflavin-S (ThS) fluorescence. We tested D-WKIVIT and D-WVFKIS alongside the original design, D-TLKIVW. We observe that both D-WKIVIT and D-WVFKIS reduce fibril formation of the target design molecule, VQIVYK (Figure 5.4 (c) and (d)). The three effective D-peptides, D-TLKIVW, D-WKIVIT, and D-WVFKIS, delay fibril formation by approximately 3-fold relative to VQIVYK alone, while negative control D-TAKIVW does not effect fibril formation. D-WKIVIT appears to be more potent at reducing VQIVYK fibril formation than D-TLKIVW. Similarly, all three D-peptides effectively reduce fibril formation of two longer tau constructs, K18 (4 repeat) and K19 (3 repeat), by about 2-fold and 3-fold, respectively, relative to tau alone (Figure 5.4(e) and (f); (g) and (h), respectively).

Additionally, we observe that the newly designed D-peptides exhibit concentration-dependent inhibitory effects of tau fibril formation, similar to D-TLKIVW (19). We incubated K19 with several different ratios of each designed D-peptide: 1:0.1, 1:0.5, 1:1 and 1:2 of 50μM K19 to D-peptide. Decreasing molar ratios of K19 to D-peptide lead to an increased reduction in K19 fibril formation (Supplementary Figure 5.7). In these assays, D-TLKIVW and D-WKIVIT appear more effective than D-WVFKIS at reducing K19 fibril formation. The computed binding affinity of D-WVFKIS is -8.1 kcal/mol, which is comparable to that of D-WKIVIT (-8.1 kcal/mol) and slightly weaker than that of D-TLKIVW (-8.4 kcal/mol). The *in vitro* validation of these D-peptides bolsters the robustness of the design process.

Application of design technique leads to optimized D-peptide inhibitors

After validating the efficacy of the D-peptide inhibitors developed using our novel design method, we used the method to generate variants of the previously characterized design, D-TLKIVW, with the goal of improving its efficacy *in vitro*. The optimized sequences varied from the original sequence at the third amino acid position. Indeed, the optimized D-peptides bound to VQIVYK fibrils more strongly than D-TLKIVW (Figure 5.5(a)). First, we tested the efficacies of the optimized D-peptides to reduce fibril formation of the target design molecule, VQIVYK. We observe that the optimized D-peptides elicit mixed effects on VQIVYK fibril formation (Figure 5.5(b) and (c)). D-TL(Cit)IVW and D-TLRIVW reduce VQIVYK fibril formation with similar efficacy to D-TLKVIW. D-TL(Orn)IVW and D-TLTIVW reduce VQIVYK fibril formation better than the negative control, but not as potently as D-TLKVIW. Intriguingly, D-TLQIVW and D-TLAIVW, which were the strongest binders of VQIVYK fibrils in the NMR binding experiments, do not reduce VQIVYK fibril formation (Figure 5.5(b) and (c)). The optimized D-peptides exhibit similar effects when they were tested against longer tau constructs (Figure 5.5(d) and (e)): D-TL(Cit)IVW and D-TLRIVW robustly inhibited K18 and K19 fibril formation. D-TLTIVW, D-TL(Orn)IVW, and D-TLQIVW slightly delayed K18 and K19 fibril formation, and D-TLAIVW did not inhibit fibril formation.

DISCUSSION

The bottleneck between pharmaceutical therapeutics designed *in silico* and their efficacies against their design targets *in vitro* necessitates tools for "weeding out" ineffective designs before *in vitro* testing is initiated. Here, we attempt to widen this bottleneck by developing a novel system for evaluating binding efficacies using MD simulations, which we term REX-CF MD.

The results from our REX-CF MD simulations support some our previously formulated hypotheses (19). Previous studies using gold-labeled D-peptide inhibitors suggested that the inhibitors could bind to the top or bottom of fibrils (19). Indeed, a snapshot taken of the lowest points in the PMF profile show that, the lowest and the second lowest energy conformers of the four effective D-peptide inhibitors (D-TLKIVW, D-TWKLVL, D-WKIVIT, and D-WVFKIS) were bound to the top or bottom of the VQIVYK fibril (Figure 5.3).

At these binding sites, the effective D-peptide inhibitors can occupy two different sites on the top or bottom of the VQIVYK fibril, which we term the leading-end or the grooved-end (Supplementary Figure 5.2). The PMF profile in Figure 5.2(a) shows that D-peptide inhibitors that bind to the top or bottom of the VQIVYK fibril also interact with the VQIVYK molecule in the adjacent β-sheet. For example, the most favored binding mode of D-TLKIVW, BP3, forms two Van der Waals interactions between the inhibitor and the adjacent VQIVYK: D-LEU2 and ILE3 and D-ILE4 and VAL1. Also, the second most favorable binding mode, TA1, makes a π- π interaction between D-TRP6 and TYR5 of the adjacent VQIVYK molecule as well as Van der Waals interactions between D-ILE4 and ILE3 of VQIVYK stretch (Figure 5.3(a)). Only VQIVYK molecules bound to the grooved-end can interact with VQIVYK molecules on the adjacent sheet, thus, these results indicate that the D-peptide inhibitors bound with increased affinity to the grooved-ends over the leading-ends.

Additionally, our MD simulations reveal that the designed D-peptide inhibitors bind to VQIVYK fibrils with a strong preference for extended β-sheet secondary structure (34). Thus, these findings support our initial choice of design templates where extended D-peptide backbones were aligned to maximize the number of hydrogen bonds to the adjacent VQIVYK molecule.

Our MD simulations reveal that D-TLKIVW binds to the VQIVYK fibril in either a parallel or anti-parallel orientation, even though the original design protocol only tested parallel binding (19). On the top of the fibril, an anti-parallel (TA1: -8.2 kcal/mol) and a parallel (TP1: -7.9 kcal/mol) binding mode show stronger or comparable binding affinity to VQIVYK monomer to the same position on the fibril (-8.0 kcal/mol; Figure 5.3 (a)). In contrast D-TLKIVW aligned in a parallel orientation to the bottom of the fibril (BP3: -8.4 kcal/mol), is 1 kcal/mol more favorable than the anti-parallel orientation on the same end (BA2: -7.4 kcal/mol). We observed a similar propensity for parallel and anti-parallel orientations for the newly designed D-peptides, D-TWKLVL and D-WVFKIS.

Last, our MD simulations reveal that the D-peptide inhibitors reduce fibril formation by competitive inhibition because the binding affinity of a single VQIVYK molecule for the fibril is reduced when D-peptide is bound to the same fibril (Supplementary Figure 5.5).

We applied what we learned from our analysis of previously designed D-peptide inhibitors to develop two novel D-peptide inhibitors. The newly designed D-peptides in this study, D-WVFKIS and D-WKIVIT, delay fibril formation of three different tau constructs. We observe that the D-peptides have a ratio-dependent effect, where lower molar ratios of tau to D-peptide are more potent. Moreover, newly designed D-WKIVIT was as effective as D-TLKIVW at delaying tau fibril formation.

The newly designed and optimized D-peptides that reduce fibril formation also possess strong predicted binding affinity to VQIVYK fibrils (Figure 5.6), thus resulting in a negative correlation between *in vitro* fibril growth reduction and tight predicted binding affinity. In addition, the re-optimized designs, D-TL(Cit)IVW and D-TLRIVW, exhibit strong predicted binding energy and reduce Ac-VQIVYK fibril formation. However, this correlation is significantly weaker for select optimized D-peptides that did not inhibit tau fibril formation *in vitro.* D-TLQIVW and D-TLAIVW, which were predicted to bind Ac-VQIVYK as strongly as D-TL(Cit)IVW, do not delay fibril formation *in vitro.* Taken together, these results suggest that bulky positively charged residues at the third position contribute to the potency of D-peptide inhibitors. Of note, the use of computationally less demanding solvation models may be the source of the systematic errors. Thus, the use of more sophisticated continuum solvation models or explicit solvation simulations are necessary in the future.

In order to more definitively prove that our novel design method generates bona fide, specific inhibitors of tau fibril formation that may serve as promising pharmaceutical therapeutics, our D-peptide inhibitors must be validated in more physiologically relevant systems, like cell culture models of tau aggregation (35). Intriguingly, preliminary studies in such models suggest that D-WVFKIS and D-WKIVIT reduce tau aggregation and seeding (Seidler, *et al.* Unpublished data).

MATERIALS AND METHODS

Structure-based design using Rosetta

We used the atomic structure of VQIVYK as our model of a VQIVYK fibril for our computational structure-based design (5). We hypothesized that inter-molecular hydrogen bonds are present between the designed D-peptide and the VQIVYK fibril. Thus, there are four potential binding sites: the grooved-end or the leading-end on the top or bottom of the fibril (Supplementary Figure 5.2a). The two binding sites on the top or the bottom of the fibril are different due to the 2_1 screw axis present in the crystal symmetry. The 2_1 screw axis causes each β-sheet to be translated one-half an intra-sheet distance of 4.8 Å. MD simulations with VQIVYK monomer reveal that peptides bound to the grooved-ends on the top or bottom of the fibril possess stronger binding affinity, likely because of non-bonded interactions across β-sheets and backbone hydrogen bonding. This is discussed in greater detail in the Results section. Based on our MD simulations results, we chose to design D-peptides that specifically recognized the grooved-ends.

To design the new D-peptide inhibitors, we first placed a D-hexaalanine at the grooved-ends on the top and the bottom of the VQIVYK fibril to maximize inter-peptide hydrogen bonds. The D-hexaalanine can be either in parallel (P) or in anti-parallel (A) relative to the VQIVYK molecules of the fibril (Supplementary Figure 5.2 b). The binding sites allow for three different hydrogen bonding positions, labeled "1", "2" or "3" (Supplementary Figure 5.2 c). In total, this allows for 12 different initial backbone arrangements for D-peptide designs (Supplementary Figure 5.2 c). We used Rosetta software (36,37) to search for the optimal amino acid sequences to template the top and bottom of the VQIVYK fibril.

MD simulations of peptides interacting with the VQIVYK fibril

Each peptide was modeled using Charmm22 all-atom force field (38). We modeled a D-amino acid by taking the mirror image of the corresponding L-amino acid; Charm22 force field maintains energetic symmetry between L- and D- isomer of an amino acid. Thus we used the parameter set without modifications. We used an effective energy function (EEF1) continuum solvation model to reduce the computational demand associated with explicit treatment of solvent (39). Charmm v35 was used for the entire MD simulation (40).

Initially, the VQIVYK fibril, which consists of 8 VQIVYK molecules, was located at the center of a tetrahedral simulation box with a radius of 35 Å. Periodic boundary condition (PBC) with a cubic simulation box (60 $Å^3$) was used to mimic an infinitely large system. Langevin dynamics with a small friction constant (5 ps^{-1}) controlled desired temperature of each replica. Replica-exchange attempts were made every 1.0 ps and lasted for 10 ns.

We combined conformational flooding (CF) with replica-exchange MD simulation (41). Herein the simulation method is termed as replica exchange-conformational flooding (REX-CF). We simulated 40 identical replicas of the system with a temperature range spanning 270 K to 400 K. Half of the replicas experienced a harmonic boost energy whose maximum is 15 Å from the center of the steric zipper interface of the VQIVYK fibril;

$$E_{boost} = \begin{cases} -\frac{1}{2}k_{boost}(r - r_{center})^2 + E_{offset} & (10\text{ Å} < r < 20\text{ Å}) \\ 0 & (r \leq 10\text{ Å } or\ r \geq 20\text{ Å}) \end{cases}$$

where $k_{boost} = 0.32\ \text{kcal/mol/Å}^2$, $r_{center} = 15\text{ Å}$, and $E_{offset} = 4.0\ \text{kcal/mol}$. Supplementary Figure 5.1 shows how the boosting potential (E_{boost}) flattens the overall free energy profile of the binding of VQIVYK monomer to the VQIVYK fibril. Replica-exchange trials were repeated every 1.0 ps and lasted for 10 ns per replica. We modified Charmm v36 to implement REX-CF algorithm.

Analysis of binding energy profile and bound conformation of the designed D-peptide inhibitors

After finishing 10 ns REX-CF MD simulation, we analyzed the binding energy profile as a function of center-of-mass distance (r) between the center-of-mass (CM) of the VQIVYK fibril and the CM of a D-peptide. The radial distribution function of r is defined as

$$p(r) = \frac{P(r)}{4\pi r^2}$$

where $p(r)$ is the radial distribution function and $P(r)$ is the probability of finding a D-peptide at radial distance r. The radial distribution function is normalized to give $\int_0^{R_{max}} p(r)\, 4\pi r^2 dr = 1$, where R_{max} is 30 Å. The potential of mean force (PMF) that a D-peptide experiences near the steric zipper interface of the fibril is defined as

$$G(r) = -k_B T \log\left(p(r)\right)$$

where k_B is the Boltzmann constant and T is absolute temperature. We used weighted histogram analysis method (WHAM) (42) to integrate the histogram from different simulation temperatures.

The binding energy of each designed D-peptide was computed by comparing the difference in PMF between its lowest point and $r > 30$ Å. As seen in Figure 5.2, the profile became flat when $r > 30$ Å, reflecting the lack of interaction between the D-peptide and the VQIVYK fibril.

Finally, we carried out structural cluster analysis, as there is a multitude of conformations sampled near the top and bottom of the steric zipper interface. We grouped similar conformers having heavy atom (all atoms except hydrogen) RMSD < 2.0 Å using a hierarchical clustering method. We combined the analysis with energy density of states (DOS) information produced by the performed WHAM analysis to give absolute binding free energy (ΔG_{bind}) for each structural cluster.

^{1}H NMR sample preparation and measurements

The ^{1}H NMR sample preparation and measurements were conducted as described previously (19). Ac-VQIVYK-NH_2 (Genscript) was dissolved at 1 mM in 25 mM MOPS, pH 7.2, and incubated at room temperature for at least 24 hours. Fibrils were washed with water, concentrated using an Amicon ultracentrifugal filter with a 3-kDa molecular mass cut-off and then resuspended in water to a final concentration (by monomer) of 4 mM.

NMR samples were prepared with 5% D_2O and 10 mM NaOAc, pH 5.0. D-peptides were diluted 1:10 from 1 mM stocks in water. Fibrillar Ac-VQIVYK-NH_2 was added at indicated concentrations to make a final volume of 550 µL. 1H NMR spectra measured at 500 MHz were collected on a Bruker DRX500 at 283 K. Water resonance was suppressed through presaturation. Spectra were processed with XWINNMR 3.6.

Tau fibril inhibition assays

The efficacy of each designed D-peptide at reducing tau fibril formation was examined using Thioflavin-S (ThS) fluorescence. We tested three different constructs of tau: Ac-VQIVYK-NH_2 (purchased from CS Bio), K18, and K19. Recombinant K18 and K19 were purified as described previously (19). ThS fluorescence was measured with excitation and emission wavelengths of 440 and 510 nm, respectively. Each D-peptide was tested in triplicate or quadruplicate. Lag times were calculated by choosing an arbitrary fluorescence threshold for each sample to reach. Samples were incubated in black 96-well plates (Nunc) and readings were recorded at varying times using a SpectraMax M5 (Molecular Devices). All peptides (purchase from either CS Bio and Celtek) were dissolved in 100% DMSO, and then diluted in reaction buffer to a final 10% DMSO in each reaction.

To test the D-peptides against Ac-VQIVYK, 100 µM Ac-VQIVYK was incubated 1:1 with D-peptide in 25 mM MOPS pH 7.2 and 100 µM ThS (MP Bio). The reaction was incubated at 25°C without agitation, and readings were taken every 2 minutes. To test D-peptides against K18, 50 µM K18 was incubated 1:1 with D-peptide in 250 mM sodium phosphate buffer pH 7.4, 12.5 µM heparin sulfate (Sigma), 1 mM DTT, and 10 µM ThS. The reaction was incubated at 37°C without agitation, and readings were taken every 15 minutes.

Initial tests of D-peptides against K19 used 50 µM K19 (as quantified by BCA assay) incubated 1:1 with D-peptide in 250 mM sodium phosphate buffer pH 7.4, 12.5 µM heparin sulfate, 1 mM DTT, and 10 μM ThS. The reaction was incubated at 37°C with shaking, and readings were taken every 15 minutes. D-peptides were subsequently tested at varying molar ratios with 50 μM K19 in 1X PBS, 12.5 μM heparin sulfate, 1 mM DTT, and 10 μM ThS. The reaction was incubated at 37°C with shaking, and readings were taken every 15 minutes.

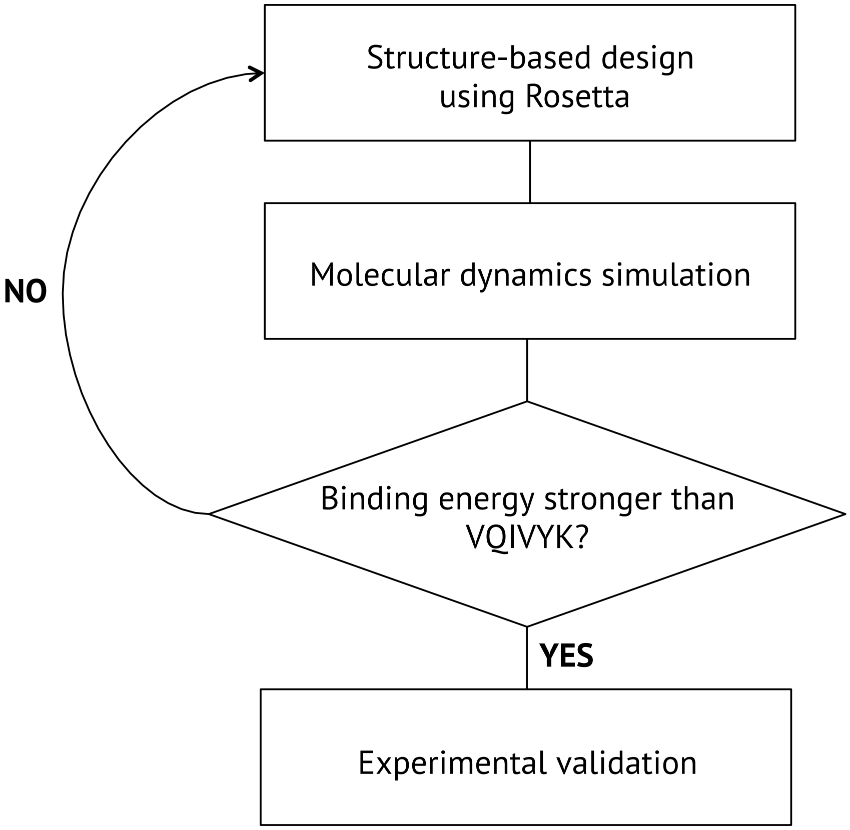

Figure 5.1. Strategy for the design and optimization of D-peptide inhibitors. First, D-peptide inhibitors were designed using the Rosetta program suite. Next, D-peptide inhibitors with the highest Rosetta scores were subject to MD simulation. If a designed sequence exhibited stronger binding energy to the VQIVYK fibril than a single VQIVYK molecule, then we tested its efficacy in delaying tau fibril formation *in vitro*. If a design sequence did not exhibit stronger binding energy than VQIVYK, then it was subjected to another round of design and optimization.

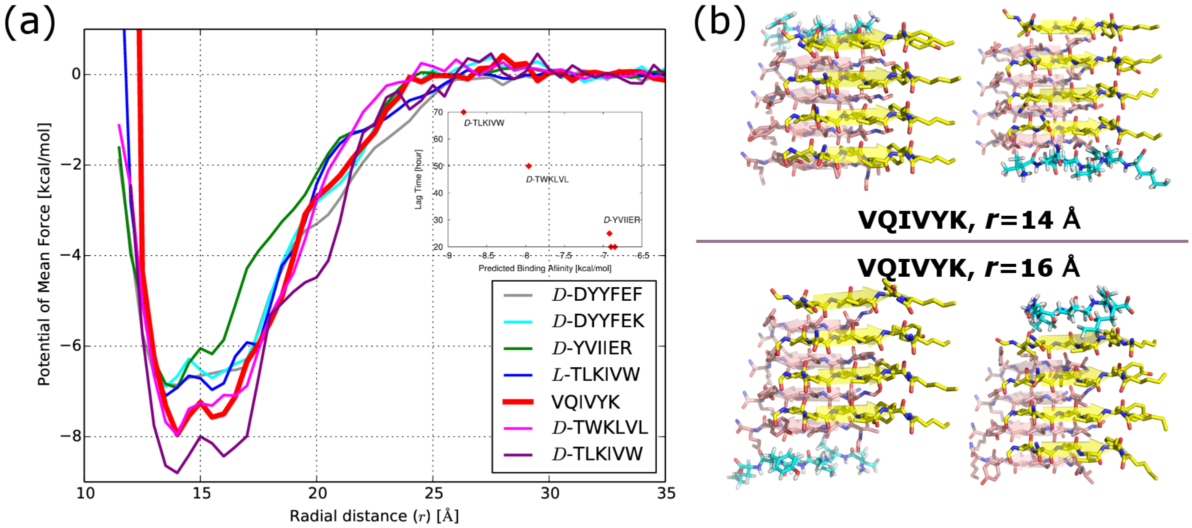

Figure 5.2. Effective inhibitors bind to the top and bottom of the VQIVYK fibril. (a) Potential of mean force (PMF) profile of the VQIVYK fibril and previously designed D-peptide inhibitors. In the PMF profile of a single VQIVYK molecule to be added to the VQIVYK fibril (red), the global minimum occurs at r = 14 Å which coincides with two hydrogen bonding sites on the top and bottom of the fibril. The most potent inhibitor *in vitro,* D-TLKIVW, has its lowest PMF score at r = 14 Å (dark purple), which coincides with the lowest PMF score of VQIVYK. D-TLKIVW, along with potent inhibitor D-TWKLVL, was predicted to have a higher or comparable binding affinity for the VQIVYK fibril than a single VQIVYK molecule. Predicted binding affinity and the lag time for fibril formation reduction *in vitro* show good correlation (Inset). Fibril growth kinetics data was reported previously (19). **(b)** Representative conformations of a single VQIVYK molecule (cyan) on top and bottom of the fibril (composed of two sheets in yellow and pink). Representative MD snapshots of the lowest energy conformation at two minimums on the PMF profile (r = 14 Å and 16 Å) are shown.

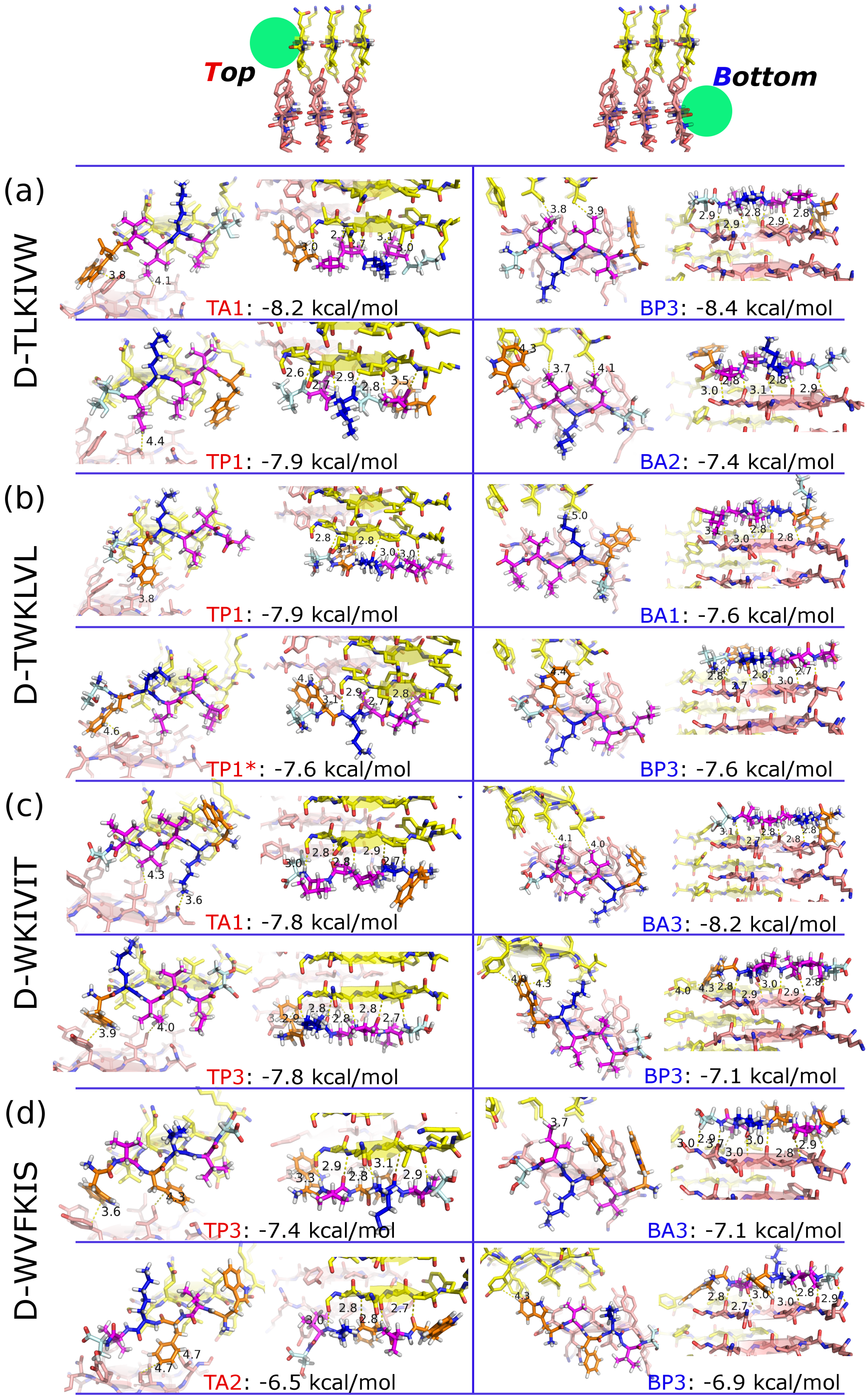

Figure 5.3. Predicted binding modes of the D-peptide inhibitors with the

lowest energies. Representative snapshots of the lowest and the second lowest binding energy clusters of **(a)** D-TLKIVW, **(b)** D-TWKLVL, **(c)** D-WKIVIT, and **(d)** D-WVFKIS are presented. The naming convention of each hydrogen bonding pattern is explained in Supplementary Figure 5.2. It is noted that TP1* of D-TWKLVL is oriented similarly to TP1, but is shifted to the N-terminus by 2 amino acids.

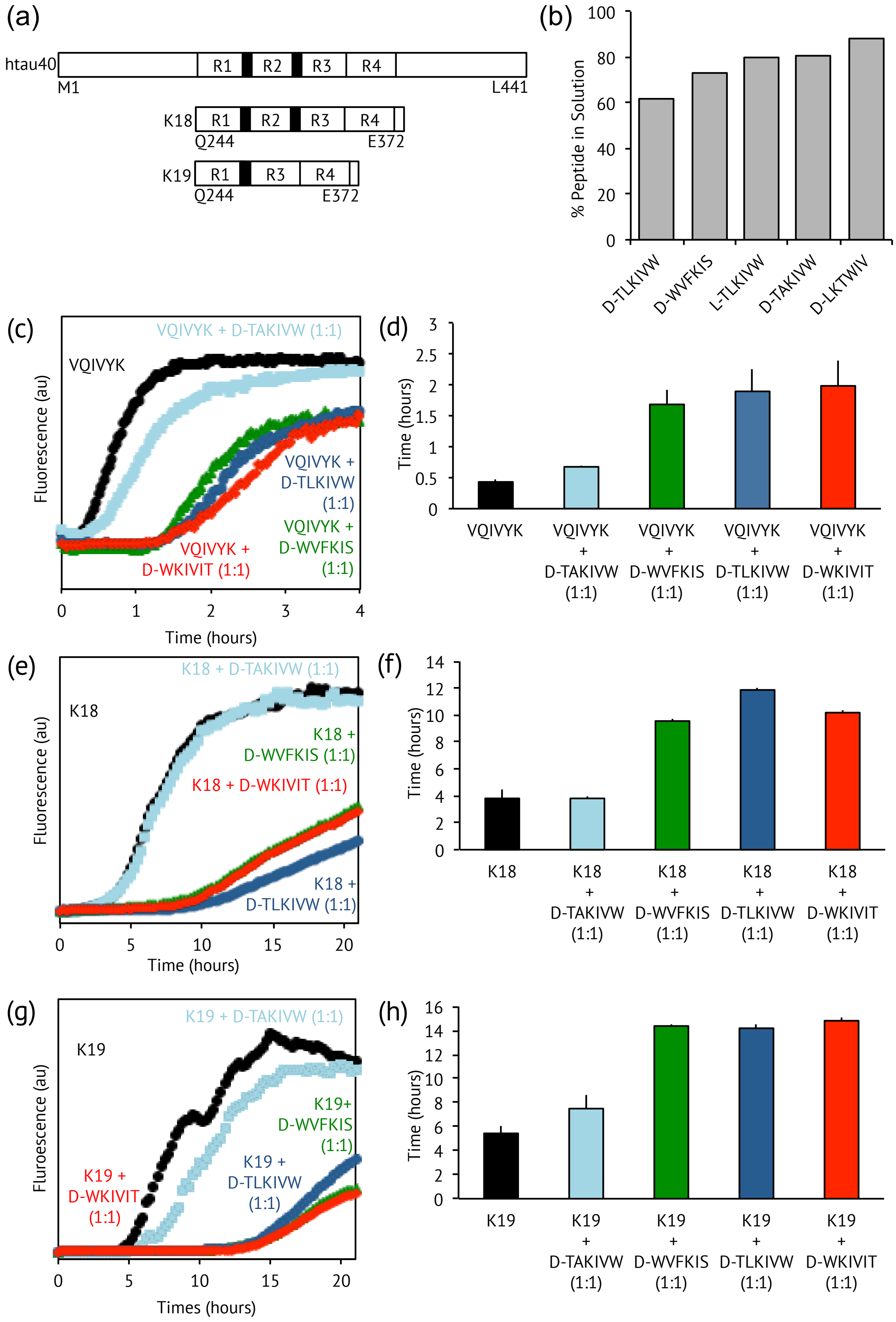
(a)
htau40
R1
R2
R3
R4
M1
L441
K18
R1
R2
R3
R4
Q244
E372
K19
R1
R3
R4
Q244
E372
(b)
% Peptide in Solution
100
80
60
40
20
0
D-TLKIVW
D-WVFKIS
L-TLKIVW
D-TAKIVW
D-LKTWIV
(c)
VQIVYK + D-TAKIVW (1:1)
VQIVYK
VQIVYK + D-TLKIVW (1:1)
VQIVYK + D-WVFKIS (1:1)
VQIVYK + D-WKIVIT (1:1)
Fluorescence (au)
0
1
2
3
4
Time (hours)
(d)
Time (hours)
3
2.5
2
1.5
1
0.5
0
VQIVYK
VQIVYK + D-TAKIVW (1:1)
VQIVYK + D-WVFKIS (1:1)
VQIVYK + D-TLKIVW (1:1)
VQIVYK + D-WKIVIT (1:1)
(e)
K18 + D-TAKIVW (1:1)
K18
K18 + D-WVFKIS (1:1)
K18 + D-WKIVIT (1:1)
K18 + D-TLKIVW (1:1)
Fluorescence (au)
0
5
10
15
20
Time (hours)
(f)
Time (hours)
14
12
10
8
6
4
2
0
K18
K18 + D-TAKIVW (1:1)
K18 + D-WVFKIS (1:1)
K18 + D-TLKIVW (1:1)
K18 + D-WKIVIT (1:1)
(g)
K19 + D-TAKIVW (1:1)
K19
K19+ D-WVFKIS (1:1)
K19 + D-TLKIVW (1:1)
K19 + D-WKIVIT (1:1)
Fluroescence (au)
0
5
10
15
20
Times (hours)
(h)
Time (hours)
16
14
12
10
8
6
4
2
0
K19
K19 + D-TAKIVW (1:1)
K19 + D-WVFKIS (1:1)
K19 + D-TLKIVW (1:1)
K19 + D-WKIVIT (1:1)

Figure 5.4. Newly designed D-peptides bind VQIVYK fibrils and delay fibril formation of different tau constructs. **(a)** Schematic of tau constructs. Full-length tau (htau40) contains 4 repeat (R) domains. K18 contains all 4 R domains, whereas K19 lacks R2. The black bars represent the hexepeptide amyloid spines, VQIINK and VQIVYK, respectively. **(b)** Ac-VQIVYK-NH_2 binds designed D-peptide inhibitors and not negative controls. The graph shows the percent of D-peptide inhibitor in solution after incubation with Ac-VQIVYK-NH_2 fibrils. Less peptide in solution indicates stronger binding affinity to Ac-VQIVYK-NH_2 fibrils. **(c)-(h)** Newly designed D-peptides reduce tau fibril formation. In each experiment, a different tau construct was incubated alone (black) or with equimolar concentrations of either negative control D-TAKIVW (light blue), D-WVFKIS (green), D-TKIVW (dark blue) or D-WKIVIT (red) in the presence of 100 µM Thioflavin-S (ThS) in assay buffer. **(c)** 100 µM Ac-VQIVYK-NH_2 incubated alone forms fibrils in under 0.5 hours. **(d)** Lag times plots show the delay in fibril formation. Errors represent 1 standard deviation of triplicates. **(e)** 50 µM K18 incubated alone forms fibrils in just under 4 hours. D-TAKIVW (negative control) has little to no effect on lag time. **(f)** Lag times plots show the delay in fibril formation. Errors represent 1 standard deviation of triplicates. **(g)** 50 µM K19 incubated alone forms fibrils in 5 hours. D-TAKIVW (negative control) has little to no effect on lag time. **(h)** Lag times plots show the delay in fibril formation. Errors represent 1 standard deviation of triplicates.

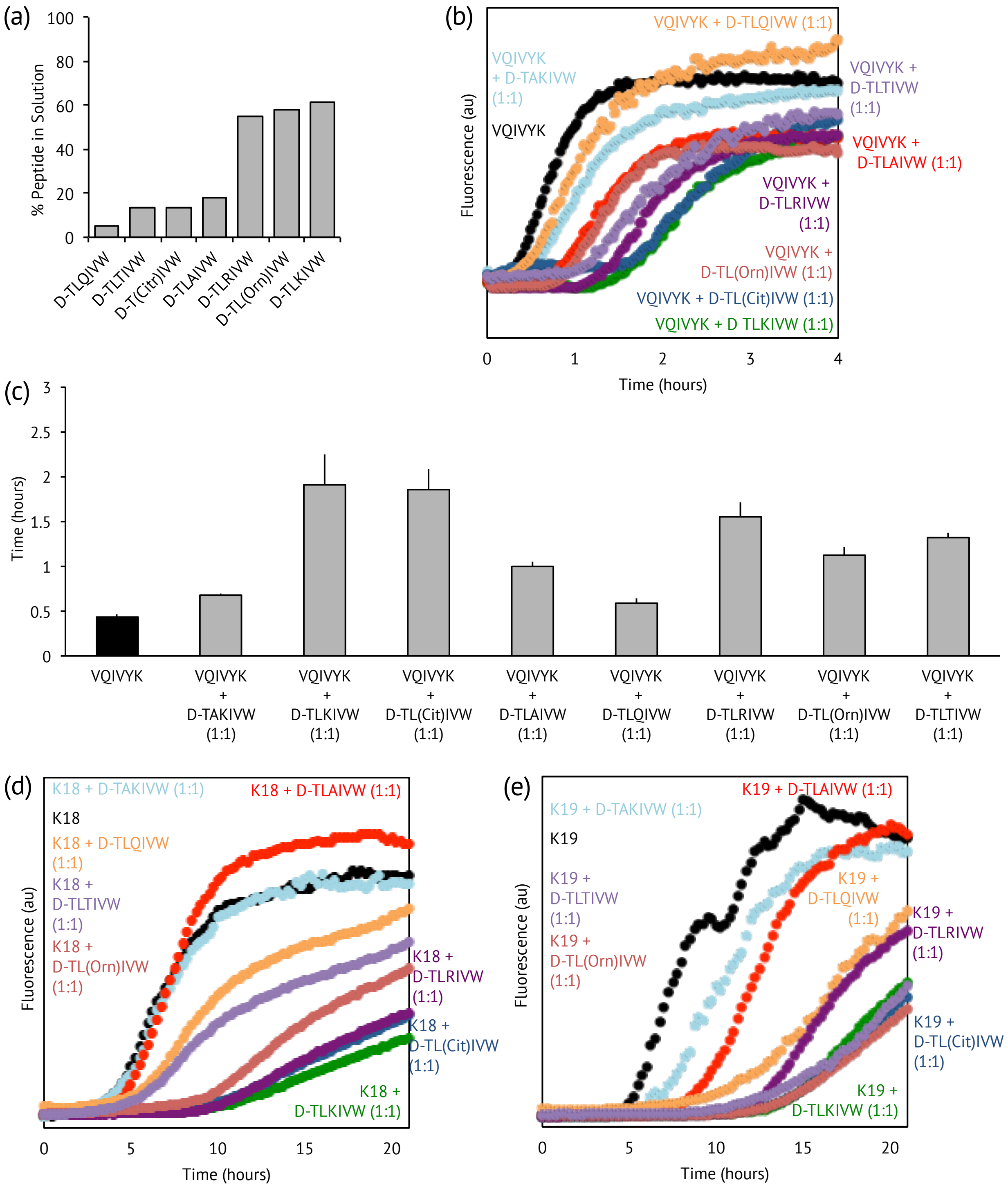

Figure 5.5. Select optimized D-peptides bind VQIVYK fibrils and delay fibril formation of different tau constructs. (a) Ac-VQIVYK-NH_2 binds most optimized D-

peptide inhibitors more specifically than the original D-peptide design D-TLKIVW. The graph shows the percent of D-peptide inhibitor in solution after incubation with Ac-VQIVYK-NH_2 fibrils. **(b)-(e)** Newly designed D-peptides delay tau fibril formation. In each experiment, a different tau construct was incubated alone (black) or with equimolar concentrations of either D-TLKIVW (dark green), D-TL(Cit)IVW (dark blue), D-TLAIVW (red), D-TLQIVW (orange), D-TLRIVW (dark purple), D-TL(Orn)IVW (rose), D-TLTIVW (light purple), or negative control D-TAKIVW (light blue) in the presence of 100 µM Thioflavin-S (ThS) in assay buffer. **(b)** 100 µM Ac-VQIVYK-NH_2 incubated alone forms fibrils in under 0.5 hours. **(c)** Lag times plots show the delay in fibril formation. Errors represent 1 standard deviation of triplicates. **(d)** 50 µM K18 incubated alone forms fibrils in just under 4 hours. D-TAKIVW (negative control) has little to no effect on lag time. **(e)** 50 µM K19 incubated alone forms fibrils in 5 hours. D-TAKIVW (negative control) has little to no effect on lag time.

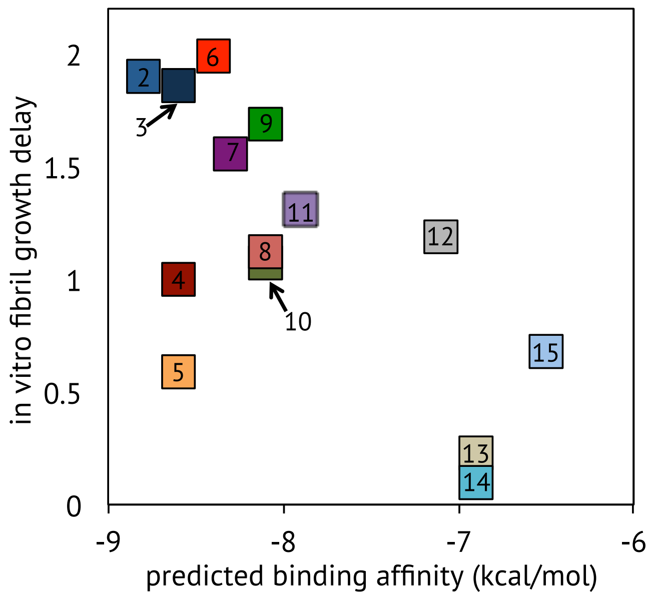

Figure 5.6. Plot of predicted binding affinity versus *in vitro* fibril growth delay. MD-developed D-peptide inhibitors with strong predicted binding affinities potently delay Ac-VQIVYK-NH_2 fibril formation. 2: D-TLKIVW, 3: D-TL(Cit)IVW , 4: D-TLAIVW , 5: D-TLQIVW , 6: D-WKIVIT , 7: D-TLRIVW , 8: D-TL(Orn)IVW , 9: D-WVFKIS , 10: D-TWKLVL, 11: D-TLTIVW, 12: L-TLKIVW, 13: D-YVIIER, 14: D-DYYFEK, 15: D-TAKIVW. The two exceptions are D-TLAIVW and D-TLQIVW. VQIVYK is not shown.

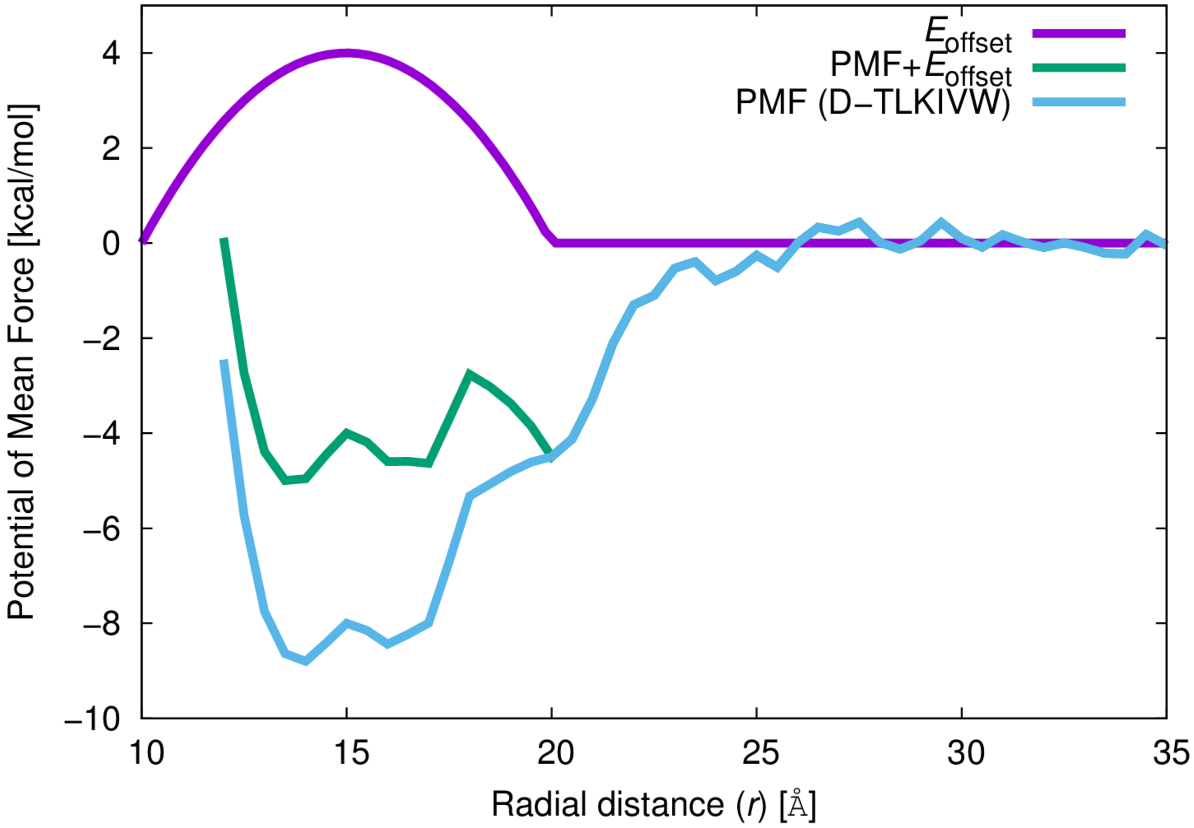

Supplementary Figure 5.1. The boost potential (E_{boost}) creates an energy penalty that promotes the sampling of unbound states. Without this energy penalty, the MD simulations will search for conformations near the bottom of the energy well (-9 kcal/mol). Searching for conformations at this position makes calculating the energy of the unbound state, which is essential for calculating the binding energy (ΔG) difficult to do. When simulating D-TLKIVW bound to the VQIVYK fibril, the minimum in the potential of mean force (PMF) is elevated to -5 kcal/mol, allowing for the sampling of a sufficient number of unbound states ($r > 25$ Å) more frequently.

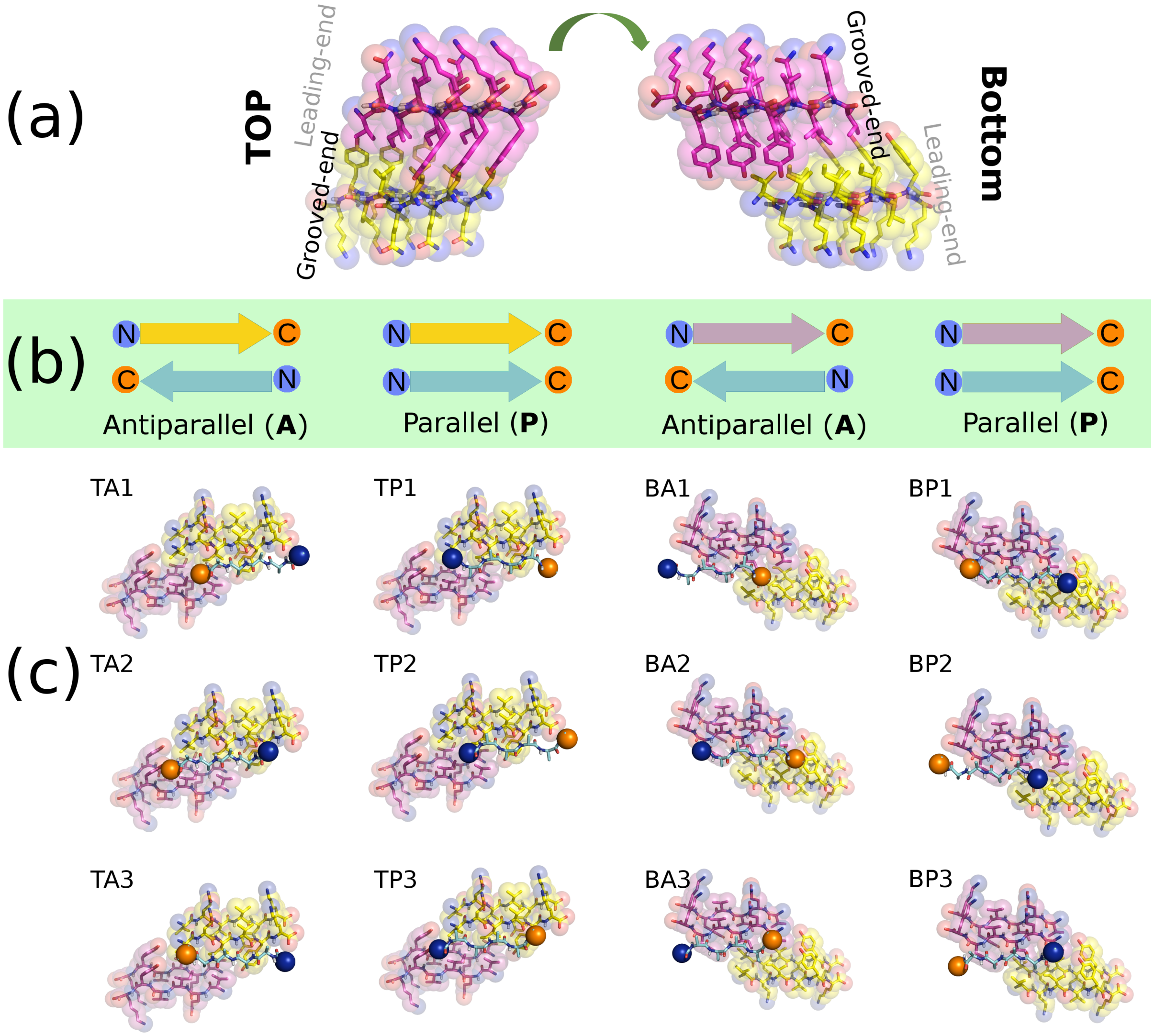

Supplementary Figure 5.2. Putative binding modes of designed D-peptide inhibitors. (a) Possible sites at which the D-peptide inhibitors can bind to the top (T) and bottom (B) of the VQIVYK fibril. The two binding sites on either side of the fibril are termed the leading-end and the grooved-end. **(b)** Schematic showing that the D-peptide inhibitors (cyan) can align parallel (P) or anti-parallel (A) to the ends of the single VQIVYK molecules in the VQIVYK fibril (yellow or pink). **(c)** Given that each designed D-peptide inhibitor can bind in three different conformations at the ends of fibrils, and that there are four fibril ends were these inhibitors can bind, there are twelve putative binding modes of designed D-peptide inhibitors in total. We assumed D-peptides maximize intermolecular hydrogen bonding. Cα atoms of amide and carboxylic termini of the D-peptide inhibitor are highlighted in blue and orange, respectively. D-peptide inhibitors are shown in cyan and the sheets of the fibril are shown in yellow and pink.

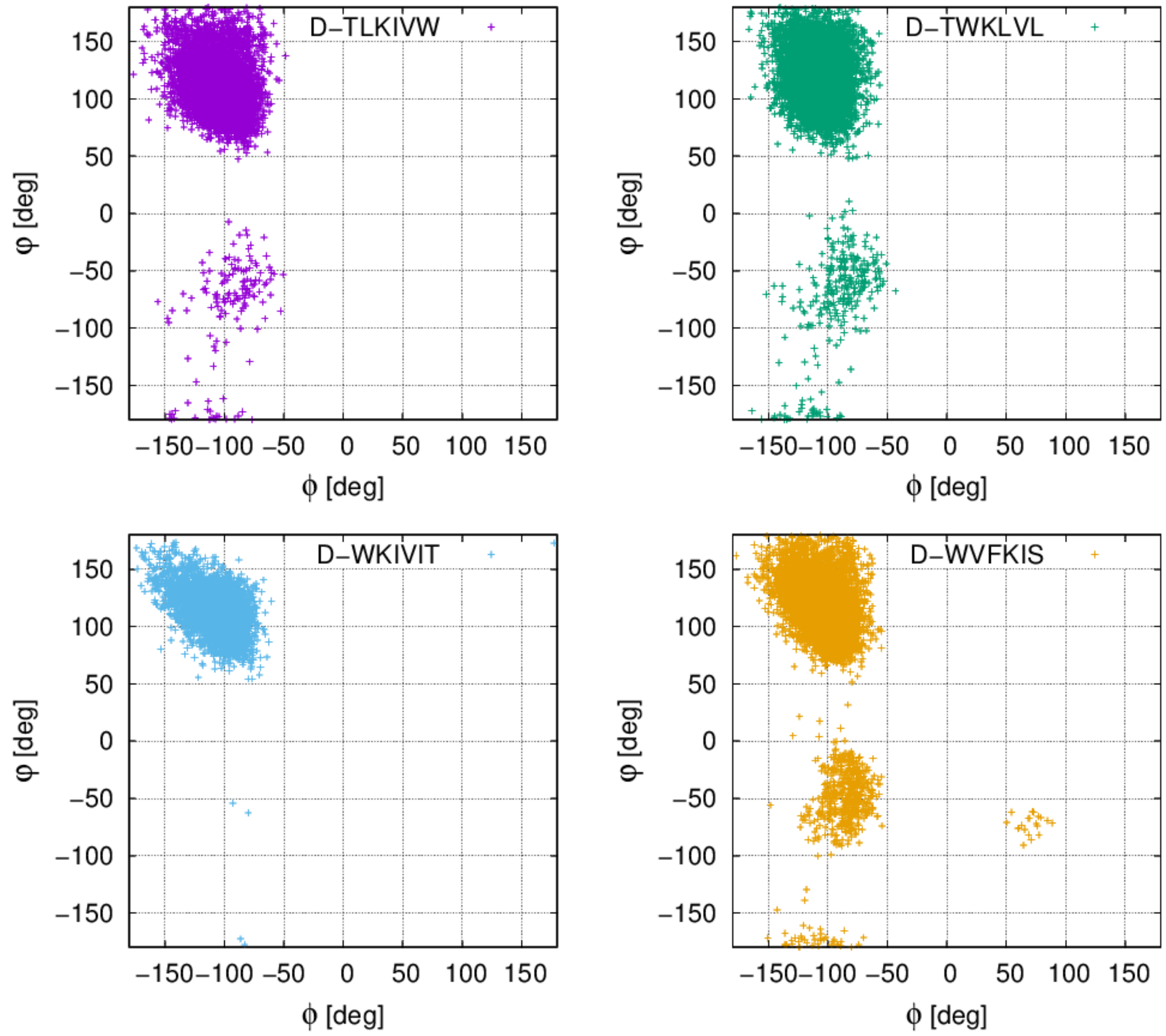

Supplementary Figure 5.3. Ramachandran plot of designed D-peptide inhibitors. We analyzed snapshots from MD simulations where the inhibitors are bound to the VQIVYK fibril. Almost all (φ,ψ) pairs are in the extended ß-sheet region. For D-WVFKIS, a fraction of (φ,ψ) are in unfavored region: (φ,ψ) is near (90,-90). This is because the inhibitor possesses a kink between 1D-TRP and 2D-VAL upon binding to the bottom of the VQIVYK fibril (Figure 5.2 d). The signs of (φ,ψ) angles are inverted to make the plot comparable to that of L-amino acids.

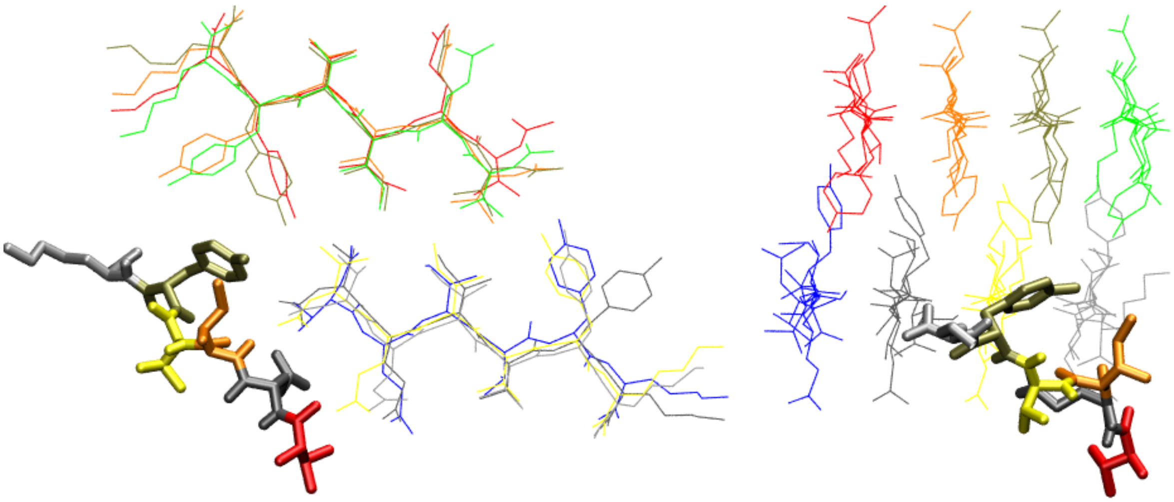

Supplementary Figure 5.4. MD snapshot revealing how a single VQIVYK molecule can bind nonspecifically to the VQIVYK fibril. The single molecules are shown as thicker sticks and the molecules that compose the fibril are shown as thinner lines.

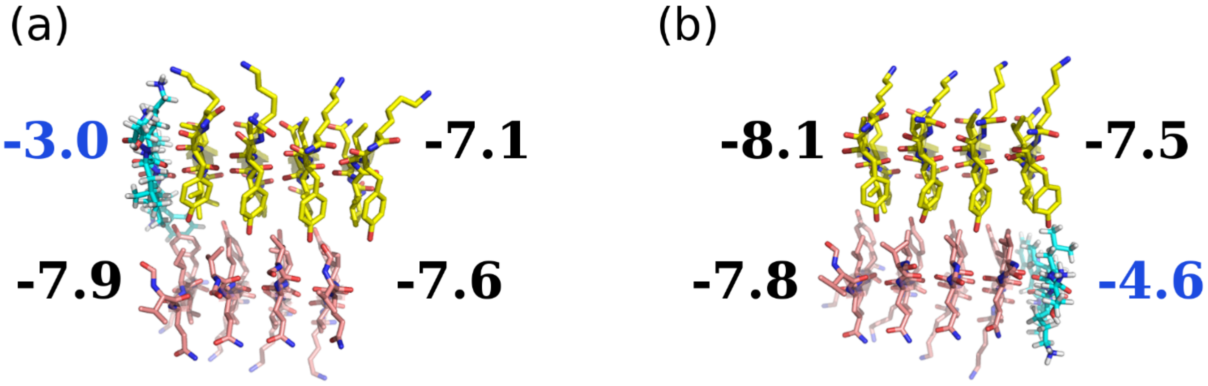

Supplementary Figure 5.5. D-peptide inhibitors prevent VQIVYK molecules from binding to the growing ends of VQIVYK fibrils. D-TLKIVW binds to two sites on the VQIVYK fibril: the grooved-end on the top (T1 in Figure5.3 (a)) **(a)** and to the grooved-end on the bottom of the VQIVYK fibril (B1 in Figure 5.3 (a)) **(b)**. When D-TLKIVW is bound to one of these sites, the binding strength of a VQIVYK molecule to the fibril is significantly reduced (-3.0 from -8.1 kcal/mol **(a)** and -4.6 from -7.6 kcal/mol **(b)**). Additionally, these results suggest that D-TLKIVW molecules must bind to the fibril at both sites in order to reduce fibril formation. The binding energy for a VQIVYK molecule to bind to the fibril at other sites, like the leading-ends of fibrils, is not affected by D-TLKIVW bound to the grooved-ends fibril (binding energies shown in black). D-TLKIVW is shown in cyan and the sheets of the VQIVYK fibril are shown in yellow and pink. Units for computed binding energy (ΔG_{bind}) of each binding site is kcal/mol.

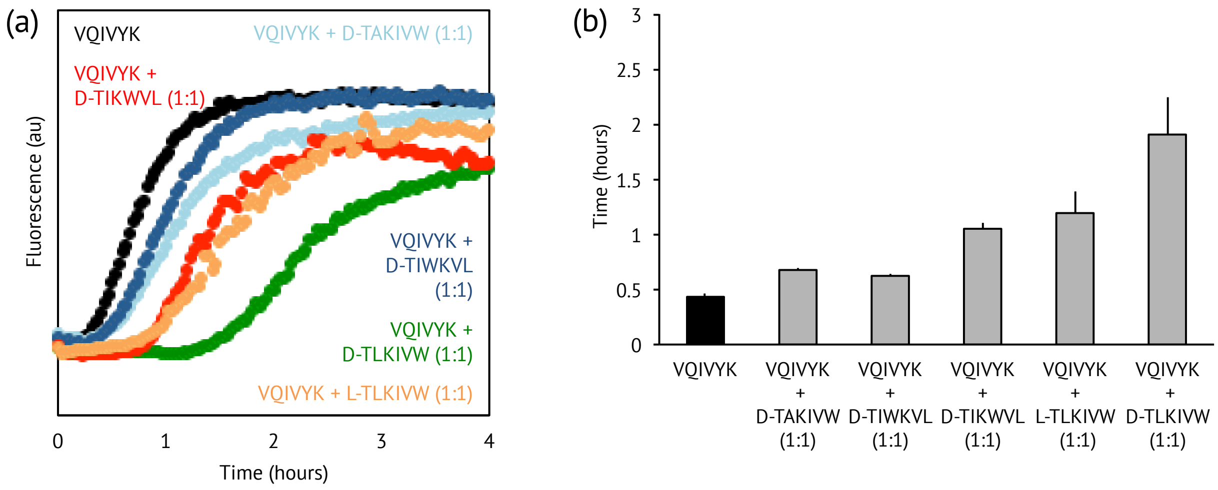

Supplementary Figure 5.6. Negative control peptides do not reduce Ac-VQIVYK-NH$_2$ fibril formation *in vitro*. **(a)** 100 μM Ac-VQIVYK-NH$_2$ incubated alone forms fibrils in under 0.5 hours. Negative control D-TAKIVW has little to no effect on fibril formation. Scrambled D-peptides, D-TIWKVL and D-TIKWVL, have little to no effect on fibril formation. The L-form negative control L-TLKIVW moderately delays fibril formation, but not nearly as effectively as designed D-peptide D-TLKIVW. **(b)** Lag times plots show the delay in fibril formation. Errors represent 1 standard deviation of triplicates.

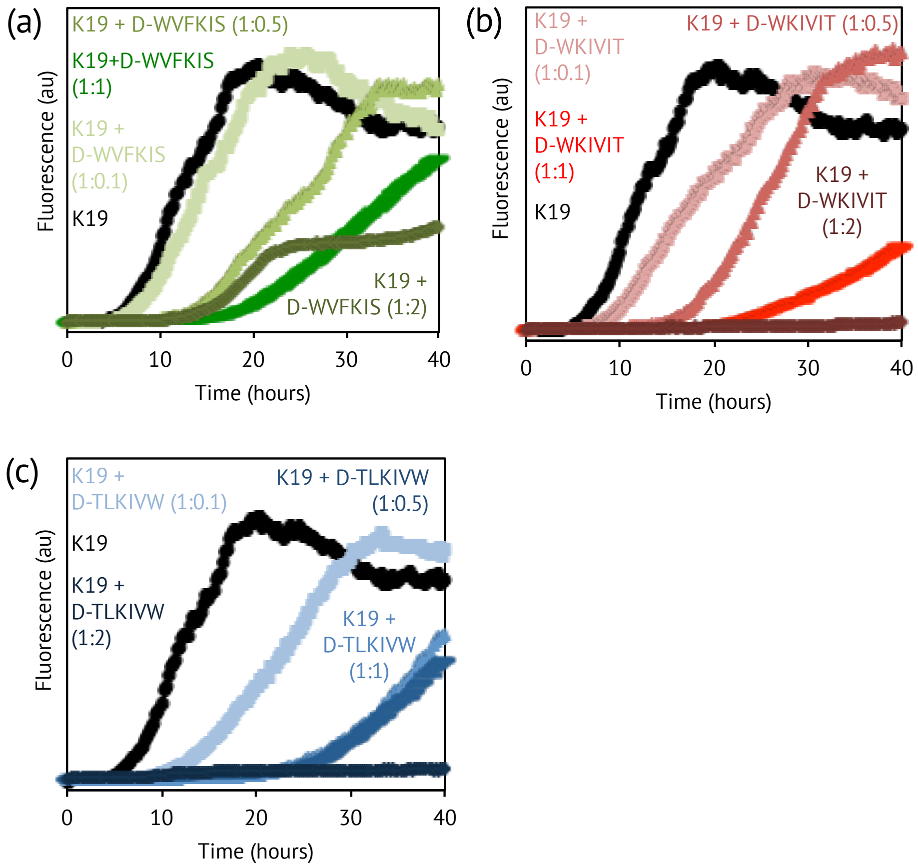

Supplementary Figure 5.7. Designed D-peptides delay K19 fibril formation in a concentration-dependent manner. **(a)** D-WVFKIS was tested at different molar ratios (1:0.1, 1:0.5, 1:1, and 1:2) for its ability to delay K19 fibril formation. Ratios 1:1 and 1:2 of K19 to D-WVFKIS were most effective. **(b)** D-WKIVIT was tested at the same molar ratios as D-WVFKIS for its ability to delay K19 fibril formation. Ratios 1:1 and 1:2 of K19 to D-WKIVIT were most effective. **(c)** D-TLKIVW was tested at the same molar ratios as D-WVFKIS for its ability to delay K19 fibril formation. Ratios 1:1 and 1:2 of K19 to D-TLIVW were most effective.

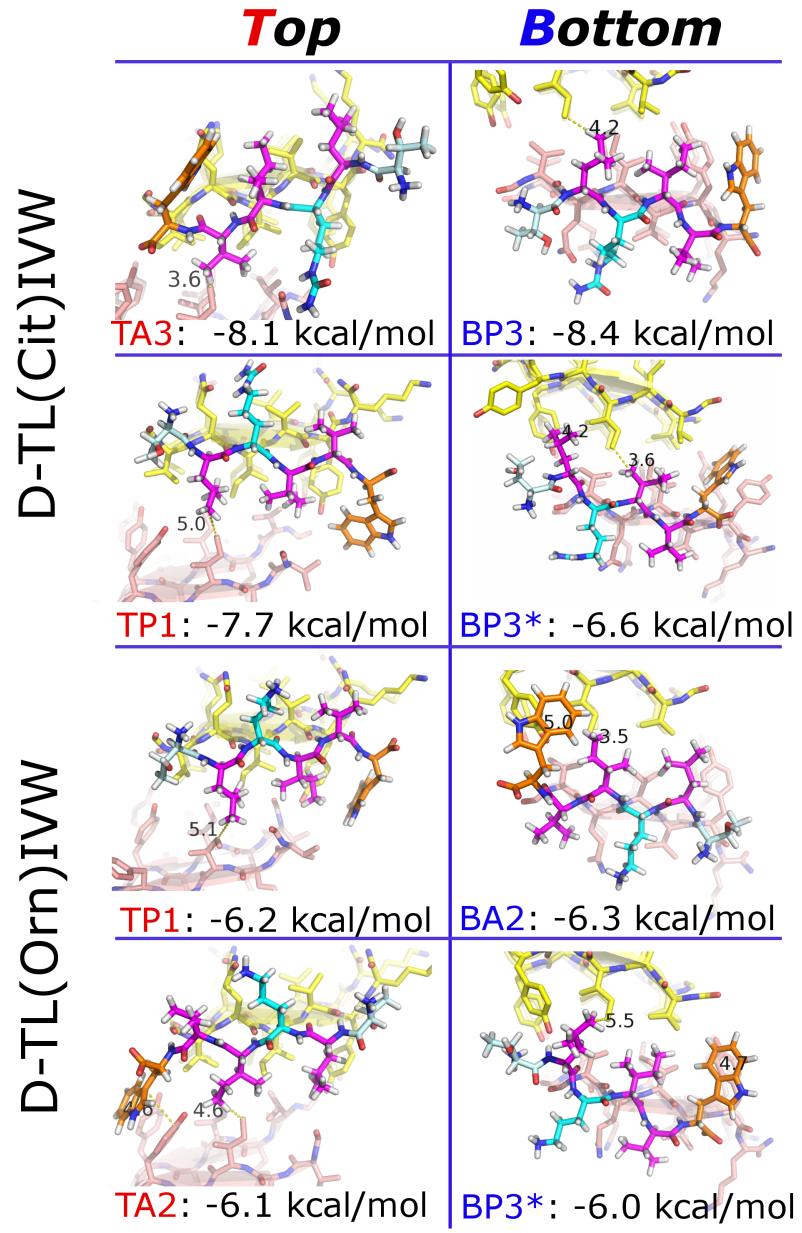

Supplementary Figure 5.8. Multiple binding modes of D-TL(Cit)IVW and D-TL(Orn)IVW. BP3 has identical backbone orientation to BP3, but the hydrogen bond registry is shifted toward the N-terminus by 2 amino acids. A schematic explaining the abbreviations for the binding modes is shown in Supplementary Figure 5.2.

Table 5.1. Predicted binding affinity and effectiveness at delaying fibril formation *in vitro*. The binding affinity (ΔG_{bind}) of each inhibitor was computed using REX-CF MD simulations. The *in vitro* fibril growth delay (ΔT_{Fiber}) measures the fibril formation delay observed in the ThS assays. In the ThS assays, D-peptides were used at equimolar concentrations with 100 μM Ac-VQIVYK-NH$_2$. The assay conditions are described in more detail in the Methods section.

	Inhibitor sequence	**Predicted binding affinity (ΔG_{bind})**	**In vitro fibril growth delay (ΔT_{Fiber})**
1	VQIVYK	-8.0 kcal/mol	0.433 ± 0.033
2	D-TLKIVW	-8.8 kcal/mol	1.899 ± 0.353
3	D-TL(Cit)IVW	-8.6 kcal/mol	1.856 ± 0.222
4	D-TLAIVW	-8.6 kcal/mol	1.000 ± 0.058
5	D-TLQIVW	-8.6 kcal/mol	0.589 ± 0.051
6	D-WKIVIT	-8.4 kcal/mol	1.989 ±0.417
7	D-TLRIVW	-8.3 kcal/mol	1.556 ± 0.158
8	D-TL(Orn)IVW	-8.1 kcal/mol	1.122 ± 0.0834
9	D-WVFKIS	-8.1 kcal/mol	1.689 ± 0.222
10	D-TWKLVL	-8.1 kcal/mol	1.072 + 0.061
11	D-TLTIVW	-7.9 kcal/mol	1.311 ± 0.069
12	D-TIWKVL	-7.5 kcal/mol	0.396 + 0.187
13	L-TLKIVW	-7.1 kcal/mol	1.189 ± 0.201
14	D-YVIIER	-6.9 kcal/mol	0.228 + 0.093

15	D-TIKWVL	-6.9 kcal/mol	0.505 + 0.440
16	D-DYYFEK	-6.9 kcal/mol	0.094+ 0.039
17	D-TAKIVW	-6.5 kcal/mol	0.678 ± 0.019
18	D-LKTWIV	-5.5 kcal/mol	0.266 ± 0.206

REFERENCES

1. Eisenberg D, Jucker M. 2012 The amyloid state of proteins in human diseases. *Cell* **148**:1188–1203. doi:10.1016/j.cell.2012.02.022

2. Sunde M, Serpell LC, Bartlam M, Fraser PE, Pepys MB, Blake CC. 1997 Common core structure of amyloid fibrils by synchrotron X-ray diffraction. *J Mol Biol* **273**:729–739. doi:10.1006/jmbi.1997.1348

3. Eisenberg DS, Sawaya MR. 2017 Structural Studies of Amyloid Proteins at the Molecular Level. *Annu Rev Biochem* **86**:null. doi:10.1146/annurev-biochem-061516-045104

4. Nelson R, Sawaya MR, Balbirnie M, Madsen AØ, Riekel C, Grothe R, Eisenberg D. 2005 Structure of the cross-beta spine of amyloid-like fibrils. *Nature* **435**:773–778. doi:10.1038/nature03680

5. Sawaya MR, Sambashivan S, Nelson R, Ivanova MI, Sievers SA, Apostol MI, Thompson MJ, Balbirnie M, Wiltzius JJW, McFarlane HT, Madsen AØ, Riekel C, Eisenberg D. 2007 Atomic structures of amyloid cross-β spines reveal varied steric zippers. *Nature* **447**:453–457. doi:10.1038/nature05695

6. Härd T, Lendel C. 2012 Inhibition of Amyloid Formation. *J Mol Biol*1–25. Available at: http://dx.doi.org/10.1016/j.jmb.2011.12.062

7. Cheng B, Gong H, Xiao H, Petersen RB, Zheng L, Huang K. 2013 Inhibiting toxic aggregation of amyloidogenic proteins: A therapeutic strategy for protein misfolding diseases. *Biochim Biophys Acta - Gen Subj* **1830**:4860–4871. doi:10.1016/j.bbagen.2013.06.029

8. Rational design of potent human transthyretin amyloid disease inhibitors. 2000 *Nat Struct Mol Biol Publ online 01 May 2000; | doi101038/75225* **7**:431. doi:10.1038/75225

9. Baral PK, Swayampakula M, Rout MK, Kav NN V, Spyracopoulos L, Aguzzi A, James MNG. 2014 Structural basis of prion inhibition by phenothiazine compounds. *Structure* **22**:291–303. doi:10.1016/j.str.2013.11.009

10. Makley LN, McMenimen KA, DeVree BT, Goldman JW, McGlasson BN, Rajagopal P, Dunyak BM, McQuade T, Thompson AD, Sunahara R, Klevit RE, Andley UP, Gestwicki JE. 2015 Pharmacological chaperone for alpha-crystallin partially restores transparency in cataract models. *Science (80-)* **350**:674–677. doi:10.1126/science.aac9145

11. Waddington Cruz M, Benson MD. 2015 A Review of Tafamidis for the Treatment of Transthyretin-Related Amyloidosis. *Neurol Ther* **4**:61–79. doi:10.1007/s40120-015-0031-3

12. Gauthier S, Feldman HH, Schneider LS, Wilcock GK, Frisoni GB, Hardlund JH, Moebius HJ, Bentham P, Kook K a, Wischik DJ, Schelter BO, Davis CS, Staff RT, Bracoud L, Shamsi K, Storey JMD, Harrington CR, Wischik CM. 2016 Efficacy and safety of tau-aggregation inhibitor therapy in patients with mild or moderate Alzheimer's disease: a randomised, controlled, double-blind, parallel-arm, phase 3 trial. *Lancet* **6736**: doi:10.1016/S0140-6736(16)31275-2

13. Hyung S-J, DeToma AS, Brender JR, Lee S, Vivekanandan S, Kochi A, Choi J-S, Ramamoorthy A, Ruotolo BT, Lim MH. 2013 Insights into antiamyloidogenic properties of the green tea extract (-)-epigallocatechin-3-gallate toward metal-associated amyloid-β species. *Proc Natl Acad Sci U S A* **110**:3743–8. doi:10.1073/pnas.1220326110

14. Porat Y, Abramowitz A, Gazit E. 2006 Inhibition of Amyloid Fibril Formation by Polyphenols: Structural Similarity and Aromatic Interactions as a Common Inhibition Mechanism. *Chem Biol Drug Des* **67**:27–37. doi:10.1111/j.1747-0285.2005.00318.x

15. Landau M, Sawaya MR, Faull KF, Laganowsky A, Jiang L, Sievers SA, Liu J, Barrio JR, Eisenberg D. 2011 Towards a Pharmacophore for Amyloid. *PLoS Biol* **9**:e1001080. doi:10.1371/journal.pbio.1001080

16. Xue W-F, Hellewell a. L, Gosal WS, Homans SW, Hewitt EW, Radford SE. 2009 Fibril Fragmentation Enhances Amyloid Cytotoxicity. *J Biol Chem* **284**:34272–34282. doi:10.1074/jbc.M109.049809

17. Cohen SIA, Linse S, Luheshi LM, Hellstrand E, White DA, Rajah L, Otzen DE, Vendruscolo M, Dobson CM, Knowles T. 2013 Proliferation of amyloid-β42 aggregates occurs through a secondary nucleation mechanism. *Proc Natl Acad Sci U S A* **110**:9758–63. doi:10.1073/pnas.1218402110

18. Jiang L, Liu C, Leibly D, Landau M, Zhao M, Hughes MP, Eisenberg D. 2013 Structure-based discovery of fiber-binding compounds that reduce the cytotoxicity of amyloid beta. *Elife*1–27. doi:10.7554/eLife.00857

19. Sievers SA, Karanicolas J, Chang HW, Zhao A, Jiang L, Zirafi O, Stevens JT, Münch J, Baker D, Eisenberg D. 2011 Structure-based design of non-natural amino-acid inhibitors of amyloid fibril formation. *Nature* **475**:96–100. doi:10.1038/nature10154

20. Saelices L, Johnson LM, Liang WY, Sawaya MR, Cascio D, Ruchala P, Whitelegge J, Jiang L, Riek R, Eisenberg DS. 2015 Uncovering the mechanism of aggregation of human transthyretin. *J Biol Chem* **290**:28932–28943. doi:10.1074/jbc.M115.659912

21. Soragni A, Janzen DM, Johnson LM, Lindgren AG, Thai-Quynh Nguyen A, Tiourin E, Soriaga AB, Lu J, Jiang L, Faull KF, Pellegrini M, Memarzadeh S, Eisenberg DS. 2016 A Designed Inhibitor of p53 Aggregation Rescues p53 Tumor Suppression in Ovarian Carcinomas. *Cancer Cell* **29**:90–103. doi:10.1016/j.ccell.2015.12.002

22. Zheng J, Liu C, Sawaya MR, Vadla B, Khan S, Woods RJ, Eisenberg D, Goux WJ, Nowick JS. 2011 Macrocyclic β-Sheet Peptides That Inhibit the Aggregation of a Tau-Protein-Derived Hexapeptide. *J Am Chem Soc* **133**:3144–3157. Available at: http://pubs.acs.org/doi/abs/10.1021/ja110545h

23. Cruz M, Tusell JM, Grillo-Bosch D, Albericio F, Serratosa J, Rabanal F, Giralt E. 2004 Inhibition of beta-amyloid toxicity by short peptides containing N-methyl amino acids. *J Pept Res* **63**:324–328. doi:10.1111/j.1399-3011.2004.00156.x

24. Kokkoni N, Stott K, Amijee H, Mason JM, Doig AJ. 2006 N-Methylated Peptide Inhibitors of β-Amyloid Aggregation and Toxicity. Optimization of the Inhibitor Structure. *Biochemistry* **45**:9906–9918.

25. Kawashima H, Sohma Y, Nakanishi T, Kitamura H, Mukai H, Yamashita M, Akaji K, Kiso Y. 2013 A New Class of Aggregation Inhibitors of Amyloid-β Peptide Based on an O-Acyl Isopeptide. *Bioorganic Med Chem Lett* **21**:6323–6327.

26. Spillantini MG, Goedert M. 2013 Tau pathology and neurodegeneration. *Lancet Neurol* **12**:609–622. doi:10.1016/S1474-4422(13)70090-5

27. Lindert S, Meiler J, McCammon JA. 2013 Iterative Molecular Dynamics—Rosetta Protein Structure Refinement Protocol to Improve Model Quality. *J Chem Theory Comput* **9**:3843–3847. doi:10.1021/ct400260c

28. Wang J, Ma C, Fiorin G, Carnevale V, Wang T, Hu F, Lamb RA, Pinto LH, Hong M, Klein ML, DeGrado WF. 2011 Molecular Dynamics Simulation Directed Rational Design of Inhibitors Targeting Drug-Resistant Mutants of Influenza A Virus M2. *J Am Chem Soc* **133**:12834–12841. doi:10.1021/ja204969m

29. Kiss G, Pande VS, Houk KN. 2013 "Molecular Dynamics Simulations for the Ranking, Evaluation, and Refinement of Computationally Designed Proteins," in, 145–170. doi:10.1016/B978-0-12-394292-0.00007-2

30. Chodera JD, Mobley DL, Shirts MR, Dixon RW, Branson K, Pande VS. 2011 Alchemical free energy methods for drug discovery: progress and challenges. *Curr Opin Struct Biol* **21**:150–160. doi:10.1016/j.sbi.2011.01.011

31. Grubmüller H. 1995 Predicting slow structural transitions in macromolecular systems: Conformational flooding. *Phys Rev E* **52**:2893–2906. doi:10.1103/PhysRevE.52.2893

32. Babin V, Roland C, Darden TA, Sagui C. 2006 The free energy landscape of small peptides as obtained from metadynamics with umbrella sampling corrections. *J Chem Phys* **125**:204909. doi:10.1063/1.2393236

33. Kuriyan J, Konforti B, Wemmer D. 2012 *The Molecules of Life: Physical and Chemical Principles*. 1st ed. Garland Science (2012).

34. Kabsch W, Sander C. 1983 Dictionary of protein secondardy structure: pattern recognition of hydrogen-bonded and geometrical features. *Biopolymers* **22**:2577–2637.

35. Holmes BB, Furman JL, Mahan TE, Yamasaki TR, Mirbaha H, Eades WC, Belaygorod L, Cairns NJ, Holtzman DM, Diamond MI. 2014 Proteopathic tau seeding predicts tauopathy in vivo. *Proc Natl Acad Sci* **111**:E4376–E4385. doi:10.1073/pnas.1411649111

36. Dantas G, Kuhlman B, Callender D, Wong M, Baker D. 2003 A large scale test of computational protein design: folding and stability of nine completely redesigned globular proteins. *J Mol Biol* **332**:449–60.

37. Kuhlman B, Dantas G, Ireton GC, Varani G, Stoddard BL, Baker D. 2003 Design of a Novel Globular Protein Fold with Atomic-Level Accuracy. *Science (80-)* **302**:1364–1368. doi:10.1126/science.1089427

38. MacKerell AD, Bashford D, Bellott M, Dunbrack RL, Evanseck JD, Field MJ, Fischer S, Gao J, Guo H, Ha S, et al. 1998 All-atom empirical potential for molecular modeling and dynamics studies of proteins. *J Phys Chem B* **102**:3586–616. doi:10.1021/jp973084f

39. Lazaridis T, Karplus M. 1999 Effective energy function for proteins in solution. *Proteins* **35**:133–52. Available at: http://www.ncbi.nlm.nih.gov/pubmed/10223287 [Accessed March 9, 2017]

40. Brooks BR, Brooks CL, Mackerell AD, Nilsson L, Petrella RJ, Roux B, Won Y, Archontis G, Bartels C, Boresch S, et al. 2009 CHARMM: The biomolecular simulation program. *J Comput Chem* **30**:1545–1614. doi:10.1002/jcc.21287

41. Sugita Y, Okamoto Y. 1999 Replica-exchange molecular dynamics method for protein folding. *Chem Phys Lett* **314**:141–151. doi:10.1016/S0009-2614(99)01123-9

42. Kumar S, Rosenberg JM, Bouzida D, Swendsen RH, Kollman PA. 1992 THE weighted histogram analysis method for free-energy calculations on biomolecules. I. The method. *J Comput Chem* **13**:1011–1021. doi:10.1002/jcc.540130812